NONEQUILIBRIUM QUASIPARTICLES IN SUPERCONDUCTING QUBITS

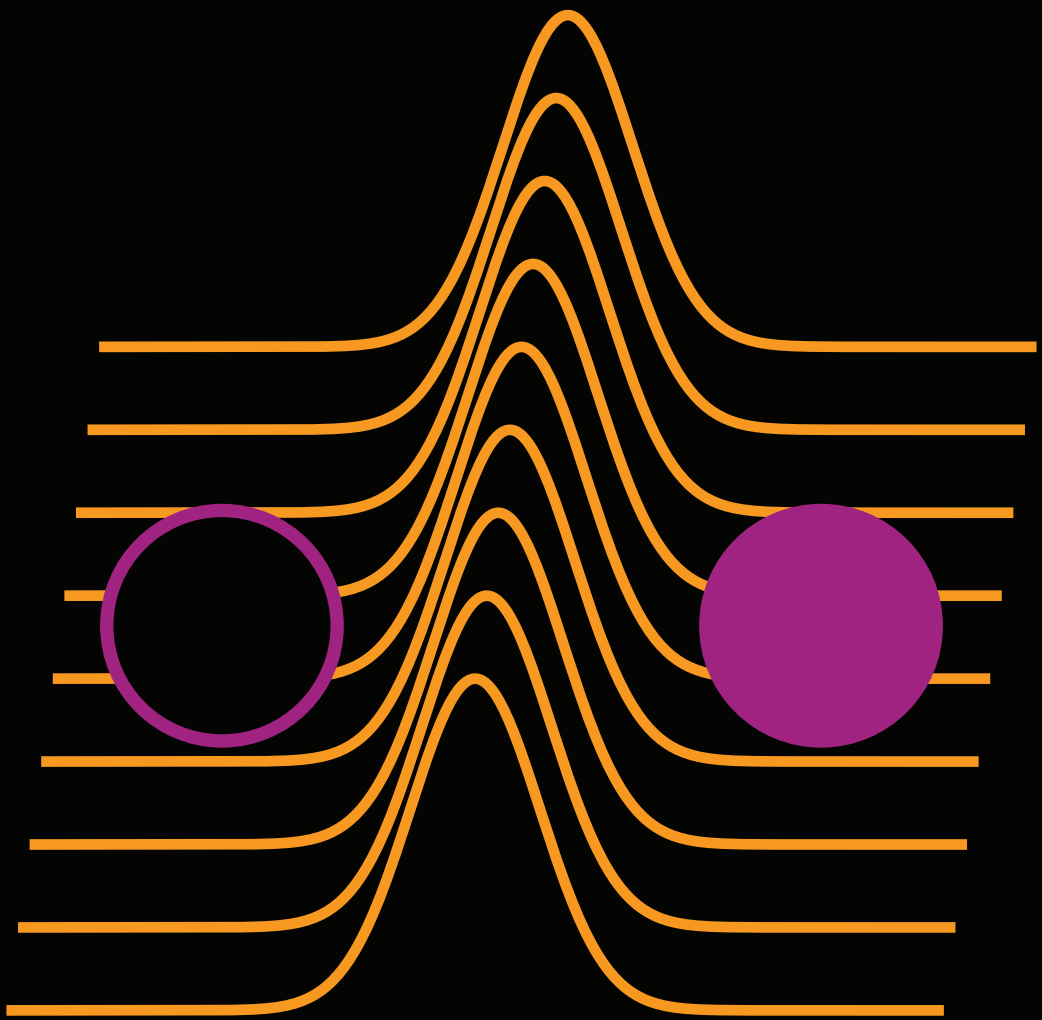

KYLE SERNIAK

Abstract

Nonequilibrium Quasiparticles in Superconducting Qubits

Kyle Serniak

2019

Nonequilibrium quasiparticle excitations (QPs) can constitute a significant source of dissipation in superconducting quantum devices. Surprisingly, the precise mechanisms by which these QPs are generated are to this day unknown. This dissertation describes our recent work seeking to understand the dynamics of nonequilibrium QPs and the limits they impose on the coherence of superconducting qubits. In the popular transmon qubit, QPs can cause dissipation when they tunnel across the Josephson junction of the circuit. Our experiments have focused on detecting changes in the charge-parity of offset-charge-sensitive transmon qubits: a signature of these QP tunneling events. Specifically, we extract QP-induced relaxation and excitation rates by correlating changes in the charge parity of the device with transitions between qubit states. This is achieved both by coherent mapping of charge parity onto the qubit state and by direct-dispersive detection of the joint qubit and charge-parity state. We find that QP-induced dissipation can be on equal footing with all other loss mechanisms and that QPs can be the dominant source of residual qubit excited-state population. Additionally, we have identified another mechanism that can induce both dissipation and charge parity switches, namely photon-assisted QP generation and tunneling (PAT) processes. Finally, we demonstrated that improved high-frequency RF filtering can significantly attenuate QP generating radiation, extending the energy relaxation time of transmon that was previously limited by QP-related processes by a factor of two.

NONEQUILIBRIUM QUASIPARTICLES IN SUPERCONDUCTING QUBITS

A Dissertation
Presented to the Faculty of the Graduate School
of
Yale University
in Candidacy for the Degree of
Doctor of Philosophy

by
Kyle Serniak

Dissertation Director: Michel H. Devoret

December 2019

Contents

List of Figures

List of Tables

List of Symbols

Acronyms

ABS	Andreev bound state
AC	alternating current ($\omega > 0$)
BCS	Bardeen-Cooper-Schrieffer (theory of superconductivity)
CPB	Cooper-pair box
cQED	circuit quantum electrodynamics
DC	direct current ($\omega = 0$)
DOS	density of states
EBPG	electron-beam pattern generator
EM	electromagnetic
HEMT	high-electron-mobility transistor
JJ	Josephson junction
JPC	Josephson parametric converter
LPF	low-pass filter
NMP	1-methyl-2-pyrrolidone
OCS	offset-charge sensitive
OFHC	oxygen-free high-conductivity
PAT	photon-assisted QP generation and tunneling
QHO	quantum harmonic oscillator
QIP	quantum information processing
QP	quasiparticle excitation
RF	radio-frequency
RF-SET	radio-frequency single electron transistor
SEM	scanning electron microscope
SIS	superconductor-insulator-superconductor
SNR	signal-to-noise ratio
SQUID	superconducting quantum interference device
TE	transverse electric

Constants

h	Planck's constant
$\hbar$	reduced Planck's constant ($= h/2\pi$)
e	charge of an electron
m_e	mass of an electron
Φ_0	magnetic flux quantum ($= h/2e$)
ϕ_0	reduced magnetic flux quantum ($= \hbar/2e$)
k_B	Boltzmann constant
R_q	superconducting resistance quantum ($= h/(2e)^2$)
G_q	superconducting conductance quantum ($= 1/R_q$)

Normal conductors

k	electron momentum
k_F	Fermi momentum
λ_F	Fermi wavelength
ε_F	Fermi energy
ξ_k	electron kinetic energy with momentum k, relative to ε_F
ν_n	normal state density of states
ν_0	normal density of states at the Fermi energy
$f_{\text{F.D.}}(\varepsilon)$	Fermi-Dirac energy distribution
d	electronic mean free path

BCS superconductivity

Δ	superconducting energy gap
T_c	superconducting critical temperature
ν_s	superconducting density of states
$\tilde{\nu}_s$	approximate superconducting density of states near the gap edge
$\hat{c}_{ls}, \hat{c}_{ls}^\dagger$	fermionic annihilation and creation operators for electrons in state l with spin s
$V_{kk'}$	BCS interaction parameter

H_{BCS}	BCS Hamiltonian
$H_{\mathrm{BCS}}^{\mathrm{eff}}$	effective, mean-field BCS Hamiltonian
u_k, v_k	BCS occupation factors ($\lvert u_k\rvert^2 + \lvert v_K\rvert^2 = 1$)
$\hat{\gamma}_{ks}, \hat{\gamma}_{ks}^{\dagger}$	fermionic annihilation and creation operators for QP excitations of state k and spin s in a BCS superconductor
Δ_k	BCS pair potential for electrons with momentum k
$\lvert\mathrm{BCS}\rangle_{\mathrm{G}}$	BCS ground-state wavefunction
$\lvert\mathrm{vac.}\rangle$	wavefunction representing an electron "vacuum" with no occupation

Superconducting materials

Δ_{Al}	superconducting energy gap of Al
Δ_{Nb}	superconducting energy gap of Nb
Δ'	proximitized superconducting energy gap
T_c^{Al}	critical temperature of Al
T_c^{Ti}	critical temperature of Ti
T_c'	proximitized superconducting critical temperature
d_{Al}	thickness of a layer of Al
d_{Ti}	thickness of a layer of Ti
l_c^{bulk}	superconducting coherence length in bulk material
l_c^{eff}	effective superconducting coherence length in a thin film

Quasiparticle density

N_{CP}	total number of Cooper pairs
N_{QP}	total number of QPs
n_{QP}	density of QPs
n_{CP}	density of Cooper pairs
x_{QP}	density of QPs normalized by n_{CP} ($= N_{\mathrm{QP}}/N_{\mathrm{CP}} = n_{\mathrm{QP}}/n_{\mathrm{CP}}$)
$x_{\mathrm{QP}}^{\mathrm{th.}}$	thermally generated QP density
x_{QP}^{0}	nonequilibrium contribution to x_{QP}

Quasiparticle kinetics

ε_k	QP excitation energy
ε'_k	QP excitation energy in the single-particle picture
$f(\varepsilon)$	QP energy distribution
$g(\varepsilon)$	energy dependent QP generation rate
η_g	Coupling efficiency of QP-generating radiation
$P_g(\varepsilon)$	QP-generation spectrum
$P_{\mathrm{BB}}(\varepsilon)$	blackbody power spectrum
T_{BB}	blackbody temperature
$I^s_{\mathrm{e\text{-}ph}}$	collision integral for electron-phonon scattering
$I^p_{\mathrm{e\text{-}ph}}$	collision integral for electron-pair-phonon scattering
$I_{\mathrm{e\text{-}e}}$	collision integral for electron-electron scattering
$N(\varepsilon)$	phonon energy distribution
T_{ph}	phonon temperature
τ_0	electron-phonon-scattering timescale
Γ_{cool}	characteristic timescale for QP cooling to the gap edge

Josephson junctions

I_J	Josephson supercurrent
V_J	voltage across a Josephson junction
L_J	Josephson inductance
τ_c	conduction channel transparency
$\bar{\tau}_c$	average channel transparency of a JJ
R_N	normal-state resistance of a JJ
I_0	critical current of a Josephson Junction ($\approx \frac{\pi\Delta}{2eR_N}$)
A	area of a Josephson junction
G_t	tunnel conductance of a JJ
φ	superconducting phase difference across a JJ
ε_A	Andreev-bound-state energy
I_A	Andreev current

Quantum bits

$\|\psi\rangle$	a general qubit state
$\|0\rangle$	ground state of a qubit
$\|1\rangle$	excited state of a qubit
$\hat{\sigma}_i$	a general Pauli operator
$\hat{\sigma}_x$	Pauli x operator
$\hat{\sigma}_y$	Pauli y operator
$\hat{\sigma}_z$	Pauli z operator
θ	polar angle describing a qubit Bloch vector
ϕ	azimuthal angle describing a qubit Bloch vector
$\vec{S}$	polarization vector in the Pauli basis
ρ_q	density operator
w_i	classical probability weights in a mixed state
$\|\pm\rangle$	positive or negative superposition state: $\frac{1}{\sqrt{2}}\left(\|0\rangle \pm \|1\rangle\right)$
$\hat{H}_q$	general qubit Hamiltonian
ω_{01}	qubit transition frequency
$\mathcal{P}_i$	equilibrium population of qubit state $\|i\rangle$

General decoherence

T_1	qubit energy relaxation time
T_ϕ	qubit pure-dephasing time
T_2	qubit coherence time ($= (1/2T_1 + 1/T_\phi)^{-1}$)
Γ_{ij}	total transition rate from qubit state $\|i\rangle$ to $\|j\rangle$
$\hat{F}_i$	a noisy environmental variable that couples to $\hat{\sigma}_i$ of the qubit
ϕ_F	phase accumulation from due to noise source F
$S_{FF}[\omega]$	power spectral density of fluctuations of a variable $\hat{F}$

Quantum circuits

$\hat{Q}$	charge operator
$\hat{I}$	current operator

$\hat{\Phi}$	flux operator
$\hat{V}$	voltage operator
$\hat{\varphi}$	dynamical phase operator
$\hat{n}$	Cooper-pair number operator
$\hat{n}'$	single-electron number operator
$\hat{\Phi}$	flux operator
U_i	energy stored in element i
C	capacitance
L	inductance
G	conductance
R	resistance
E_J	Josephson coupling energy
E_C	single-electron charging energy
E_L	inductive energy
$\hat{H}_{\mathrm{QHO}}$	Hamiltonian for the quantum harmonic oscillator
$\hat{a}, \hat{a}^\dagger$	bosonic annihilation and creation operators for photon excitations in a QHO
φ_{zpf}	zero-point fluctuations of the phase
n_{zpf}	zero-point fluctuations of the Cooper-pair number
Z_0	characteristic impedance of an LC oscillator ($= \sqrt{L/C}$)
ω_{LC}	resonant frequency of an LC oscillator ($= \sqrt{1/LC}$)
$Y[\omega]$	frequency-dependent admittance of a circuit element
U_x	potential energy associated with variable x

Cooper-pair box/transmon

$\hat{H}_{\mathrm{CPB}}$	Cooper-pair-box Hamiltonian
$\hat{H}_{\mathrm{t-mon}}$	transmon Hamiltonian neglecting charging effects
n_g	dimensionless offset charge
P	charge parity
p	charge-parity measurement outcome
$\lvert i, p\rangle$	joint plasmon (i) and charge-parity (p) state of a transmon

C_J	capacitance intrinsic to a Josephson junction
L_J	inductance of a Josephson junction
C_g	gate capacitance
C_S	coplanar capacitance shunting a Josephson junction
C_Σ	total capacitance shunting a Josephson junction
V_g	gate voltage
ω_p	circuit plasma frequency
$\epsilon_{i,p}$	eigenenergy of transmon state $\|i,p\rangle$
$\delta\epsilon_i$	charge dispersion of the i-th plasmon state
$\overline{\epsilon_i}$	time averaged energy of the i-th plasmon state, assuming ergodic fluctuations of offset charge and/or charge parity
$\overline{f_{ij}}$	time averaged f_{ij} ($= \overline{\epsilon_j} - \overline{\epsilon_i}$)
ω_p	plasma frequency of the transmon ($= \sqrt{8E_J E_C}/\hbar$)
$f_{ij}^{pp'}$	transition frequency between states $\|i,p\rangle$ and $\|j,p'\rangle$
$\omega_{ij}^{pp'}$	transition frequency between states $\|i,p\rangle$ and $\|j,p'\rangle$ in angular units ($= 2\pi f_{ij}^{pp'}$)
δf_{01}	maximum deviation of f_{01}^{pp} from $\overline{f_{01}}$
ρ_i^p	probability of occupying state $\|i,p\rangle$
$\tilde{\rho}(j,pp'\|i)$	probability of measuring state $\|j,p'\rangle$ given an initial state $\|i,p\rangle$
E_{J1}, E_{J2}	Josephson energies of the two junctions in a SQUID
$\Gamma_{ij}^{pp'}$	total transition rate from transmon state $\|i,p\rangle$ to state $\|j,p'\rangle$

Circuit QED

K	anharmonicity of a qubit
$\chi_{i,p}$	dispersive shift of a resonator from transmon state $\|i,p\rangle$
χ_{qr}	relative qubit dispersive shift of a readout resonator ($\chi_0^p - \chi_1^p$)
χ_{JC}	Jaynes-Cummings dispersive shift
ω_r	bare readout-mode resonant frequency
g	coupling rate between a qubit and a readout mode
κ_r	readout photon decay rate

QP-induced dissipation

$\hat{H}_q$	bare qubit Hamiltonian
$\hat{H}_{\mathrm{QP}}$	bare QP Hamiltonian
$\hat{H}_{\mathrm{QP},\hat{\varphi}}$	QP-qubit coupling Hamiltonian
$\hat{H}_{\mathrm{el}}$	full electronic Hamiltonian ($= \hat{H}_q + \hat{H}_{\mathrm{QP}} + \hat{H}_{\mathrm{QP},\hat{\varphi}}$)
$\Gamma_{ij}^{\mathrm{QP}}$	QP-induced transition rate from $\|i\rangle$ to $\|j\rangle$
Γ_{QP}	global scale for QP-induced transition rates
$S_{\mathrm{QP}}^{\pm}$	QP-tunneling spectral functions
$\Gamma_{ij}^{\mathrm{PAT}}$	PAT-induced transition rate from $\|i\rangle$ to $\|j\rangle$
Γ_{PAT}	global scale for PAT-induced transition rates
$\Gamma_{ij}^{\mathrm{esc}}$	QP-induced transition rate when tunneling off of a small superconducting island
$S_{\mathrm{PAT}}^{\pm}$	QP-tunneling spectral functions
T_{eff}	effective QP temperature
t	electron tunneling amplitude
ω_ν	frequency of PAT-inducing mode
V_ν	voltage induced across the JJ by a single photon in mode ν
$\varphi_\nu^{\mathrm{zpf}}$	zero-point fluctuations of phase induced by mode ν
$\bar{n}_\nu$	average photon occupation of mode ν
T_P	charge-parity lifetime
τ_{ss}	recovery time to steady-state QP density after a QP-injection pulse

Experimental setup

T	experimental temperature
τ	various experimental time delays defined in context
R	complex reflection coefficient
I_m	in-phase (real) component of R
Q_m	quadrature (imaginary) component of R
$\overline{I_m}$	integrated I_m
$\overline{Q_m}$	integrated Q_m

f_{spec}	frequency of a spectroscopy tone
f_{ro}	carrier frequency for readout pulses
ω_{ro}	carrier frequency for readout pulses in angular units ($= 2\pi f_{\text{ro}}$)
M_i	transmon measurement indexed by integer i
m_i	outcome of measurement M_i
$\mathcal{F}_g$	global fidelity of a charge-parity mapping sequence
ζ_P^{ij}	probability of an error during a measurement of charge parity P, given an initial transmon plasmon state i and final state j
$S_{11}^{i,p}(\omega)$	reflection coefficient of the readout mode when the transmon is in state $\|i,p\rangle$
σ	standard deviation of a Gaussian distribution
$\mathcal{F}$	readout fidelity
Φ_{ext}	externally applied magnetic flux through a loop
v	volume of a superconducting island
Γ_m	measurement rate
$\bar{n}_r$	average photon occupation of the readout mode during measurement

Acknowledgements

Completing a Ph. D. would be absolutely impossible without the kindness and support of those around you. This extends far beyond someone helping to explain a complex concept: thoughtful conversation and words of encouragement from a friend and colleague can truly make a world of difference. Here, I would like to state explicitly my gratitude to some of the key figures that made my past six years at Yale productive, entertaining, and enjoyable.

I would like to first thank my advisor, Michel Devoret, for his guidance, support, and trust over the years. Michel's constant curiosity toward science is inspirational, and the intuition he has developed for a vast array of topics has taught me the importance of creativity in experimental physics. I have benefited immensely from the group environment that he has helped build at Yale, which, in addition to setting a standard for collaboration that I hope to continue far into the future, has fostered the skills necessary for me to be an independent researcher. I've also enjoyed our conversations about music and sci-fi movies, of which I hope there are many more.

Each of my committee members have shaped my view of science and research in various ways. Leonid Glazman, in addition to being an excellent lecturer in the few courses I was able to take from him, has instilled in me the importance of conveying information in the most succinct and accurate way. This is not always an easy task, and doing so with his relaxed demeanor is certainly something to strive for. Dan Prober is another truly inspiring educator: he actively takes the steps necessary to ensure that his students *learn* from the classes that he teaches. From historical context in the classroom to spontaneous demos in the hallway on the 4th floor of Becton, Dan can always be found with insight and cheer. I've always appreciated Rob Schoelkopf's ability to distill a broad experimental problem down to its most technical and fundamental tasks, attacking it from the ground up. He has taught me that it is truly important to understand every aspect of a problem and make sure that you're aware of (and able to convey to others) the context and implications of even a seemingly small task. I'd also like to express my gratitude to Joe Aumentado, who served as the external reader for this dissertation. Each time I chat with him at a conference I leave encouraged that academia can be (at least in some instances) exactly what we would hope: a community of researchers willing to take the time to learn from each other.

I really can't thank Luigi Frunzio enough for his dedication to keeping

Michel's and Rob's groups running smoothly. The time that Luigi and I have shared fixing the Plassys, the Leskers, the dicer, etc., is probably best characterized not by a number of hours but by a number of work-months, during which his presence made the tasks infinitely more enjoyable. A jovial quip from Luigi is enough to make you smile even after hours of struggling with a machine. I'll never forget his booming laugh and crazy stories, and I'll try my best to remember the innumerable helpful tips he's given me about science and life in general. Shyam Shankar took on a similar role in our group, somehow balancing research and advising with various administrative tasks. We could always depend on Shyam for advice on any aspect of our experiments and to let us know when we were making a big deal out of nothing. His even keel will make him an excellent professor, and I hope he institutes a strong coffee culture with his new group.

I had the pleasure of working with a few theorists during my Ph. D. from whom I learned a lot about the world of superconductivity. In addition to Leonid, I owe Gianluigi Catelani and Manuel Houzet a huge debt of gratitude for their time and patience. When I'd say something incorrect each one of them had a distinct, but equally kind, way of letting me know it, and they were all quick to help me understand. I value their friendship, and sincerely hope to collaborate with them more in the future.

Fortunately for me, there were a few postdocs that I was able to work closely with for a few years each. I thank Ioan Pop for helping me navigate my earliest days in the group, getting me started down the quasiparticle path, and teaching me qubit fabrication (most importantly, how to do it *right*). Between Ioan and Luigi, I could not have asked for better instructors in the art of Josephson device fabrication. I'm glad that Ioan and I overlapped, and I appreciate his friendship and guidance to this day. I am also very glad that I was able to work with Gijs de Lange soon after he joined the group, as he was instrumental in my development as an experimentalist and is also a great friend. When faced with a problem in the lab, Gijs always seemed to either have the requisite knowledge on hand from experience or know the perfect reference, often solving the issue with one fell swoop. Even though Valla Fatemi just joined the group about a year ago, he has really hit the ground running. I've enjoyed and benefited from his enthusiasm toward science and life, and have absolutely no doubt that he will continue to have an excellent career in science.

The past four years were spent working closely with Max Hays, and I really

wouldn't have had it any other way. Max is incredibly smart and never seems overwhelmed when it comes time to tackle hard problems. I'm very proud that I was able to contribute to his experiments on InAs nanowire devices, and his efforts toward the quasiparticle experiments presented in this dissertation were truly invaluable. We learned a lot together, including but not limited to each others respective caffeine limits, scootering skills, and preferred sentence lengths. Max has become one of my best friends, and I am very grateful that we were able to share a good portion of our graduate student years together.

Now, our experiments studying quasiparticles in transmons are in the very capable hands of Spencer Diamond. He began contributing to these projects as soon as he landed on the 4th floor, which really speaks to his work ethic and dedication. In addition to being an A+ student in all things experimental, he has taken over most of my responsibilities related to fabrication equipment and, in a few years, it will be his responsibility to pass on Ioan's teachings to yet another generation of graduate students. I'm certain that he is up to the task. I look forward to seeing what happens in Spencer's future, and hope that I get to be a part of it.

It is extremely important to acknowledge those behind the scenes that make daily life in the lab run smoothly. Chris Axline, Nick Frattini, Mike Hatridge, Anirudh Narla, and Chris Wang have put in an extraordinary number of hours into fridge upkeep so that we can literally cool down our experiments. Luke Burkhart and Ioannis Tsioutsios have spent significant time (with many others mentioned above) alongside Luigi and I maintaining fabrication equipment so that we can actually make devices. We are all indebted to the administrative staff in the Applied Physics office and YQI: Florian Carle, Devon Cimini, Terri Evangeliste, Stephanie Hessing, Giselle Maillet, Nuch Graves, Racquel Miller, and Maria Rao, for their hard work and support over the years. I'm very thankful to Mike Rooks in YINQE and Mike Power in the cleanroom (along with the rest of the cleanroom staff) whose expertise we've all benefited from on countless occasions.

I had a ton of fun sonifying our data with Luke, Florian, and Spencer Topel, culminating in our performances of Quantum Sound. Being able to share our science with others through experimental music was truly a highlight of the past year, and I thank all of those who helped make that happen.

In addition to all of those listed above, I've enjoyed the friendship

of many others who worked in Becton, including Jacob Blumoff, Teresa Brecht, Philippe Campagne-Ibarcq, Ben Chapman, Kevin Chou, Yiwen Chu, Alec Eickbusch, Yvonne Gao, Sumita Ghosh, Alex Grimm, Reinier Heeres, Vijay Jain, Prash Kharel, Angela Kou, Zaki Leghtas, Brian Lester, Zlatko Minev, Mazyar Mirrahimi, Shantanu Mundhada, Wolfgang Pfaff, Vladimir Sivak, Clarke Smith, Katrina Sliwa, Matt Reagor, Phil Reinhold, Steven Touzard, Jaya Venkatraman, Uri Vool, and Evan Zalys-Geller, among others, many of whom I have been lucky enough to collaborate with over the years.

It is said time and time again that the 4th floor of Becton (and more broadly, the quantum information groups at Yale) is a very special place to work. That is for good reason, because even from my first week I was struck by the camaraderie that has been built within the group. It's a place where everyone tries to build each other up, both scientifically and socially. It's a place where the consensus is often to save the torque wrench for tomorrow and grab a beer after a tough day in lab. I found examples like this to be the glue that binds the 4th floor together, because honestly, sometimes you need to take a step back from things. I'll miss the long lunches, coffee breaks, happy hours, karaoke nights, ski trips, post-March-Meeting vacations, weddings, backyard cookouts, etc., that we have shared, though I am comforted by the fact that this experience has gifted me with what I'm sure will be many lifelong friendships.

I'm very grateful to my parents, Diane and Rich, for teaching me the value of hard work and for their constant encouragement over the years.

Finally, I feel extremely fortunate to thank my best friend and partner Taylor. None of this would have been possible without her unwavering love and support. Taylor and our dog, Jack, have been a constant source of joy even in the roughest times. This dissertation is for you.

1 Introduction

The goal of this dissertation is to introduce the reader to the physics of nonequilibrium quasiparticle excitations (QPs) in superconductors and how they interact with superconducting qubits for quantum information processing. QPs are fundamental electronic excitations out of the superconducting ground state which can couple directly to the electromagnetic modes of a superconducting quantum circuit. These QPs constitute an intrinsic source of decoherence in superconducting qubits, placing a fundamental limit on qubit performance, along with that of a wide variety of other superconducting devices. It is therefore of broad interest to understand and mitigate the effects of these QP excitations. Even neglecting this technical motivation, the fact that the observed number of QPs is more than ten orders-of-magnitude greater than would be expected at the temperature of our experiments remains unexplained and therefore captivating.

1.1 Motivation

One of the most promising candidate platforms for scalable, fault-tolerant quantum information processing is based on superconducting electrical circuits that behave quantum mechanically [Devoret and Schoelkopf 2013; Vool and Devoret 2017]. In this particular implementation, physical qubits—the quantum analog of transistors—are embodied by anharmonic oscillators made of superconducting metals [Bouchiat et al. 1998; Mooij et al. 1999; Koch et al. 2007; Manucharyan 2012]. The quantum state of a superconducting qubit can be prepared and manipulated coherently by AC voltages at microwave frequencies ($\sim$ GHz). Generators, waveguides, and filters that operate in this frequency band are commercially available, which greatly simplifies the construction of new experimental setups while reducing cost. However, operating in this frequency range requires very low temperatures ($\lesssim$ 100 mK) to reach the quantum regime, which is typically achieved with dilution refrigerators or nuclear demagnetization refrigerators.

The performance of superconducting qubits has improved significantly over the last few decades, and is already good enough to demonstrate elementary single- and two-qubit operations [Yamamoto et al. 2003; DiCarlo et al. 2009]. Unfortunately, the fidelity of these operations is not yet at the level required

for large-scale quantum computation involving hundreds or thousands (or even many more!) qubits contributing to a distributed quantum algorithm. Many groups are seeking to implement quantum error-correction techniques, which may overcome the imperfections of state-of-the-art devices by encoding information in clever ways that can be insensitive to certain types of errors [Gottesman, Kitaev, and Preskill 2001; Fowler et al. 2012; Mirrahimi et al. 2014]. While it is more or less agreed upon that some form of quantum error correction will be necessary in a universal quantum computer in order to reduce error rates to an acceptable level, improvements to the physical devices themselves will relieve some of the burden by making individual qubits more robust.

Improvements to single-qubit performance extend what's called the qubit *coherence* time T_2, which itself is a function of two timescales. The *energy relaxation* time T_1 is the timescale on which a prepared qubit state decays to the thermal-equilibrium distribution of eigenstates. The *dephasing* time T_ϕ is the timescale on which the certainty of the phase of a superposition state decays (in the absence of energy relaxation). The total decoherence rate $1/T_2 = 1/2T_1 + 1/T_\phi$ directly measures the rate of mixing between anti-parallel superposition states of the qubit. Broadly speaking, decoherence arises due to the qubit interacting with its environment, which can never be completely eliminated in order to preserve the ability of an experimenter to control and readout the qubit state. Significant improvements to these timescales are generally few and far between [Paik et al. 2011; Wang et al. 2019], as it is not trivial to determine the exact mechanisms that limit T_1 and T_ϕ. Currently, we believe that dephasing times are limited by photon shot noise [Sears et al. 2012; Wang et al. 2019], which shifts the qubit transition frequency in the presence of a fluctuating photon population in the other electromagnetic modes to which the qubit is coupled. Regarding the relaxation time, we believe that most devices are limited by a combination of two mechanisms that can absorb energy stored in the qubit: imperfect dielectric materials [Wang et al. 2015; Dunsworth et al. 2017; Calusine et al. 2018; Woods et al. 2019] and nonequilibrium quasiparticle excitations (QPs) in the superconductors that make up our devices [Martinis, Ansmann, and Aumentado 2009; Catelani et al. 2011; Wang et al. 2014; Serniak et al. 2018]. Understanding and mitigating the latter mechanism has been the motivation of the work presented in this dissertation [Serniak et al. 2018; Serniak et al. 2019; Houzet et al. 2019].

The superconducting state is characterized by pair-correlated occupation of

electron levels around Fermi energy. These Cooper-paired electrons support a dissipationless DC supercurrent and are responsible for nearly perfect diamagnetism. An important consequence of the pair interaction is the opening of a gap (2Δ) in the electronic density of states centered at the chemical potential. When cooled to temperatures well below the critical temperature $T_c = \Delta/1.76k_B$ at which superconductivity appears, any electronic QP excitations above this gap should be suppressed as long as $T \ll \Delta/k_B$. In practice, however, we find that the fraction of Cooper pairs broken into QP excitations x_{QP}, also called the QP density, typically falls in the range of 10^{-9}–10^{-5}. We can predict the ratio of thermally generated QP excitations to Cooper pairs $x_{\mathrm{QP}}^{\mathrm{th.}}$ with the relation [Catelani et al. 2011]

$$x_{\mathrm{QP}}^{\mathrm{th.}} = \sqrt{2\pi k_{\mathrm{B}} T/\Delta}\, e^{-\Delta/k_{\mathrm{B}}T}. \tag{1.1}$$

Let's consider a device made out of thin-film Al, our favorite superconductor, sitting at the base temperature of a dilution refrigerator ($\sim$ 20 mK). Inserting into Eq. 1.1 the known value of $T_c^{\mathrm{Al}} \approx 1.35$ K (for a film 20 nm thick [Chubov, Eremenko, and Pilipenko 1969]), which corresponds to a superconducting energy gap $\Delta \approx 205$ μeV, one would expect a thermally generated $x_{\mathrm{QP}}^{\mathrm{th.}} \sim 10^{-52}$! This huge discrepancy between observation and expectation defines what we mean by *nonequilibrium* QPs in our devices. BCS superconductivity and QP excitations will be discussed in depth in Chapter 3.

These nonequilibrium QPs are fundamental electronic excitations out of the superconducting ground state which can couple directly to the electromagnetic modes of a superconducting qubit, potentially limiting both T_1 and T_ϕ (depending on the qubit). Our work has focused on understanding their effect in the popular transmon qubit [Bouchiat et al. 1998; Koch et al. 2007; Paik et al. 2011], which is constructed by shunting a Josephson junction (JJ) with a large capacitance. Our JJs are superconductor-insulator-superconductor tunnel junctions, which for the intents and purposes of this section act as nonlinear inductors, across which Cooper pairs and QPs can tunnel. The aforementioned combination of elements creates a circuit with eigenstates (Fig. 1.1) similar to that of a simple harmonic oscillator, but the JJ nonlinearity makes it such that the energy required to add another excitation decreases with the total excitation number (the circuit has negative *anharmonicity*). There are a few names for this circuit: the Cooper-pair box and the transmon, that denote the parameter regime in which a given device operates but are otherwise topologically equivalent.

We write the Hamiltonian of the Cooper-pair-box/transmon circuit as

$$\hat{H}_{\text{CPB}} = 4E_C \left(\hat{n} - n_g + \frac{P-1}{4} \right)^2 - E_J \cos\hat{\varphi}, \tag{1.2}$$

which contains two operators: $\hat{\varphi}$ is the difference of the superconducting phase across the junction and $\hat{n}$ is the number of Cooper pairs that have traversed the junction. The energy spectrum of the circuit is fully described by the Josephson coupling energy E_J, the single-electron charging energy E_C,[1] and a continuous parameter n_g, which is the dimensionless offset-charge difference between the two junction electrodes, with units of Cooper-pair number. Here we also include a parameter P, the charge parity of the circuit, which is defined as the parity of the number of *electrons* that have crossed the JJ, and can take values of ± 1 depending on if the number is even or odd. When QPs tunnel across the JJ they will change the charge parity, effectively shifting n_g by $1/2$. With this in mind, we can index the eigenstates of the transmon $|i, p\rangle$ with two discrete labels: i denotes the plasmon-excitation number and p denotes the charge parity, and include this effect directly in the Hamiltonian.

In the extreme transmon limit $E_J/E_C \gg 1$ (and in practice, $E_J/E_C \approx 50$–200) the qubit transition frequency is effectively insensitive to offset-charge fluctuations. In the Cooper-pair box limit ($E_J/E_C \approx 1$), there is extreme dispersion of the energy levels with respect to offset charge. Further details of this circuit as a function of E_J/E_C will be discussed in Chapter 4. What's important to note here is that in the intermediate regime, which we call the *offset-charge-sensitive* (OCS) transmon regime ($E_J/E_C \approx 20$), one can directly detect the discrete change in the eigenspectrum corresponding to charge-parity switches [Fig. 1.2]. Because OCS devices are are quite similar in most ways to traditional transmons, they are an excellent proxy with which to probe QP dynamics. In fact, with these devices we can directly measure the rates of QP-induced transitions! These experiments will be described in Chapter 6.

The rates of these transitions can be calculated theoretically due to the fact that QPs are so intimately related to the physics of superconducting qubits. Since superconducting qubits are described by marrying quantum circuit theory and BCS superconductivity, it is natural to include the effects of nonequilibrium QPs

[1] It may be surprising to see an electrical circuit described by energy scales, however these can be cast in terms of traditional parameters like capacitance and inductance, as described in the caption of Fig. 1.1. This will be developed further in later chapters.

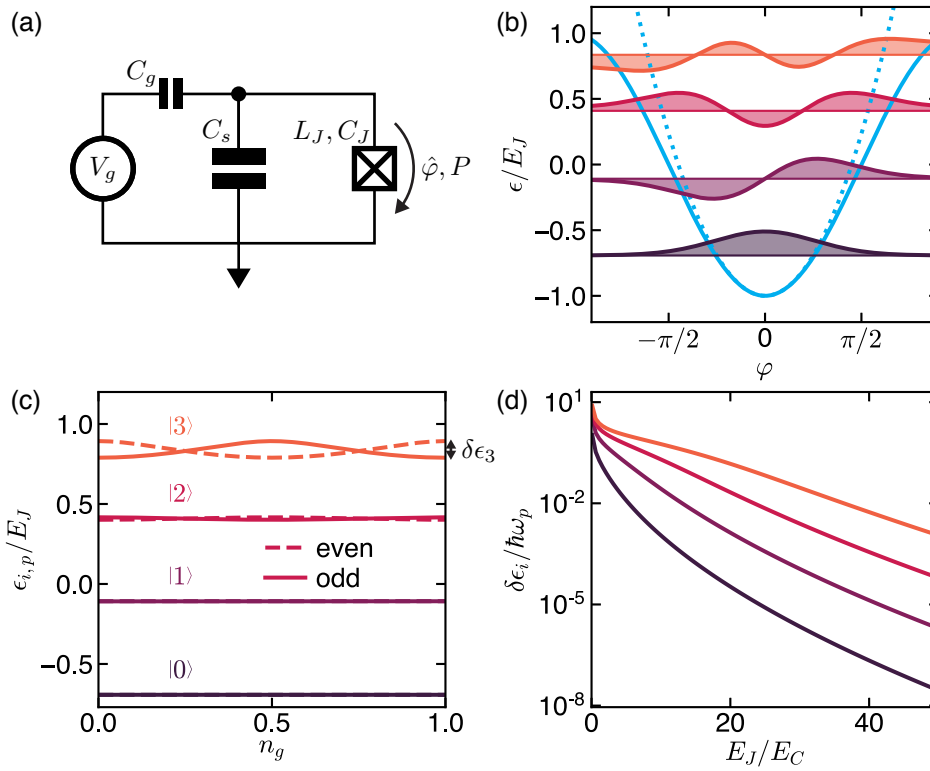

Figure 1.1 | (a) The transmon circuit, which is parameterized by the single-electron charging energy $E_C = e^2/2C_\Sigma$ (where $C_\Sigma = C_J + C_S + C_g$) and the Josephson coupling energy $E_J = \phi_0^2/L_J$, where e is the charge of an electron and $\phi_0 = \hbar/2e$ is the reduced flux quantum. The operator $\hat{\varphi}$ is the dynamical superconducting phase difference across the JJ, marked by a boxed "x". An offset charge $n_g = C_g V_g/2e$ can be imposed between the two JJ electrodes by a capacitively-coupled voltage source V_g. As described in the text, when a single QP tunnels through the JJ, the charge parity P can change between "even" and "odd." (b) The transmon potential (solid blue), compared to a harmonic potential (dashed blue), with plasmon eigenstates of the transmon represented in the φ-basis. Thin lines indicate the eigenenergies of the states. Chosen parameters reflect $E_J/E_C = 19$ in order to emphasize the anharmonicity of the circuit. (c) Transmon eigenspectrum vs n_g, separated into distinct charge-parity manifolds. The energy difference of plasmon state i between different manifolds is called the charge dispersion $\delta\epsilon_i(n_g)$. (d) Maximum charge dispersion $\delta\epsilon_i$ of the plasmon states as a function of E_J/E_C, normalized by the product of the plasma frequency $\omega_p = \sqrt{8E_J E_C}$ and $\hbar$.

directly in a coupling Hamiltonian, which takes the simple form of single electron tunneling across the JJ.

$$\hat{H}_{\mathrm{QP},\hat{\varphi}} = t \sum_{l,r,s} e^{i\hat{\varphi}/2} \hat{c}^{\dagger}_{rs} \hat{c}_{ls} + \mathrm{H.c.} \tag{1.3}$$

The above hopping Hamiltonian takes an electron with spin s from the left side of the junction ($\hat{c}_{ls}$) and puts it on the right side ($\hat{c}^{\dagger}_{rs}$). In this process, the electron picks up a phase factor, where $\hat{\varphi}$ is the dynamical phase across the junction, coupling the electron to the qubit. In BCS superconductivity, these electrons are dressed by the pairing interaction, giving QP excitations in the superconductor a mixture of electron and hole character. This modifies the above tunneling Hamiltonian and allows for interference effects between tunneling processes. Chapter 5 is dedicated to understanding the coupling between superconducting qubits and QPs, and further development of this tunneling Hamiltonian will be presented

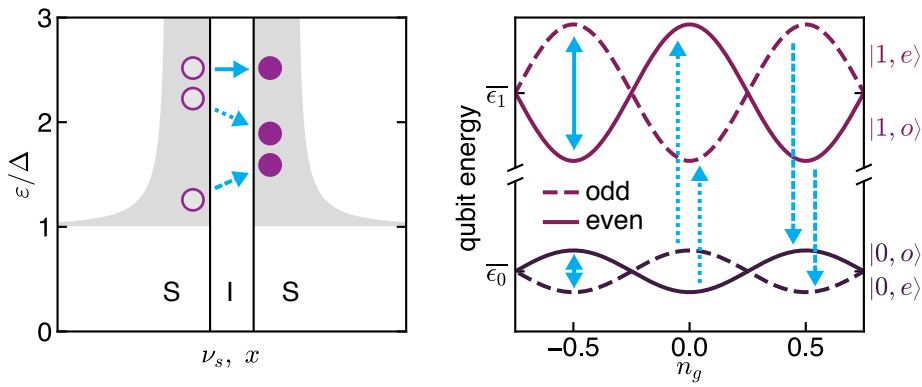

Figure 1.2 | QP tunneling in the OCS transmon. Left: Density of QP states ν_s in the excitation representation versus the reduced energy ε/Δ in the leads of a superconductor-insulator-superconductor (SIS) JJ. The x-axis also represents position x across the junction. The blue arrows indicate tunneling processes of QPs, shown as purple dots. Solid arrows correspond to plasmon-state-conserving processes, dashed arrows represent QP-induced qubit relaxation, and dotted arrows represent QP-induced qubit excitation. Right: Offset-charge dispersion of the two lowest energy plasmon eigenstates of an OCS transmon separated into charge-parity manifolds. The energies $\overline{\epsilon_0}$ and $\overline{\epsilon_1}$ are time-averaged energies of the ground and first-excited plasmon states, respectively, assuming ergodic fluctuations of $\hat{n}$ and/or charge parity. Arrows correspond to those in in the left panel. Detecting transitions between charge-parity manifolds can probe QP dynamics.

there.

Assuming that the nonequilbrium QP population has an energy distribution that closely resembles a thermal, Fermi-Dirac distribution [Martinis, Ansmann, and Aumentado 2009; Goldie and Withington 2013], the QP-induced bound on the T_1 of transmon qubits would be [Catelani et al. 2011]

$$\frac{1}{T_1} \geq \frac{x_{\mathrm{QP}}}{\pi}\sqrt{\frac{2\Delta\omega_{01}}{\hbar}}. \tag{1.4}$$

The aforementioned range of x_{QP} therefore limits $T_1 \lesssim 1$ μs-10 ms, with current state-of-the-art transmons falling right in the middle of that range ($T_1 \approx 100$ μs). It is therefore important to determine whether or not QPs are the dominant relaxation mechanism in our qubits, and if so, to figure out how to mitigate their effects. Furthermore, under the same thermal assumption, the observed x_{QP} would correspond to an effective electron temperature of ~ 150 mK. Under these conditions, the ratio of the QP-induced excitation rate $\Gamma_{01}^{\mathrm{QP}}$ of the qubit to the QP-induced relaxation rate $\Gamma_{01}^{\mathrm{QP}}$ will obey Boltzmann statistics and detailed balance, leading one to predict that

$$\frac{\Gamma_{01}^{\mathrm{QP}}}{\Gamma_{10}^{\mathrm{QP}}} = e^{-\hbar\omega_{01}/k_B T} \approx 0.28, \tag{1.5}$$

which shows that QP-induced excitation should be suppressed relative to QP-induced relaxation at low temperature.

Our experiments [Chapter 6] indicated that this was, however, not the case, and that QP-related transitions were just as likely to excite the qubit as to relax it [Serniak et al. 2018]. This is contrary to the above arguments, though recently we developed a theory that may explain this phenomenon [Houzet et al. 2019]. This theory of these photon-assisted tunneling (PAT) processes will be presented in Chapter 5, and experiments that could possibly distinguish this mechanism from nonequilibrium QP tunneling will be discussed in Chapter 8.

1.2 Results of the dissertation

Our work has utilized OCS transmons to probe the rates of decoherence induced by nonequilibrium QPs in superconducting qubits. Technically speaking, the goal was to detect changes in the transition spectrum corresponding to switches

between the two charge-parity manifolds of states. This relies on detecting the charge parity of the circuit in a single shot, which, akin previous works in other devices [Naaman and Aumentado 2006; Court et al. 2008; Shaw et al. 2008], has been achieved in OCS transmons with state-of-the-art energy-relaxation times. We accomplished this task in two ways: by performing coherent manipulations within the qubit subspace to map the charge-parity onto the plasmon state of an OCS transmon [Ristè et al. 2013; Serniak et al. 2018], and by taking advantage of the natural, charge-parity dependent coupling between the OCS transmon and an ancillary readout mode to perform direct dispersive readout of the joint charge-parity and plasmon eigenstate [Serniak et al. 2019]. The latter is similar to "quantum capacitance" measurements [Shaw et al. 2009], but extended to the quantum regime in the language of circuit QED [Blais et al. 2004; Zhu et al. 2013].

These methods allow for studies of QP-induced decoherence by correlating charge-parity switches with changes in the plasmon state of the transmon. Contrary to many coherence studies that seek to understand and reduce loss from imperfect dielectric materials [Wang et al. 2015; Dunsworth et al. 2017; Calusine et al. 2018; Woods et al. 2019], our experiments are able to determine, without the need for broad statistics, whether *individual qubits* are limited by QP-related dissipation. This allows for faster feedback when optimizing parameters of the device or the experimental setup to reduce QP-induced loss. By modeling the time dynamics of the system, we were able to extract all relevant transition rates of the device, and found that QP-induced relaxation was on equal footing with other forms of loss, indicating that if our device were free of QPs, T_1 would increase to $\sim 200\ \mu$s. Surprisingly, we found that *excitation* events of the transmon were usually correlated with charge-parity switches, indicating that QP-related processes can be responsible for the residual excited-state population in our devices. Furthermore, we found that QP-induced relaxation and excitation occurred at the same rate, suggesting that if charge-parity switches were indeed caused by nonequilibrium QPs, their energy distribution would not be well approximated by a Fermi-Dirac distribution that accounts for their apparent density $x_{\mathrm{QP}} \approx 10^{-7}$.

Throughout our experiments, we had assumed that charge-parity switches were coming from nonequilibrium QPs already present in the device.[2] We have now identified another process involving QPs can also produce charge-parity switches: photon-assisted QP generation and tunneling (PAT) processes concen-

[2]Note that at the time of this writing, this assumption is neither confirmed or discounted.

trated at the JJ in our devices [Houzet et al. 2019]. Theoretically, this mechanism would predict that the ratio of of PAT-induced excitation and relaxation events will be close to unity and that the presence of gap-engineered QP traps would not effect the rate of this interaction, consistent with the results presented in Chapters 6 and 7. Experiments to probe whether or not PAT processes are the dominant source of charge-parity switches are currently underway, and will be reviewed in Chapter 8 of this dissertation.

We demonstrated that the rate of charge-parity switches, our proxy for QP density, could be reduced to negligible levels (at least until the limit on T_1 due to dielectric loss is improved) by careful filtering of high-frequency radiation on the microwave lines used to address the qubit. By adding an additional high-frequency filter near the qubit-cavity system, we found the charge-parity lifetime could be increased by almost two orders-of-magnitude, to the extent that qubit decoherence was no longer limited significantly by QPs. In this regime, we measured the T_1 of the aforementioned device to be ≈ 200 μs, in perfect agreement with our predictions. These experimental techniques demonstrate a glimmer of certainty in the otherwise subtle world of coherence studies. By performing experiments tailored toward exposing the effects of QP-induced decoherence in *individual* devices, one can determine with certainty whether or not QPs are limiting that device. Arguably, this should be a prerequisite experiment for anyone interested in studying the effects of dielectric losses or other mechanisms of decoherence in order to exclude the effects of nonequilibrium QPs.

These projects began in an attempt to reduce QP-induced decoherence by implementing gap-engineered QP traps in our devices. This involved depositing bilayers of Al and Ti, another superconductor with a smaller superconducting gap, without breaking vacuum such that there will be a proximity effect between the two layers and the gap of the Al JJ electrodes would be reduced. This notion of a proximitized-superconducting QP trap has the potential to produce efficient traps without introducing additional losses. We found that by including these QP traps in transmon devices, experimentally generated QPs were evacuated away from the JJ faster than in devices without traps, however the steady-state charge-parity lifetime was unchanged. These results are presented briefly in Chapter 7, and though for a time this was extremely confusing, our recent theoretical developments may explain this effect [Houzet et al. 2019], as gap-engineered QP traps would have no effect on dissipation induced by PAT events.

2 Quantum Information with Superconducting Circuits

The many research fields related to the term *quantum computing* have grown by leaps and bounds over the last few decades. This chapter serves as a brief over view of the basic units of quantum computing technologies—qubits—and to introduce the strengths of (and challenges facing) the field of superconducting quantum circuits.

2.1 Quantum bits

In 1982, Richard Feynman proposed storing and manipulating information encoded in the state of a quantum system [Feynman 1982]. Since then, realizing this task has motivated decades of scientific endeavors and occupied the minds of researchers across many fields of experimental physics. In fact, this challenge is in many ways analogous to that of the tasks pursued in the 1940's to engineer the first solid-state computers, as it has been fueled by the development of basic hardware that is capable of storing and processing information. The field of quantum information science has grown by leaps and bounds over recent years, due in no small part to the expected applications of quantum computers. Scientists, and now the general public due to increased popularization of the field, anticipate that quantum-based technologies will be crucial to solving complex problems in cryptography, drug design, climate modeling, and many-body physics to name a few.

The backbone of traditional (classical) computers is the voltage-biased transistor functioning as a switch, where a control voltage turns the switch "on" and "off". The two switch configurations construct the basis for binary digital logic: the state of the transistor represents one "bit" of information. Electric current flowing through the transistor denotes the "0" logical state, and no current flowing denotes the "1" logical state. The quantum analog to one bit of information is called a "qubit" (just a portmanteau of "quantum" and "bit"). It is a two-level *quantum* system that is distinguishable from a classical system in that it can ex-

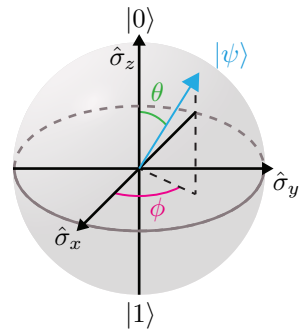

Figure 2.1 | Bloch sphere representation of a single qubit state. Pure states of the two-level qubit are represented by points on the surface of the Bloch sphere and are fully parameterized by the polar angle θ and azimuthal angle ϕ. The energy eigenstates $|0\rangle$ and $|1\rangle$ are located at the North and South poles, respectively.

hibit effects of quantum coherence. Particularly, these qubits can utilize the quantum notions of superposition and entanglement to create more complex states than just the energy eigenstates $|0\rangle$ (the ground state) or $|1\rangle$ (the excited state). In general, any *pure* quantum state of a single qubit can be decomposed and written as

$$|\psi\rangle = \cos\frac{\theta}{2}|0\rangle + e^{i\phi}\sin\frac{\theta}{2}|1\rangle\,. \tag{2.1}$$

This general qubit state can be represented by one of the infinite number of points on the surface of a Bloch sphere [Fig. 2.1]. Here, θ and ϕ represent the polar and azimuthal angles, respectively, that fully constrain the wavefunction $|\psi\rangle$ describing the state of the qubit. This simple example shows the effect of *quantum superposition*, in which the state of the qubit can be decomposed into a coherent, weighted sum of energy eigenstates, where the prefactors are probability amplitudes, and therefore their squares must sum to one.[1] By measuring the state of the qubit in the correct basis (in this case measuring the $\hat{\sigma}_z$ component of the qubit), the superposition will be projected into either $|0\rangle$ or $|1\rangle$. The basis states of the Bloch sphere are the Pauli operators $\hat{\sigma}_i$ defined as

$$\hat{\sigma}_x = \begin{pmatrix} 0 & 1 \\ 1 & 0 \end{pmatrix},\ \hat{\sigma}_y = \begin{pmatrix} 0 & -i \\ i & 0 \end{pmatrix},\ \text{and}\ \hat{\sigma}_z = \begin{pmatrix} 1 & 0 \\ 0 & -1 \end{pmatrix}. \tag{2.2}$$

[1] Indeed, $\cos^2\frac{\theta}{2} + \left|e^{i\phi}\right|^2 \sin^2\frac{\theta}{2} = 1$ for all θ and ϕ.

Equivalently to Eq. 2.1, the state of the qubit can also be represented as a polarization vector in the basis of the Pauli operators $\vec{S} = \left(\langle\hat{\sigma}_x\rangle, \langle\hat{\sigma}_y\rangle, \langle\hat{\sigma}_z\rangle\right)$, where the components $\langle\hat{\sigma}_i\rangle = \langle\psi|\,\hat{\sigma}_i\,|\psi\rangle$ denote the expectation value of the operator $\hat{\sigma}_i$. The standard transform between spherical and Cartesian coordinates allows one to switch between pictures.[2]

Not all states are pure states, however, and qubits can occupy states where there is *classical* probability to be in either one or the other. These *mixed* states (and pure states, as well) can be described by the density operator $\rho_q = \sum_i w_i\,|\psi_i\rangle\,\langle\psi_i|$, which is a sum over all statistically possible quantum states with *classical probability* weights w_i. For a two-level qubit in the Pauli basis, this can be written

$$\rho_q = \frac{1}{2}\left(I + \langle\hat{\sigma}_x\rangle\hat{\sigma}_x + \langle\hat{\sigma}_y\rangle\hat{\sigma}_y + \langle\hat{\sigma}_z\rangle\hat{\sigma}_z\right) \tag{2.3}$$

where I is the identity operator. In the density operator formalism, operator expectation values can be computed by $\langle\hat{\sigma}_i\rangle = \mathrm{Tr}\left(\rho_q\hat{\sigma}_i\right)$, for example. Pure states have $\mathrm{Tr}(\rho_q^2) = 1$ by definition, which distinguishes them from mixed states, which have $\frac{1}{2} \leq \mathrm{Tr}(\rho_q^2) < 1$. Another way of saying this is that the amplitude of the Bloch vector describing a mixed state is < 1, or that mixed states reside within the Bloch sphere as opposed to on its surface. For this reason, the density operator formalism is particularly useful for describing mixed states. Before continuing, it's worth writing down the density matrix $\rho_q\left(|\psi\rangle\right)$ for a few common states represented in the energy eigenbasis. Energy eigenstates (eigenstates of $\hat{\sigma}_z$) are particularly simple:

$$\rho_q\left(|0\rangle\right) = \begin{pmatrix} 1 & 0 \\ 0 & 0 \end{pmatrix} \qquad \rho_q\left(|1\rangle\right) = \begin{pmatrix} 0 & 0 \\ 0 & 1 \end{pmatrix}, \tag{2.4}$$

where one can intuit that the diagonal elements of $\rho_q\left(|\psi\rangle\right)$ indicate the *populations* of the energy eigenstates—the probabilities that they will be the outcome of a projective measurement in the $\hat{\sigma}_z$-basis. For the elementary real superpositions of energy eigenstates $|\pm\rangle = (|0\rangle \pm |1\rangle)/\sqrt{2}$ (which are in fact eigenstates of $\hat{\sigma}_x$) we can compute

$$\rho_q\left(|\pm\rangle\right) = \rho_q\left(\frac{|0\rangle}{\sqrt{2}} \pm \frac{|1\rangle}{\sqrt{2}}\right) = \frac{1}{2}\begin{pmatrix} 1 & \pm 1 \\ \pm 1 & 1 \end{pmatrix}. \tag{2.5}$$

[2] $\langle\hat{\sigma}_x\rangle = \sin\theta\cos\phi$, $\langle\hat{\sigma}_y\rangle = \sin\theta\sin\phi$, and $\langle\hat{\sigma}_z\rangle = \cos\theta$.

The above superposition is what we would call maximally coherent. In contrast, a maximally mixed state would be given by a classical statistical mixture of occupying each of the energy eigenstates half the time: $M = \frac{1}{2}|0\rangle + \frac{1}{2}|1\rangle$. In this case,

$$\rho_q(M) = \frac{\rho_q(|0\rangle)}{2} + \frac{\rho_q(|1\rangle)}{2} = \frac{1}{2}\begin{pmatrix}1 & 0\\ 0 & 0\end{pmatrix} + \frac{1}{2}\begin{pmatrix}0 & 0\\ 0 & 1\end{pmatrix} = \frac{1}{2}\begin{pmatrix}1 & 0\\ 0 & 1\end{pmatrix}. \quad (2.6)$$

The obvious difference between Eq. 2.5 and Eq. 2.6 being the lack of off-diagonal components in the mixed state. These are often called *coherences*, as their magnitude indicates a coherent superposition as opposed to a mixed state. One can also confirm that $\mathrm{Tr}\left(\rho_q\left(|\pm\rangle\right)^2\right) = 1$, while $\mathrm{Tr}\left(\rho_q(M)^2\right) = 1/2$, indicating that M is a maximally mixed state.

2.2 Qubit decoherence

The fragility of quantum information is a severe impediment to the realization of full, fault tolerant quantum computation. In essence, if the dynamics of the qubit take it from a pure state towards a mixed state, at least some of the quantum information is lost. In the absence of engineered projective measurements, a qubit prepared in a superposition state is only useful as long as the angles θ and ϕ are well defined. In reality, however, this doesn't last forever: information about those angles is lost due to *decoherence*. This occurs via coupling to unmonitored environmental degrees of freedom which can gain information about the quantum state, effectively measuring the qubit. This coupling gives the qubit a sensitivity to environmental parameters that can "kick" the state of the qubit around on the Bloch sphere, and once the experimenter loses track of that position it is impossible to recover. The exact mechanisms by which this happens depend on the physical implementation of the qubit and how it is coupled to the environment. Understanding and controlling these couplings is the primary goal in trying to improve the performance of physical qubits.

These efforts seek to improve the *coherence time* of the qubit T_2, which can be limited by two types of noise processes. First, there are processes that induce qubit transitions by having some spectral component at the qubit transition frequency f_{01}. These processes reduce the *energy relaxation time* T_1, which is defined as the timescale on which the autocorrelation function of the qubit state decays

to thermal equilibrium. Second, there are processes that produce noise on the energy of the qubit states such that f_{01} fluctuates in time. These contribute to the *pure dephasing* time T_ϕ, which is the timescale after which the phase ϕ of a superposition $|\Psi\rangle = 1/\sqrt{2}\left[|0\rangle + \exp(i\phi)\,|1\rangle\right]$ is no longer well defined due to spectral diffusion. This definition assumes the absence of T_1 processes.

In order to describe these noise processes mathematically, we'll start with a generic qubit Hamiltonian. In the absence of any coupling to the environment, any two level qubit can be represented by a simple qubit Hamiltonian

$$\hat{H}_q = \frac{\hbar\omega_{01}}{2}\hat{\sigma}_z \tag{2.7}$$

that simply takes into account the energy difference $\hbar\omega_{01}$ between qubit eigenstates in terms of the transition frequency between them ω_{01}. With this is a foundation, we will build Hamiltonians with environmental couplings in order to illustrate the effects of different types of noise.

2.2.1 Energy relaxation

Energy relaxation, also called depolarization, refers to processes that produce noise on the polar angle θ, which couple to $\hat{\sigma}_x$ and $\hat{\sigma}_y$ of the qubit. These processes can induce transitions between energy eigenstates. In terms of the density matrix, these processes mix the diagonal elements (the populations), as well as induce decoherence of the off-diagonal elements. There are two rates associated with T_1, the qubit relaxation rate Γ_{10} and the qubit excitation rate Γ_{01}, which combine to give $1/T_1 = \Gamma_{10} + \Gamma_{01}$. The notation Γ_{ij} denotes the transition rate from qubit state $|i\rangle$ to qubit state $|j\rangle$. To describe these processes, lets consider a simple qubit Hamiltonian that includes noise coupling to σ_x (equivalently, it could couple to σ_y). This can be written as

$$\hat{H} = \frac{\hbar\omega_{01}}{2}\hat{\sigma}_z + \frac{\hbar}{2}\hat{F}_x\hat{\sigma}_x \tag{2.8}$$

where $\hat{F}_x$ is a noisy environmental variable that can induce rotations about the $\hat{\sigma}_x$-axis of the Bloch sphere. We will assume that the fluctuations of $\hat{F}_x$ are stationary. In the absence of other environmental couplings, the noise coupling to the $\hat{\sigma}_x$ component of the qubit can be characterized by the power spectral density

of $S_{xx}[\omega] = S_{FF}[\omega]$:

$$S_{xx}[\omega] = \int_{-\infty}^{\infty} e^{i\omega t} \left\langle \hat{F}_x(t)\hat{F}_x(0) \right\rangle dt \tag{2.9}$$

which is defined here as the Fourier transform of the autocorrelation function of $\hat{F}_x$ [Clerk et al. 2010]. Assuming small fluctuations, we can use perturbation theory in the form of Fermi's golden rule to calculate the transition rate between some initial energy eigenstate $|i\rangle$ to some final energy eigenstate $|j\rangle$ induced by this noisy environment. In doing so, we take as the bare Hamiltonian $\hat{H}_q = \frac{\hbar\omega_{01}}{2}\hat{\sigma}_z$ and the perturbing Hamiltonian $\hat{H}_1 = \frac{\hbar}{2}\hat{F}_x\hat{\sigma}_x$. Writing it in the most convenient and general form, Fermi's golden rule states that the transition rate between eigenstates of a quantum system coupled to some environmental noise is

$$\Gamma_{ij} = \frac{1}{\hbar^2} \left| \langle j | \hat{H}_1 | i \rangle \right|^2 S_{xx}[\omega_{ij}]. \tag{2.10}$$

Here, $\langle j| \hat{H}_1 |i\rangle$ is the transition matrix element of $\hat{H}_1$ linking eigenstates $|i\rangle$ and $|j\rangle$, and Γ_{ij} is the transition rate from $|i\rangle$ to $|j\rangle$. $S_{xx}[\omega_{ij}]$ represents the component of the noise at the transition frequency ω_{ij}. State transitions during which the qubit loses energy are said to be of positive frequency (ω_{01}), while transitions during which the qubit gains energy are said to have negative frequency ($-\omega_{01}$). This matrix element represents coupling strength of the environmental noise to the qubit. This noise will be responsible for both relaxation excited state back to the ground state as well as qubit *excitation*. Although spontaneous qubit excitation is relatively rare in most practical cases, it is important to consider as it effects T_2 identically to qubit relaxation. Restricting our discussion to the two levels of a qubit we find:

$$\begin{aligned} \Gamma_{10} &= \frac{1}{\hbar^2} \left| \langle 0 | \hat{H}_1 | 1 \rangle \right|^2 S_{FF}[\omega_{01}], \text{ and} \\ \Gamma_{01} &= \frac{1}{\hbar^2} \left| \langle 1 | \hat{H}_1 | 0 \rangle \right|^2 S_{FF}[-\omega_{01}]. \end{aligned} \tag{2.11}$$

As long as $\hat{H}_1$ is Hermitian, $\langle 0| \hat{H}_1 |1\rangle = \langle 1| \hat{H}_1 |0\rangle$, therefore the ratio of excitation to relaxation rates will be given by $S_{FF}[-\omega]/S_{FF}[\omega]$. Detailed balance states that the ratio of these rates will be equal to the ratio of the equilibrium populations of $|1\rangle$ and $|0\rangle$, $\mathcal{P}_1/\mathcal{P}_0$. With elementary statistical mechanics we can compute this in terms of an effective temperature T (assuming that the qubit is coupled to an

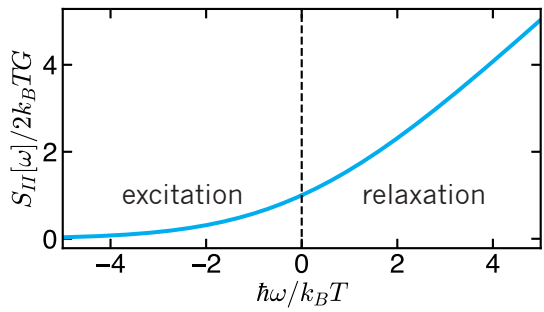

Figure 2.2 | Quantum power spectral density of current noise $S_{II}[\omega]$ emitted by a conductor (with conductance G) at temperature T, which in the quantum regime $k_BT \ll \hbar\omega$ is asymmetric between positive and negative frequencies $\pm\omega$.

environmental bath in thermal equilibrium) as

$$\frac{\Gamma_{01}}{\Gamma_{10}} = \frac{S_{FF}[-\omega_{01}]}{S_{FF}[\omega_{01}]} = \frac{\mathcal{P}_1}{\mathcal{P}_0} = e^{-\hbar\omega_{01}/k_BT}. \tag{2.12}$$

As we will discuss in Chapters 5 and 6, measuring these rates can be a useful diagnostic tool with which to probe the source of qubit depolarization. A so-called "hot" qubit, where there is significant excited state population described by an effective temperature greater than the temperature of the cryostat could just be a result of poor thermalization of the qubit to the cryostat. However, as will be discussed in later chapters, a large residual excited-state population could also indicate a specific form of decoherence induced by a process coupling the qubit to both superconducting quasiparticles and high-frequency photons in the environment [Serniak et al. 2018; Houzet et al. 2019].

As an example, one source of noise that clearly demonstrates the aforementioned thermal properties is the natural current noise produced by a conductor [Nyquist 1928]. The power spectral density of current fluctuations through a conductor at temperature T, is [Schoelkopf et al. 2003; Clerk et al. 2010]

$$S_{II}[\omega] = \hbar\omega \left(\coth \frac{\hbar\omega}{2k_BT} + 1 \right) \mathrm{Re}\left\{ Y[\omega] \right\}, \tag{2.13}$$

which just depends on the frequency of interest, temperature, and the admittance of the conductor $Y[\omega]$, which for simplicity we will assume is classical and con-

stant, $Y[\omega] = Y[-\omega] = G$ (where G is the conductance).[3] As depicted in Fig. 2.2 and evident from Eq. 2.13, $S_{II}[\omega]$ is asymmetric about $\omega = 0$—a defining characteristic of quantum noise—and obeys detailed balance (Eq. 2.12)[4]. The correspondence principle is satisfied in the high-temperature limit of $k_B T \gg \hbar\omega$ in that $S_{II}[\omega]$ becomes symmetric. This will be important in analogy with the dissipative quasiparticle current through a josephson junction, as will be discussed in Chapter 5.

2.2.2 Qubit dephasing

We will now consider qubit dephasing, by which knowledge of the azimuthal angle ϕ is destroyed, in the absence of depolarization. In analogy to the energy relaxation processes that couple to the longitudinal components of the qubit state ($\hat{\sigma}_x$ and $\hat{\sigma}_y$), dephasing processes couple to $\hat{\sigma}_z$ directly. In other words, these processes only effect the off-diagonal elements the density matrix, and do not induce transitions between energy eigenstates. A generic coupling of this type could be included in the qubit Hamiltonian in the same way as in Eq. 2.8.

$$H = \frac{\hbar\omega_{01}}{2}\hat{\sigma}_z + \frac{\hbar}{2}\hat{F}_z\hat{\sigma}_z. \tag{2.14}$$

The noisy variable $\hat{F}_z$ now couples to $\hat{\sigma}_z$, which effectively shifts the qubit frequency ω_{01} by $\hat{F}_z$. Thats why, colloquially, people refer to dephasing processes as inducing noise on the transition frequency of the qubit. We will assume that the noise is stationary with an average value of zero. As a consequence of this noise, the qubit superposition will accumulate an additional phase [Ithier et al. 2005]

$$\phi_F = \int_0^t \hat{F}_z(t')dt' \tag{2.15}$$

It's worth emphasizing that low frequency accumulation of the phase is not always detrimental. In fact, there are experimental protocols that can coherently reverse the accumulation of phase (Hahn echo sequences and other dynamical decoupling techniques [Bylander et al. 2011]), rendering noise near $\omega = 0$ harmless. If these techniques are not implemented, and assuming the noise is station-

[3] This is also called the fluctuation-dissipation theorem [Kubo 1966].

[4] As a reminder, $\coth x = \frac{e^x + e^{-x}}{e^x - e^{-x}}$.

ary and uniform at low frequencies,

$$\langle e^{i\phi_F} \rangle = \left\langle e^{-\int_0^t d\tau \hat{F}_z(\tau)} \right\rangle \approx e^{-\frac{1}{2}\left\langle \left(\int_0^t d\tau \hat{F}_z(\tau)\right)^2 \right\rangle} \approx e^{-\frac{1}{2}S_{FF}[0]t}. \tag{2.16}$$

We're left with a phase that diffuses on a timescale

$$T_\phi = \frac{2}{S_{FF}[0]} \tag{2.17}$$

in the absence of qubit depolarization, otherwise known as the *pure dephasing time*.

2.2.3 The decoherence time T_2

Energy relaxation processes and dephasing processes combine to decohere a qubit prepared in a superposition state. The coherence time T_2 is related to the others by $1/T_2 = 1/2T_1 + 1/T_\phi$. This is the decay timescale for the magnitude of the off-diagonal terms of the density matrix. It can be thought of very similarly to T_1, but instead of representing decay between eigenstates of σ_z ($|0\rangle$ and $|1\rangle$), it describes decay between eigenstates of σ_x ($|+\rangle$ and $|-\rangle$). While this derivation will not be presented here, there are two ways of thinking about the problem. First, the noise processes in the previous two sections can be decomposed as Kraus operators that reduce the off-diagonal elements of the density matrix [Preskill 1998; Yu and Eberly 2003]. The second, and more involved, approach follows the Bloch-Redfield theory of decoherence [Wangsness and Bloch 1953; Redfield 1957]. The final result shows how the density matrix evolves as a function of time, in terms of T_1 and T_2. If the qubit is initialized in a superposition state $|\psi\rangle_s = \alpha|0\rangle + \beta|1\rangle$, the evolution follows this form where, for convenience, we assume that the environment is at $T = 0$:

$$\rho_q\left(|\psi_s\rangle\right)(t) = \begin{pmatrix} 1 + (|\alpha|^2 - 1)e^{-t/T_1} & \alpha\beta^* e^{-t/T_2} \\ \alpha^*\beta e^{-t/T_2} & |\beta|^2 e^{-t/T_1} \end{pmatrix}. \tag{2.18}$$

Since $T = 0$, there is no steady-state population of $|1\rangle$. Extending the above to finite temperatures just complicates the diagonal elements, and can be found by solving the usual Bloch equations for the qubit polarization. Because quantum information processing relies on operations where a qubit is prepared in a superposition state, T_2 is an important figure-of-merit for single-qubit performance.

2.3 Requirements for physical qubits

Physical qubits can be realized in any quantum system from which a 2D Hilbert space can be constructed and coherently controlled. Natural quantum systems often have many energy eigenstates ($|0\rangle$, $|1\rangle$, $|2\rangle$, ...), and can be used as a qubit so long as a computational basis of two energy eigenstates can somehow be isolated from the rest. This requires negligible equilibrium population of states outside of the computational basis (lets say $|0\rangle$ and $|1\rangle$, though the basis need not be the two lowest energy eigenstates), as well as the ability to coherently control population dynamics between the qubit basis states. Both conditions can be trivially met in quantum systems with only two energy eigenstates, of which there are a few practical examples such as the spin degree of freedom of single electrons and some nuclei in an applied magnetic field. Otherwise, the first condition can be satisfied if $\hbar\omega_{01} \gg k_B T$, such that the system will be in the ground state $|0\rangle$ the vast majority of the time and transitions to higher excited states due to thermal fluctuations will be rare. The second condition can be satisfied in multi-state systems in which the Hamiltonian doesn't couple the computational basis states to any additional states, or in systems where the transition spectrum is sufficiently sparse such that even though there is no intrinsic protection built into the Hamiltonian, transitions between states can be individually addressed. These include cold atoms, trapped ions, and superconducting artificial atoms.

Unfortunately, the above conditions aren't the only ingredients required for quantum-computing glory. Reaching the quantum regime of $\hbar\omega_{01} \gg k_B T$ puts a constraint on the frequency difference between basis states purely due to the cryogenic technologies that are currently available and cost effective.[5] The most prevalent low-temperature cryostat is the ^{3}He/^{4}He dilution refrigerator, which is commercially available from multiple manufacturers and can typically sustain base temperatures of $10 - 20$ mK for months at a time. With this in mind, ω_{01} needs to be greater than ~ 1 GHz in order to reach the quantum regime in those cryostats. Other refrigeration methods, such as adiabatic paramagnetic or nuclear demagnetization can reach similar (even slightly lower) temperatures, but suffer from lower cooling power and require frequent remagnetization, meaning that every so often one must warm-up the experiment and apply a strong polar-

[5] Neglecting driven-dissipative techniques that have been developed for cooling quantum systems to their ground state.

izing magnetic field on the order of a few Tesla.[6]

Furthermore, it is required that the quantum system can be controlled much faster than any other dynamics of the system. This timescale is called the *gate time*, the time it takes to perform some logic gate. Most crucially, one must be able to perform many operations on the qubit within the coherence time. Both the gate time and T_2 depend on the exact embodiment of the qubit and the limitations that that architecture imposes. The next section will discuss how artificial atoms are implemented in superconducting quantum circuits and the decoherence mechanisms relevant to that implementation.

2.4 Superconducting qubits

Qubits encoded in the state of a superconducting quantum circuit go beyond satisfying the aforementioned basic requirements, and are considered to be one of the leading candidate platforms for fault-tolerant quantum computation. Superconducting qubits can be fabricated using standard micro- and nano-fabrication techniques, and controlled using commercially available RF equipment that was developed for use in radar systems. These combine to make experiments on superconducting qubits relatively accessible, with one downside being that experiments need to be performed at temperatures far below the superconducting critical temperature of thin-film Al ($T_c \approx 1.3$ K), the material of which most superconducting qubits are based, as well as below the convenient operating frequencies of a few GHz. This is typically achieved in dilution refrigerators, which present a significant cost barrier.

The amazing thing about superconducting qubits is that they can be represented theoretically as combinations of classical circuit elements operating in the quantum regime. This means that the parameters of the qubit are defined by values of capacitors, inductors, and the backbone of our species of quantum circuits: the Josephson junction. Josephson junctions (JJs) are superconducting tunnel junctions that act as nonlinear inductors. This nonlinearity is the most crucial component of superconducting qubit circuits, particularly to achieve coherent qubit control with standard microwave-frequency drives.

[6] Which is an additional cost barrier in and of itself.

2.4.1 Superconducting quantum circuits

Elementary electricity and magnetism courses that teach the physics of electrical circuits typically speak in terms of two degrees of freedom: voltage and current. This is always treated classically because the macroscopic behavior of lumped-element circuits doesn't rely on any inherently "quantum" effects when writing down Kirchhoff's laws. However, this doesn't mean that circuits *can't* be treated in the quantum regime under the necessary circumstances. In doing just that, we will use the variables Q and Φ, which denote the excess charge on one side of the circuit element and the flux difference across the element, respectively, in place of position and momentum. They are defined as integrals of the classical current I or voltage V:

$$Q(t) = \int_{-\infty}^{t} I(t')dt' \quad \text{and} \quad \Phi(t) = \int_{-\infty}^{t} V(t')dt. \tag{2.19}$$

The limits of integration indicate that the charge and flux remember the history of the circuit. In order to make all of these dynamical variables "quantum," one just puts a "hat" on them to promote them to operators:

$$Q \to \hat{Q} \qquad I \to \hat{I} \qquad \Phi \to \hat{\Phi} \qquad V \to \hat{V}. \tag{2.20}$$

The operators $\hat{Q}$ and $\hat{\Phi}$ are canonically conjugate, and analogously to position and momentum, $\hat{Q} = -i\hbar\frac{\partial}{\partial\Phi}$ and the commutator $[\hat{\Phi}, \hat{Q}] = -i\hbar$. For the time being, we'll only consider dissipationless circuits, meaning there will be no explicit conductors or resistors, just lossless elements like capacitors, inductors, and nonlinear elements. With this in mind, the simplest Hamiltonian we can write down is that of the quantum, harmonic LC-oscillator (QHO)

$$\hat{H}_{\text{QHO}} = \frac{\hat{Q}^2}{2C} + \frac{\hat{\Phi}^2}{2L} \tag{2.21}$$

where the first term corresponds to the energy stored in the capacitor, and the second corresponds to the magnetic energy in the inductor.[7] Though we will not cover it here, one can write the Hamiltonian for any circuit, no matter how complicated with the methods discussed in the recent review of Ref. Vool and

[7] Note that the energies agree with the typical formulas $U_C = \frac{1}{2}CV^2$ and $U_L = \frac{1}{2}LI^2$ via the constitutive relations of capacitors and inductors.

Devoret 2017.

In a Hamiltonian, we're used to parameterizing terms with coupling rates and energies, partially because it's cleaner to work in unitless coordinates. To this end, and since we'll be dealing with superconductors, we will work with the charge number operator $\hat{n} = \hat{Q}/2e$ (note the $2e$, as this is the number of Cooper pairs) and the phase difference operator $\hat{\varphi} = \hat{\Phi}/\phi_0$, where $\phi_0 = \hbar/2e$ is the reduced magnetic flux quantum. The canonical commutator now takes the form $[\hat{\varphi}, \hat{n}] = i$. The QHO Hamiltonian now takes the form

$$\hat{H}_{\text{QHO}} = 4e^2 \frac{\hat{n}^2}{2C} + \phi_0^2 \frac{\hat{\varphi}^2}{2L} \tag{2.22}$$

As mentioned in the introduction, we typically parameterize the Hamiltonian in terms of energies, so here we define the single-electron charging energy $E_C = \frac{e^2}{2C}$ and the inductive energy $E_L = \frac{\phi_0^2}{L}$.

The QHO can also be written in terms of ladder operators $\hat{a}$ and $\hat{a}^\dagger$: bosonic annihilation and creation operators for excitations (photons) in the oscillator. Our dynamical variables can be mapped to these ladder operators by $\hat{\varphi} = \varphi_{\text{zpf}}(\hat{a} + \hat{a}^\dagger)$ and $\hat{n} = -in_{\text{zpf}}(\hat{a} - \hat{a}^\dagger)$, where the magnitudes of zero point fluctuations are given by $\varphi_{\text{zpf}} = \sqrt{\hbar Z_0/2}/\phi_0$ and $n_{\text{zpf}} = \sqrt{\hbar/2Z_0}/2e$, where $Z_0 = \sqrt{L/C}$ is the characteristic impedance of the oscillator. In these two forms, the QHO Hamiltonian is represented

$$\hat{H}_{\text{QHO}} = 4E_C\hat{n}^2 + \frac{E_L}{2}\hat{\varphi}^2 = \hbar\omega_{LC}\left(\hat{a}^\dagger\hat{a} + \frac{1}{2}\right), \tag{2.23}$$

where the oscillator resonant frequency $\omega_{LC} = \sqrt{8E_L E_C}$, also called the *plasma frequency* defines the frequency difference between eigenstates. Here we can see that the eigenstates of the QHO are eigenstates of the excitation number operator $\hat{a}^\dagger\hat{a}$, also called Fock states.

But what's so quantum about whats been stated here? Surely, describing any old LC-oscillator on a circuit board with operators shouldn't make it "quantum?" That's because quantum effects are washed away when the oscillator is strongly coupled to a lossy environment. This adds dissipation to the system, which makes the eigenstates of the oscillator *coherent states*, which are superpositions of Fock states. In the presence of dissipation, quantum effects are only visible when the total energy stored in the oscillator is close to $\hbar\omega_{LC}$. This can be achieved by cooling the oscillator to the quantum regime where $k_B T \ll \hbar\omega_{LC}$,

but even then there are still electronic degrees of freedom that can dissipate energy stored in the oscillator, which won't make a good qubit.[8] In order to enter the quantum regime with little intrinsic dissipation, one needs to construct the oscillators out of superconducting materials, which would ideally be dissipationless at frequencies below the superconducting gap $2\Delta/h$. More details on the superconducting state will be discussed in Chapter 3.

2.4.2 Josephson-junction-based qubits

So in order to study the quantum nature of electronic circuits, we've resigned ourselves to work at low temperatures with superconducting devices. There's still an issue in that the $\hat{\varphi}^2$ potential of the QHO makes it such that the energy differences between all nearest neighbor eigenstates are all identical: $\hbar\omega_{LC}$. This makes it impossible to separately address transitions between eigenstates with simple microwave drives. Without any source of nonlinearity this will always be the case, hence the need for nonlinear circuit elements if we would like to construct qubits from our quantum circuits. If we wish to keep things simple (and generally we do), the simplest thing would be to replace either the linear capacitor and linear inductor of the SHO with a nonlinear version. Luckily, these superconducting elements exist in micromechanical superconducting resonators [Teufel et al. 2011], and the more ubiquitous Josephson junction (JJ) [Josephson 1962].

The most common embodiment of a JJ is is formed by a superconductor-insulator-superconductor tunnel junction [Fig. 2.3]. The important part here is that there are two superconductors sandwiching another material, which can be an insulator, a normal metal, a semiconductor, or even a ferromagnet, depending on the application. The microscopic details of superconductivity and JJs will be discussed in Chapter 3, but that won't hinder the discussion of JJs from the standpoint of quantum circuit theory. For the intents and purposes of this section, a JJ is a nonlinear inductor, with a current phase relation given by

$$I_J = I_0 \sin\varphi. \tag{2.24}$$

[8] This is just stating the Joule-Lenz law, that metallic conductors will dissipate with a power $= I^2R$, where R is the resistance of the conductor.

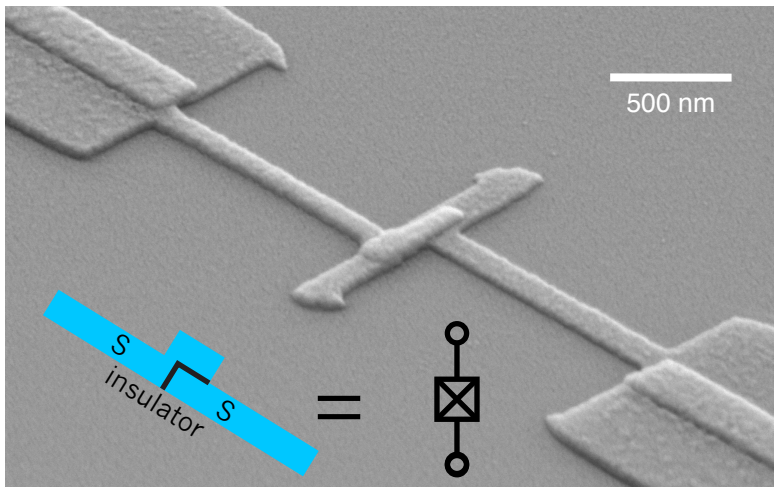

Figure 2.3 | Scanning electron micrograph of an Al/AlOx/Al Josephson junction fabricated using the "bridge-free" technique. As this device was fabricated on an insulating sapphire substrate, it was necessary to deposit a thin anti-charging layer (iridium) for imaging. Image was taken at a rotation angle of 45° with a 60° tilt.

where I_0 is the critical current of the JJ—the maximum DC supercurrent that the junction can support without dissipation. Combining the above equation with the definition of $\hat{\varphi}$ in terms of $\hat{V}$ allows us to calculate the associated nonlinear inductance.[9]

$$\begin{aligned} V_J &= L_J \frac{\partial I_J}{\partial t} \\ \phi_0 \frac{\partial \varphi}{\partial t} &= L_J I_0 \frac{\partial \sin\varphi}{\partial \varphi} \frac{\partial \varphi}{\partial t} \\ L_J &= \frac{\phi_0}{I_0 \cos\varphi} \end{aligned} \tag{2.25}$$

It's nice to note a convenience: the $T = 0$ critical current of the JJ can be computed from knowable junction parameters by the Ambegaokar-Baratoff relation

$$I_0 = \frac{\pi\Delta}{2eR_n}, \tag{2.26}$$

[9]The current phase relation 2.24 is referred to as the first Josephson relation, with the definition $V_J = \phi_0 \frac{\partial \varphi}{\partial t}$ referred to as the second.

where R_n is the normal state resistance of the junction. It's important to mention that L_J is fundamentally different than a linear inductance, as no magnetic energy is actually stored in the JJ. Instead, it is a *kinetic inductance*, which stores energy in the motion of charge carriers without sustaining an additional magnetic field. The energy stored in a JJ (U_J) can be computed similarly to a regular inductor by calculating the work done to "charge" the JJ with current at some time t:

$$U_J(t) = \int_0^t I_J V_J dt' = \phi_0 \int_0^{\varphi_0} I_0 \sin\varphi d\varphi = \phi_0 I_0 \left(1 - \cos\varphi_0\right). \tag{2.27}$$

After charging the JJ is left with some fixed phase bias φ_0. Since constant terms in the Hamiltonian just add a rotation to the dynamics of the eigenvectors, we typically ignore the "1" and write

$$U_J = -E_J \cos\varphi_0, \tag{2.28}$$

Where $E_J = I_0\phi_0 = \frac{\phi_0^2}{L_J} = \frac{\pi\Delta\phi_0^2}{\hbar R_n}$ is the Josephson coupling energy.

The linear inductor of the QHO can be replaced with a JJ in order to create an *anharmonic* quantum oscillator, which nowadays is called the transmon qubit. The circuit topology of the transmon is identical to a device called the Cooper-pair box, it is just operated in a different parameter regime. The distinctions are important, so much so that the circuit will get its own chapter in this dissertation [Chapter 4]. Neglecting charging effects due to environmental degrees of freedom[10], the Hamiltonian of the circuit reads

$$\hat{H}_{\mathrm{t-mon}} = 4E_C\hat{n}^2 - E_J\cos\hat{\varphi} \tag{2.29}$$

This superconducting qubit is compared with the QHO in Fig. 2.4. The wavefunctions and eigenenergies are only slightly different when choosing parameters appropriate for comparison, but the difference is enough to make a significant technological impact. The right panel shows that the transition frequencies between nearest-neighbor eigenstates *decreases*, with increasing level index i, which is exactly the ingredient necessary to address transitions independently with microwave-frequency voltage pulses. We define the *anharmonicity* of the qubit to be $K = \omega_{12} - \omega_{01}$, the magnitude of which determines how quickly

[10] This is valid in the regime $E_J \gg E_C$, also known as the transmon regime

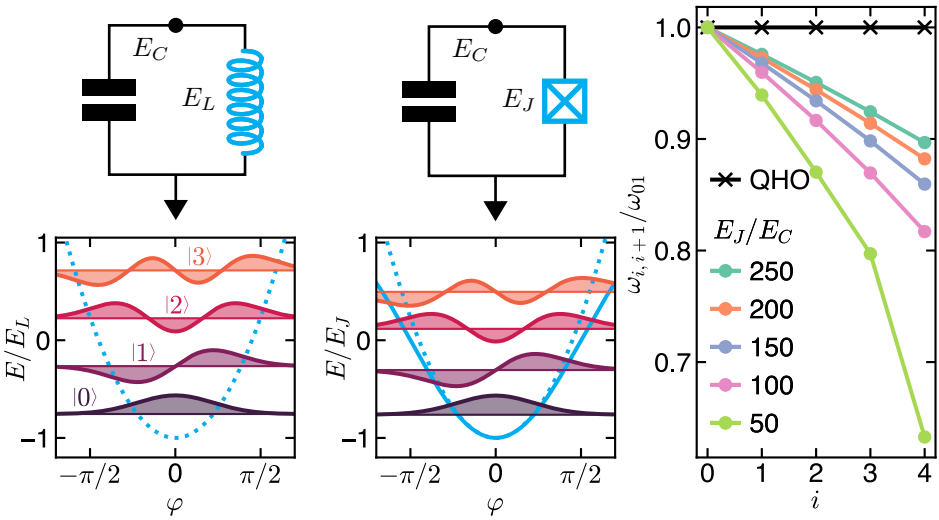

Figure 2.4 | Left: Quantum harmonic oscillator circuit, parameterized by energies E_L and E_C. Below, harmonic potential (blue dashed line) with circuit eigenergies normalized by E_L, and overlaid wavefunctions. Center: Cooper-pair box/transmon circuit, parameterized by energies E_J and E_C. Below, comparing the transmon potential (blue solid line) to the harmonic potential with circuit eigenenergies normalized by E_J, and overlaid wavefunctions. Right: transition frequencies $\omega_{i,i+1}$ (normalized by ω_{01}) between nearest-neighbor eigenstates $|i\rangle$ and $|i+1\rangle$, for the QHO (black) and for a transmon circuit for a variety of E_J/E_C (colors). The circuit anharmonicity decreases with increasing E_J/E_C.

one can do operations on the qubit, and in most cases the faster the better. The transmon qubit is perhaps the simplest superconducting qubit, which supports its popularity throughout the field.

Transmons satisfy the the technological requirements necessary to implement a qubit, but it is by no means the only circuit that does so. Fig. 2.5 compares the transmon circuit to two other common superconducting qubits: the C-shunt flux qubit [You et al. 2007; Yan et al. 2016] and the fluxonium [Manucharyan et al. 2009; Pop et al. 2014]. Both of these alternatives have a transition spectrum that is tunable by an externally applied magnetic flux through a superconducting loop containing JJs, and can attain much larger anharmonicity than the transmon. The loop of a C-shunt flux qubit contains three to four JJs, one of which has E_J smaller by a factor α. The fluxonium JJ is shunted by a large inductance such that $E_L \ll E_C < E_J$. This inductance is so large that it's called a *superin-*

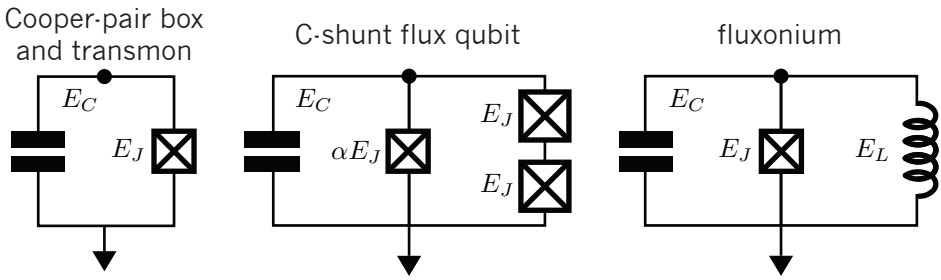

Figure 2.5 | Three examples of common superconducting qubits. The transmon, the capacitively-shunted (C-shunt) flux qubit, and the fluxonium qubit. While they may appear to be variations on a theme, there are significant differences make one device more advantageous over the others for certain situations.

ductance since its impedance is on the order of the resistance quantum for Cooper pairs $R_q = \frac{h}{(2e)^2} \approx 6.5\ \mathrm{k}\Omega$. The superinductance is typically implemented with an array of large JJs [Masluk et al. 2012] or, as recently demonstrated, with a high-kinetic-inductance superconductor wire [Hazard et al. 2019].

2.4.3 Decoherence of superconducting qubits

Coherence times of superconducting qubits have increased many orders of magnitude over the last few decades, with state-of-the-art qubits having measured T_1 and T_2 on the order of $100\ \mu$s. With gate times as low as 10 ns in some cases, this means that about 10^4 single-qubit operations can be performed before decoherence, which together display the primary advantage of the supeconducting qubit architecture: it's possible to do a lot of fast operations. Achieving this level of coherence has primarily come from three realizations.

First, confining energy to a single microwave mode in the presence of other microwave modes is not trivial. By cleaning up the microwave environment and controlling the coupling to the other modes in the system, the spontaneous emission of photons from the qubit into the microwave environment can be suppressed. This loss mechanism is known as the Purcell effect, and the limits that it imposes on qubits are now relatively well understood [Houck et al. 2008]. Unfortunately, the Purcell limit cannot be extended infinitely, as the ability for an experimenter to measure the qubit relies on there being some coupling to an ancillary readout mode, but this *can* be made arbitrarily small with properly engi-

neered microwave filters. In some sense, the Purcell limit is the ultimate technical limit on qubit coherence.

Second, not every material is lossless. Normal metals, for instance, are very efficient dissipators since they have $\sim 10^{23}$ electronic degrees of freedom with a large density of states. Less obvious is that insulators can have defects in the bulk and especially at surfaces that can absorb energy from the qubit. Vacuum, however is indeed a lossless dielectric. By engineering the qubit to maximize the amount of energy stored in vacuum, coherence times of qubits and superconducting resonators have improved significantly [Paik et al. 2011; Minev, Pop, and Devoret 2013].

Third, the most enticing property of superconductors, namely the lack of lossy QP excitations, breaks down in the presence high-frequency radiation. This is not a surprising effect, but for some time it was not understood to what level these excitations would limit qubit performance. By equipping experimental setups with better shielding at *infrared* frequencies, the density of QP excitations has decreased and resulted in improved qubit and resonator performance [Córcoles et al. 2011; Barends et al. 2011].

So, what currently limits T_1 and T_2 in superconducting qubits? Generally speaking, there's no obvious answer, as so many details about the materials used in qubit devices and the environment to which they are coupled varies between different experimental setups and certainly varies between laboratories. It is generally believed that dephasing times are limited by photon shot noise [Sears et al. 2012; Wang et al. 2019], which shifts the qubit transition frequency in the presence of a fluctuating photon population in the other electromagnetic modes to which the qubit is coupled. In flux-tunable qubits, flux noise can also be a limiting factor when biased away from so-called *sweet spots*, where the derivative of ω_{01} with respect to flux is zero.[11]

As far as *dissipation* mechanisms limiting T_1 are concerned, we believe that there are two primary culprits. First, lossy imperfections at the *surfaces* of dielectric materials can contribute to both capacitive (coupling to electric field) and inductive (coupling to current or magnetic field). These could be dislocations in the crystal structure or paramagnetic impurities on the surface acting as two-level fluctuators. The second mechanism (and the subject of this dissertation) is that of QP excitations in the superconductors that make up the qubit electrodes. If ev-

[11] The same goes for qubits that are tunable with an electrostatic gate, in which charge noise can be a significant detriment to phase coherence.

erything in the system was thermalized to the base temperature of our cryostats ($\sim$ 20 mK), the QP-induced limit on T_1 *could* be longer than the lifetime of the universe![12] Surprisingly, there appear to be many orders of magnitude more QPs than would be expected, which can significantly limit qubit T_1. The rest of this dissertation will describe in detail the physics of these nonequilibrium QPs and how they couple to and cause dissipation in superconducting qubits. This includes a new mechanism that couples the qubit to both QPs and high-frequency photons in a four-body process that we call photon-assisted quasiparticle generation and tunneling (PAT) [Houzet et al. 2019]. Finally, there will be a discussion of the devices and techniques we implemented to probe QP-induced dissipation, with experimental data and results [Serniak et al. 2018; Serniak et al. 2019] presented in the final chapters.

[12]This assumes the device had an even number of electrons when it was cooled down. If the number of electrons is odd the QP-induced limit on coherence can actually be pretty severe, as will be discussed in Chapter 5.

3

Quasiparticle Excitations in BCS Superconductors

The gapped energy spectrum of superconductors, along with the advent of modern cryogenic techniques which ensure a relative lack of excitations above the superconducting gap, has spawned many technologies based on thin-film superconducting devices. In fact, when cooled to dilution refrigerator temperatures $T \approx 20$mK, there are so few excitations that signatures of their spontaneous production by high-frequency photons and phonons can be directly detected by simple DC transport and/or RF reflectometry experiments. Devices operating under these principles include microwave kinetic inductance detectors (MKIDs), superconducting nanowire single photon detectors (SNSPDs), and transition-edge sensors (TESs). Each of these utilize quasiparticle excitations (QPs) — fundamental excitations out of the BCS ground state — as a measurable resource that makes the detector "click." Superconducting qubits, on the other hand, rely on the macroscopic coherence of the superconducting ground state to function efficiently, and the presence of any QP excitations will limit their performance to *some* level. If the entire experimental setup was in thermal equilibrium at 20 mK there would be so few QPs that it wouldn't be an issue for qubits, however there is overwhelming evidence for an abundance of *nonequilibrium* QPs, which *can* limit state-of-the-art qubits. In this chapter, we will review the superconducting ground state and consider the excited states of a superconductor in which QP excitations are present. Then, we will discuss the plethora of observations that indicate a nonequilibrium density of QPs and discuss the energy distribution of these QPs via analysis of a kinetic equation. Finally, we will conclude with a brief discussion of Josephson-junction physics.

3.1 BCS superconductivity

Superconducting materials are typically characterized by their unique electrodynamic properties, namely their support of perfect DC conductivity and perfect diamagnetism (at least in bulk, type-I superconductors), which are exhibited at

temperatures less than T_c, the critical temperature below which the material undergoes a second-order phase transition into the superconducting state. It took nearly 50 years after the first discovery of these properties for a consistent microscopic theory to be developed by Bardeen, Cooper, and Schrieffer [Bardeen, Cooper, and Schrieffer 1957]. They describe the phenomenon of superconductivity as arising through phonon-mediated interaction between time-reversed pairs of electrons (opposite spin and momenta). So-called "good" BCS superconductors have an energy gap Δ in the electronic density of states around the Fermi energy ε_F, however the pairing interaction is weak such that $\Delta \ll \varepsilon_F$. This gap is related to the critical temperature T_c at which the material enters the superconducting phase by $\Delta = 1.74 k_B T_c$, in the weak coupling limit.[1]

3.1.1 The BCS Hamiltonian

This section draws from and combines the discussions of BCS in Refs. de Gennes 1999, Tinkham 2004, and Bretheau 2013. Before considering the microscopic details that make a superconductor a superconductor, we should establish a simple picture for normal metals. Until otherwise noted, we will assume to be working at $T = 0$. In a normal metal, and assuming independent electrons, the many-body Hamiltonian of the electron system can be written as

$$H_{\text{n.m.}} = \sum_{ks} \xi_k \hat{c}^\dagger_{ks} \hat{c}_{ks} \tag{3.1}$$

Above, $\hat{c}_{ks}$ is the fermionic annihilation operator for electrons with momentum k and spin s. The total energy of the electron system is just a sum over the energies associated with level occupation, with $\xi_k = \hbar^2 k^2 / 2m_e - \varepsilon_F$ being the kinetic energy of an electron with mass m_e and momentum k with respect to the Fermi energy ε_F, and $\hat{c}^\dagger_{ks}\hat{c}_{ks}$ giving the occupation of the electron state indexed by k and s. In a BCS superconductor, the energy of the system is described by the "BCS-pairing Hamiltonian," which adds to the electrons in a normal metal a pair-

[1] While this prefactor may seem at first glance to be a numerical artifact, $1.76 = \pi / e^\gamma$, where γ is the Euler-Mascheroni constant.

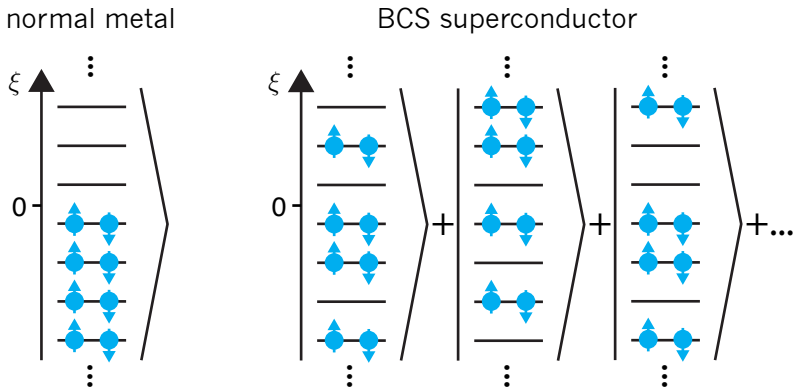

Figure 3.1 | Occupied levels in a normal metal and superconductor in 1D. Here, horizontal lines represent levels that can be occupied by time-reversed pairs of electrons, which have opposite spin and momenta: $k\uparrow$ and $-k\downarrow$. Not shown are the degenerate pairs with transposed spin. In a normal metal (left) at $T=0$, these levels are occupied by electron-like particles up to the Fermi energy ($\xi=0$) in the ground state. In a BCS superconductor (right), the ground state is a coherent superposition of all combinations of levels being either doubly-occupied with electrons or doubly-occupied with holes. This pair correlation extends above and below the Fermi energy, and decays on an energy scale given by the superconducting energy gap Δ.

interaction term:

$$H_{\text{BCS}} = \sum_{ks} \xi_k \hat{c}^\dagger_{ks} \hat{c}_{ks} + \sum_{k,k'} V^*_{kk'} \hat{c}^\dagger_{k\uparrow} \hat{c}^\dagger_{-k\downarrow} \hat{c}_{-k'\downarrow} \hat{c}_{k'\uparrow} \tag{3.2}$$

The first term in Eq. 3.2 is the same as above, and the second term represents the attractive interaction (for $V_{kk'}<0$) that coherently shuffles pairs of electrons with opposite spin and momenta $\pm k$ to states with momenta $\pm k'$. This introduces correlations in the occupation of states with opposite momenta, and therefore the expectation value of operator products in Eq. 3.2 (e.g. $\langle \hat{c}_{-k'\downarrow} \hat{c}_{k'\uparrow} \rangle$)[2] will be nonzero, in contrast to a normal metal. Even at this stage in the discussion there is evidence of many body entanglement, of which many see superconductivity as an archetypal example. Assuming the superconductor is not too small, there will be many Cooper pairs contributing to the condensate and therefore the fluctuations

[2]Here, $\langle\rangle$ denotes the time average

of $\hat{c}_{-k'\downarrow}\hat{c}_{k'\uparrow}$ will be relatively small. These ingredients suggest the applicability of a mean-field approach, which turns out is convenient for considering excited states of the system. We'll make the mean-field approximation by setting

$$\hat{c}_{-k'\downarrow}\hat{c}_{k'\uparrow} = \langle \hat{c}_{-k'\downarrow}\hat{c}_{k'\uparrow}\rangle + \left(\hat{c}_{-k'\downarrow}\hat{c}_{k'\uparrow} - \langle \hat{c}_{-k'\downarrow}\hat{c}_{k'\uparrow}\rangle\right) \tag{3.3}$$

and so on for other operator pairs. Brackets denote the time average of the operator product, and the term in parentheses represents small fluctuation from the mean. We'll then neglect terms that are second-order in this small parameter. This substitution results in an effective pairing Hamiltonian

$$\begin{aligned} H_{\text{BCS}}^{\text{eff}} = \sum_{ks} \xi_k \hat{c}_{ks}^\dagger \hat{c}_{ks} + \sum_{kk'} V_{kk'} \Big(& \langle \hat{c}_{k\uparrow}^\dagger \hat{c}_{-k\downarrow}^\dagger \rangle \langle \hat{c}_{-k'\downarrow}\hat{c}_{k'\uparrow}\rangle \\ & + \langle \hat{c}_{k\uparrow}^\dagger \hat{c}_{-k\downarrow}^\dagger \rangle \left(\hat{c}_{-k'\downarrow}\hat{c}_{k'\uparrow} - \langle \hat{c}_{-k'\downarrow}\hat{c}_{k'\uparrow}\rangle\right) \\ & + \left(\hat{c}_{k\uparrow}^\dagger \hat{c}_{-k\downarrow}^\dagger - \langle \hat{c}_{k\uparrow}^\dagger \hat{c}_{-k\downarrow}^\dagger \rangle\right) \langle \hat{c}_{-k'\downarrow}\hat{c}_{k'\uparrow}\rangle \Big) \end{aligned} \tag{3.4}$$

where some terms will cancel to give

$$\begin{aligned} H_{\text{BCS}}^{\text{eff}} = \sum_{ks} \xi_k \hat{c}_{ks}^\dagger c_{ks} + \sum_{kk'} V_{kk'} \Big(& \langle \hat{c}_{-k'\downarrow}\hat{c}_{k'\uparrow}\rangle \hat{c}_{k\uparrow}^\dagger \hat{c}_{-k\downarrow}^\dagger + \langle \hat{c}_{k\uparrow}^\dagger \hat{c}_{-k\downarrow}^\dagger \rangle \hat{c}_{-k'\downarrow}\hat{c}_{k'\uparrow} \\ & - \langle \hat{c}_{k\uparrow}^\dagger \hat{c}_{-k\downarrow}^\dagger \rangle \langle \hat{c}_{-k'\downarrow}\hat{c}_{k'\uparrow}\rangle \Big) \end{aligned} \tag{3.5}$$

Now we will define $\Delta_k = -\sum_{k'} V_{kk'} \langle \hat{c}_{-k'\downarrow}\hat{c}_{k'\uparrow}\rangle$, the BCS pair potential. With this substitution, the effective BCS Hamiltonian begins to take on an intuitive form.

$$H_{\text{BCS}}^{\text{eff}} = \sum_{ks} \xi_k \hat{c}_{ks}^\dagger \hat{c}_{ks} - \sum_k \left(\Delta_k^* \hat{c}_{-k\downarrow}\hat{c}_{k\uparrow} + \Delta_k \hat{c}_{-k\downarrow}^\dagger \hat{c}_{k\uparrow}^\dagger + \text{constant}\right) \tag{3.6}$$

The pair potential can be thought of as the energy that is saved when an electron enters the Cooper pair condensate (often called the *condensation energy*), with the pair of bilinear operators representing the Cooper pairs. In order to diagonalize the BCS mean-field Hamiltonian, we perform what is known as the Bogoliubov-Valatin transformation, redefining

$$\begin{aligned} \hat{c}_{k\uparrow} &= u_k^* \hat{\gamma}_{k\downarrow} + v_k \hat{\gamma}_{k\uparrow}^\dagger \\ \hat{c}_{-k\downarrow}^\dagger &= -v_k^* \hat{\gamma}_{k\downarrow} + u_k \hat{\gamma}_{k\uparrow}^\dagger. \end{aligned} \tag{3.7}$$

Here, the electron creation/annihilation operators are now decomposed as superpositions of other fermionic operators, with $|u_k|^2+|v_k|^2 = 1$ to conserve probability. These new fermionic operators create and destroy what we call Bogoliubov quasiparticle excitations (QPs). It is important to mention here that the transformation above is written in a particular form corresponding to the *excitation picture* of superconductivity, which will be discussed in the next section. Continuing, we will invert the transformation:

$$\begin{aligned}\hat{\gamma}^\dagger_{k\uparrow} &= u^*_k \hat{c}^\dagger_{k\uparrow} - v^*_k \hat{c}_{-k\downarrow} \\ \hat{\gamma}^\dagger_{k\downarrow} &= u^*_k \hat{c}^\dagger_{-k\downarrow} + v^*_k \hat{c}_{k\uparrow}.\end{aligned} \tag{3.8}$$

These Bogoliubov operators obey the usual fermionic anticommutation relation $\{\hat{\gamma}^\dagger_{k\downarrow}, \hat{\gamma}_{k\downarrow}\} = 1$, and are a superposition of electron creation ($c^\dagger$) and hole creation (c) operators. We can show that the Bogoliubov transformation diagonalizes the Hamiltonian with the proper selection of u_k's and v_k's. Skipping the algebra, from Eq. 3.6 we find

$$H^{\text{eff}}_{\text{BCS}} = E_{\text{GS}} + \sum_k \sqrt{\xi_k^2 + |\Delta_k|^2}(\hat{\gamma}^\dagger_{k\downarrow}\hat{\gamma}_{k\downarrow} + \hat{\gamma}^\dagger_{k\uparrow}\hat{\gamma}_{k\uparrow}) \tag{3.9}$$

Here, $E_{\text{GS}} = \sum_k (\xi_k - \varepsilon_k + \Delta_k \langle \hat{c}^\dagger_{k\uparrow}\hat{c}^\dagger_{-k\downarrow}\rangle)$ is the total energy of the superconducting ground state, and the sum term gives the energy of QP excitations at positive (spin $\uparrow$) and negative (spin $\downarrow$)[3] energies with respect to the Fermi level. This is measured relative to the normal-metal ground state energy, is linear in the volume of the superconductor and scales as Δ^2. At this point, we'll make a simplifying assumption that the BCS interaction strength $V_{kk'} = V$, independent of momentum as long as $\xi_k, \xi_{k'} < \hbar\omega_D$, the Debye frequency, which acts as the cutoff for the phonon-mediated pair interaction. With this, we see that $\Delta_k = \Delta$ is also independent of momentum. As evidenced by Eq. 3.9, the energy of these fundamental QP excitations $\varepsilon_k = \sqrt{\xi_k^2 + \Delta^2}$, which has a minimum of Δ at $\xi_k = 0$. For this reason, Δ is called the superconducting energy gap for single-particle excitations. All of this was made possible by choosing the proper values of u_k and v_k:

[3] Our choice to spin-polarize excitations of positive and negative energy is for convenience and fits within the excitation representation of superconductivity that will be described later. For the current discussion, this assignment is inconsequential.

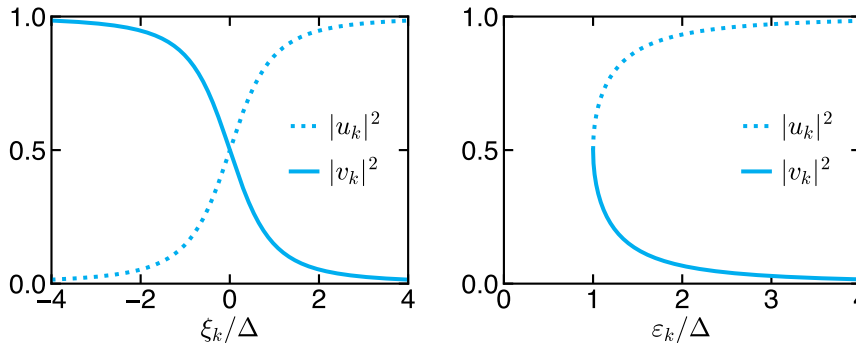

Figure 3.2 | Magnitude squared of the BCS occupation factors u_k and v_k as a function of relative quasiparticle kinetic energy ξ_k (left) and the interaction-dressed total quasiparticle energy ε_k (right), with each energy scale normalized by the gap Δ.

$$|v_k|^2 = 1 - |u_k|^2 = \frac{1}{2}\left(1 - \frac{\xi_k}{\varepsilon_k}\right) = \frac{1}{2}\left(1 - \frac{\xi_k}{\sqrt{\xi_k^2 + \Delta^2}}\right) \tag{3.10}$$

The dependence of u_k and v_k on ξ_k indicates that the electron-hole character of the QP excitation is a function of its energy [Fig. 3.2]. This gives rise to interesting interference effects in QP-transport processes.

3.1.2 Single-particle density of states

Since $\Delta \ll \varepsilon_F$ in the weak-coupling regime of BCS, we can approximate the normal density of states $\nu_n(\xi)$ as constant with a value equal to its value at the Fermi level $\nu_0 \equiv \nu_n(\varepsilon_F)$. From this, we can compute the density of states for excitations of a BCS superconductor

$$\nu_s = \nu_0 \frac{d\xi}{d\varepsilon} = \mathrm{Re}\left\{\frac{\varepsilon}{\sqrt{\varepsilon^2 - \Delta^2}}\right\}. \tag{3.11}$$

Mathematically, the superconducting density of states ν_s is infinite at Δ, however this is will never be the case in physical systems due to broadening of the energy levels. Notably, $\nu_s = 0$ for $\varepsilon < \Delta$, producing the famous superconducting energy gap 2Δ for pairs of QP excitations when $T = 0$.

It's important to note that our choice to work in the excitation picture is just

that: a choice, which defines the form of the Bogoliubov transform Eq. 3.8. Now for a bit of nomenclature: generally speaking, dressed electrons in a normal metal are sometimes called quasiparticles, as they are not simply electrons moving in free space. Along this line, electrons in a superconductor that are additionally dressed by the pair-interaction, are often called Bogoliubov quasiparticles, or Bogoliubons, for the sake of distinguishing them. In the excitation picture of superconductivity, as the name suggests, we have distinguished Bogoliubons that are *excitations* out of the ground state from those that contribute to the condensate. Those excitations we call *QP excitations*[4], which is the traditional nomenclature from many-body physics. The excitation picture of superconductivity is compared with the *single-particle picture*, which is perhaps more intuitive to compare with a normal metal in Fig. 3.3. Moving from the single-particle to excitation picture we have transformed hole-like excitations at energies $< \varepsilon_F$ into particles. These hole excitations remove spin $\uparrow$, and therefore create spin $\downarrow$. The assumption here being that there is no asymmetry between particle and hole excitations (no charge imbalance).

3.2 QP excitations out of the BCS ground state

We managed to massage the BCS coupling Hamiltonian (3.2) into a diagonal form (3.9) where the Bogoliubov operators (3.8) create QP excitations out of the superconducting ground state, and we did all of this without writing down any sort of ground-state wavefunction for the superconductor. Due to its diagonal form, its clear to look for a ground state wavefunction $|\text{BCS}\rangle_{\text{G}}$ that satisfies the relations

$$\hat{\gamma}_{k\uparrow} |\text{BCS}\rangle_{\text{G}} = \hat{\gamma}_{k\downarrow} |\text{BCS}\rangle_{\text{G}} = 0, \tag{3.12}$$

indicating that the BCS ground state is devoid of QPs. BCS took a ground-state wavefunction of the form

$$|\text{BCS}\rangle_{\text{G}} = \prod_k (u_k + v_k e^{i\varphi} \hat{c}^\dagger_{k\uparrow} \hat{c}^\dagger_{-k\downarrow}) |\text{vac.}\rangle \tag{3.13}$$

[4] denoted in this section and the rest of this dissertation as QPs

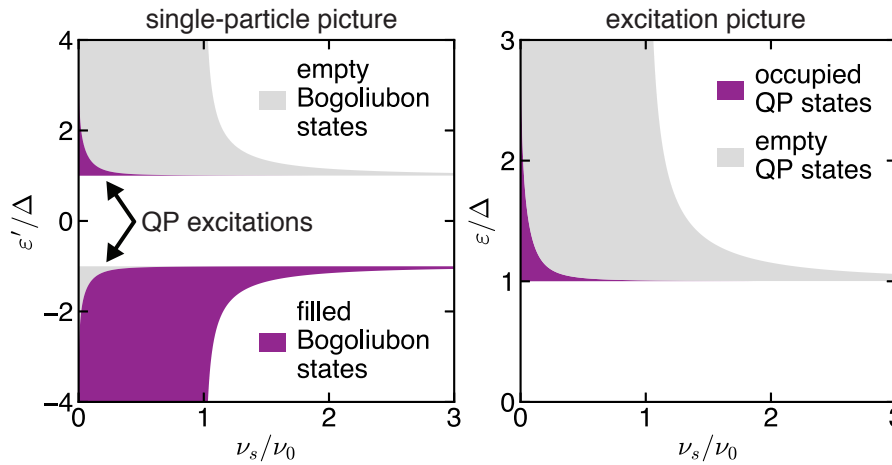

Figure 3.3 | Density of states and QP excitations in the single-particle picture and the excitation picture. One arrives at the excitation by taking the states in the single-particle picture (with energies ε'), transforming all the particles below the Fermi energy into holes (and vice versa), and then flipping the negative energy states across $\varepsilon' = 0$. Energy windows in the excitation picture have twice the degeneracy of those in the single-particle picture.

in the phase basis. This BCS ground state is made up of a coherent superposition of occupied and unoccupied time-reversed electron pairs. Here, we've chosen to make the occupation factors u_k and v_k real, extracting the phase between them, φ, explicitly. Now the u_k's and v_k's have an intuitive definition, they are the probability amplitudes for a pair being empty or occupied, respectively, and φ is the phase of the superconducting order parameter. Finally, $|\text{vac.}\rangle$ is a state representing an *electron vacuum*, upon which the condensate is built. It's important to note that the above wavefunction does not conserve particle number, but has a well defined superconducting phase φ. Taking the Fourier transform of Eq. 3.13 performs what is called the "Anderson projection," and is well defined in partice number, allowing φ to fluctuate. When the QP operators act on the ground state, they definitively break a Cooper pair, leaving an unpaired electron-hole excitation.

$$\begin{aligned}\hat{\gamma}^\dagger_{k\uparrow}|\text{BCS}\rangle_\text{G} &= \hat{c}^\dagger_{k\uparrow}\prod_{k'\neq k}(u_{k'} + v_{k'}e^{i\varphi}\hat{c}^\dagger_{k'\uparrow}\hat{c}^\dagger_{-k'\downarrow})\,|\text{vac.}\rangle \\ \hat{\gamma}^\dagger_{k\downarrow}|\text{BCS}\rangle_\text{G} &= \hat{c}^\dagger_{-k\downarrow}\prod_{k'\neq k}(u_{k'} + v_{k'}e^{i\varphi}\hat{c}^\dagger_{k'\uparrow}\hat{c}^\dagger_{-k'\downarrow})\,|\text{vac.}\rangle\end{aligned} \tag{3.14}$$

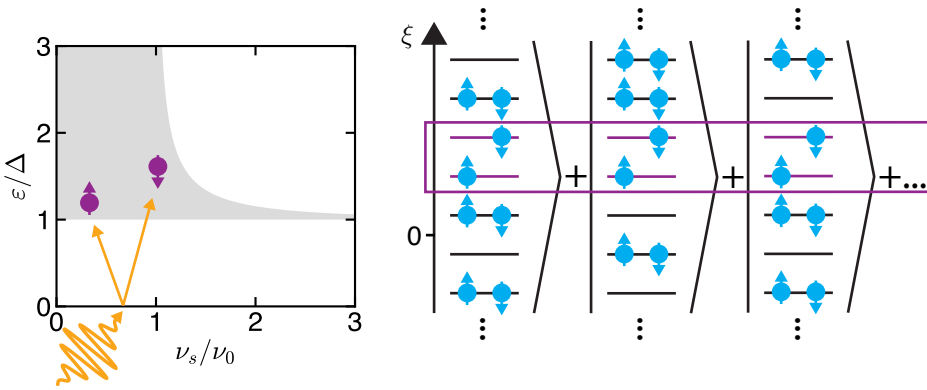

Figure 3.4 | A pair of QP excitations (purple) in an isolated superconductor, obtained from acting $\hat{\gamma}^\dagger_{ks}\hat{\gamma}^\dagger_{k'\bar{s}}$ on the BCS ground state, where $\bar{s}$ is the opposite spin of s. This is depicted in the excitation picture (left) and in a wavefunction schematic (right) near the Fermi energy ($\xi = 0$) [see Fig. 3.1]. Fermion-number parity must be conserved in an isolated superconductor, indicating that QPs must be generated in pairs requiring total energy $\geq 2\Delta$, which could come from high-frequency phonons or photons (orange). In the wavefunction schematic, this has the effect of definitively occupying states $k\uparrow$ and $-k'\downarrow$, removing their corresponding time-reversed pairs from the coherent superposition of many-body states that is the BCS ground state (indicated by the purple box).

Each QP excited in the system necessarily removes a Cooper-pair level from the condensate, and requires an excitation energy $\varepsilon_k = \sqrt{\xi_k^2 + \Delta^2}$. The diagonal form of the Hamiltonian (3.9) is in direct analogy to a normal metal, with the transformation $\hat{c}_{ks} \to \hat{\gamma}^\dagger_{ks}$, which makes sense with the fact that states with QP excitations are the excited energy eigenstates of a superconductor.

3.3 Thermal QPs

As temperature is increased from $T = 0$, there will be some probability that QPs will be excited above the gap. When cooled to temperatures well below the critical temperature $T_c = \Delta/1.76k_B$ at which superconductivity appears, any electronic QP excitations should be suppressed as long as $T \ll \Delta/k_B$. We define three quantities that describe how many quasiparticles there are in a device: the total number of quasiparticles in the device N_{QP}, the number of quasiparticles per

unit volume n_{QP}, and the number of quasiparticles normalized by the number of Cooper pairs $x_{QP} = n_{QP}/n_{CP} = N_{QP}/N_{CP}$. We'll mainly focus the normalized density x_{QP}, since it is an intrinsic quantity that can be applied more generally across different devices. Simply, one can find x_{QP} by integrating all of the filled states in the excitation picture[5]:

$$x_{QP} = \frac{1}{\nu_0}\int_0^\infty f(\varepsilon)\nu_s(\varepsilon)d\varepsilon. \tag{3.15}$$

To present a compact, analytical formula for the density of thermally-generated QPs $x_{QP}^{th.}$, we will make two assumptions: first, that the excited QPs have a Fermi-Dirac distribution in energy[6]

$$f(\varepsilon) = f_{FD}(\varepsilon) = \frac{1}{e^{\varepsilon/k_BT}+1}, \tag{3.16}$$

and second, that there are very few QPs such that they are localized very near the gap edge. This second assumption allows us to express the approximate superconducting density of states $\tilde{\nu}_s(\varepsilon) = \nu_0/\sqrt{2(\varepsilon-\Delta)}$ for $\varepsilon \geq \Delta$. With this, we can evaluate Eq. 3.15 to find the ratio of thermally generated QP excitations to Cooper pairs $x_{QP}^{th.}$ with the relation [Catelani et al. 2011]

$$x_{QP}^{th.} \approx \sqrt{2\pi k_B T/\Delta}e^{-\Delta/k_BT}. \tag{3.17}$$

This is valid for $T \ll \Delta$, and can also be thought of as the fraction of broken Cooper pairs: $x_{QP} = n_{QP}/n_{CP} = n_{QP}/2\nu_0\Delta$, where n_{QP} is the number of QPs per unit volume and n_{CP} is the number of Cooper pairs per unit volume[7]. We will return the discussion of QPs in the next section.

What happens to the gap Δ in the presence of QP excitations at finite temperature? We previously defined the pair potential in terms of expected electron occupation, and we saw that the pair potential and the superconducting gap are numerically the same. Lets compute Δ_k (keeping the k-dependence for general-

[5]The lower limit of integration here is 0, not Δ, to include situations where ν_s does not agree perfectly with the BCS prediction. For instance, some disordered superconductors show evidence of a *soft gap*, where the coherence peaks are broadened and there are many available subgap QP states.

[6]The validity of this assumption will be discussed in a later section. SPOILER ALERT: it's a reasonably good approximation.

[7]In superconducting Al films, $n_{CP} = 4 \times 10^6\ \mu m^{-3}$

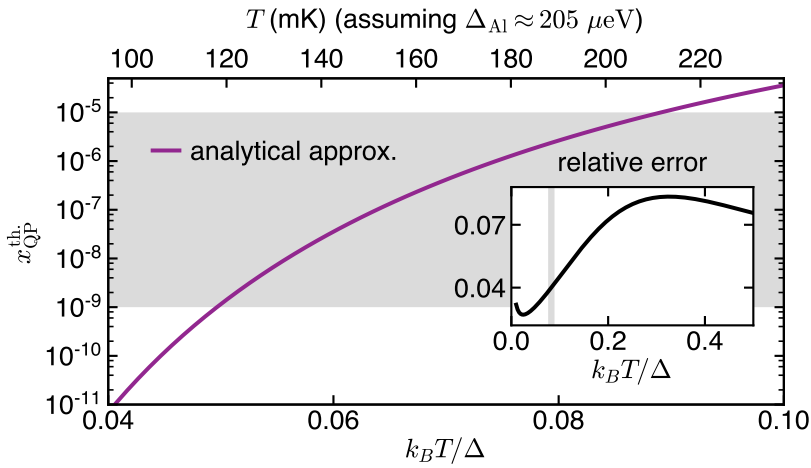

Figure 3.5 | Thermally generated QP density $x_{\mathrm{QP}}^{\mathrm{th.}}$ as a function of T/Δ calculated using the analytical approximation in Eq. 3.17. The gray shaded region indicates the range of residual x_{QP}^{0} observed empirically at low temperature. Inset: relative error of Eq. 3.17 to exact numerical integration assuming a Fermi-Dirac distribution of QPs (Eq. 3.15). The small, grey band indicates the same band as in the main figure.

ity) in terms of Bogoliubov operators:

$$\begin{aligned}\Delta_k = -\sum_{k'} V_{kk'}\langle c_{-k'\downarrow}c_{k'\uparrow}\rangle &= -\sum_{k'} V_{kk'}\langle(-v_{k'}\hat{\gamma}_{k'\uparrow}^{\dagger} + u_{k'}^{*}\hat{\gamma}_{k'\downarrow})(u_{k'}^{*}\hat{\gamma}_{k'\uparrow} + v_{k'}\hat{\gamma}_{k'\downarrow}^{\dagger})\rangle \\ &= -\sum_{k'} V_{kk'}u_{k'}^{*}v_{k'}\langle 1 - \hat{\gamma}_{k'\uparrow}^{\dagger}\hat{\gamma}_{k'\uparrow} - \hat{\gamma}_{k'\downarrow}^{\dagger}\hat{\gamma}_{k'\downarrow}\rangle.\end{aligned} \tag{3.18}$$

We can recognize $\langle\hat{\gamma}_{k'\uparrow}^{\dagger}\hat{\gamma}_{k'\uparrow}\rangle$ and $\langle\hat{\gamma}_{k'\downarrow}^{\dagger}\hat{\gamma}_{k'\downarrow}\rangle$ as being the occupation probability of electron-like and hole-like QP states with energy ε_k:

$$\langle\hat{\gamma}_{k'\uparrow}^{\dagger}\hat{\gamma}_{k'\uparrow}\rangle = \langle\hat{\gamma}_{k'\downarrow}^{\dagger}\hat{\gamma}_{k'\downarrow}\rangle = f(\varepsilon_{k'}). \tag{3.19}$$

Substituting to get the equation fully in terms of energies

$$\Delta_k = -V\sum_{k'}\frac{\Delta_{k'}}{2\varepsilon_{k'}}\tanh\left(\frac{\varepsilon_{k'}}{2k_BT}\right) \tag{3.20}$$

and taking it to the continuum limit and making the constant-interaction approximation gives the familiar self-consistency equation in integral form for the gap Δ

as a function of T

$$-\frac{1}{\nu_0 V} = \int_0^{\hbar\omega_D} d\xi_{k'} \frac{1}{2\sqrt{\xi_{k'}^2 + \Delta^2}} \tanh\left(\frac{\sqrt{\xi_{k'}^2 + \Delta^2}}{k_B T}\right) \tag{3.21}$$

where the Debye frequency ω_D sets the cutoff energy of the phonon-mediated pair interaction. Sending $\Delta \to 0$ gives the familiar form of the equation for the critical temperature T_c at which superconductivity appears

$$k_B T_c = 1.13\hbar\omega_D e^{-1/\nu_0 V}. \tag{3.22}$$

Along with direct measurements of T_c, one can use this to estimate the effective pair-coupling strength V.

3.4 Nonequilibrium QPs

QP excitations can significantly hinder the performance of a variety of superconducting devices, typically to an extent that scales linearly with the QP density, which motivates the broad goal of reducing x_{QP}. Though possible in certain experiments, it is a luxury to be able to count the total number of QPs in a given device. More often than not, an empirical x_{QP} is attained by comparing an extrinsic metric, such as T_1 of a qubit, to theoretical limits imposed by a certain *thermally generated* x_{QP}. With these techniques, experimenters infer that x_{QP} typically falls in the range of 10^{-9}–10^{-5} [Aumentado et al. 2004; Segall et al. 2004; Naaman and Aumentado 2006; Shaw et al. 2008; Martinis, Ansmann, and Aumentado 2009; Barends et al. 2011; Saira et al. 2012; Pop et al. 2014; Visser et al. 2014a; Nsanzineza and Plourde 2014; Wang et al. 2014; Vool et al. 2014; Visser et al. 2014b; Bal et al. 2015; Taupin et al. 2016; Gustavsson et al. 2016; Serniak et al. 2018; Grünhaupt et al. 2018; Serniak et al. 2019][8], which corresponds to an effective QP temperature $T_{\mathrm{QP}}^{\mathrm{eff}} \approx 120$–$210$ mK, much greater than the temperature at which our experiments are performed. Most JJ based-superconducting devices are based on thin films of Al, and are thermally anchored to the mixing chamber of a dilution refrigerator (~ 20 mK). If we insert this temperature into Eq. 3.17 along with $\Delta \approx 205\ \mu\mathrm{eV} = 1.76 k_B T_c$, one would expect $x_{\mathrm{QP}}^{\mathrm{th.}} \sim 10^{-52}$! This discrepancy that there are many, *many* orders of magnitude more QPs than

[8] and many more!

expected defines the presence of what we refer to as *nonequilibrium* QPs in our devices.

The exact source of these nonequilibrium QPs is to this day unknown, but has been the motivation for many theoretical works [Bespalov et al. 2016; Catelani and Basko 2019; Houzet et al. 2019] which may guide future experiments.

3.5 Kinetics of nonequilibrium QPs

Here we write and solve numerically the kinetic equation governing the occupation function $f(\varepsilon)$ for QPs in a superconductor subject to environmental coupling [Kaplan et al. 1976; Chang and Scalapino 1977; Martinis, Ansmann, and Aumentado 2009; Catelani, Glazman, and Nagaev 2010; Goldie and Withington 2013]. The kinetic equation computes the derivative of the QP occupation function, and includes scattering processes between these different QP states as well as pair generation and pair recombination. This can be decomposed into contributions from different interactions:

$$\frac{df(\varepsilon)}{dt} = g(\varepsilon) + I^{s}_{\text{e-ph}} + I^{p}_{\text{e-ph}} + I_{\text{e-e}} \tag{3.23}$$

The first term accounts for generation of QPs, and its energy dependence will depend on the exact processes that create QPs in our circuit. In general, we can write it as

$$g(\varepsilon) = \eta_g P_g(\varepsilon)\nu_s(\varepsilon), \tag{3.24}$$

where $P_g(\varepsilon)$ is the power spectrum of QP-generating radiation, $\nu_s(\varepsilon)$ is the superconducting density of states, and η_g is an absorption efficiency, which need not be constant as a function of ε, however we will assume so here. A plausible mechanism for non-equilibrium QP generation is via blackbody radiation from fridge components at an elevated temperature. This source of photon flux can be characterized by the traditional blackbody power spectrum:

$$P_{\text{BB}}(\varepsilon) \propto \frac{\varepsilon^3}{e^{\varepsilon/k_B T_{\text{BB}}} - 1}. \tag{3.25}$$

While this may be the most realistic case, we will consider the extreme case of QP injection in a narrow band of energies, in an attempt to reach a steady-state $f(\varepsilon)$ that deviates maximally from the typically assumed Fermi-Dirac distrubu-

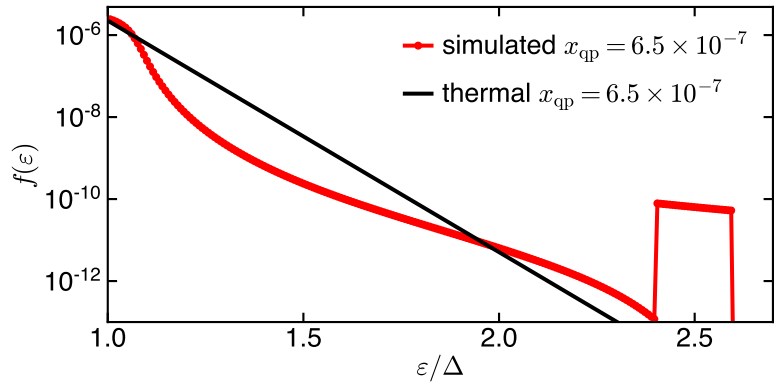

Figure 3.6 | Numerical simulation of the QP kinetic equation to determine the equilibrium QP energy distribution $f(\varepsilon)$ in the presence of electron-phonon scattering and a constant generation source between 2.4Δ and 2.6Δ.

tion [Eq. 3.16]. The the second and third terms in Eq. 3.23 correspond to electron-phonon scattering and recombination processes, respectively. Electron-phonon scattering will tend to cool quasiparticles toward the gap edge assuming that the phonons are well-thermalized to the fridge temperature, with a phonon occupation distribution

$$N(\varepsilon) = \frac{1}{e^{\varepsilon/k_B T_{\rm ph}} - 1}. \tag{3.26}$$

The electron-phonon scattering collision integral shuffles QPs from state ε to ε_1

$$\begin{aligned} I^s_{\text{e-ph}} = &\frac{1}{\tau_0 \Delta \nu_0} \int_\Delta^\varepsilon d\varepsilon_1 \left(\frac{\varepsilon - \varepsilon_1}{\Delta}\right)^2 \left(1 - \frac{\Delta^2}{\varepsilon\varepsilon_1}\right) \nu_s(\varepsilon_1) \\ &\times \Big\{[1 - f(\varepsilon)] f(\varepsilon_1) N(\varepsilon - \varepsilon_1) \\ &\quad - f(\varepsilon)[1 - f(\varepsilon_1)][N(\varepsilon - \varepsilon_1) + 1]\Big\} \\ &+ \frac{1}{\tau_0 \Delta \nu_0} \int_\varepsilon^\infty d\varepsilon_1 \left(\frac{\varepsilon - \varepsilon_1}{\Delta}\right)^2 \left(1 - \frac{\Delta^2}{\varepsilon\varepsilon_1}\right) \nu_s(\varepsilon_1) \\ &\times \Big\{[1 - f(\varepsilon)] f(\varepsilon_1)[N(\varepsilon - \varepsilon_1) + 1] \\ &\quad - f(\varepsilon)[1 - f(\varepsilon_1)] N(\varepsilon - \varepsilon_1)\Big\}, \end{aligned} \tag{3.27}$$

accounts for both heating and cooling of QPs due to phonons. The phonon-induced pair-scattering collision integral

$$I^{p}_{\text{e-ph}} = \frac{1}{\tau_0 \Delta \nu_0} \int_{\Delta}^{\infty} d\varepsilon_1 \left(\frac{\varepsilon+\varepsilon_1}{\Delta}\right)^2 \left(1+\frac{\Delta^2}{\varepsilon\varepsilon_1}\right) \nu(\varepsilon_1) \times \Big\{ [1-f(\varepsilon)][1-f(\varepsilon_1)] N(\varepsilon+\varepsilon_1) - f(\varepsilon) f(\varepsilon_1) [N(\varepsilon+\varepsilon_1)+1] \Big\} \tag{3.28}$$

includes terms corresponding to thermal-phonon-induced recombination and generation of QPs, however the latter is strongly suppressed at low temperatures.

QPs can scatter with each other as indicated by $I_{\text{e-e}}$, however this term will be negligible if x_{QP} is small and if we restrict ourselves to only considering QPs with energy $< 3\Delta$. Above this threshold energy 3Δ, a QP can cool to the gap edge by breaking a Cooper pair in a "QP multiplication" process, and the large density of states will make the process comparable in strength to phonon scattering.

The QP occupation function can be obtained by integrating the kinetic equation. Fig. 3.6 shows the numerically simulated $f(\varepsilon)$ subject to the interactions described above, and compares it to a thermal distribution that corresponds to approximately the same x_{QP}. The QP kinetic equation is solved by iteration, with each consecutive estimate $f_{j+1}(\varepsilon) = f_j(\varepsilon) + \delta f_j(\varepsilon)\delta t$ with timesteps of $\delta t = 20$ ns, with final refinement at 1 ns timesteps. Numerical inputs are $\Delta = \Delta_{\text{Al}} = 205\ \mu$eV, electron-phonon scattering rate $\tau_0 = 438$ ns [Kaplan et al. 1976], and equilibrium phonon temperature $T_{\text{ph}} = 35$ mK. The product $\eta_g P_g(\varepsilon)$ is chosen arbitrarily to produce a reasonable QP density and gives $x_{\text{QP}} = 6.5 \times 10^{-7}$ in steady-state. As evident in Fig. 3.6, the distribution is not quite Fermi-Dirac, but the deviation is relatively minute, confirming that a thermal distribution is a valid approximation. There is a visible feature corresponding to the QP injection between 2.4Δ and 2.6Δ, however this is more than three orders of magnitude smaller than $f(\Delta)$.

3.6 Josephson effects

As the work in this dissertation relies on Josephson-junction based superconducting qubits, it would be remiss not to mention the underlying physics of Josephson junctions. The nonlinear current-phase relation of a Josephson tunnel junction is the backbone of the vast majority of superconducting quantum circuits, save for

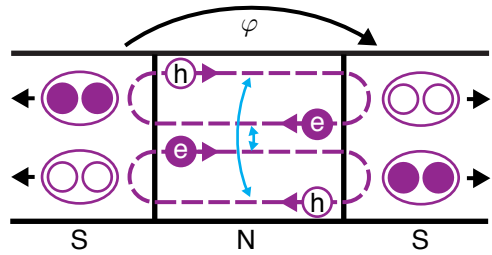

Figure 3.7 | Schematic of a superconductor-normal metal-superconductor junction with a pair of Andreev bound states responsible for a phase-dependent supercurrent through the junction. Andreev reflection processes scatter an electron (hole) into a hole (electron) with opposite spin and momentum, transferring charge of magnitude $2e$ into the superconducting condensate.

purely-linear superconducting resonators. The two Josephson relations describe the dynamics of the current and superconducting phase φ across the junction:

$$\begin{aligned} I_J &= I_0 \sin\varphi \\ V_J &= \phi_0 \frac{d\varphi}{dt} \end{aligned} \tag{3.29}$$

At the heart of our modern understanding of the Josephson effect are Andreev bound states: states with energies less than Δ that are localized at minima of the superconducting pair potential. In practice, this potential landscape can come from any superconductor-X-superconductor sandwich, where X can be a normal metal, semiconductor, insulator, ferromagnet, or a superconductor with a different Δ. A thorough discussion of the Bogoliubov-de Gennes formalism used to describe Andreev physics can be found in Landry Bretheau's thesis from the Quantronics group in Saclay [Bretheau 2013], and discussion of long-junction phenomena will be considered in the future thesis of Max Hays. Here we will describe some of the basic results relevant for large, weakly transmissive tunnel barriers, such as commonly used Al/AlOx/Al Josephson junctions.

On the microscopic level, a defining characteristic of superconductor is that electrons impinging from a normal metal will undergo Andreev reflection processes at the N-S interface. Andreev reflection differs from traditional (specular) reflection in that not only is momentum exchanged, but also charge. A normal electron with $|\xi| < \Delta$ will bounce off of a superconductor as a hole with oppo-

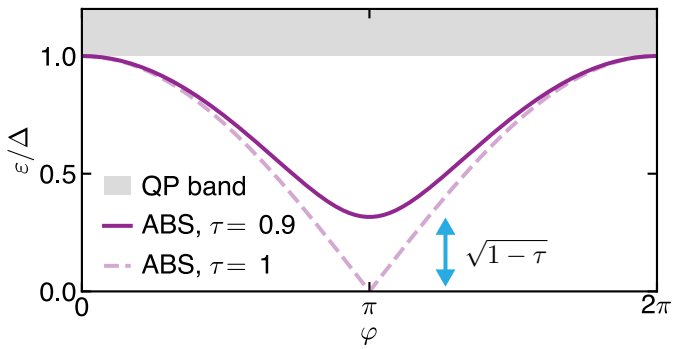

Figure 3.8 | The Andreev-bound-state energy has a minimum at phase bias $\varphi = \pi$. This phase dispersion separates the bound state from the single particle density of states at all values $\varphi \neq 0(\mathrm{mod}2\pi)$.

site spin and momentum [Fig. 3.7]. These Andreev reflection processes allow for current biasing of superconducting leads with bias voltages less than the gap. If a normal region is sandwiched between two superconductors, constructive interference can produce Andreev bound states: subgap states within the junction responsible for the coherent transport of Cooper pairs.

We'll consider a "short" JJ (length much smaller than the superconducting coherence length [9]) with just a single conduction channel. In this quasi-1D junction, without breaking time-reversal symmetry, there are two spin-degenerate Andreev bound states (referred to as the Andreev doublet) at energy

$$\varepsilon_A(\varphi, \tau) = \Delta\sqrt{1 - \tau \sin^2(\varphi/2)} \tag{3.30}$$

in the excitation picture (relative to ε_F), a is depicted in Fig. 3.8. The addition of an arbitrary transmission coefficient τ for the conduction channel couples the two ABS because it give the possibility for specular reflection within the weak link, which induces a transition from one bound state to the other, as shown in figure.

These Andreev bound states are of particular interest to the solid state quantum computing community, and condensed matter physicists in general. The ABS represents an engineerable Fermionic few-level system, which can inter-

[9] In bulk Al, the coherence length $l_c^{\mathrm{bulk}} \approx 1.2\mu$m, however this is reduced in dirty superconductors to an effective value $l_c^{\mathrm{eff}} \approx \sqrt{l_c^{\mathrm{bulk}} l_{\mathrm{MFP}}}$, where l_{MFP} is the electronic mean-free-path. In thin film superconductors, this is limited by the thickness d of the film, giving $l_c^{\mathrm{eff}} \approx \sqrt{l_c^{\mathrm{bulk}} d}$.

face naturally with the superconducting qubit technology and circuit QED. Results from the Quantronics group at Saclay, who have has pioneered the study of ABS [Bretheau et al. 2013; Olivares et al. 2014; Janvier et al. 2015] have shown the coherent manipulation of these states in a superconducting atomic-point contact. Furthermore, studies of Andreev bound states in proximitized semiconductor nanowires [van Woerkom, Geresdi, and Kouwenhoven 2015; Hays et al. 2018; Tosi et al. 2019] are of relevance to topological quantum computing. Systems with large spin-orbit coupling and a large g-factor may enter a topological regime when proximitized by a typical s-wave superconductor. This topological regime may play host to Majorana bound states (with properties similar to those of the ABS in the trivial regime) at the boundaries of the topological superconductor which may prove useful as topologically-protected qubits in their own solid-state quantum computing architecture.

As discussed in Chapter 2, the phase difference φ and the number of particles transferred are conjugate variables, therefore we can express the current through this junction via Hamilton's equations of motion as

$$I_A(\delta,\tau) = -\frac{1}{\phi_0}\frac{d\varepsilon_A}{d\varphi} = \frac{\Delta}{4\phi_0}\frac{\tau\sin(\varphi)}{\sqrt{1-\tau\sin^2(\varphi/2)}}. \tag{3.31}$$

This shows that there is a non-zero DC supercurrent[10] which flows with the only requirement that there is a phase difference imposed, not a voltage. The phase difference is an integral over all past time of the applied voltage, so as long as some voltage was applied at some point in the past, there is the potential for a persistent supercurrent to flow through the junction. This is one of the most fundamental features of superconductivity, enabled by Andreev bound states.

As is evident from Eq. 3.31, if the channel is very opaque ($\tau \ll 1$) we recover the sinusoidal current phase relation described in Chapter 2 that is characteristic of a Josephson tunnel junction. In reality, SIS Josephson junctions (of which most transmon qubits are based) typically have millions of conduction channels contributing to Cooper pair transport. With this in mind, we can calculate the critical current of the junction I_0 from mesoscopic transport by considering N

[10] This assumes that the Andreev doublet is in its *ground state*, with no QPs occupation. As long as $\varepsilon_A \gg k_B T$, this formula is a good approximation for the *average* Andreev current.

parallel ABSs all with the same phase bias:

$$I_J = \sum_{i=1}^{N} \frac{\Delta\tau_i}{4\phi_0}\sin(\varphi), \tag{3.32}$$

From which we can identify the critical current as

$$I_0 = \sum_{i=1}^{N} \frac{\Delta\tau_i}{4\phi_0} = \frac{\Delta\bar{\tau}}{4\phi_0}\frac{A}{\left(\lambda_F/2\right)^2} \tag{3.33}$$

with the factor $\frac{A}{(\lambda_F/2)^2}$ accounting for the total number of conduction channels in the junction, where A is the junction area and λ_F is the Fermi wavelength, and $\bar{\tau}$ is the average channel transparency. From the Landauer formula we can calculate the total resistance of the junction in the normal state to be $R_n = \frac{R_Q(\lambda_F/2)^2}{A\bar{\tau}}$ with $R_Q = h/2e^2$ the single electron quantum of resistance, which allows us to compare with Eq. 2.26:

$$I_0 = \frac{\Delta\bar{\tau}}{4\phi_0}\frac{A}{\left(\lambda_F/2\right)^2} \stackrel{?}{=} \frac{\pi\Delta}{2eR_n}, \tag{3.34}$$

which can be shown to agree. If we consider an Al/AlOx/Al Josephson junction with a critical current density $= 50\ \mathrm{A/cm^2}$,[11] that would correspond to an average channel transparency $\bar{\tau} = 5 \times 10^{-8}$.[12]

[11] Which is reasonable given standard junction fabrication techniques

[12] This assumes a Fermi wavelength $\lambda_F = 0.1$ nm and gap $\Delta = 1.76 k_B T_c$ with $T_c = 1.35$ K.

4

From the Cooper-Pair Box to the Transmon

This chapter will describe various properties of the Cooper-pair-box/transmon circuit, and emphasize the utility of an oft-maligned parameter regime of offset-charge sensitivity which we call the *OCS regime* of the circuit. It is in this regime that charging effects and quasiparticle dynamics can be studied in great detail. In spite of reduced coherence due to charge sensitivity, OCS transmons are an ideal proxy for understanding the effects of QP-induced dissipation in traditional transmons. The discussion in next sections follows closely that of Refs. [Koch et al. 2007; Serniak et al. 2019].

4.1 Properties of the circuit

The CPB/transmon circuit is simply that of a capacitively-shunted Josephson Junction (JJ) with capacitive coupling to charges in its environment [Fig. 4.1]. Electromagnetic excitations of the CPB/transmon are plasma oscillations of Cooper-pair density, and can be visualized similarly to those in a superconducting dipole antenna. The next sections we will detail the distinguishing features of the plasmon eigenstates of the transmon: namely charging effects due to the high-impedance Josephson junction and anharmonicity of the transition spectrum. Furthermore, we will introduce the notion of charge-parity which is a crucial observable of the circuit for experiments probing the effects of nonequilibrium QPs in superconducting qubits.

4.1.1 Offset charge and charge parity

When the Cooper-pair box (CPB)/transmon was briefly introduced in the Chapter 2, charge dynamics were almost completely neglected: an issue that will be remedied here. Revisiting the CPB circuit diagram and Hamiltonian of Chapter 2, we will start by adding an important contribution to the dynamics of the system, the *offset charge* n_g. The potential energy stored in a capacitor increases quadratically with the amplitude of a DC voltage applied across the capacitor.

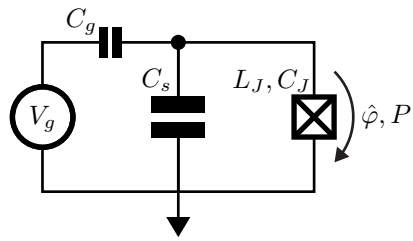

Figure 4.1 | Circuit diagram of a Cooper-pair box/transmon coupled to charges in the environment (this is identical to Fig. 1.1(a)). Fluctuating charges in the environment produce noise on the reduced charge offset $n_g = C_g V_{\text{env}}/2e$, where C_g is an effective gate capacitance and e is the electron charge. In the transmon regime, devices are fabricated with a large capacitance C_s shunting the JJ. The symbols L_J and C_J are the inductance and the native capacitance of the JJ, respectively. These are related to the characteristic energies of the circuit: the Josephson energy $E_J = \phi_0^2/L_J$ and the single-electron charging energy $E_C = e^2/2C_\Sigma$, where $C_\Sigma = C_J + C_s + C_g$. Finally, $\hat{\varphi}$ and P denote the difference in superconducting phase across the junction and the number parity of QPs that have tunnelled across the junction, respectively.

This voltage has the effect of inducing an excess charge $|Q| = C|V|$ on each side of the capacitor. In the case of the CPB, this can be accounted for by adding a voltage bias V_g across the JJ, which could be capacitively coupled via an electrostatic gate as depicted in Fig. 4.1. Including this effect produces the CPB Hamiltonian in its traditional form

$$\hat{H}_{\text{CPB}} = 4E_C \left(\hat{n} - n_g\right)^2 - E_J \cos\hat{\varphi}. \tag{4.1}$$

The dimensionless offset charge $n_g = C_g V_g/2e$ is a continuous parameter in the Hamiltonian, and has "units" of the number of Cooper pairs. This n_g can be tuned by an electrostatic gate, but is always subject to contributions from drifting environmental charges. This Hamiltonian is a function of two operators: $\hat{n}$ is the number of Cooper pairs that have been transferred through the JJ via Andreev reflection, and $\hat{\varphi}$ is the dynamical superconducting phase difference across the JJ. As described in Chapter 2, E_C is the charging energy associated with a single electron on one junction electrode and E_J is the Josephson coupling energy.

Now, how do QPs fit into this picture? When a QP tunnels across the junction it transfers a charge $\pm e$, which would have the same effect as shifting n_g by $\pm 1/2$. As we will show momentarily, the Hamiltonian is symmetric with translation by

integer Cooper-pair charge ($2e$, which shifts n_g by ± 1), prompting us to define the *charge parity* P which denotes the parity of the total number of *electrons* that have traversed the JJ. To take into account the charge parity in the Hamiltonian, we make the transformation

$$n_g \to n_g + \frac{P-1}{4} \tag{4.2}$$

which separates the contribution of QP tunneling from the effect imposed by an external gate voltage. The experimental relevance of this transformation relies on a separation of timescales between n_g fluctuations and QP tunneling events that change P. We will show that this is a valid assumption, with large n_g drift occurring on the timescale of minutes, and charge-parity switches occurring once per $\sim$ ms. The parameter P will switch between values ± 1 depending if the charge parity is even ($P = 1$) or odd ($P = -1$). This convention is chosen such that the charge-parity term does not contribute when the charge parity is even. Again, coherent Cooper-pair transport does not change charge parity, but QP tunneling will. With this transformation, the full CPB Hamiltonian now reads

$$\hat{H}_{\text{CPB}} = 4E_C \left(\hat{n} - n_g + \frac{P-1}{4} \right)^2 - E_J \cos\hat{\varphi}. \tag{4.3}$$

In order to keep things general (and for convenience when discussing QP dynamics in the OCS regime) we will index the eigenstates of the circuit $|i, p\rangle$ by two discrete labels: i denotes the plasmon-excitation number and p denotes the charge parity. For readability, we will indicate i numerically (0,1,2...) and p with label "e" or "o," for "even" and "odd" charge parity, respectively. In examples where the charge-parity is not important (such as the single-charge degeneracy point $n_g = 0.25$), the index p may be dropped.

4.1.2 Charge dispersion

The above discussion of offset charge and charge-parity would be unnecessary if the eigenspectrum of the circuit was not effected by these quantities, and in most QIP applications they can indeed be neglected because the circuit is engineered in a parameter regime that negates their effect on the transmon spectrum. However, these effects are interesting to study in order to characterize QP and

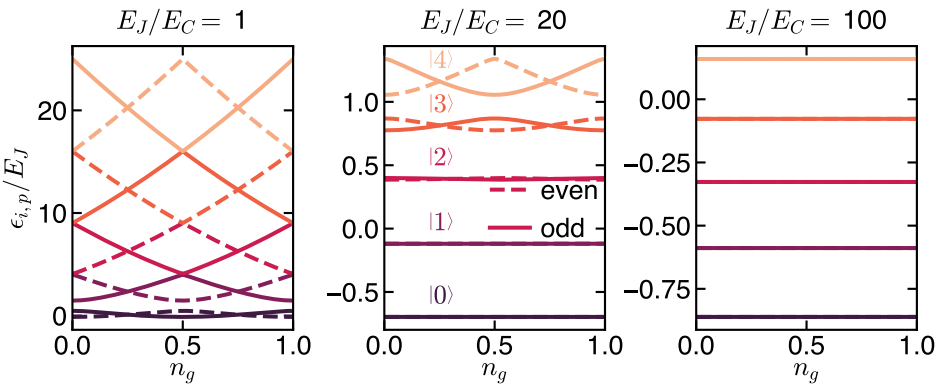

Figure 4.2 | Eigenenergies $\epsilon_{i,p}$ normalized by E_J as a function of n_g, indexed by plasmon state i and charge parity p, for the five lowest-energy plasmon states, from the CPB regime (left) to the transmon regime (right). Increasing E_J/E_C decreases the sensitivity of the spectrum to charging effects.

offset-charge dynamics, and devices can similarly be engineered to have an experimentally convenient degree of sensitivity. The control knob that one has to control this sensitivity is the ratio E_J/E_C.

The eigenspectrum of the circuit from the CPB regime ($E_J/E_C \approx 1$) to the transmon regime ($E_J/E_C \gg 1$) (represented as $E_J/E_C = 100$) is depicted in Fig. 4.2, alongside our weapon of choice for studying QP dynamics, the OCS transmon regime ($E_J/E_C \approx 20$). Shown are the eigenenergies $\epsilon_{i,p}(n_g)$ of the joint plasmon and charge-parity states as a function of n_g, emphasizing that the eigenstates are separated into two charge-parity *manifolds*. Beyond that, the most striking feature is the qualitative change in the eigenspectrum as a function of E_J/E_C. As the ratio E_J/E_C is increased, the eigenenergies $\epsilon_{i,p}(n_g)$ becomes less and less sensitive to n_g. This is quantified by the *charge dispersion* $\delta\epsilon_i$ of the i-th plasmon state, defined as $\delta\epsilon_i = |\epsilon_{i,e}(0) - \epsilon_{i,o}(0)|$ (or equivalently $|\epsilon_{i,e}(0) - \epsilon_{i,e}(1/2)|$).

The charge dispersion of the five lowest energy plasmon states is shown in Fig. 4.3 as a function of E_J/E_C. In the transmon limit, charging effects and the presence of two charge-parity manifolds are typically neglected because the charge dispersion decreases approximately exponentially with $\sqrt{E_J/E_C}$ [Koch et al. 2007] [Fig. 4.3], and the splitting of the two lowest plasmon levels (those relevant for coherent manipulation in quantum computing architectures) is overcome by other sources of dephasing at the ~ 10 kHz level [Gambetta et al. 2006;

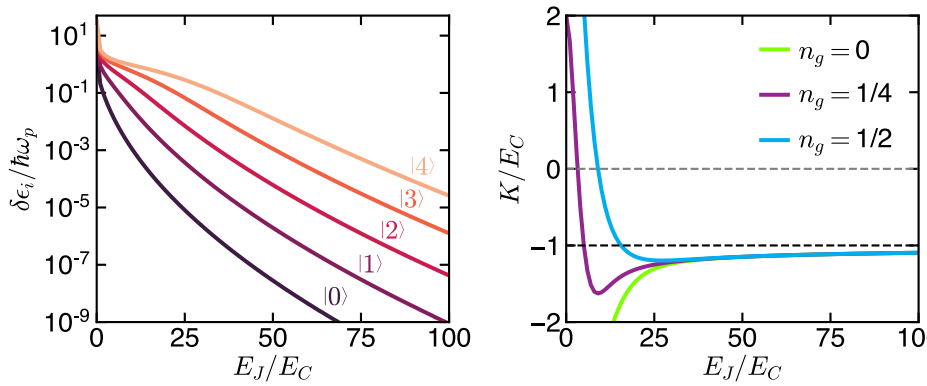

Figure 4.3 | Left: charge dispersion $\delta\epsilon_i$ for the five lowest plasmon eigenstates, as a function of E_J/E_C. Right: qubit anharmonicity $K(n_g) = \omega_{12}(n_g) - \omega_{01}(n_g)$ normalized by the E_C as a function of E_J/E_C, for the three values of n_g with even charge parity. Here, E_J is swept with fixed $E_C/2\pi = 350$ MHz. The black dashed line represents the asymptotic limit that $K = -E_C$ when $E_J/E_C \to \infty$. The grey dashed line indicates $K = 0$, which is sometimes referred to as the defining line between the CPB and transmon regime.[1]

Sears et al. 2012; Wang et al. 2019]. We will end up sacrificing a bit of coherence in the OCS regime in order to probe QP and charge dynamics.

4.1.3 Anharmonicity

As discussed in Chapter 2, there is some minimum amount of nonlinearity necessary for a multilevel quantum circuit to be considered a useful physical qubit. This is quantified by the *anharmonicity* of the circuit $K = \omega_{12} - \omega_{01}$, which is depicted alongside the charge dispersion in Fig. 4.3. There, K is normalized by E_C and plotted for the extreme values of n_g: the point where f_{01} is maximum ($n_g = 0$), where f_{01} is minimum ($n_g = 1/2$), and at the single-charge degeneracy point ($n_g = 1/4$). At large E_J/E_C, all curves converge to E_C. However it's important to note this is only the case in the *extreme* transmon limit, and K deviates from E_C by about 10% even at $E_J/E_C \approx 100$.

Reasonably large anharmonicity is crucial for achieving fast qubit operations with high fidelity using microwave pulses. For example, the Pauli-X gate (anal-

[1] This is Michel's definition, that transmons cross (*trans-*) the point of zero anharmonicity (*-mon*).

ogous to the classical NOT gate) induces a π-rotation of the qubit around the $\hat{\sigma}_x$-axis, and can be accomplished by applying a short microwave pulse with carrier frequency f_{01}. Care must be taken when engineering these pulses to avoid leakage of the transmon state into higher levels ($|2\rangle$ and above), which can be minimized using pulses with special envelopes (for example, see Ref. Chow et al. 2010). This is due to the broad spectral width of fast pulses. In the simplest example of a pulse with a Gaussian envelope, the pulse length, which is proportional to the gate time, must be $\gtrsim 3/K$ in order to avoid significant leakage. For simple schemes utilizing only the two lowest transmon eigenstates as a qubit basis, large anharmonicity is always preferred as long as charge-dispersion is sufficiently suppressed.

4.1.4 Eigenvectors

The time-independent Schrodinger equation for the circuit can be solved analytically when represented in the phase basis

$$\left[4E_C\left(-i\frac{\partial}{\partial\hat{\varphi}} - n_g + \frac{P-1}{4}\right)^2 - E_J\cos\hat{\varphi}\right]|i,p\rangle = \epsilon_{i,p}\,|i,p\rangle\,, \tag{4.4}$$

where it takes the form of the Mathieu equation when massaged into the correct parameterization. While the phase basis eigenvectors are relatively convenient when calculating QP-induced transition matrix elements [Chapter 5], we favor numerical simulations in the charge ($\hat{n}$) basis. The $\hat{n}$ basis is more convenient for calculating dispersive shifts with a resonator (see next section) and can be extended to also study QP-induced transition rates.

As discussed in the last chapter, the Josephson effect arises due to coherent transport of Cooper pairs across the JJ, which, by the language used above, would change $\hat{n}$. Consequently, we can express the Josephson term in its conjugate basis in terms of $\hat{n}$, which yields a Hamiltonian with only one degree of freedom. This allows us to write the Hamiltonian in terms of charge and charge eigenstates as

$$\hat{H}_{\text{CPB}} = \sum_n \left\{4E_C\left(n - n_g + \frac{P-1}{4}\right)^2|n\rangle\langle n| - \frac{E_J}{2}\left(|n\rangle\langle n+1| + |n+1\rangle\langle n|\right)\right\}, \tag{4.5}$$

which is convenient to diagonalize numerically. As a general rule, one must include more than $i_{\max}(E_J/32E_C)^{1/8}$ charge basis states n to compute the spectrum

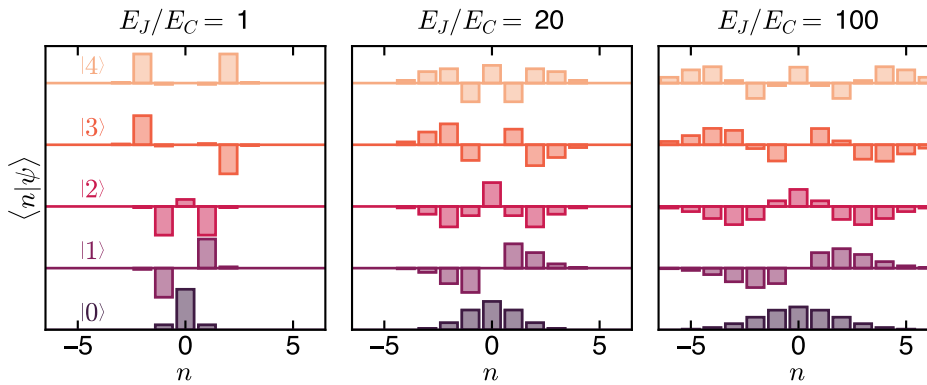

Figure 4.4 | Plasmon eigenstates represented in the $\hat{n}$-basis with $n_g = 0$, from the CPB regime (left) to the transmon regime (right).

up to a maximum plasmon index $i_{\max}$ [Girvin 2014]. In this form, the Josephson term clearly couples nearest-neighbor charge states, corresponding to the transfer of individual Cooper pairs across the JJ. The Cooper-pair box (CPB) is often called a "charge" qubit, in the sense that the qubit-basis eigenstates are *approximately* eigenstates of the charge operator $\hat{n}$. This is only strictly true in the limit that $E_J/E_C \to 0$. As shown in Fig. 4.4, as E_J/E_C is increased, the wavefunctions become more and more delocalized superpositions of n-states.

4.2 Transmon-cavity coupling

In principle, because the eigenspectrum of an OCS transmon can vary significantly with n_g, so too can the coupling between the OCS transmon and the ancillary mode used to read out its state. An OCS transmon coupled to a single linear readout mode is described by the Hamiltonian [Blais et al. 2004; Koch et al. 2007]

$$\hat{H} = \hat{H}_{\text{CPB}} + \hbar\omega_r \hat{a}^\dagger \hat{a} + \hbar g \hat{n} \left(\hat{a} + \hat{a}^\dagger\right). \tag{4.6}$$

The first term is the CPB Hamiltonian presented above, and the second term describes the energy stored in the readout mode. There, ω_r is the bare readout mode frequency, g is the capacitive coupling rate between the OCS transmon and the readout mode, and $\hat{a}$ is a bosonic annihilation operator for excitations in the bare readout mode. The coupling term $\hbar g \hat{n}(\hat{a} + \hat{a}^\dagger)$ takes the form of a standard

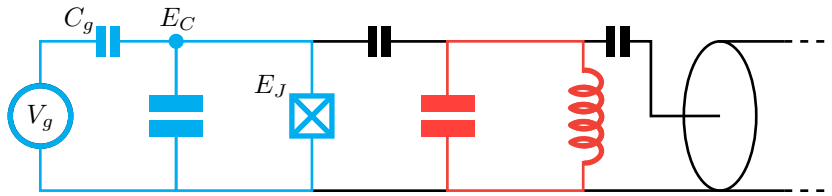

Figure 4.5 | Circuit diagram of an OCS transmon coupled to an ancillary readout resonator, which is itself coupled to a microwave transmission line.

dipole coupling, and produces a transmon-state-dependent dispersive shift $\chi_{i,p}$ of the readout-mode frequency relative to ω_r. Such dispersive shifts are the basis for qubit readout in cQED. Up to second order in perturbation theory, $\chi_{i,p}$ (also called the Lamb shift) can be written [Manucharyan 2012]

$$\chi_{i,p} = g^2 \sum_{j \neq i} \frac{2\omega_{ij}^{pp} \left| \langle j,p|\hat{n}|i,p\rangle \right|^2}{(\omega_{ij}^{pp})^2 - \omega_r^2}, \tag{4.7}$$

which is valid for $g \left| \langle j,p|\hat{n}|i,p\rangle \right| \ll (\omega_{ij}^{pp} - \omega_r)$. Here, ω_{ij}^{pp} is the transition frequency between transmon states $|i,p\rangle$ and $|j,p\rangle$. In a QHO, the charge matrix elements $\langle j,p|\hat{n}|i,p\rangle$ coupling non-nearest-neighbor i and j are strictly zero due to wavefunction symmetry. This however, is not *strictly* true for the transmon in any experimentally reasonable regime, as evidenced by the numerical simulation in Fig. 4.6. That said, in a traditional weakly anharmonic transmon, $\chi_{i,p}$ is very well approximated by including only nearest-neighbor terms, except in the rare case where a transmon transition is nearly resonant with the readout mode, as near degeneracy can cause significant changes as evidenced from Eq. 4.7. For this reason, it is especially important to include non-nearest-neighbor contributions to $\chi_{i,p}$ in CPB and OCS regimes, in which the charge dispersion of the transmon levels can significantly change the detuning of transition frequencies from the readout mode.

It is important to note here a discrepancy with what people often call the "dispersive shift" or "chi," which harkens back to the days of spins coupled to cavities described with the Jaynes-Cummings Hamiltonian. For clarity we will drop the charge-parity index p as it is not relevant here. When the quantum system coupled to a cavity is restricted to only two levels, the dispersive shift corresponding to each level will only include one term of the above sum. Due to Hermiticity,

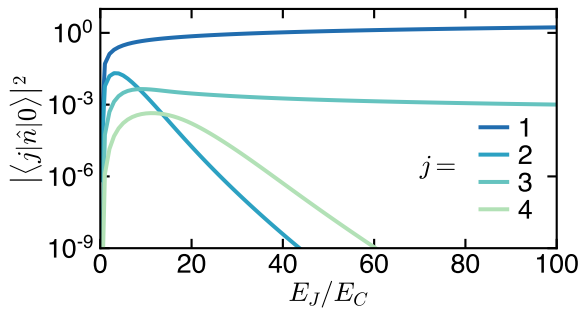

Figure 4.6 | Charge matrix elements $|\langle j|\hat{n}|i\rangle|^2$ for transitions out of the $|0\rangle$ plasmon state at $n_g = 0.25$ such that there is no dependence on charge parity.

the matrix elements $\langle 0|\,\hat{n}\,|1\rangle = \langle 1|\,\hat{n}\,|0\rangle$, which leads to the two states having dispersive shifts of equal magnitude but opposite sign due to the sign of the transition frequencies. In *that* language, the distance between cavity frequencies corresponding to $|0\rangle$ and $|1\rangle$ is $2\chi_{\mathrm{JC}} = \chi_1 - \chi_0 = 2\chi_0 \approx g^2/(\omega_{01} - \omega_r)$, which is only attainable by absorbing the matrix elements and a factor involving the frequencies of order unity into g^2.

4.3 OCS transmon

Devices fabricated in the intermediate OCS regime of E_J/E_C combine the most convenient parts of the CPB and transmon extremes to gain sensitivity to charge fluctuations and QP dynamics. Although reintroducing charge sensitivity to the transmon is generally a bad idea for quantum information experiments, we accept the corresponding reduction of coherence in exchange for experimental visibility of charge-parity dynamics. In order to do so, the name of the game will be to detect changes in the transition spectrum due to changes in charge parity, which occur when QPs are transferred across the JJ.

4.3.1 Physical device

If you met an OCS transmon on the street, you probably wouldn't notice anything that particularly distinguishes it from the crowd of traditional, weakly-anharmonic transmons. They are fabricated using the same materials and tech-

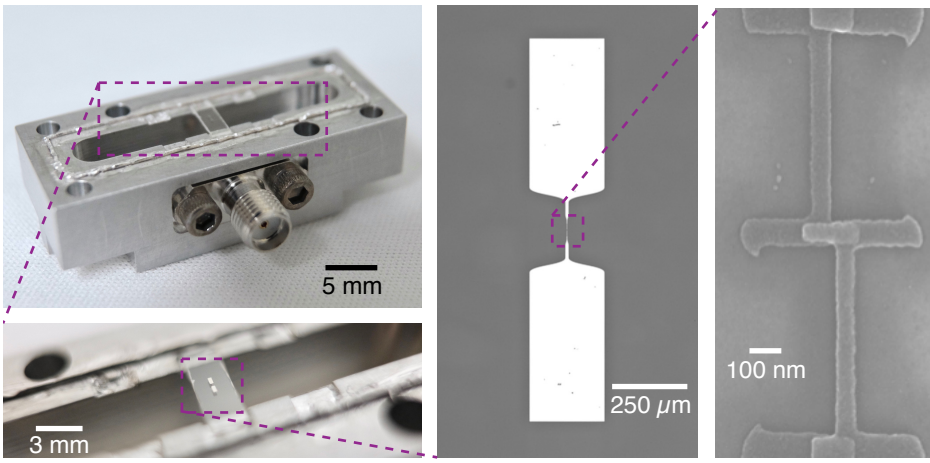

Figure 4.7 | Top left shows a photograph of one half of the 3D waveguide cavity resonator used to readout the OCS transmon (in this case, it was machined from 6061 Al, a superconducting alloy). Zooming in, the bottom left shows the sapphire substrate hosting the transmon mounted in the center of the cavity. Zooming in further, the center panel shows an optical micrograph of the OCS transmon, with large coplanar capacitor paddles that define E_C. On the right is a scanning electron micrograph (SEM) of an Al/AlOx/Al Josephson tunnel junction fabricated using the "bridge-free" technique [Lecocq et al. 2011]. This device is representative of those used in Refs. Serniak et al. 2018 and Serniak et al. 2019.

niques[2], housed in the same enclosures, and their states can be measured through the same sorts of ancillary readout modes. One difference that *does matter* is the susceptibility to various sources of noise via transition matrix elements, which for comparison are plotted as a function of E_J/E_C throughout this thesis. We find that these typically vary by factors of order unity between the range of E_J/E_C representative of traditional transmons ≈ 100 and that of our OCS devices ≈ 20.

A physical device representative of those discussed in the remainder of the thesis is shown in Fig. 4.7. All OCS transmon samples described in this thesis are what would be colloquially referred to as *3D transmons* [Paik et al. 2011], as they were mounted in a 3D rectangular waveguide cavity (machined from either 6061 Al or OFHC Cu[3]). The fundamental TE mode[4] of this cavity resonator was used as the ancillary readout mode by which the qubit state is probed. In the ex-

[2]See Appendix A for details on the fabrication techniques
[3]OFHC stands for "oxygen-free high-conductivity"
[4]TE stands for "transverse electric"

perimental implementations described in this thesis, this mode is characterized by a resonant frequency frequency $f_r \sim 9$ GHz and linewidth $\kappa_r/2\pi \sim 2$ MHz. Importantly, we do not include a electrostatic gate to bias n_g of the OCS transmon, instead relying on temporal-stochastic tuning to sample the majority of the n_g range. Luckily, the requisite drift occurs on the convenient timescale of a few minutes.[5]

4.3.2 Experimental setup

All samples presented in this dissertation were thermally anchored to the mixing chamber stage of an Oxford Triton 200 cryogen-free dilution refrigerator, with a base temperature of ≈ 20 mK. All signals addressing the qubit/cavity system were transmitted through the same microwave input line. The transmon state is read out by detecting the amplitude and phase of a signal reflected from the input of the cavity.[6] The cold RF setup is detailed in Fig. 4.8, and here we will follow the signal path.

The input line is attenuated in stages to ensure that the noise on the input of the cavity is relatively well thermalized to 20 mK. For optimal thermalization efficiency all of this attenuation would occur at the mixing chamber stage where the temperature is lowest, such that all of the re-emitted noise from the attenuator[7] would be at 20 mK, however this is avoided in practice due to the relatively large heat load that would put on the mixing chamber. Instead, 60 dB of explicit microwave attenuation is distributed over multiple temperature stages as depicted in Fig. 4.8, with additional attenuation coming from the stainless-steel microwave input lines. After this attenuation, the signal passes through a K & L 12 GHz low-pass filter (LPF). This is a tubular cavity filter, which offers 50 dB rejection only up to ≈ 26 GHz, which means that it may not be sufficient to out higher frequency radiation, such as pair-breaking radiation at frequencies $< 2\Delta \approx 100$ GHz. For this we rely on homemade cavity filters filled with commercially available Eccosorb CR-110, which is marketed as a high-frequency absorber [Halpern et al. 1986], though we have not been able to directly test its insertion loss at high frequency. However, we do have clear evidence that they reduce the flux of QP generating radiation at the input of the cavity, as will be

[5] See Fig. 4.9.
[6] See Ref. Krantz et al. 2019 for a recent review of readout techniques.
[7] This is just Johnson noise, which is characterized by the electron temperature of the attenuator.

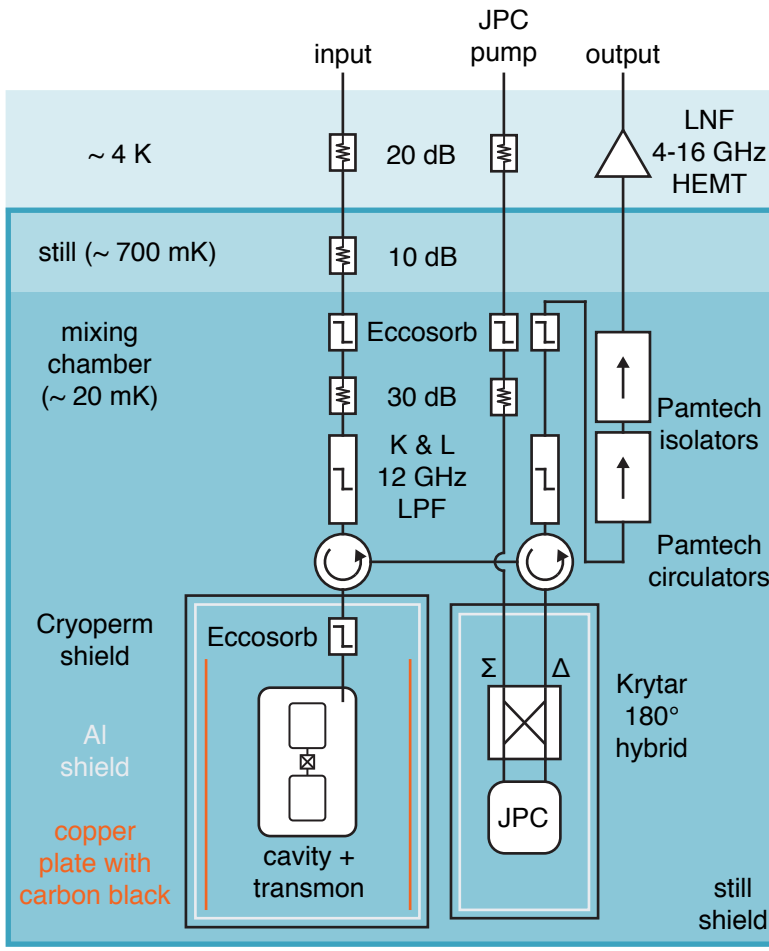

Figure 4.8 | Example wiring diagram of the cryogenic microwave measurement setup. The details presented here represent good practice with respect to reducing QP induced dissipation, more of which will be addressed in Chapter 7.

discussed in later chapters. Furthermore, we found that by placing an additional Eccosorb filter within the Cryoperm and Al shields was crucial to achieving the largest suppression of QP generation. We note that the coldest radiation shield that is not depicted is thermalized to the still plate (~ 700 mK) of the dilution refrigerator.

Our devices were measured in the dispersive regime of circuit-QED [Blais et al. 2004], and a Josephson parametric converter (JPC) [Bergeal et al. 2010] was used to achieve a single-shot qubit-readout fidelity of ≈ 0.97 in 3.84 μs with single-photon-level readout-resonator occupation. The JPC amplifies in reflection, which necessitates the inclusion of microwave circulators to route the amplified signal out of the fridge without irradiating the qubit/cavity. These circulators present a significant source of loss that limits the measurement efficiency, which makes the quest for quantum-limited *directional* amplifiers (that amplify in transmission) an important goal for large-scale quantum computation [Macklin et al. 2015]. The output line includes its own K & L and Eccosorb filters, going into two isolators to protect the qubit/cavity system from noise from the high-electron-mobility transistor amplifier (HEMT). The HEMT in our experiment was produced by Low Noise Factory, and has an operable range between 4 and 16 GHz.

QP dynamics are known to be influenced by a few aspects of the experimental setup. For instance, magnetic fields can induce vortices which have been shown to trap QPs, reducing QP induced dissipation [Nsanzineza and Plourde 2014; Wang et al. 2014], though this advantage can be undermined by vortex flow dissipation if the magnetic field at the sample is too strong [Wang et al. 2014]. To minimize stray magnetic field at the sample, the transmon/cavity was mounted in its own Cryoperm magnetic shield, separate from the JPC, and special care was taken to not include any strongly magnetic materials inside the shield in order to establish a baseline understanding of QP dynamics in our system. One exception to this is the Eccosorb filter which is weakly magnetic, but without large-scale magnetic order. The sample holder/readout cavity was mounted to a copper bracket using brass screws and Mo washers, which were tested prior to use with a magnetometer. Mo washers are a useful insurance in the world of cryogenic thermalization because they have a relatively small thermal expansion coefficient. A copper plate coated with carbon black suspended in Stycast was placed inside the Cryoperm shield and thermalized to the sample mounting bracket with copper braid. This is an attempt to absorb any photons that leak

into the shield, which was shown to improve device performance due to the reduction of QP generating radiation [Barends et al. 2011; Córcoles et al. 2011]. An OFHC Cu thermalization braid was attached directly to the Al readout cavity, providing a direct thermal link to the mixing chamber stage.

4.3.3 Two-tone spectroscopy

The simplest feature with which we can characterize an OCS transmon is the n_g and dependence of f_{01}. To a good approximation, $f_{01}(n_g) = \delta\epsilon_1 \cos(2\pi n_g)/h$. One way characterize the drift of n_g as a function of time via $f_{01}(n_g)$ is to perform two-tone spectroscopy, in which the frequency of one tone f_{spec} is varied around $f_{01}(n_g)$ to induce Rabi oscillations between $|0,p\rangle$ and $|1,p\rangle$. This tone is turned off and another tone is applied at fixed frequency f_{ro}, which is detected and demodulated at room temperature to find the complex measurement response $R = I_m + iQ_m$. Each plasmon state of the OCS transmon will correspond to a different response R, which is how we perform readout in the framework of circuit QED. We apply a rotation on R such that the information discriminating between $|0,p\rangle$ and $|1,p\rangle$ is contained fully in the I_m quadrature, which is plotted as a function of $f_{\text{spec.}}$ and time in Fig. 4.9.

At each timestep, the response goes dark at two frequencies (sometimes overlapping) denoting smaller average response $\overline{I_m}$. These frequencies are precisely where f_{spec} is resonant with f_{01}^{ee} or f_{01}^{oo}, the $|0,e\rangle$ to $|1,e\rangle$ and $|0,o\rangle$ to $|1,o\rangle$ transi-

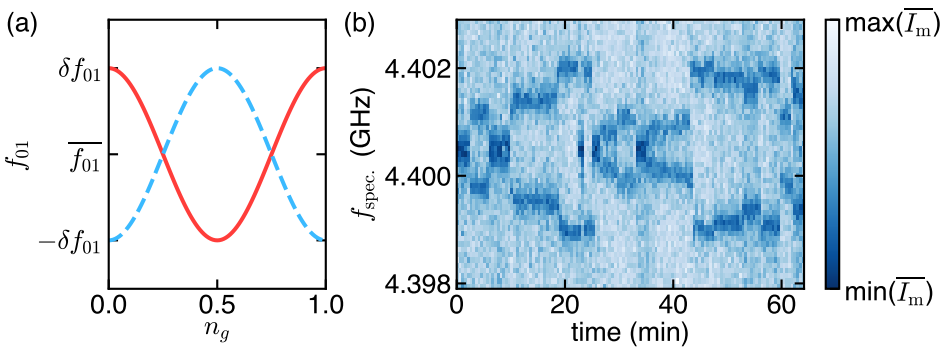

Figure 4.9 | Left: Theoretically calculated f_{01} as a function of n_g and charge parity. Right: Repeated two-tone spectroscopy measurements show offset-charge drift on a timescale of minutes, with charge-parity switches occuring much faster than the measurement time (≈ 40 s).

tion frequencies, respectively. These two frequencies are symmetrically detuned from the average transition frequency $\overline{f_{01}} = f_{01}^{pp}(0.25)$ for both even and odd p. This is evidence that at each timestep the measurement sweep samples both charge-parity states, which means that detecting individual QP-tunneling events will require a much faster measurement, as will be detailed in later chapters.

5

QP-Qubit Coupling

Dissipation to nonequilibrium superconducting quasiparticle (QP) excitations is an intrinsic limitation to the coherence of superconducting qubits. The source of these nonequilibrium QPs is not fully understood, as there are orders of magnitude more of them than would be expected at experimental temperatures. These QPs can induce transitions of the qubit when interacting with high-impedance parts of the circuit, namely when they tunnel across JJs [Catelani et al. 2011]. Additionally, high-frequency photons in the environment can couple to the superconducting condensate *and* the qubit, generating QPs at the JJ in a process that can also result in qubit transitions [Houzet et al. 2019]. The purpose of this chapter is to present the machinery required to calculate the expected transition rates of a qubit due to both of these processes: traditional QP tunneling across JJs, and photon-assisted QP generation and tunneling (PAT). Luckily, measurements to determine whether *individual* devices are limited by these QP processes exist for transmon qubits, which offer straightforward metrics to assess the efficacy of various QP reduction techniques. We will compute all possible charge-parity transition rates in these devices and present numerical results that can be compared with experiments [Ristè et al. 2013; Serniak et al. 2018; Serniak et al. 2019].

5.1 Full electronic Hamiltonian

The qubit degrees of freedom can be written alongside those those of QPs in a general electronic Hamiltonian

$$\hat{H}_{\text{el}} = \hat{H}_q + \hat{H}_{\text{QP}} + \hat{H}_{\text{QP},\hat{\varphi}}. \tag{5.1}$$

At this stage we will keep things general and not specify the form of $\hat{H}_q$, which is just the Hamiltonian of the isolated superconducting qubit under consideration. Working in the excitation picture, $\hat{H}_{\text{QP}}$ is simply the energy corresponding to occupied quasiparticle states on the right and left junction electrodes:

$$\hat{H}_{\text{QP}} = \sum_{l,s} \varepsilon_l \hat{\gamma}_{ls}^\dagger \hat{\gamma}_{ls} + \sum_{r,s} \varepsilon_r \hat{\gamma}_{rs}^\dagger \hat{\gamma}_{rs} \tag{5.2}$$

Here, QP states on the right (left) of the junction are indexed by r (l) and have energy ε_r (ε_l). The term $\hat{H}_{\mathrm{QP},\hat{\varphi}}$ is an electron tunneling Hamiltonian that couples the qubit phase degree of freedom $\hat{\varphi}$ to the QPs tunneling across the junction:

$$\hat{H}_{\mathrm{QP},\hat{\varphi}} = t \sum_{l,r,s} e^{i\hat{\varphi}/2} \hat{c}^{\dagger}_{rs} \hat{c}_{ls} + \mathrm{H.c.} \tag{5.3}$$

Here $\hat{c}_{ls}$ is the fermionic annihilation operator for an *electron* occupying state l with spin s on the left side of the JJ, and $\hat{c}^{\dagger}_{ls}$ is its Hermitian conjugate. This term has the effect of transferring an electron from one side of the junction to the other with a tunneling rate $t/\hbar$. The presence of the dynamical phase $\hat{\varphi}$ couples these electrons (and as we will see, QP excitations) to the qubit which allows for the exchange of energy. Here we will develop this tunneling Hamiltonian to see the effects of nonequilibrium QPs.

In a superconductor, pair-correlated level occupation mixes electrons and holes, therefore the electronic excited states (QPs) have mixed electron-hole character. As described in Chapter 3, these QP excitations can be described by performing the Bogoliubov-Valentin transformation

$$\begin{aligned} \hat{c}_{l\uparrow} &= u^*_l \hat{\gamma}_{l\downarrow} + v_l \hat{\gamma}^{\dagger}_{l\uparrow} \\ \hat{c}^{\dagger}_{-l\downarrow} &= -v^*_l \hat{\gamma}_{l\downarrow} + u_l \hat{\gamma}^{\dagger}_{l\uparrow}, \end{aligned} \tag{5.4}$$

where, again, $\hat{\gamma}_{l\downarrow}$ is a fermionic annihilation operator for a QP excitation in state l with spin $\downarrow$. Since we have accounted for the dynamical phase explicitly in the tunneling Hamiltonian, we will henceforth treat the u's and v's as real. To study the full effect of $\hat{H}_{\mathrm{QP},\hat{\varphi}}$, we will make the above substitution, expand, and rearrange to emphasize the terms that conserve QP excitation number and those that do not. Including the Hermitian conjugate term and writing spin terms explicitly we find

$$\begin{aligned} \hat{H}_{\mathrm{QP},\hat{\varphi}} = t \sum_{l,r} \Big[& e^{i\hat{\varphi}/2} \Big(u_r \hat{\gamma}^{\dagger}_{r\uparrow} + v_r \hat{\gamma}_{r\downarrow} \Big) \Big(u_l \hat{\gamma}_{l\uparrow} + v_l \hat{\gamma}^{\dagger}_{l\downarrow} \Big) \\ & - e^{-i\hat{\varphi}/2} \Big(u_r \hat{\gamma}_{r\uparrow} + v_r \hat{\gamma}^{\dagger}_{r\downarrow} \Big) \Big(u_l \hat{\gamma}^{\dagger}_{l\uparrow} + v_l \hat{\gamma}_{l\downarrow} \Big) \\ & + e^{i\hat{\varphi}/2} \Big(- v_r \hat{\gamma}_{r\uparrow} + u_r \hat{\gamma}^{\dagger}_{r\downarrow} \Big) \Big(- v_l \hat{\gamma}^{\dagger}_{l\uparrow} + u_l \hat{\gamma}_{l\downarrow} \Big) \\ & - e^{-i\hat{\varphi}/2} \Big(- v_r \hat{\gamma}^{\dagger}_{r\uparrow} + u_r \hat{\gamma}_{r\downarrow} \Big) \Big(- v_l \hat{\gamma}_{l\uparrow} + u_l \hat{\gamma}^{\dagger}_{l\downarrow} \Big) \Big]. \end{aligned} \tag{5.5}$$

We can distribute the products to get terms that are second order in fermionic operators

$$\begin{aligned}\hat{H}_{\mathrm{QP},\hat{\varphi}} = t\sum_{l,r}\Big[& e^{i\hat{\varphi}/2}\Big(u_r u_l\hat{\gamma}^\dagger_{r\uparrow}\hat{\gamma}_{l\uparrow} + u_r v_l\hat{\gamma}^\dagger_{r\uparrow}\hat{\gamma}^\dagger_{l\downarrow} \\ & \qquad + v_r u_l\hat{\gamma}_{r\downarrow}\hat{\gamma}_{l\uparrow} + v_r v_l\hat{\gamma}_{r\downarrow}\hat{\gamma}^\dagger_{l\downarrow}\Big) \\ & + e^{-i\hat{\varphi}/2}\Big(-u_r u_l\hat{\gamma}_{r\uparrow}\hat{\gamma}^\dagger_{l\uparrow} - u_r v_l\hat{\gamma}_{r\uparrow}\hat{\gamma}_{l\downarrow} \\ & \qquad - v_r u_l\hat{\gamma}^\dagger_{r\downarrow}\hat{\gamma}^\dagger_{l\uparrow} - v_r v_l\hat{\gamma}^\dagger_{r\downarrow}\hat{\gamma}_{l\downarrow}\Big) \\ & + e^{i\hat{\varphi}/2}\Big(v_r v_l\hat{\gamma}_{r\uparrow}\hat{\gamma}^\dagger_{l\uparrow} - v_r u_l\hat{\gamma}_{r\uparrow}\hat{\gamma}_{l\downarrow} \\ & \qquad - u_r v_l\hat{\gamma}^\dagger_{r\downarrow}\hat{\gamma}^\dagger_{l\uparrow} + u_r u_l\hat{\gamma}^\dagger_{r\downarrow}\hat{\gamma}_{l\downarrow}\Big) \\ & + e^{-i\hat{\varphi}/2}\Big(-v_r v_l\hat{\gamma}^\dagger_{r\uparrow}\hat{\gamma}_{l\uparrow} + v_r u_l\hat{\gamma}^\dagger_{r\uparrow}\hat{\gamma}^\dagger_{l\downarrow} \\ & \qquad + u_r v_l\hat{\gamma}_{r\downarrow}\hat{\gamma}_{l\uparrow} - u_r u_l\hat{\gamma}_{r\downarrow}\hat{\gamma}^\dagger_{l\downarrow}\Big)\Big],\end{aligned} \tag{5.6}$$

regroup terms of like operator products, taking care to track the correct phase factors

$$\begin{aligned}\hat{H}_{\mathrm{QP},\hat{\varphi}} = t\sum_{l,r}\Big[& \Big(u_r u_l e^{i\hat{\varphi}/2} - v_r v_l e^{-i\hat{\varphi}/2}\Big)\hat{\gamma}^\dagger_{r\uparrow}\hat{\gamma}_{l\uparrow} \\ & + \Big(u_r v_l e^{i\hat{\varphi}/2} + v_r u_l e^{-i\hat{\varphi}/2}\Big)\hat{\gamma}^\dagger_{r\uparrow}\hat{\gamma}^\dagger_{l\downarrow} \\ & + \Big(v_r u_l e^{i\hat{\varphi}/2} + u_r v_l e^{-i\hat{\varphi}/2}\Big)\hat{\gamma}_{r\downarrow}\hat{\gamma}_{l\uparrow} \\ & + \Big(v_r v_l e^{i\hat{\varphi}/2} - u_r u_l e^{-i\hat{\varphi}/2}\Big)\hat{\gamma}_{r\downarrow}\hat{\gamma}^\dagger_{l\downarrow} \\ & + \Big(-u_r u_l e^{-i\hat{\varphi}/2} + v_r v_l e^{i\hat{\varphi}/2}\Big)\hat{\gamma}_{r\uparrow}\hat{\gamma}^\dagger_{l\uparrow} \\ & - \Big(u_r v_l e^{-i\hat{\varphi}/2} + v_r u_l e^{i\hat{\varphi}/2}\Big)\hat{\gamma}_{r\uparrow}\hat{\gamma}_{l\downarrow} \\ & - \Big(v_r u_l e^{-i\hat{\varphi}/2} + u_r v_l e^{i\hat{\varphi}/2}\Big)\hat{\gamma}^\dagger_{r\downarrow}\hat{\gamma}^\dagger_{l\uparrow} \\ & + \Big(-v_r v_l e^{-i\hat{\varphi}/2} + u_r u_l e^{i\hat{\varphi}/2}\Big)\hat{\gamma}^\dagger_{r\downarrow}\hat{\gamma}_{l\downarrow}\Big],\end{aligned} \tag{5.7}$$

and write it in a condensed form by pulling the spin index back into the sum

$$\begin{aligned}\hat{H}_{\mathrm{QP},\hat{\varphi}} = t\sum_{l,r,s}\Big[&(u_r u_l e^{i\hat{\varphi}/2} - v_r v_l e^{-i\hat{\varphi}/2})\hat{\gamma}^\dagger_{rs}\hat{\gamma}_{ls} \\ &+ (u_r v_l e^{i\hat{\varphi}/2} + v_r u_l e^{-i\hat{\varphi}/2})\hat{\gamma}^\dagger_{rs}\hat{\gamma}^\dagger_{l\bar{s}}\Big] + \mathrm{H.c.}\end{aligned} \tag{5.8}$$

where $\bar{s}$ denotes the opposite spin of s. Here we are left with one term that conserves QP excitation number ($\hat{\gamma}^\dagger_{rs}\hat{\gamma}_{ls}$) and one term that creates two QP excitations ($\hat{\gamma}^\dagger_{rs}\hat{\gamma}^\dagger_{l\bar{s}}$). Finally, we can expand the complex exponentials to find

$$\begin{aligned}\hat{H}_{\mathrm{QP},\hat{\varphi}} = t\sum_{l,r,s}\Bigg\{&\left[(u_r u_l - v_r v_l)\cos\frac{\hat{\varphi}}{2} + i(u_r u_l + v_r v_l)\sin\frac{\hat{\varphi}}{2}\right]\hat{\gamma}^\dagger_{rs}\hat{\gamma}_{ls} \\ &+ \left[(u_r v_l + v_r u_l)\cos\frac{\hat{\varphi}}{2} + i(u_r v_l - v_r u_l)\sin\frac{\hat{\varphi}}{2}\right]\hat{\gamma}^\dagger_{rs}\hat{\gamma}^\dagger_{l\bar{s}}\Bigg\} \\ &+ \mathrm{H.c.}\end{aligned} \tag{5.9}$$

For an isolated qubit with no drives, and for $\hbar\omega_{01} \ll 2\Delta$, only the QP-number-conserving terms in the tunneling Hamiltonian will contribute. These are processes that we refer to as *QP tunneling* processes, as they represent the tunneling of nonequilibrium QPs that already exist in the JJ leads from one side of the junction to the other. If, however, there is high frequency radiation $\gtrsim 2\Delta$ in the qubit environment, QP-pair creation can occur at the junction ($\hat{\gamma}^\dagger_{rs}\hat{\gamma}^\dagger_{l\bar{s}}$). The coupling rate of photons at the junction should be much greater than that of phonons, so we refer to these processes as photon-assisted QP generation and tunneling (PAT) processes. Both processes will induce transitions of the qubit and, in the case of the CPB/transmon, can be detected as a change of charge parity in the device.

5.2 QP tunneling

We'll first consider the transition rates between qubit states i and j accompanied by a transition of a Bogoliubon from state l on the left electrode to state r on the right electrode (QP tunneling processes). The simplified tunneling Hamiltonian

reads

$$\hat{H}_{\mathrm{QP},\hat{\varphi}} = t\sum_{l,r,s}\left[(u_r u_l - v_r v_l)\cos\frac{\hat{\varphi}}{2} + i(u_r u_l + v_r v_l)\sin\frac{\hat{\varphi}}{2}\right]\hat{\gamma}_{rs}^{\dagger}\hat{\gamma}_{ls} + \mathrm{H.c.} \quad (5.10)$$

Here we're only including the QP-excitation-conserving term of 5.9, under the assumptions that $\hbar\omega_{ij} \ll 2\Delta$ and there are no sources of pair-breaking radiation in the environment. The QP induced qubit transition rates can be computed using Fermi's Golden Rule

$$\Gamma_{ij}^{\mathrm{QP}} = \frac{1}{\hbar}\sum_{l,r,s}\left|\langle j,r|\hat{H}_{\mathrm{QP},\hat{\varphi}}|i,l\rangle\right|^2 \delta_{\epsilon_i-\epsilon_j+\varepsilon_l-\varepsilon_r} \quad (5.11)$$

where $|i,l\rangle$ represents the initial joint qubit and QP state. The sum is over all QP states, with the Kronecker delta enforcing energy conservation. Conveniently, we can factor the $\hat{\varphi}$ dependence of the matrix element out of the sum, leaving the following simplified form.

$$\Gamma_{ij}^{\mathrm{QP}} = \Gamma_{\mathrm{QP}}\left(\left|\langle j|\cos\frac{\hat{\varphi}}{2}|i\rangle\right|^2 S_{\mathrm{QP}}^{-}[\omega_{ij}] + \left|\langle j|\sin\frac{\hat{\varphi}}{2}|i\rangle\right|^2 S_{\mathrm{QP}}^{+}[\omega_{ij}]\right) \quad (5.12)$$

Here, Γ_{QP} is a global factor for QP tunneling that depends on parameters of the JJ. The factors $S_{\mathrm{QP}}^{\pm}$ are QP spectral functions which include coherence effects arising in the QP tunneling process. They necessarily account for the availability and degeneracy of initial and final QP states separated in energy by $\hbar\omega_{ij}$. Writing the product of these factors directly in the excitation picture of superconductivity:

$$\begin{aligned}\Gamma_{\mathrm{QP}}S_{\mathrm{QP}}^{\pm}[\omega_{ij}] = \frac{8t^2}{\hbar}\int_0^\infty d\varepsilon_l \int_0^\infty d\varepsilon_r f(\varepsilon_l)\left[1-f(\varepsilon_r)\right]\nu_s(\varepsilon_l)\nu_s(\varepsilon_r) \\ \times (u_r u_l \pm v_r v_l)^2 \\ \times \delta(\epsilon_i - \epsilon_j + \varepsilon_l - \varepsilon_r).\end{aligned} \quad (5.13)$$

The first line of the integral accounts for the degeneracy of initial and final states l and r,[1] the second line accounts for the QP energy dependence of the tunneling matrix elements, and the third line enforces energy conservation. The factor of eight is a product of three factors of two: one for spin degeneracy, and two for

[1] As a reminder, $f(\varepsilon)$ is the QP energy distribution function, and $\nu_s(\varepsilon)$ is the superconducting density of states.

the doubling of the density of states in the excitation picture. Here we repeat the definition of the u's and v's from Eq. 3.10

$$u_l, v_l = \frac{1}{2}\sqrt{1 \mp \frac{\xi_l}{\sqrt{\xi_l^2 + \Delta^2}}} = \frac{1}{2}\sqrt{1 \mp \frac{\sqrt{\varepsilon_l^2 - \Delta^2}}{\varepsilon_l}} \tag{5.14}$$

from which we can compute the QP tunneling coherence factors $(u_r u_l \pm v_r v_l)^2$

$$\begin{aligned}(u_r u_l \pm v_r v_l)^2 =& \frac{\xi_r \xi_l \pm \Delta^2 + \sqrt{(\xi_r^2 + \Delta^2)(\xi_l^2 + \Delta^2)}}{2\sqrt{(\xi_r^2 + \Delta^2)(\xi_l^2 + \Delta^2)}} \\ =& \frac{\sqrt{(\varepsilon_r^2 - \Delta^2)(\varepsilon_l^2 - \Delta^2)} \pm \Delta^2 + \varepsilon_r \varepsilon_l}{2\varepsilon_r \varepsilon_l}.\end{aligned} \tag{5.15}$$

The first term in the numerator will integrate to zero in a more careful calculation, assuming no charge mode disequilibrium[2] [Tinkham 2004] and therefore we will remove it from the rest of the discussion. With this, the coherence factors can be simplified into a slightly more familiar form:

$$\frac{\pm\Delta^2 + \varepsilon_r \varepsilon_l}{2\varepsilon_r \varepsilon_l} = \frac{1}{2}\left(1 \pm \frac{\Delta^2}{\varepsilon_r \varepsilon_l}\right) \tag{5.16}$$

This term has the effect of fully suppressing S_{QP}^{-} for QPs at the gap edge. Substituting back into $S_{\mathrm{QP}}^{\pm}$ we see that

$$\begin{aligned}\Gamma_{\mathrm{QP}} S_{\mathrm{QP}}^{\pm}[\omega_{ij}] = \frac{8t^2}{\hbar}\int_0^\infty d\varepsilon_l \int_0^\infty d\varepsilon_r f(\varepsilon_l)\left[1 - f(\varepsilon_r)\right]\nu_s(\varepsilon_l)\nu_s(\varepsilon_r) \\ \times \frac{1}{2}\left(1 \pm \frac{\Delta^2}{\varepsilon_l \varepsilon_r}\right) \\ \times \delta(\epsilon_i - \epsilon_j + \varepsilon_l - \varepsilon_r).\end{aligned} \tag{5.17}$$

Energy conservation via the Dirac delta function can be enforced by selecting only the contribution where $\varepsilon_r = \varepsilon_l - \hbar\omega_{ij}$. Finally, we can write t^2 in terms of physical device parameters as it is related to the tunnel conductance of the junction is given by $t^2 = G_t/G_q \pi \nu_0^2$, where G_t is the tunnel conductance and $G_q = (2e)^2/h$ is the conductance quantum for Cooper pairs. The Ambegaokar-Baratoff relation

[2] Charge-mode equilibrium holds in the absence of specific QP injection at negative or positive energies and when there is no strong difference in chemical potential between JJ electrodes.

(Eq. 2.26) states $E_J = G_t\Delta/2G_q$ which gives $t^2 = 2E_J/\pi\Delta\nu_0^2$, finally yielding

$$\Gamma_{\rm QP}S^{\pm}_{\rm QP}[\omega_{ij}] = \frac{16E_J}{\pi\hbar\Delta\nu_0^2}\int_0^\infty d\varepsilon_l f(\varepsilon_l)\left[1-f(\varepsilon_l-\hbar\omega_{ij})\right]\nu_s(\varepsilon_l)\nu_s(\varepsilon_l-\hbar\omega_{ij}) \times\left[1\pm\frac{\Delta^2}{\varepsilon_l(\varepsilon_l-\hbar\omega_{ij})}\right]. \tag{5.18}$$

Here we will distinguish

$$\Gamma_{\rm QP} = \frac{16E_J}{\pi\hbar} \tag{5.19}$$

and

$$S^{\pm}_{\rm QP}[\omega_{ij}] = \frac{1}{\Delta\nu_0^2}\int_0^\infty d\varepsilon_l f(\varepsilon_l)\left[1-f(\varepsilon_l-\hbar\omega_{ij})\right]\nu_s(\varepsilon_l)\nu_s(\varepsilon_l-\hbar\omega_{ij}) \times\left[1\pm\frac{\Delta^2}{\varepsilon_l(\varepsilon_l-\hbar\omega_{ij})}\right] \tag{5.20}$$

to aid in our comparison with photon-assisted tunneling processes. With this, one can calculate any QP-tunneling induced transition rate given knowledge of the $\sin\hat{\varphi}/2$ and $\cos\hat{\varphi}/2$ matrix elements. In the case of a transmon, these can be computed numerically either in the phase basis (using the Mathieu functions form of the wavefunctions) or in a modified charge basis, as will be discussed in Section 5.4.1.

The integral in Eq. 5.20 can approximated analytically when $\varepsilon_l, \hbar\omega_{ij} \ll \Delta$, by [Catelani 2014]

$$\begin{aligned} S^{+}_{\rm QP}[\omega_{ij}] &\simeq \Delta e^{-\Delta/T_{\rm eff}}e^{\omega_{ij}/2T_{\rm eff}}\left[K_0\left(\frac{\omega_{ij}}{2T_{\rm eff}}\right)+\frac{\omega_{ij}}{4\Delta}K_1\left(\frac{\omega_{ij}}{2T_{\rm eff}}\right)\right], \\ S^{-}_{\rm QP}[\omega_{ij}] &\simeq \frac{\hbar\omega_{ij}}{2}e^{-\Delta/T_{\rm eff}}e^{\omega_{ij}/2T_{\rm eff}}\left[K_1\left(\frac{\omega_{ij}}{2T_{\rm eff}}\right)-\frac{\omega_{ij}}{4\Delta}K_0\left(\frac{\omega_{ij}}{2T_{\rm eff}}\right)\right], \end{aligned} \tag{5.21}$$

where K_m is the modified Bessel function of the second kind of order m, assuming the QP energy distribution $f(\varepsilon)$ is a Fermi-Dirac distribution function with characteristic temperature $T_{\rm eff}$.

5.3 Photon-assisted tunneling

Our recent work identified another mechanism of QP-related decoherence that can cause charge-parity switches: namely that of photon-assisted QP generation and tunneling across a high-impedance JJ [Houzet et al. 2019]. Above we neglected terms that did not conserve QP number because they would violate energy conservation as long as $\hbar\omega_{ij} < 2\Delta$. However, in the presence of additional drives from the environment, those pair creation terms can become important.

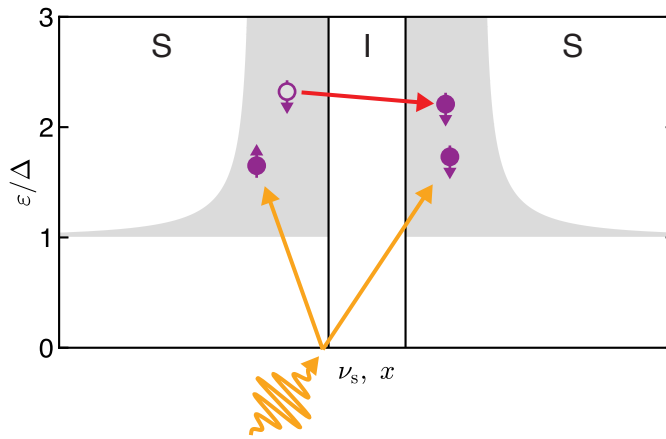

Figure 5.1 | Schematic of a superconductor-insulator-superconductor (SIS) tunnel junction, illustrating QP tunneling (red arrow) and photon-assisted tunneling (orange arrows).

The effect of an AC electric field coupled to the qubit-QP system is to impose a time-dependent phase difference across the junction. We will consider a single environmental mode at frequency ω_ν, inducing $\varphi = \hat{\varphi} + \frac{2eV}{\hbar\omega_\nu}\sin\omega_\nu t$, where V is the voltage induced by photons in this mode across the junction, and is proportional to the total electric field. The zero-point fluctuations of the phase of the qubit induced by this mode will be

$$\varphi_\nu^{\mathrm{zpf}} = \frac{2eV_\nu}{\hbar\omega_\nu} \tag{5.22}$$

where V_ν is the voltage drop across the JJ due to half a photon occupying this mode. If we assume $\varphi_\nu^{\mathrm{zpf}} \ll 1$, to first order we find the relevant QP tunneling

operators become

$$\begin{aligned}\cos\frac{\hat{\varphi}}{2} &\to \cos\frac{\hat{\varphi}}{2} - \varphi_\nu^{\mathrm{zpf}} \sin\frac{\hat{\varphi}}{2}\sin\omega_\nu t,\\ \sin\frac{\hat{\varphi}}{2} &\to \sin\frac{\hat{\varphi}}{2} + \varphi_\nu^{\mathrm{zpf}} \cos\frac{\hat{\varphi}}{2}\sin\omega_\nu t\end{aligned} \tag{5.23}$$

using standard trigonometric identities and limits. The first term corresponds to the traditional QP tunneling processes discussed above. Of interest now is the second term, which can generate pairs of QPs at the JJ provided $\hbar\omega_\nu \gtrsim 2\Delta$. We now return to the QP-tunneling Hamiltonian in the presence of this high-frequency mode and taking into account the above transformation:

$$\begin{aligned}\hat{H}_{\mathrm{QP},\hat{\varphi}} = t\frac{\varphi_v^{\mathrm{zpf}}}{2}&\sin(\omega_\nu t)\\ &\times\sum_{l,r,s}\Bigg\{\left[(u_r u_l - v_r v_l)\sin\frac{\hat{\varphi}}{2} + i(u_r u_l + v_r v_l)\cos\frac{\hat{\varphi}}{2}\right]\hat{\gamma}_{rs}^\dagger\hat{\gamma}_{ls}\\ &\quad+\left[(u_r v_l - v_r u_l)\cos\frac{\hat{\varphi}}{2} + i(u_r v_l + v_r u_l)\sin\frac{\hat{\varphi}}{2}\right]\hat{\gamma}_{rs}^\dagger\hat{\gamma}_{l\bar{s}}^\dagger\Bigg\}\\ &\quad+\mathrm{H.c.}\end{aligned} \tag{5.24}$$

where we neglected the terms that are unaffected by the high-frequency drive. Now that energy can be conserved, the pair-tunnelling term will dominate the first term by a factor of order $1/x_{\mathrm{QP}}$, and we will henceforth neglect the term proportional to $\hat{\gamma}_{rs}^\dagger\hat{\gamma}_{ls}$. The transition rate due to photon-assisted QP tunneling (PAT) can now be written via Fermi's golden rule:

$$\Gamma_{ij}^{\mathrm{PAT}} = \frac{1}{\hbar}\sum_{l,r,s}\left|\langle j,\hat{\gamma}_{rs}^\dagger\hat{\gamma}_{l\bar{s}}^\dagger\mathrm{SC}|\hat{H}_{\mathrm{QP},\hat{\varphi}}|i,\mathrm{SC}\rangle\right|^2\delta_{\hbar\omega_\nu-\varepsilon_l-\varepsilon_r+\epsilon_i-\epsilon_j} \tag{5.25}$$

Where SC denotes the initial electronic state of the superconducting condensate, including potential QP excitations. The PAT process produces produces a pair of QPs $\hat{\gamma}_{rs}^\dagger$ and $\hat{\gamma}_{l\bar{s}}^\dagger$. As with the case of QP tunneling, the QP-photon contribution can be factored away from the qubit-related part of the matrix element, and can be written as

$$\Gamma_{ij}^{\mathrm{PAT}} = \Gamma_{\mathrm{PAT}}\left(\left|\langle j|\cos\frac{\hat{\varphi}}{2}|i\rangle\right|^2 S_{\mathrm{PAT}}^-[\omega_{ij}] + \left|\langle j|\sin\frac{\hat{\varphi}}{2}|i\rangle\right|^2 S_{\mathrm{PAT}}^+[\omega_{ij}]\right). \tag{5.26}$$

The PAT spectral functions $S^{\pm}_{\mathrm{PAT}}$ take into account the degeneracy and availability of pairs of final QP states, assuming there are, on average, $\bar{n}_\nu$ photons occupying mode ν.

$$\begin{aligned}\Gamma_{\mathrm{PAT}} S^{\pm}_{\mathrm{PAT}}[\omega_{ij}] = \bar{n}_\nu \frac{8}{\hbar}\left(t\frac{\varphi_\nu^{\mathrm{zpf}}}{2}\right)^2 \int_0^\infty d\varepsilon_l \int_0^\infty d\varepsilon_r \nu_s(\varepsilon_l)\nu_s(\varepsilon_r) \\ \times (u_r v_l \pm v_r u_l)^2 \\ \times \delta(\hbar\omega_\nu - \varepsilon_l - \varepsilon_r + \epsilon_i - \epsilon_j).\end{aligned} \tag{5.27}$$

Here, we've made the assumption that there are very few QPs already excited, neglecting terms like $\left[1 - f(\varepsilon_l)\right] \approx 1$ that describe the availability of final QP states. Just as in the QP-tunneling example, there is a coherence factor $(u_r v_l \pm v_r u_l)^2$ that takes into account interference between electron and hole trajectories.

$$\begin{aligned}(u_r v_l \pm v_r u_l)^2 =& \frac{-\xi_r\xi_l \pm \Delta^2 + \sqrt{(\xi_r^2+\Delta^2)(\xi_l^2+\Delta^2)}}{2\sqrt{(\xi_r^2+\Delta^2)(\xi_l^2+\Delta^2)}} \\ =& \frac{1}{2}\left(1 \pm \frac{\Delta^2}{\varepsilon_r\varepsilon_l}\right)\end{aligned} \tag{5.28}$$

In the second line, we made the same assumption as before that there is no charge imbalance, and under this constraint the coherence factor for pair generation is the same as that for QP scattering. Energy conservation is ensured by setting $\varepsilon_r = \hbar\omega_v + \hbar\omega_{ij} - \varepsilon_l$. Putting this all together, we find

$$\begin{aligned}\Gamma_{\mathrm{PAT}} S^{\pm}_{\mathrm{PAT}}[\omega_{ij}] = \bar{n}_\nu \frac{2E_J}{\pi\hbar\Delta\nu_0^2}\left(\varphi_\nu^{\mathrm{zpf}}\right)^2 \int_0^\infty d\varepsilon_l \nu_s(\varepsilon_l)\nu_s(\hbar\omega_\nu + \hbar\omega_{ij} - \varepsilon_l) \\ \times \left[1 \pm \frac{\Delta^2}{\varepsilon_l(\hbar\omega_\nu + \hbar\omega_{ij} - \varepsilon_l)}\right].\end{aligned} \tag{5.29}$$

and distinguish

$$\Gamma_{\mathrm{PAT}} = \bar{n}_\nu \frac{2E_J}{\pi\hbar}\left(\varphi_\nu^{\mathrm{zpf}}\right)^2 \tag{5.30}$$

from

$$\begin{aligned}S^{\pm}_{\mathrm{PAT}}[\omega_{ij}] = \frac{1}{\Delta\nu_0^2}\int_0^\infty d\varepsilon_l \nu_s(\varepsilon_l)\nu_s(\hbar\omega_\nu + \hbar\omega_{ij} - \varepsilon_l) \\ \times \left[1 \pm \frac{\Delta^2}{\varepsilon_l(\hbar\omega_\nu + \hbar\omega_{ij} - \varepsilon_l)}\right].\end{aligned} \tag{5.31}$$

The above integral can be expressed analytically as [Houzet et al. 2019]

$$S^{\pm}_{\mathrm{PAT}}[\omega_{ij}] = (z+2)E\left(\frac{z-2}{z+2}\right) - 4\frac{z+1\pm 1}{z+2}K\left(\frac{z-2}{z+2}\right). \tag{5.32}$$

For simplicity, we've defined $z = (\hbar\omega_{ij} + \hbar\omega_\nu)/\Delta$, the total energy available to produce QPs via the PAT process.

The rate calculation above pertains to a single high-frequency photon mode, with some average occupation, that can couple to the qubit. The coupling strength is determined by the global factor Γ_{PAT}, which itself depends on the phase fluctuations induced by photons in the mode, characterized by $\varphi_\nu^{\mathrm{zpf}}$. This coupling efficiency to the qubit depends on the exact geometry and topology of the circuit. The experimentally relevant embodiment (for our experiments [Serniak et al. 2018; Serniak et al. 2019]) of a transmon qubit coupled to a 3D waveguide cavity (Fig. 4.7) was considered in Ref. Houzet et al. 2019. Here we will describe the calculation qualitatively, and quote the main results.

The qubit couples to modes that are polarized parallel to the JJ electrodes: in the case of a 3D transmon, you can picture a dipole antenna with a JJ at the center. The high-frequency modes of interest in this embodiment are TE modes confined to a superconducting box which also houses the transmon. As long as the wavelength of the pair-breaking radiation is still longer than the long dimension of this antenna (say a few millimeters), one can treat the qubit as not perturbing the field too much[3]. Additionally, the impedance of the transmon must be high enough such that it can be treated as an open circuit, which is approximately satisfied when $\sqrt{E_C/E_J} \gg 1/137$, the fine structure constant. Under these assumptions, and after a detailed analysis, Houzet et al. 2019 found that, for an average mode,

$$\Gamma_{\mathrm{PAT}} \approx \bar{n}_\nu \frac{g^2\omega_r}{\pi\omega_{ij}\omega_\nu}, \tag{5.33}$$

where g is the *vacuum-Rabi coupling rate* to the fundamental TE mode of the 3D cavity characterized by ω_r. This is the mode typically used for dispersive readout of the qubit [Paik et al. 2011] in this architecture, hence the subscript r. One can measure/estimate g in various ways, and it is typically engineered to fall in the range of $2\pi\times$40 MHz–150 MHz [Koch et al. 2007], which in general is dependent on ω_{ij}. While monochromatic radiation may seem unrealistic, the finite density

[3] This is a sort of "dipole approximation."

of microwave modes in the 3D cavity, as well as distributed coupling strengths to the qubit, may make it such that some narrow frequency ranges dominate. Treating broad spectrum radiation is not particularly complicated, and will be considered later.

5.4 Single-charge-tunneling matrix elements

The aforementioned QP-induced transition rates will vary depending on the exact Hamiltonian of the qubit. Here we consider the charge-parity transition matrix elements of a transmon qubit $\langle j, \bar{p}| \cos\frac{\hat{\varphi}}{2} |i, p\rangle$ and $\langle j, \bar{p}| \sin\frac{\hat{\varphi}}{2} |i, p\rangle$. QP- and PAT-induced transitions between any plasmon states *without* a change in charge parity are strictly forbidden

$$\langle i, p| \sin\frac{\hat{\varphi}}{2} |j, p\rangle = \langle i, p| \cos\frac{\hat{\varphi}}{2} |j, p\rangle = 0. \tag{5.34}$$

In the following, we will restrict our discussion to the plasmon state indices 0 and 1, with p denoting a charge-parity state and $\bar{p}$ representing the opposite charge parity. First we will present numerically exact matrix elements, and then compare them to analytical approximations for the large E_J/E_C transmon limit.

5.4.1 Numerical computation in the single-charge basis

We can compute the QP-tunneling matrix elements taking some cues from traditional numerical diagonalization of the transmon Hamiltonian. The transmon Hamiltonian can be written in the charge basis as:

$$\hat{H}_q = \sum_n 4E_C(\hat{n} - n_g)^2 |n\rangle \langle n| - \frac{E_J}{2}\left(|n\rangle \langle n+1| + |n+1\rangle \langle n|\right) \tag{5.35}$$

Here, $\hat{n}$ represents the number of Cooper pairs that have tunneled across the junction, and the natural unit of charge transfer is $2e$. This Hamiltonian is *parametric* in n_g, and can be diagonalized independently at all values of n_g. All of the eigenstates of the transmon can be written as superpositions of $|n\rangle$-states, and become more delocalized in n with increasing E_J/E_C. Charge-parity switches result in a change of n_g by $\pm 1/2$, which is visible as a change in $\langle n\rangle$. Since we are interested in the tunneling of QPs, a more natural basis is one where states can be written

in terms of changes of charge by $1e$. We introduce the single-charge operator $\hat{n}'$, and rewrite the Hamiltonian as

$$\hat{H}_q = \sum_{n'} \left[E_C(\hat{n}' - 2n_g)^2 \left|n'\right\rangle \left\langle n'\right| - \frac{E_J}{2} \left(\left|n'\right\rangle \left\langle n'+2\right| + \left|n'+2\right\rangle \left\langle n'\right| \right) \right], \quad (5.36)$$

where E_C assumes its role as a *single-electron* charging energy. Here we choose to not modify n_g in this basis to preserve continuity with the n-basis result where changes in charge parity correspond to shifts of n_g by $1/2$. In this basis, the even- and odd-charge-parity ($p = e, o$) states are all eigenstates of the Hamiltonian with the same parameter n_g, with wavefunctions depicted in Fig. 5.2. Conveniently, one can write the relevant QP tunneling operators as single-charge tunneling op-

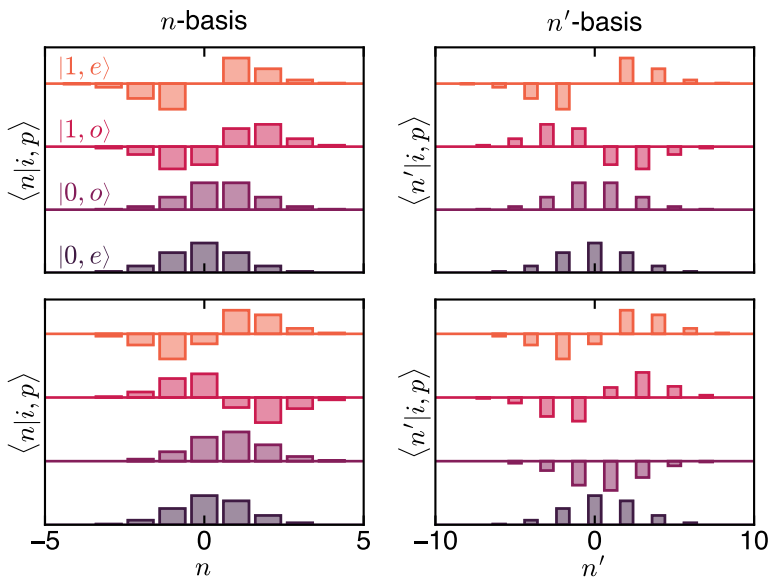

Figure 5.2 | Wavefunctions of the even- and odd-charge-parity ground and excited states of a transmon qubit, depicted in the traditional charge basis (left) and the single-charge basis (right). The top row depicts the wavefunctions at $n_g = 0$, and the bottom row at $n_g = 0.25$. Wavefunction components are offset vertically for visibility. Here, $E_J/E_C = 23$.

erators

$$\cos\frac{\hat{\varphi}}{2} = \frac{1}{2}\sum_{n'}\left(\left|n'\right\rangle\left\langle n'+1\right| + \left|n'+1\right\rangle\left\langle n'\right|\right)$$
$$\sin\frac{\hat{\varphi}}{2} = \frac{1}{2i}\sum_{n'}\left(\left|n'\right\rangle\left\langle n'+1\right| - \left|n'+1\right\rangle\left\langle n'\right|\right) \tag{5.37}$$

by analogy with the $\cos\hat{\varphi}$ term.[4]

5.4.2 Transmon limit

In the transmon limit ($E_J/E_C \gg 1$) the expressions for the matrix elements take the following approximate forms [Catelani 2014]. If the QPs are localized in energy near the gap edge $u_k u_p \approx v_k v_p \approx 1/2$, and therefore the $\sin\frac{\hat{\varphi}}{2}$ term will dominate the transition rate between plasmon states, which can be expressed

$$\langle 1,\bar{p}|\sin\frac{\hat{\varphi}}{2}|0,p\rangle \simeq \left(\frac{E_C}{8E_J}\right)^{1/4} \tag{5.38}$$

This statement is independently strengthened by intuition: as odd indexed plasmon states have even wavefunctions with respect to phase and odd indexed plasmon states have even wavefunctions, an odd function (such as sine) will be able to drive transitions while an even function (in this example, cosine) will not. The limiting case of the cosine term is

$$|\langle 1,\bar{p}|\cos\frac{\hat{\varphi}}{2}|0,p\rangle| \propto |\sin(2\pi n_g)|\frac{\sqrt{\delta\epsilon_0\delta\epsilon_1}}{\omega_p}\left(\frac{E_C}{E_J}\right)^{1/3} \tag{5.39}$$

where $\delta\epsilon_i$ is the charge dispersion of the i-th plasmon state of the transmon. This is smaller than the sine term by a factor of order $\delta\epsilon_1/\omega_p$ (see Fig. 4.3). The plasmon-state-conserving rates will feel both terms. The cosine term will again be suppressed due to the coherence factor, but will fight back against the sine term due to the symmetry of the wavefunctions.

$$|\langle i,\bar{p}|\sin\frac{\hat{\varphi}}{2}|i,p\rangle| \propto |\sin(2\pi n_g)|\left(\frac{2}{3}\right)^{2/3}\Gamma\left(\frac{1}{3}\right)\left(\frac{E_C}{8E_J}\right)^{1/6}\frac{\delta\epsilon_i}{\omega_p} \tag{5.40}$$

[4] This comes from the fact that $\hat{\varphi}$ and $\hat{n}$ are canonically conjugate, and therefore $e^{\pm i\hat{\varphi}}$ can be seen as a translation of $\hat{n}$ by one [de Gennes 1999]. Analogously, $e^{\pm i\hat{\varphi}/2}$ is a translation of $\hat{n}'$ by one.

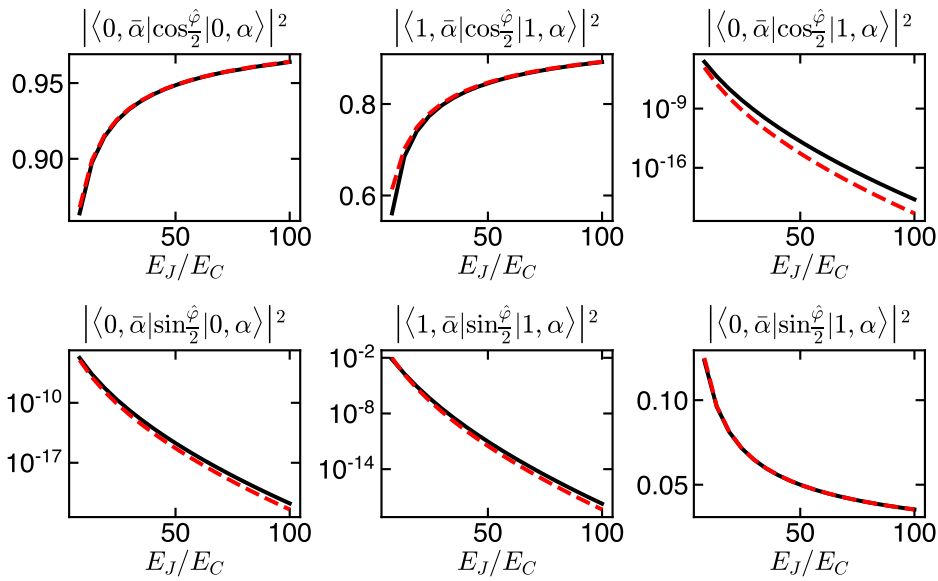

Figure 5.3 | Charge-parity transition matrix elements for a transmon qubit, as a function of E_J/E_C. Solid lines are numerically computed in the single-charge basis, and dashed lines are analytic approximations in the transmon regime.[6] All curves evaluated at $n_g = 0.24$.

where $\Gamma(x)$ is the gamma function.[5]

$$\langle i,\bar{p}|\cos\frac{\hat{\varphi}}{2}|i,p\rangle \simeq 1-\left(i+\frac{1}{2}\right)\sqrt{\frac{E_C}{8E_J}}-\frac{3}{2}\left(i+\frac{1}{4}\right)\frac{E_C}{8E_J} \tag{5.41}$$

These analytical expressions for the charge-parity transition matrix elements are plotted alongside the matrix elements as computed numerically in the single-charge basis in Fig. 5.3, as a function of E_J/E_C. The dominant matrix elements only vary by factors of order unity between the OCS regime and the traditional transmon regime, demonstrating that the OCS transmon is an excellent proxy for studying, and hopefully understanding, QP dynamics in state-of-the-art transmons. There is good agreement between the approximations and exact solutions, especially for the dominant matrix elements which have no appreciable dependence on n_g.

[5] The gamma function is defined as $\Gamma(z)=\int_0^\infty x^{z-1}e^{-x}dx$ where z is complex.

[6] The analytic approximations for $|\langle 0,\bar{p}|\cos\frac{\hat{\varphi}}{2}|1,p\rangle|^2$ and $|\langle i,\bar{p}|\sin\frac{\hat{\varphi}}{2}|i,p\rangle|^2$ are only computed up to a constant prefactor.

5.5 QP-induced transition rates

Combining the above sections, we can compute the QP induced transition rates due to "traditional" QP tunneling as well as photon-assisted QP generation and tunneling (PAT). Beyond the magnitude of these transition rates (which could potentially limit T_1 or T_ϕ of a qubit), another interesting notion is that of the *branching ratio* of a QP-induced transitions. When a QP tunnels across the JJ of a transmon, the charge-parity state will definitely change, but the plasmon state may or may not change. The relative rates of plasmon-state-preserving to plasmon-state-changing processes can inform us about the charge-parity-switching mechanism. Restricting ourselves to the qubit manifold of states $|0,p\rangle$ and $|1,p\rangle$, where will be four parity-switching transition rates that we are interested in: $\Gamma_{10}^{p\bar{p}}$, $\Gamma_{01}^{p\bar{p}}$, $\Gamma_{00}^{p\bar{p}}$, and $\Gamma_{11}^{p\bar{p}}$. The relation between these rates is what we refer to as the branching ratio. For emphasis, we will call the rates $\Gamma_{ij}^{\mathrm{QP}}$ or $\Gamma_{ij}^{\mathrm{PAT}}$, with the superscript referring to the mechanism. For simplicity, we will only quote rates at $n_g = 0$ and assume that the initial charge-parity state is even.

As described in the previous sections, there are three components that go into the transition rates: a global coupling rate (Γ_{QP} or Γ_{PAT}), the single-charge tunneling matrix elements, and the spectral functions corresponding to QP tunneling or PAT processes. The coupling rates and matrix elements were already computed, which leaves the spectral functions. These are shown in Fig. 5.4. The spectral functions accompanying the $\cos\frac{\hat{\varphi}}{2}$ matrix elements (S_{QP}^{-} and S_{PAT}^{-}) are slightly suppressed from those of $\sin\frac{\hat{\varphi}}{2}$ due to the tunneling coherence factors. Notably, $S_{\mathrm{PAT}}^{\pm}$ is parameterized completely by the *sum* of $\hbar\omega_{ij} + \hbar\omega_\nu$. Here it is clear that pair-breaking processes require energies of at least 2Δ. Also, it's interesting to note that $S_{\mathrm{PAT}}^{\pm} \to (\hbar\omega_{ij} + \hbar\omega_\nu)/\Delta$ at high frequencies, making the spectral function contribution to the branching ratio of transition rates basically negligible in that regime. This is also descriptive of the broad-spectrum limit if the characteristic photon frequency $\bar{\omega}_\nu \gg \Delta/\hbar$.

With these quantities in hand, Fig. 5.5 shows the full QP-induced transition rates as a function of ω_{01} of the transmon. These are computed by keeping E_C fixed and varying E_J to vary ω_{01}. The parameters of the QP distribution are chosen in accordance with a experiments: a nonequilibrium QP density $x_{\mathrm{QP}} = 10^{-7}$, corresponding to an effective temperature $T_{\mathrm{eff}} \approx 155$ mK. Of note is the opposite trend of the rates as a function of ω_{01}, which could be used to distinguish be-

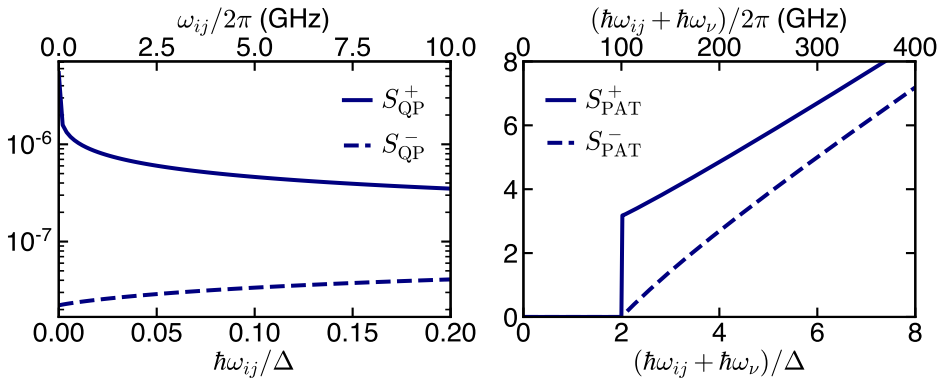

Figure 5.4 | Spectral functions for QP tunneling (left) and photon-assisted tunneling (right). Curves for $S^{\pm}_{\rm QP}$ assume a thermal distribution of QPs at an effective temperature of $\approx$ 155 mK, corresponding to $x_{\rm QP} = 10^{-7}$, and with $\Delta/h = 50$ GHz.

tween the two processes. It's interesting to compare between QP-tunneling, the actors of which are fermions, and PAT, which is is fueled by bosonic excitations. From the theory developed in Ref. Houzet et al. 2019, transition rates of a similar magnitude to those produced by a nonequilibrium QP density $x_{\rm QP} \approx 10^{-7}$ can be obtained with an average photon occupation $\bar{n}_\nu = 1.5 \times 10^{-2}$ in a mode[7] with $\omega_\nu \approx 2.8\Delta/\hbar$. As we did in that reference, we'll consider a 3D transmon design with the same QP density, which would have on the order of 5000 QPs in the device. One could interpret this as saying the charge-parity-switching efficiency of a single ≈ 150 GHz photon occupying the readout cavity is about 10^6 times that of a single QP in the device. Another way of saying it is that a single photon occupying that mode would put the same limit on transmon T_1 as would $x_{\rm QP} \approx 10^{-5}$.

Intuitively, the QP-tunneling induced transition rates depend approximately linearly on $x_{\rm QP}$: the more QPs you have, the more charge-parity transitions, as depicted in Fig. 5.6. However, the branching ratio of these parity switching rates, as illustrated by $\Gamma^{\rm QP}_{11}/\Gamma^{\rm QP}_{10}$ and $\Gamma^{\rm QP}_{01}/\Gamma^{\rm QP}_{10}$, is only weakly dependent on $x_{\rm QP}$. The first ratio can be thought of the preference for a QP to *not induce* a plasmon transition in the circuit. For QP-tunneling induced transitions, this ratio is expected to be less than 1. The second ratio is indicative of the thermodynamics of the dissi-

[7]This is a reasonable order of magnitude considering that similar occupation of a strongly-coupled readout mode will limit T_ϕ of transmons to the $\sim$ 10 μs level via photon-shot-noise dephasing [Sears et al. 2012], which isn't far from the current state of the art.

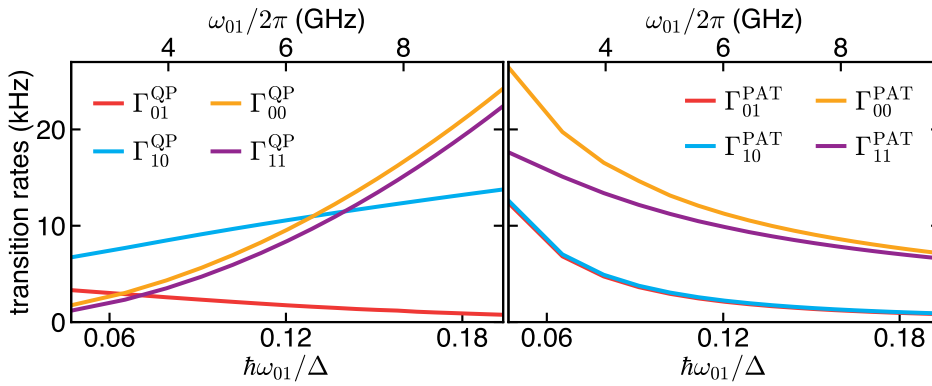

Figure 5.5 | Charge-parity transition rates for QP tunneling (left) and photon-assisted tunneling (right). In the simulation, $E_C = 355$ MHz was fixed while E_J was varied to modify ω_{01}. All simulations have set $n_g = 0$. Curves for $\Gamma_{ij}^{\mathrm{QP}}$ assume a thermal distribution of QPs at an effective temperature of $\approx$ 155 mK, corresponding to $x_{\mathrm{QP}} = 10^{-7}$, and with $\Delta/h = 50$ GHz. Curves for $\Gamma_{ij}^{\mathrm{PAT}}$ assume monochromatic high-frequency radiation at $\omega_\nu = 2.8\Delta/\hbar$, with a steady-state photon occupation $\bar{n}_\nu = 1.5 \times 10^{-2}$ and a *frequency independent* coupling rate g.

pative bath, should agree with detailed balance (Eq. 2.12) given a bath in thermal equilibrium. Moving on to the right hand side of Fig. 5.6 we show dependence of a similar parameter for PAT processes, the frequency of pair-breaking radiation ω_ν. In addition to increasing with ω_ν, the charge-parity-transition rates will increase linearly (and trivially) with photon occupation $\bar{n}_\nu$. What's interesting here is how the branching ratio changes over this range of frequencies. The ratio $\Gamma_{11}^{\mathrm{PAT}}/\Gamma_{10}^{\mathrm{PAT}}$ changes appreciably over a reasonable range of parameters, and is > 1 above $\omega_\nu \approx 2.2\Delta/\hbar$. The thermodynamic ratio $\Gamma_{01}^{\mathrm{PAT}}/\Gamma_{10}^{\mathrm{PAT}} \approx 0.95$ over the range considered.[8] These are both in stark contrast to the branching ratio of traditional QP tunneling processes.

The limits these processes impose on qubit relaxation and excitation can be expressed analytically in the transmon limit. For QP tunneling processes, [Catelani et al. 2011]

$$\Gamma_{10}^{\mathrm{QP}} \approx \frac{x_{\mathrm{QP}}}{\pi}\sqrt{2\Delta\omega_{01}}, \qquad \Gamma_{01}^{\mathrm{QP}} \approx \Gamma_{10}^{\mathrm{QP}} e^{-\hbar\omega_{01}/k_B T_{\mathrm{eff}}}, \tag{5.42}$$

[8] $\Gamma_{01}^{\mathrm{PAT}}/\Gamma_{10}^{\mathrm{PAT}} \approx 0.95$ tends toward 1 at higher and higher frequencies.

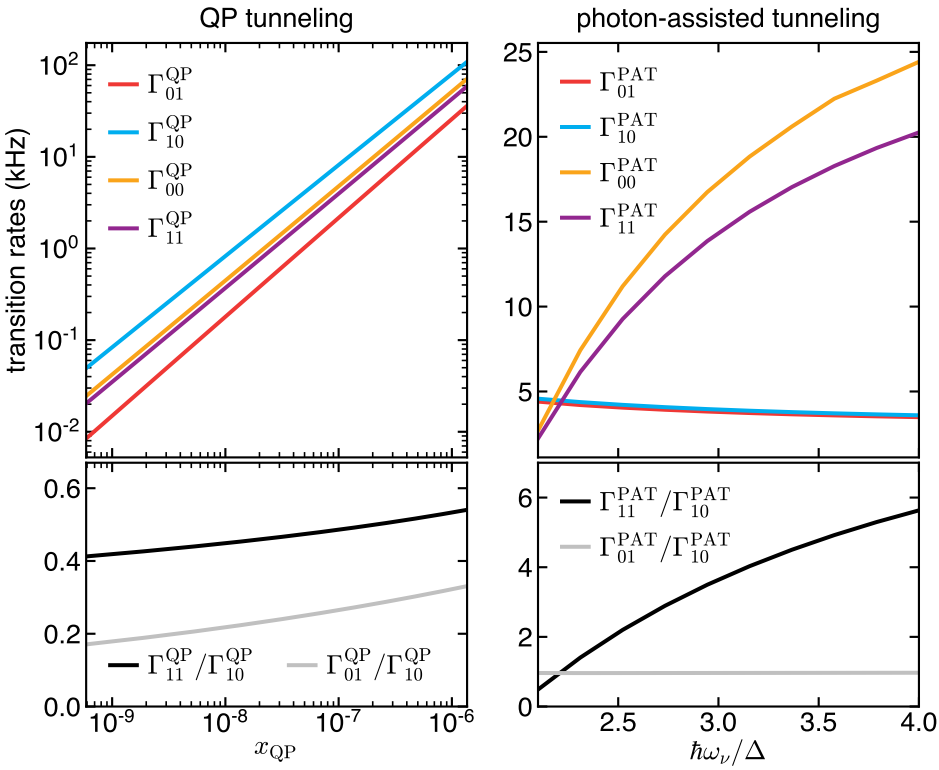

Figure 5.6 | Charge-parity transition rates for QP tunneling (left) and photon-assisted tunneling (right) as a function of relevant parameters of the dissipation source: the QP density x_{QP} for QP tunneling and the frequency of monochromatic pair-breaking radiation ω_ν for PAT. Transmon parameters are chosen to reflect those in Ref. Serniak et al. 2018. All calculations were performed with $n_g = 0$. In accordance with our physical devices, we consider superconducting Al with $\Delta/h = 50$ GHz. Curves for $\Gamma_{ij}^{\mathrm{PAT}}$ assume $\bar{n}_\nu = 1.5 \times 10^{-2}$ and a *frequency independent* coupling rate g.

and for PAT processes

$$\Gamma_{10}^{\mathrm{PAT}} \approx \Gamma_{01}^{\mathrm{PAT}} \approx \bar{n}_\nu \frac{g^2 \omega_r}{\pi \omega_{ij} \omega_\nu} \sqrt{\frac{E_C}{8E_J}}. \tag{5.43}$$

The branching ratios can also be approximated [Catelani 2014; Houzet et al. 2019]. The parameters listed above limit the T_1 of transmon qubits to $\approx 200\ \mu$s, near that measured in state-of-the-art devices.

Our treatment of monochromatic pair-breaking radiation may be sufficient given the finite density of EM modes in realistic qubit sample holders. The other extreme, which is maybe more plausible, would be a broad frequency distribution of incoming radiation. A reasonable distribution to study is that of a blackbody radiator, characterized by a power spectrum

$$P_{\mathrm{BB}}(\omega_\nu) \propto \frac{(\hbar\omega_\nu)^3}{e^{\hbar\omega_\nu / k_B T_{\mathrm{BB}}} - 1}. \tag{5.44}$$

where T_{BB} is the temperature of the blackbody. To compute the PAT-induced charge-parity transition rates arising this distribution of photons, one can average over the contributions of monochromatic radiation at frequencies weighted by the normalized spectrum. The path this radiation takes to get to the qubit is unknown, but evidence [Chapter 7] suggests that it may arrive via the microwave input/output lines. The filtering properties of microwave components at such high frequencies has not been properly characterized, so while a blackbody spectrum may not be descriptive of what reaches the cavity, is about as good an approximation as we can do.

We consider charge-parity transitions from blackbody distributed PAT processes in Fig. 5.7. For each blackbody temperature T_{BB} that defines the PAT frequency distribution we keep the total number of photons fixed to 1.5×10^{-2}. Therefore, the transition rates plateau when the characteristic photon energies approach $2\Delta/2.9$. The ratio $\Gamma_{11}^{\mathrm{PAT}}/\Gamma_{10}^{\mathrm{PAT}}$ increases linearly with T_{BB} in this range, but will plateau to a ratio of matrix elements at high blackbody temperature, when the superconducting DOS plays less of a role. In the plotted range of values, $\Gamma_{01}^{\mathrm{PAT}}/\Gamma_{10}^{\mathrm{PAT}}$ varies significantly, and therefore could be responsible for a wide variety of experimental observations.

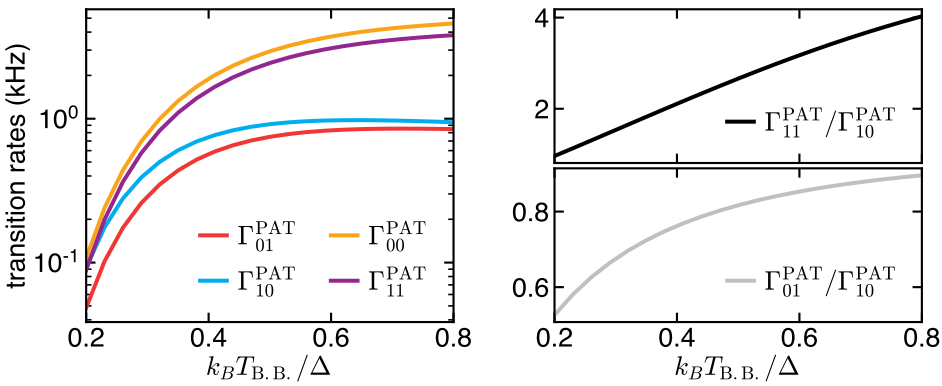

Figure 5.7 | Charge-parity transition rates due to photon-assisted tunneling processes arising from a blackbody distribution of pair-breaking radiation, with characteristic temperature T_{BB}. Transmon parameters are chosen to reflect those in Ref. Serniak et al. 2018. All calculations were performed at $n_g = 0$. In accordance with our physical devices, we consider superconducting Al with $\Delta/h = 50$ GHz. The distribution is normalized such that the total number of pair-breaking photons is 1.5×10^{-2}.

5.6 Ultimate limit on transmon coherence?

Thermal QP excitations constitute an intrinsic sort of dissipation in superconducting qubits. Lets flash-forward to a future where our qubits are perfectly isolated from pair-breaking radiation such that there are no PAT processes, and that there are no other limiting dissipation mechanisms: all issues related to fabrication and dielectric loss have been solved[9]. A typical 3D transmon device has on the order of 1×10^4 μm^3 of Al making up the two junction electrodes and shunt capacitance. That means that there are approximately 8×10^{10} electrons paired-up in the superconducting condensate. But what happens if the device cools down with an odd number of electrons? The pairwise BCS interaction would leave 1 QP excitation by default, which would on it's own give an effective $x_{\mathrm{QP}} \approx 10^{-11}$, about two orders-of-magnitude lower than the best that been observed experimentally in pure aluminum devices [Serniak et al. 2019]. Lets say that the odds are 50-50 that the qubit has an odd number of electrons versus an even number. In this scenario, half of the time you measure a new transmon, the limit on T_1 would be no

[9] Lets, for the time being, neglect the fact that the qubit needs to be addressable and read-out, so that there is no Purcell decay either.

more than a few seconds! I can only imagine the level of superstition that would develop on the 4th floor of Becton given this reality. Better bring your lucky rabbit's foot to work on the first day of new cooldown! Of course, other techniques could be employed to reduce the effect of this QP, such as the implementation of gap-engineered QP traps [Chapter 7] [Riwar et al. 2016].

5.7 Other superconducting qubits

Extending the ideas presented above to other qubit circuits is relatively straightforward. Typically, those would correspond to circuits with *more than one* JJ. QP-tunneling induced limits on the coherence of common qubits such as the SQUID transmon, flux qubit, and fluxonium are discussed in Ref. Catelani et al. 2011. It boils down to taking into account the coupling of QPs to the qubit at each individual junction and weighting them appropriately. These contributions will include the same global rates and spectral functions defined in the previous sections, with matrix elements depending on the qubit circuit. One important difference is this: it is crucial to take into account the phase drop across each junction in circuits with closed loops and a flux bias, as this can lead to QP interference effects.

6

Probing QP Dynamics in OCS Transmons

While superconducting qubits are considered to be a strong candidate architecture for large-scale, fault-tolerant quantum computation, they suffer from relatively short coherence times compared to many natural quantum systems. In all likelyhood, this downside is deeply intertwined with the strongest upsides of superconducting qubits: customization and *engineerability*. Modern nano- and micro-fabrication techniques facilitate a high degree of control over device parameters, but unfortunately introduce limitations on materials used and can potentially lead to contamination of otherwise perfect materials. Understanding these sorts of materials losses, as well as those related to the fabrication techniques, are a substantial roadblock in the way of achieving significantly longer single-qubit coherence times. Studies of these decoherence mechanisms typically rely on statistical analysis of many samples, searching for correlation between sensitivity to the loss mechanism and T_1, which is a difficult but crucial undertaking [Wang et al. 2015; Calusine et al. 2018; Woods et al. 2019]. This is due, unfortunately, to a simply stated observation: device performance is not always consistent between samples. Devices fabricated on the same wafer that were processed in parallel show varied coherence times, which suggests strong *local* coupling to materials defects or inconsistent dissipation induced by a poorly understood measurement setup. Furthermore, there are a multitude of potential culprits for qubit decoherence, which makes correlations difficult to interpret.

The measurements outlined in this chapter take a different approach to understanding decoherence: determining with certainty the limits imposed by *one particular* loss mechanism on *individual* devices. The loss mechanism is that related to nonequilibrium QP excitations in our superconducting devices, and the devices: OCS-transmon qubits. This is made possible by the intimate relationship between QPs and the physics that define our artificial atoms, namely electromagnetism and superconductivity. Quantum circuit theory and cQED utilize BCS theory in its description of superconducting qubits, and QPs can be taken into account with a natural extension of the Hamiltonian. This is important not

only for theoretical understanding of our results, but for the measurent protocol itself. We rely on the notion of the transmon *charge parity*: the parity of the number of single-charges that have traversed the JJ. When a QP tunnels across the JJ, the charge parity switches. Luckily, these switches can be detected as a change in the eigenspectrum of the OCS transmon, akin to changing the offset charge[1] n_g by $1/2$.

This chapter will detail our experimental protocols for studying QP dynamics in OCS transmons. These rely on the ability to determine the charge-parity of an OCS transmon in a single shot, and draws upon previous works by Naaman and Aumentado 2006, Court et al. 2008, Shaw et al. 2008 and Ristè et al. 2013. First, we will discuss the techniques and results of Ref. Serniak et al. 2018. This relied on coherent manipulation of the transmon's plasmon state to determine the charge-parity-dependent transmon frequency, and showed correlation between charge-parity switches and transmon *excitation* events. At the time of that writing this was very surprising, however our recent theory work in Ref. Houzet et al. 2019 may explain why this was observed: photon-assisted QP generation tunneling (PAT) processes which rely on the occupation of high frequency ($\hbar\omega_\nu > 2\Delta$) modes in our readout cavity. We will describe the agreement and discrepancies between our experiment and this theory. Then, we will present a new technique for detecting charge-parity switching events, that doesn't require any coherent manipulation of the transmon. Our work in Ref. Serniak et al. 2019 showed that, if circuit parameters are chosen properly, there can be a charge-parity-state-dependent dispersive shift of a readout mode. This enables high-fidelity dispersive detection of the transmon's charge-parity state, that doesn't suffer if $T_2 \ll T_1$.

6.1 Mapping charge-parity onto the plasmon state

To probe the interaction between nonequilibrium QPs and a transmon qubit, we slightly relax the transmon-defining condition that the Josephson coupling energy E_J is much greater than the charging energy E_C [Schreier et al. 2008; Sun et al. 2012], entering what we refer to as the offset-charge-sensitive (OCS) transmon regime. In this regime, the charge-parity-preserving ground to first-excited-state transition frequency $f_{01}^{pp} = (\epsilon_{1,p} - \epsilon_{0,p})/h$ has a measurable dependence on the charge parity p of the device, and switches between $\overline{f_{01}} \pm \delta f_{01}$ when a QP tunnels

[1] Remember: offset charge is in "units" of Cooper pair number

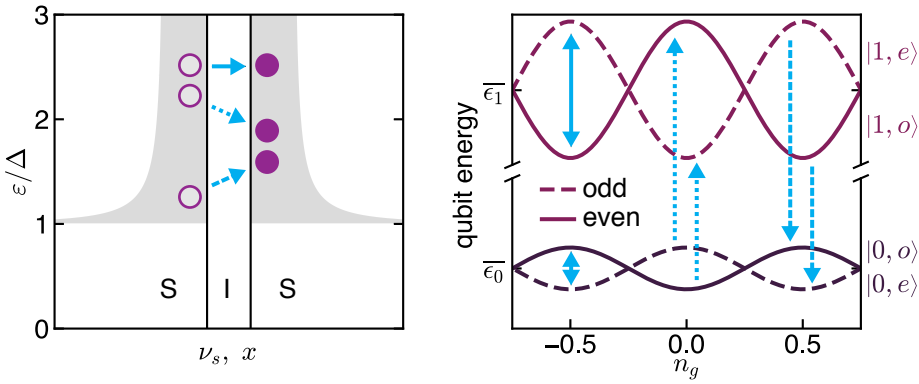

Figure 6.1 | QP-tunneling-induced transitions in transmon qubits (duplicate of Fig. 1.2). Left: density of states ν_s versus the reduced energy ε/Δ in the leads of a superconductor-insulator-superconductor (SIS) JJ, in the excitation representation. Grey arrows represent tunneling processes of QPs, shown as purple dots. Dashed, dotted, and solid lines correspond to relaxation, excitation, and interband transitions of the qubit, respectively, with associated inelastic QP scattering. Right: the two lowest plasmon energy levels of an offset-charge-sensitive transmon qubit (vertical axis not to scale) as a function of offset-charge n_g, in units of $2e$. These levels are shifted depending on the charge parity (even or odd) of the qubit. The time-average energies of the ground and first-excited plasmon states are denoted $\overline{\epsilon_0}$ and $\overline{\epsilon_1}$, respectively, assuming ergodic fluctuations of n_g and/or P. Arrows correspond to those on the left. Not shown are PAT processes, which also change the charge parity of the circuit and can induce all transitions in the right panel of the figure.

across the JJ or PAT process occurs [Fig. 4.9]. (the qubit energies switch between the manifolds indicated by solid and dashed lines in Fig. 6.1). The deviation δf_{01} is an approximately sinusoidal function of the dimensionless offset-charge n_g, which undergoes temporal fluctuations due to reconfiguration of mobile charges in the environment. Insofar as $h\delta f_{01}(n_g) \ll k_B T$, QP tunneling dynamics will not depend strongly on n_g. The authors of Ref. Ristè et al. 2013 originally took advantage of this frequency splitting to track n_g, map the charge parity onto the state of a transmon, and correlate qubit relaxation with parity switches [Catelani 2014]. Extending their experiment, we were able to extract not only the QP-induced relaxation rate, but also the QP-induced excitation rate by detailed modeling of the correlations between charge-parity switches and qubit transitions [Serniak et al. 2018].

The rest of this section will focus on a single transmon qubit with average frequency $\overline{f_{01}} = 4.400$ GHz and $E_J/E_C = 23$, corresponding to a maximum even-odd splitting $2\delta f_{01}(0) = 3.18$ MHz. The average measured relaxation time $T_1 = 95$ μs is on par with state-of-the-art transmons, and the equilibrium ground state population $\mathcal{P}_0 = 0.74$ corresponds to an effective qubit temperature of 160 mK. This is relatively anomalous for superconducting qubits, though we will show with certainty that this is correlated with charge-parity switches, implicating nonequilibrium QPs or PAT processes as the culprit. Results from a second sample with similar parameters is discussed in Section 6.1.8. Chips were mounted in an Al 3D rectangular readout cavity [Paik et al. 2011] and anchored to the mixing chamber of a cryogen-free dilution refrigerator at 20 mK. This readout mode is characterized by frequency $f_r = 9.204$ GHz and linewidth $\kappa/2\pi = 1.8$ MHz. These devices were measured in the dispersive regime of circuit-QED [Blais et al. 2004] (dispersive shift $\chi_{qr}/2\pi = \chi_{0,p} - \chi_{1,p} = 3.8$ MHz, which was approximately independent of p), where a Josephson Parametric Converter (JPC) [Bergeal et al. 2010] was used to achieve a single-shot qubit-readout fidelity of ≈ 0.97 in 3.84 μs with an average readout-resonator occupation $\bar{n}_r \approx 3$.

6.1.1 Charge-parity-independent Ramsey interferometry

Our experimental protocol relies on a separation of timescales between drift of n_g and discrete switches of P. Luckily, the dynamics of n_g are much slower than those of P. The slow background fluctuations of $\hat{n}$ were tracked by monitoring

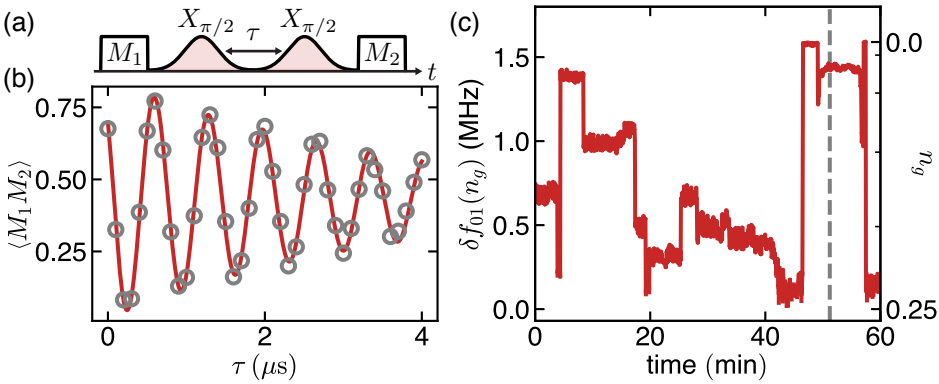

Figure 6.2 | Monitoring slow fluctuations of $\delta f_{01}(n_g)$. (a) Depiction of the Ramsey sequence. High-fidelity qubit measurements M_1 and M_2 have thresholded outcome 0 or 1, corresponding to the ground and first-excited states of the qubit, respectively. (b) Ramsey fringes of $\langle M_1 M_2 \rangle$ oscillate at $\delta f_{01}(n_g)$, which is measured every $\sim$ 4 s as shown in (c). The grey dashed line marks the frequency obtained from the fit in (b). The right-side y-axis shows the conversion from $\delta f_{01}(n_g)$ to n_g. Due to symmetry of the eigenspectrum, this measurement technique maps all values of n_g into the range $[0, 0.25]$.

$\delta f_{01}(n_g)$ using the Ramsey sequence depicted in Fig. 6.2(a). Here, an initial measurement M_1 initializes the plasmon state of the transmon in either the ground or first excited state. A $\pi/2$ pulse around the X-axis prepares the transmon in a superposition of these states. The carrier frequency of the Gaussian $\pi/2$-pulses is chosen to be $\overline{f_{01}}$, which is symmetrically detuned from f_{01}^{ee} and f_{01}^{oo} at all values of n_g. This ensures that the phase evolution of even- and odd-parity states on the equator of the Bloch sphere will interfere constructively, resulting in Ramsey fringes [Fig. 6.2(b)] characterized by a single oscillation frequency $\delta f_{01}(n_g)$ and a decay constant T_2 that is insensitive to fast charge-parity switches. Here, it is crucial that the second $\pi/2$-pulse is along the same axis as the first. Repeated Ramsey experiments [Fig. 6.2(c)] show that n_g fluctuates on a timescale of minutes, which is long enough to perform experiments that rely on prior knowledge of $\delta f_{01}(n_g)$.

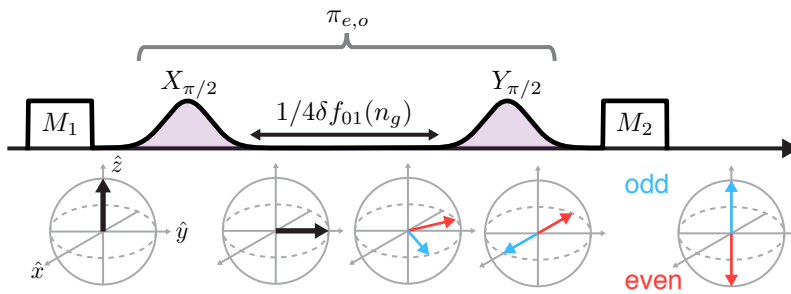

Figure 6.3 | Pulse sequence used to map the charge-parity of the OCS transmon onto its plasmon state.

6.1.2 Charge-parity-mapping pulse sequence

Using a similar pulse sequence [Fig. 6.3], we map the charge parity of the transmon onto the plasmon state [Ristè et al. 2013; Serniak et al. 2018]. Two $\pi/2$-pulses, now about orthogonal axes, are separated by a delay $\tau(n_g) = 1/4\delta f_{01}(n_g)$, which ensures that the bloch vectors corresponding to even and odd charge parity are antiparallel on the equator of the Bloch sphere at the time of the second $\pi/2$-pulse. This constitutes an effective π-pulse conditioned on charge parity ($\pi_{e,o}$). This charge-parity-mapping operation only discerns between transition frequencies greater-than or less-than $\overline{f_{01}}$, and we refer to these as "even" and "odd" charge-parity states, respectively, despite the inability to measure absolute parity. This also limits our visibility of n_g values to the "half-Brillouin zone" $[0, 1/4] \subset \mathbb{R}$. The relative phase of the $\pi/2$-pulses controls whether the $\pi_{\mathrm{e,o}}$ sequence is conditioned on even or odd charge parity. The charge parity $P = (2M_1 - 1)(2M_2 - 1)$ is calculated in post-processing.

To observe charge-parity switches in real time, we repeated the charge-parity-mapping sequence every $\Delta t_{\mathrm{exp}} = 10\ \mu$s for ~ 600 ms [Fig. 6.4(b)]. The power spectral density S_{PP} of these parity fluctuations was averaged over 20 independent charge-parity jump traces [Fig. 3]. S_{PP} was fit to the characteristic Lorentzian of a random telegraph signal,

$$S_{PP}[f] = \frac{4\mathcal{F}^2/T_P}{(2/T_P)^2 + (2\pi f)^2} + (1 - \mathcal{F}^2)\Delta t_{\mathrm{exp}}, \tag{6.1}$$

from which a charge-parity lifetime $T_P = 77 \pm 1\ \mu$s and mapping fidelity $\mathcal{F} = 0.91 \pm 0.01$ were obtained. This model assumes that charge-parity mapping

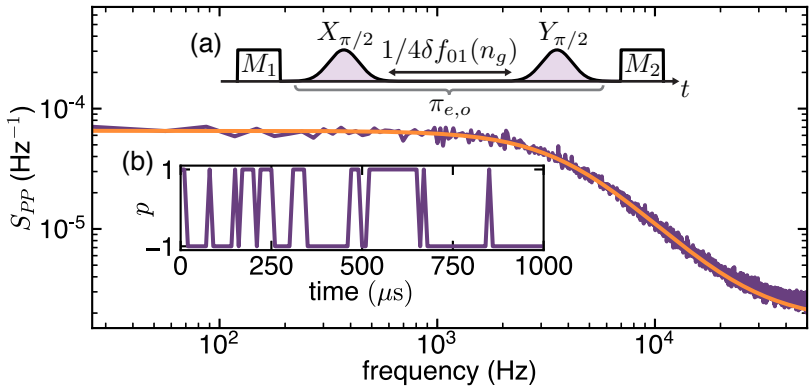

Figure 6.4 | Detecting fast charge-parity switches in an offset-charge-sensitive transmon qubit. Inset (a) Charge-parity mapping pulse sequence, which results in an effective charge-parity-conditioned π-pulse, $\pi_{e,o}$. Inset (b) A 1 ms snapshot of a ~ 600 ms long charge-parity jump trace. Main: Measured power-spectral density of charge-parity fluctuations S_{PP} (purple), with a Lorentzian fit (orange) corresponding to $T_P = 77 \pm 1\ \mu$s.

errors leading to non-unity $\mathcal{F}$ are uncorrelated with charge-parity, though T_1-related errors tend to bias toward measuring even charge parity (discussed below). A"chi-squared" analysis of the model suggests that this has a negligible effect on the output of the model. For more details, see Ref. [Machlup 1954; Ristè et al. 2013]. Each jump trace was acquired after confirming that $\delta f_{01}(n_g) \geq 1$ MHz by the monitoring of n_g described above. This conditioning was introduced to increase the fidelity $\mathcal{F}$ of the charge-parity mapping, as $\delta f_{01}(n_g)$ is less sensitive to fluctuations of n_g at near-maximum $\delta f_{01}(n_g)$; also, the qubit is less likely to dephase during the correspondingly shorter $\tau(n_g)$. As discussed in Chapter 5, the charge-parity transition rates are for all intents and purposes insensitive to n_g as long as $\delta\epsilon_0, \delta\epsilon_1 \ll k_B T$.

6.1.3 Correlating charge-parity switches and plasmon transitions

The fact that $T_P \approx T_1$ hints at the possibility that our transmon may be limited by QP-induced dissipation. Following Ref. [Catelani 2014], the total relaxation rate Γ_{10} can be decomposed into the sum of two contributions: the rate of relaxation accompanied by a charge-parity switch (Γ_{10}^{eo}), which we attribute solely

to QP-tunneling or PAT-induced loss, and the rate of relaxation from charge-parity-conserving mechanisms (Γ_{10}^{ee}), such as dielectric loss. As there is no preferred parity, these transition rates are symmetric under exchange of even and odd ($\Gamma_{ij}^{eo} = \Gamma_{ij}^{oe}$ and $\Gamma_{ij}^{ee} = \Gamma_{ij}^{oo}$). Similarly to the total relaxation rate, the total excitation rate is given by $\Gamma_{01} = \Gamma_{01}^{eo} + \Gamma_{01}^{ee}$. We resolve these distinct contributions by concatenating two parity-mapping sequences (yielding outcomes p and p') separated by a variable delay τ [Fig. 6.5(a)]. This measurement determines both the charge parity and plasmon state before and after τ, which allows us to correlate qubit transitions with charge-parity switching events. From our data, we compute $\tilde{\rho}(j, pp'|i)(\tau)$: the probability of *measuring* outcome $m_3 = j$ after a delay τ given that $m_2 = i$, with or without a parity switch ($pp' = -1$ or $+1$, respectively).

6.1.4 Master equation model

To model these quantities, we employ a master equation describing the flow of probability between different transmon states

$$\begin{aligned}\dot{\rho_i^p} = &-(\Gamma_{i\bar{i}}^{p\bar{p}} + \Gamma_{ii}^{p\bar{p}} + \Gamma_{i\bar{i}}^{pp})\rho_i^p \\ &+ \Gamma_{\bar{i}i}^{\bar{p}p}\rho_{\bar{i}}^{\bar{p}} + \Gamma_{ii}^{\bar{p}p}\rho_i^{\bar{p}} + \Gamma_{\bar{i}i}^{pp}\rho_{\bar{i}}^{p},\end{aligned} \tag{6.2}$$

where ρ_i^p is the probability of finding the system in qubit state i and charge parity p, and $\bar{i}$ is read as "not i." We evolve the above model numerically with initial conditions determined by M_2 and P, and fit all eight conditional probabilities $\tilde{\rho}(j, pp'|i)(\tau)$, a subset of which are shown in Fig. 6.5(c, d).

In addition, we calculate the charge-parity autocorrelation function $\langle PP' \rangle_{ij}(\tau)$, again conditioned on outcomes $m_2 = i$ and $m_3 = j$, respectively [Fig. 6.5(b)], and fit to functions of the form

$$\langle PP' \rangle_{ij}(\tau) = \rho_i^p(0) \left[\frac{\rho_j^p(\tau) - \rho_j^{\bar{p}}(\tau)}{\rho_j^p(\tau) + \rho_j^{\bar{p}}(\tau)} \right]. \tag{6.3}$$

The maximum correlation $\langle PP' \rangle_{ii}(0)$ is limited by the fidelity of the correlation measurement (which in principle is dependent on the readout fidelity of plasmon state i), and qualitatively, the deviation of $\langle PP' \rangle_{ij}(0)$ from this maximum amplitude is related to the ratio $\Gamma_{ij}^{eo}/\Gamma_{ij}$.

Equations 6.2 and 6.3 do not account for any measurement infidelities,

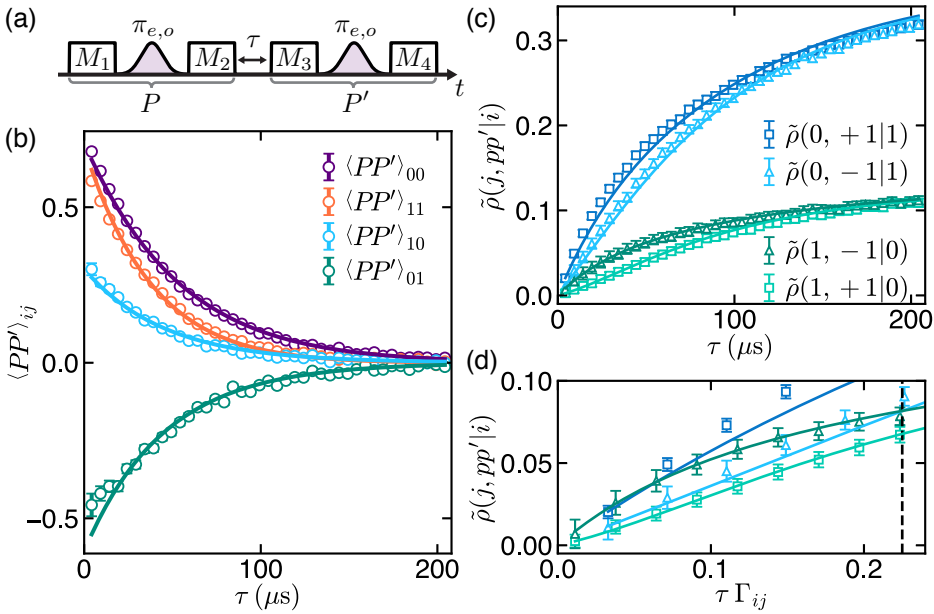

Figure 6.5 | Correlating charge-parity switches with qubit transitions. (a) Pulse sequence depicting the charge-parity correlation measurement. The charge-parity conditioning of the state-mapping sequence (whether we implement a π_e or a π_o pulse) is varied between measurements to balance charge-parity-dependent errors. (b) Charge-parity autocorrelation function $\langle PP' \rangle$ conditioned on the outcomes $m_2 = i$ and $m_3 = j$. (c) Conditioned probabilities $\tilde{\rho}(j, pp'|i)(\tau)$ with and without a charge-parity switch ($pp' = +1$ or -1, respectively). The relative amplitudes of curves with and without parity switches (triangles and squares, respectively) indicate the likelihood that those transitions were correlated with quasiparticle-tunneling events. Theory lines are obtained from a least-squares fit to the master equation described in the main text. (d) Probabilities plotted in (c) after rescaling τ by Γ_{ij}, the overall decay rate governing each curve at large τ. The crossing of curves with $pp' = -1$ (black-dashed line) indicates that charge-parity-switching events are more likely to excite than relax the transmon.

which can skew the observed correlations. These include parity- and qubit-state-dependent errors, such as spontaneous qubit transitions during the parity-mapping sequence, as well as global errors such as pulse infidelity due to uncertainty in $\delta f_{01}(n_g)$. The following few pages will detail how we take into account some of the errors inherent in this measurement scheme in our modeling of $\tilde{\rho}(j, pp'|i)(\tau)$ and $\langle PP' \rangle_{ij}(\tau)$.

Modeling correlations between qubit transitions and charge-parity switches

We measured correlations between charge-parity switches and qubit transitions, which reveals the extent to which the qubit coherence is limited by nonequilibrium quasiparticle excitations. To correlate these processes, we perform two charge-parity mapping sequences, separated by a variable delay τ [Fig. 6.5(a)]. From this, we group the measurement sequences conditioning on starting in qubit state i and parity p, and ending up in qubit state j and parity p'. We compute two quantities from this data: the conditioned probabilities of all of these events $\tilde{\rho}(j, pp'|i)(\tau)$, and the qubit-state-conditioned charge-parity autocorrelation function $\langle PP' \rangle_{ij}(\tau)$. To model the dynamics between states of the system, we define a master equation describing the dynamics of joint plasmon-state and charge-parity occupation probabilities ρ_i^p.

$$\begin{aligned}\dot{\rho_i^p} = &-(\Gamma_{i\bar{i}}^{p\bar{p}} + \Gamma_{ii}^{p\bar{p}} + \Gamma_{i\bar{i}}^{pp})\rho_i^p \\ &+ \Gamma_{\bar{i}i}^{\bar{p}p}\rho_{\bar{i}}^{\bar{p}} + \Gamma_{ii}^{\bar{p}p}\rho_i^{\bar{p}} + \Gamma_{\bar{i}i}^{pp}\rho_{\bar{i}}^{p}.\end{aligned} \tag{6.4}$$

Here, $\Gamma_{i\bar{i}}^{p\bar{p}}$ is a conditional transition rate, with i ($\bar{i}$) and p () denoting the conditioned (other) qubit state and charge parity, respectively. Because the charge dispersion of the transmon energy levels is small relative to the scale of thermal fluctuations, the conditional rates are symmetric with the exchange of p and $\bar{p}$. We evolve this master equation with initial conditions set by conditioning on the initial qubit and charge-parity state. The full model is solved numerically and fit to measured values of all eight permutations of $\tilde{\rho}(j, pp'|i)(\tau)$ and all four permutations of $\langle PP' \rangle_{ij}(\tau)$, to extract $\Gamma_{00}^{p\bar{p}}$, $\Gamma_{11}^{p\bar{p}}$, $\Gamma_{10}^{p\bar{p}}$, $\Gamma_{01}^{p\bar{p}}$, Γ_{10}^{pp}, and Γ_{01}^{pp}: all possible transition rates of the OCS transmon restricted to the qubit-manifold of plasmon states $i = 0, 1$.

The measured values of $\tilde{\rho}(j, pp'|i)(\tau)$ and $\langle PP' \rangle_{ij}(\tau)$ are susceptible to various measurement imperfections that are not included in the model above, and

we must modify our fit functions to include these infidelities. Single state-discrimination errors will on average decrease $\langle PP' \rangle_{ij}(\tau)$, and T_1 errors during the parity mapping will impart an infidelity that depends on both the charge-parity and the qubit state at the start of the parity mapping. This is because, at short τ, parity-switching events are rare, and single state-discrimination errors will necessarily give a false reading of the charge-parity. Other measurement inefficiencies are approximately independent of qubit state and charge parity, which contribute to a global fidelity $\mathcal{F}_g$ of the parity-mapping sequence. For example, because n_g varies uncontrollably in time, each sequence of pulse calibrations and parity-autocorrelation measurement must be completed on a timescale faster than a few minutes. Any variation of n_g between the tuning of pulses and the completion of the experiment will introduce qubit-pulse errors, which along with qubit dephasing during $\tau(n_g)$, contribute to $\mathcal{F}_g$. In practice, $\mathcal{F}_g$ is occasionally very low, which we attribute to spontaneous jumps of n_g between the the time when $\delta f_{01}(n_g)$ is determined and the charge-parity autocorrelation measurement. [2] Since we do not know $\mathcal{F}_g$ *a priori*, we include it in the model as an additional fit parameter, and exclude independent batches of 20000 measurement sequences which fall below a threshold $\mathcal{F}_g$. We choose this threshold to be 0.5 at low temperatures, where the vast majority of measurements meet this criteria. This threshold must be relaxed at higher fridge temperatures due to increased transmon decoherence.

State-discrimination errors can be sufficiently reduced by ignoring measurement sequences in which any of the four measurement shots do not meet a stringent state-assignment threshold. We histogram all qubit measurement shots, fit to a sum of two Gaussian distributions, and exclude measurement sequences where any of the four measurements fall near the half-way point between distributions. In practice, this thresholding removes between 10% and 50% of measurement sequences, depending on the amplitude and integration time of the readout signal, in order to achieve state-discrimination fidelity of greater than 0.9999. The readout amplitude was limited to an average photon number $\bar{n} \approx 3$ to avoid measurement induced qubit transitions [Slichter et al. 2012; Sank et al. 2016].

Each charge-parity-mapping sequence consists of an initial qubit measurement, the Ramsey pulses for parity-mapping, and a final qubit measurement.

[2] This time is limited by reloading the arbitrary waveform generator with a new measurement sequence, which takes about 20 s.

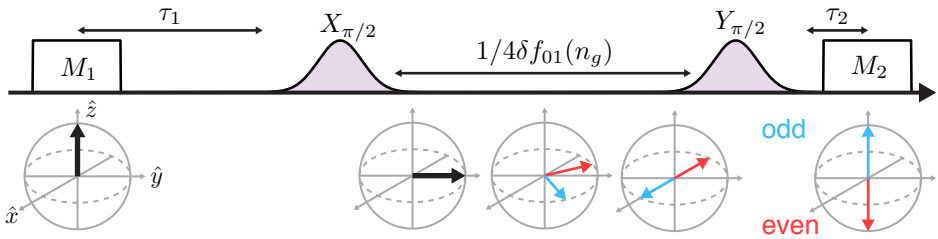

Figure 6.6 | Charge-parity mapping pulse sequence (not to scale). The charge-parity is defined as $P = (2M_1 - 1)(2M_2 - 1)$. The first $\pi/2$-pulse brings both charge-parity Bloch vectors to the equator. After a precise delay $\tau = 1/4\delta f_{01}(n_g)$, the Bloch vectors are anti-parallel. A second $\pi/2$-pulse completes the operation, enacting an effective π-pulse conditioned on being in the even charge-parity state, regardless of the outcome m_1. We can change the conditioning of the mapping by changing the phase of the first $\pi/2$-pulse by $180°$.

Because of stringent thresholding, we assume state-assignment with perfect fidelity that is determined at the midpoint of the readout pulse. There is thus a time τ_1 between the midpoint of M_1 and the beginning of the Ramsey pulses, and time τ_2 between the end of the Ramsey pulses and the midpoint of M_2, during which T_1 errors can occur [Fig. 6.6].[3] Errors during τ_1 and τ_2 from T_1 events are included explicitly in the model, and errors between the $\pi/2$-pulses are included implicitly via a global mapping fidelity $\mathcal{F}_g$.

Qubit-state dependent T_1 events affect the fidelity with which we determine the charge-parity. For example, let's say the parity-mapping sequence is chosen such that it enacts a π-pulse conditioned on being in the even charge-parity state (this will vary in the following discussion). If the system is in state $|0, o\rangle$, one would expect to measure $m_1 = 0 \rightarrow m_2 = 0$, but T_1 errors will appear as $0 \rightarrow 1$ with a probability $\Gamma_{01}(\tau_1 + \tau_2)$. If the system state is $|0, e\rangle$, one would expect to measure $0 \rightarrow 1$, but T_1 errors will appear as $0 \rightarrow 0$ with a probability $(\Gamma_{01}\tau_1 + \Gamma_{10}\tau_2)$. Similar expressions can be found for the system starting in $|1, p\rangle$. Since there is no physical preference for even or odd parity, we average over parity dependence in the error rates and only consider the probability of starting in an initial state. However, parity-dependent errors will introduce artificial correlations between P and P'. To remedy this, we vary whether each parity-mapping sequence performs an effective π-pulse on the even- or odd-charge-parity state.

[3] The time τ_1 is longer than τ_2 to leave enough time for photons from M_1 or M_3 to leak out of the readout cavity.

Assuming near-perfect state discrimination fidelity and equal probability to measure odd or even charge parity (with balanced pulse conditioning), these errors will only depend on the qubit state at the beginning of the mapping. For the first charge-parity-mapping sequence P, we define an error probability

$$\zeta_P^{ij} = (1 - \mathcal{F}_g) + \frac{1}{2}\left[\mathcal{P}_0^{ij}(\tau_1\Gamma_{01} + \tau_2\Gamma_{10}) + \mathcal{P}_1^{ij}(\tau_1 + \tau_2)\Gamma_{10}\right] \tag{6.5}$$

Above, $\mathcal{P}_a^{ij}$ is the probability that $m_1 = a$ at the beginning of P in measurement sequences with qubit-conditioning $m_2 = i$ and $m_3 = j$. Similarly, for the second parity mapping sequence P' we define

$$\zeta_{P'}^{j} = (1 - \mathcal{F}_g) + \frac{1}{2}\left[(\tau_1 + \tau_2)\Gamma_{j\bar{j}} + (\tau_1\Gamma_{j\bar{j}} + \tau_2\Gamma_{\bar{j}j})\right] \tag{6.6}$$

This error probability is independent of i, and does not have additional qubit-state weighting because we assume near-perfect conditioning of outcome j.

Without accounting for any errors, $\tilde{\rho}(j, pp'|i)(\tau) = \rho_i^p(0)\rho_j^{p'}(\tau)$. Errors in the determination of $\rho_i^p(0)$ shuffle the initial probability from the conditioned parity $\rho_i^p(0)$ to the other parity $\rho_i^{\overline{p}}(0)$ with a rate ζ_P^{ij}. We evolve the master equation with these errors accounted for in the initial conditions, in that the conditioned probability $\rho_i^{\overline{p}}(0)$ is no longer unity. Then, applying errors in the second parity mapping explicitly, we find:

$$\tilde{\rho}(j, pp'|i)(\tau) = (1 - \zeta_{P'}^j)\rho_j^{p'}(\tau) + \zeta_{P'}^j\rho_j^{\overline{p'}}(\tau). \tag{6.7}$$

We calculate $\langle PP'\rangle_{ij}(\tau)$ directly from these conditional probabilities

$$\langle PP'\rangle_{ij}(\tau) = \frac{\tilde{\rho}(j, +1|i)(\tau) - \tilde{\rho}(j, -1|i)(\tau)}{\tilde{\rho}(j, +1|i)(\tau) + \tilde{\rho}(j, -1|i)(\tau)}. \tag{6.8}$$

To extract the rates quoted in the next sections, we fit to all eight permutations of $\tilde{\rho}(j, pp'|i)(\tau)$ and all four permutations of $\langle PP'\rangle_{ij}(\tau)$ simultaneously. The slight disagreement at short τ may be due to measurement-induced qubit transitions that could be present even at low readout power [Slichter et al. 2012; Sank et al. 2016].

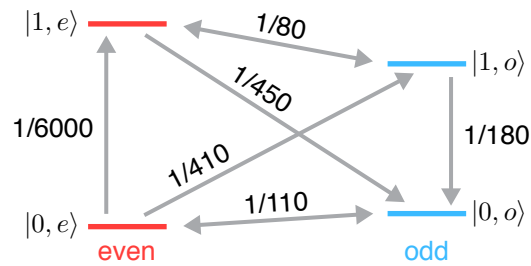

Figure 6.7 | Transition rates extracted from the master equation, in units of μs^{-1}. Note that rates are invariant under exchange of even and odd charge-parity states.

6.1.5 Extracted rates

From our model with measurement errors taken into account, we extract $1/\Gamma_{00}^{eo} = 110 \pm 1$ μs, $1/\Gamma_{11}^{eo} = 77 \pm 1$ μs, $1/\Gamma_{10}^{eo} = 447 \pm 7$ μs, $1/\Gamma_{01}^{eo} = 400 \pm 5$ μs, $1/\Gamma_{10}^{ee} = 182 \pm 1$ μs, and $1/\Gamma_{01}^{ee} = 6500 \pm 900$ μs [Fig. 6.7]. Quoted parameter standard deviations reflect the uncertainty in the data, calculated using standard statistical techniques, and do not attempt to account for any systematic error. As a check of consistency, we calculate

$$T_1 = (\Gamma_{10}^{eo} + \Gamma_{10}^{ee} + \Gamma_{01}^{eo} + \Gamma_{01}^{ee})^{-1}, \quad \mathcal{P}_0^{\mathrm{eq}} = (\Gamma_{10}^{eo} + \Gamma_{10}^{ee})T_1 \tag{6.9}$$

which were measured independently using standard measurement protocols, and

$$T_P \approx 2/(\Gamma_{00}^{eo} + \Gamma_{11}^{eo} + \Gamma_{10}^{eo} + \Gamma_{01}^{eo}), \tag{6.10}$$

as obtained from the measurement and data in Fig. 6.4.[4]. We find that they agree with these values as quoted above, and other devices were found to have similar rates.[5]

These rates have implications for our understanding of nonequilibrium QPs in our transmon qubits. First, the limit on T_1 of this device imposed by QP-related processes is no greater than $(\Gamma_{10}^{eo} + \Gamma_{01}^{eo})^{-1} = 211 \pm 3$ μs, compared to a limit of

[4] This approximate relation for T_P is due to the fact that in the aforementioned charge-parity jump experiment (Fig. 3) the qubit is taken out of equilibrium by the pulse sequence. The extracted T_P approximately averages the conditional parity-switching rates corresponding to the plasmon states $|0\rangle$ and $|1\rangle$.

[5] As we will discuss in the next section and the next chapter, a few *key* system parameters can influence these rates.

$(\Gamma_{10}^{ee} + \Gamma_{01}^{ee})^{-1} = 177 \pm 2$ μs imposed by all other loss mechanisms. This puts QP-induced dissipation on par with the sum of all other dissipation channels, contributing significantly to qubit relaxation $\Gamma_{10}^{eo}/\Gamma_{10} = 0.29 \pm 0.01$. Second, the ratio $\Gamma_{01}^{eo}/\Gamma_{01} = 0.94 \pm 0.02$ indicates that QP-induced excitation accounts for the vast majority of the residual transmon excited-state population [Fig. 4(a)]. Previous works [Wenner et al. 2013; Jin et al. 2015] had suspected something like this, but not in the way that we describe here. Finally, $\Gamma_{01}^{eo}/\Gamma_{10}^{eo} = 1.12 \pm 0.02$, which indicates that, if these rates are due to QP-tunneling processes, the energy distribution of QPs $f(\varepsilon)$ is strongly-athermal. Naïvely applying Fermi-Dirac statistics and detailed balance yields $\Gamma_{01}^{eo}/\Gamma_{10}^{eo} = \exp(-hf_{01}/k_{\mathrm{B}}T_{\mathrm{eff}}^{\mathrm{QP}})$, which would a negative effective QP temperature $T_{\mathrm{eff}}^{\mathrm{QP}} \approx -2$ K in our device. This would mean that the QP energy distribution is not localized near the gap edge, and has a characteristic energy greater than $\Delta + hf_{01}$. This is highly unlikely, as we will discuss below. In contrast to the above ratio, $\Gamma_{01}^{ee}/\Gamma_{10}^{ee} = 0.03 \pm 0.01$, indicating that the non-QP dissipative baths coupled to the transmon are relatively "cold" [Fig. 4(b)], with an effective temperature ~ 60 mK. The observation that $\Gamma_{11}^{eo} > \Gamma_{00}^{eo}$ is not yet explained by theoretical predictions [Catelani 2014]. We stress that the dependence of QP dynamics on E_J/E_C is very weak, and that these results on a device in the OCS regime apply directly to traditional transmon devices with $E_J/E_C \gg 1$.

Our analysis relies on the aforementioned model to accurately extract qubit-state-conditioned QP tunneling rates, and we claim that the ratio $\Gamma_{01}^{eo}/\Gamma_{10}^{eo}$ is well-captured by the model. To illustrate this, we plot our data along with predicted curves $\langle PP' \rangle_{ij}(\tau)$ for various fixed $\Gamma_{01}^{eo}/\Gamma_{10}^{eo}$ [Fig. 6.8]. This model is constructed by first fixing Γ_{00}^{eo} and Γ_{11}^{eo} to the values extracted from the fit to the data. These rates approximately fix T_P to the value extracted in the main text. Then, we adjust Γ_{10}^{eo}, Γ_{01}^{eo}, Γ_{10}^{ee}, and Γ_{01}^{ee} under the constraint that T_1, T_P, and $\mathcal{P}_0^{\mathrm{eq}}$ are fixed to their independently measured values for all chosen values of $\Gamma_{01}^{eo}/\Gamma_{10}^{eo}$. As displayed in Fig. S3, the model qualitatively deviates from the data when $\Gamma_{01}^{eo}/\Gamma_{10}^{eo}$ is less than ≈ 1.

6.1.6 Temperature dependence

We repeated the correlation measurement [Fig. 4] at various mixing-chamber temperatures T [Fig. 5]. We find that all parity-switching rates Γ_{ij}^{eo} increase for $T \gtrsim 140$ mK, at which point T_1, T_P, and $\Gamma_{01}^{eo}/\Gamma_{10}^{eo}$ all begin to decrease. Modeling the temperature dependence of these rates requires some ansatz about the QP

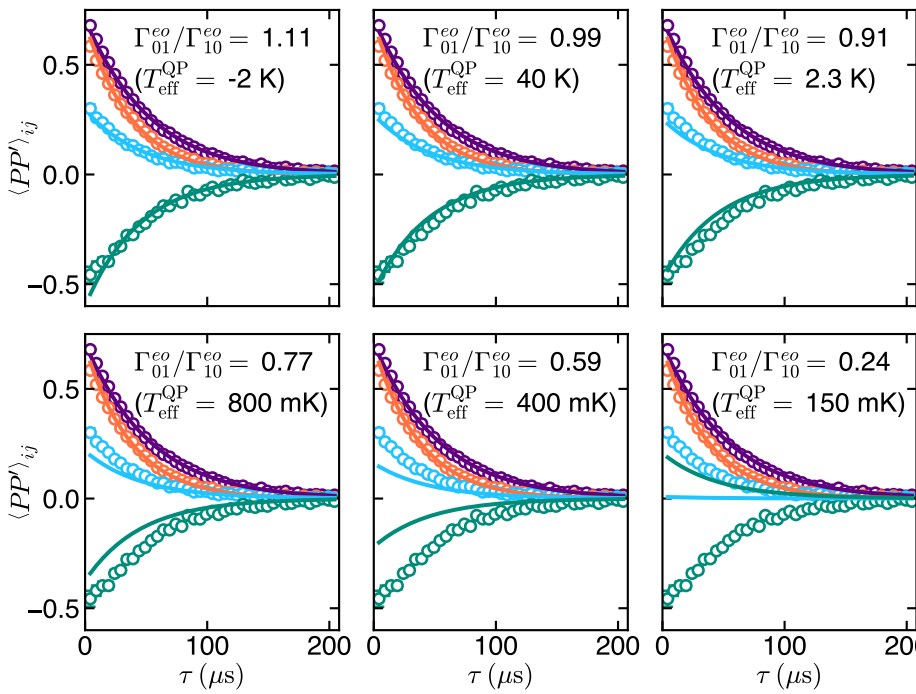

Figure 6.8 | Charge-parity-autocorrelation data [Fig. 6.5] overlaid with the master equation model of $\langle PP' \rangle_{ij}(\tau)$ for varying $\Gamma_{01}^{eo}/\Gamma_{10}^{eo}$. Deviation from the data when setting $\Gamma_{01}^{eo}/\Gamma_{10}^{eo} < 1$ shows that the model is sensitive to small fluctuations in fit parameters. Fixing the effective QP temperature to account for the apparent density of nonequilibrium QPs ($T_{\text{eff}}^{\text{QP}} = 150$ mK for $x_{\text{qp}} \approx 10^{-7}$) clearly does not accurately describe their energy distribution.

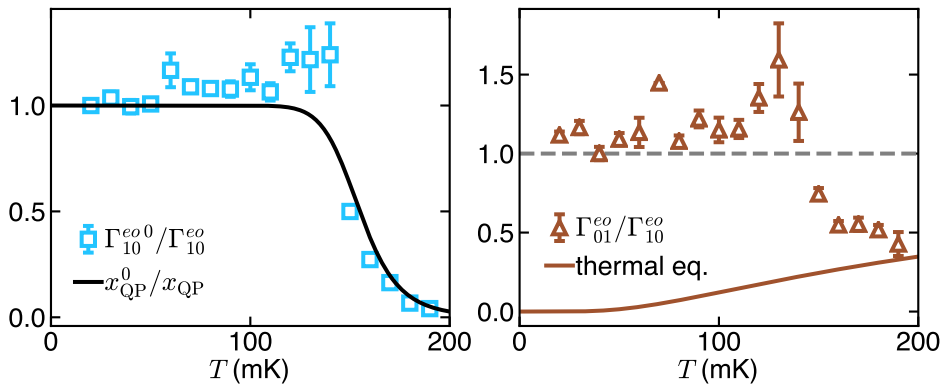

Figure 6.9 | Left: $1/\Gamma_{10}^{eo}$ normalized by its base-temperature value $1/\Gamma_{10}^{eo\,0}$, as a function of temperature. The solid black line is a fit to the thermal dependence of $x_{\rm QP}^0/x_{\rm QP}$, which gives $x_{\rm QP}^0 \approx 1 \times 10^{-7}$. Right: $\Gamma_{01}^{eo}/\Gamma_{10}^{eo}$ compared to predictions from detailed balance, assuming QPs are thermalized with the cryostat. Grey dashed line indicates the value above which $T_{\rm eff}^{\rm qp} \leq 0$.

energy distribution, which is typically assumed to be a Fermi-Dirac distribution localized near the gap edge [Martinis, Ansmann, and Aumentado 2009; Catelani et al. 2011]. Without claiming its validity, we use it to compare our results with other reports of QP density $x_{\rm QP}^0$ in superconducting circuits. If we further assume that the populations of nonequilibrium QPs and equilibrium QPs [Catelani et al. 2011] are independent, the total $x_{\rm QP}$ is the sum:

$$x_{\rm QP} = x_{\rm QP}^0 + \sqrt{2\pi k_{\rm B} T/\Delta} e^{-\Delta/k_{\rm B}T}. \tag{6.11}$$

Here $\Delta = 205\ \mu$eV, consistent with DC measurements of similar films (Δ increases with reduction of Al thickness) [Chubov, Eremenko, and Pilipenko 1969]. The QP-induced relaxation rate Γ_{10}^{eo} should scale linearly with $x_{\rm QP}$ [Martinis, Ansmann, and Aumentado 2009; Catelani et al. 2011]. We see this approximate scaling in our data [Fig. 6.9] with a slight decrease in Γ_{10}^{eo} with increasing temperature that is not predicted by our simple model, but has been previously observed [Martinis, Ansmann, and Aumentado 2009]. This model yields $x_{\rm QP}^0 \approx 1 \times 10^{-7}$, which agrees with other recent experiments [Aumentado et al. 2004; Vool et al. 2014; Nsanzineza and Plourde 2014; Pop et al. 2014; Wang et al. 2014; Gustavsson et al. 2016].

Another verification of our measurement technique is to consider the ra-

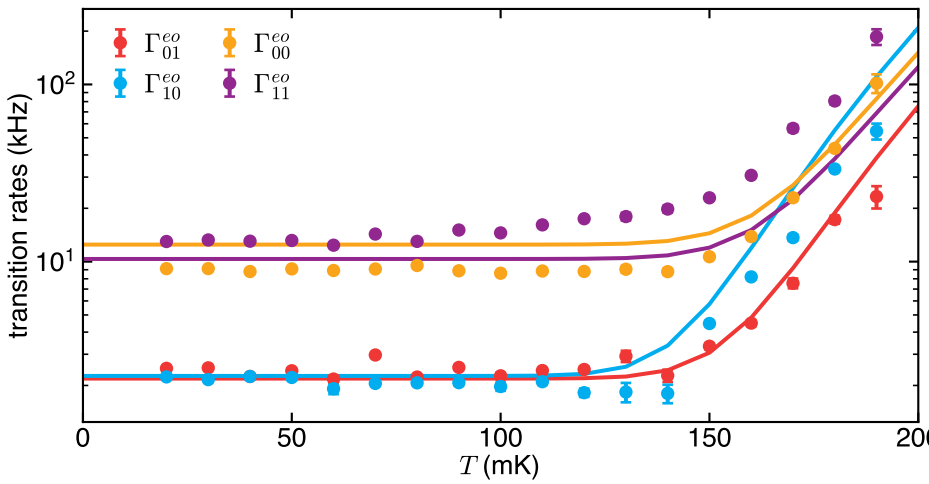

Figure 6.10 | Temperature dependence of qubit-state-conditioned parity-switching rates. Above $\sim$ 140 mK, all rates begin to increase, and $\Gamma_{01}^{eo}/\Gamma_{10}^{eo} \leq 1$ suggests that thermally generated QPs begin to outnumber nonequilibrium QPs. Simulation assumes monochromatic pair breaking radiation at a frequency $\omega_\nu/2\pi = 3.4\Delta/h$, with average occupation $\bar{n}_\nu = 9 \times 10^{-3}$.

tio $\Gamma_{01}^{eo}/\Gamma_{10}^{eo}$ as a function of fridge temperature. As evident in Fig. 6.9, the surprising result $\Gamma_{01}^{eo}/\Gamma_{10}^{eo} \approx 1$ persists up to 150 mK: the temperature where thermally generated QPs begin to dominate the charge-parity dynamics. As the temperature is increased above this threshold, $\Gamma_{01}^{eo}/\Gamma_{10}^{eo}$ approaches the expected thermal value. This is extremely comforting to see, that in a regime where we think we should understand what's going on, we actually do.

6.1.7 Comparison with PAT theory

Our recent work in Houzet et al. 2019 has alerted us to another interpretation of the aforementioned results. The charge-parity switches observed at low temperature may not have been from QP-tunneling processes, as we had originally concluded, but from photon-assisted QP generation and tunneling (PAT) processes. These PAT processes generate a pair of QPs at the JJ, and cause charge parity switches. The distinguishing feature of this process is that it can be equally likely to excite the transmon as to relax it. We can compare our measured charge-parity transition rates to the theory developed in Chapter 5 [Houzet

et al. 2019]. Fig. 6.10 shows the temperature dependence of the measured charge-parity transition rates with theoretical predictions overlaid. The theory represents a thermal distribution of QPs, contributing a transition rate (due to thermal QP-tunneling) as discussed in Chapter 5 as a function of temperature, with a fixed PAT contribution that dominates below $\approx$ 150 mK. The Cooper pair-breaking radiation responsible for PAT is modelled to be monochromatic at a frequency $\omega_\nu/2\pi = 3.4\Delta/h \approx 170$ GHz, with an average mode occupation $\bar{n}_\nu = 9\times10^{-3}$. We note that this fit could be improved by varying Δ, however we prefer to keep it fixed at $\approx h \times 50$ GHz, in accordance with DC measurements of [Chapter 7].

Though the agreement between the experimental data and our PAT theory is not perfect, we feel that, while there may be more to this story, PAT processes are a plausible explanation for *some* of the observed phenomena. At the very least, it is more likely that PAT processes are responsible for the ratio $\Gamma^{eo}_{01}/\Gamma^{eo}_{10} \approx 1$ than the other option, that QPs have some extremely athermal energy distribution. We are encouraged that as we understand more about the processes that generate QPs in our devices we may understand these results and better engineer devices to prevent against QP-induced dissipation. Further experiments are needed to fully assess the validity of these hypotheses. We will describe these experiments (that are currently underway) in the final chapter of this dissertation. One significant question still goes unaddressed, which is why $\Gamma^{eo}_{11}/\Gamma^{eo}_{00} > 1$. Because the charge dispersion of the two lowest plasmon levels $\delta\epsilon_0, \delta\epsilon_1 \ll k_B T \ll \Delta$, this ratio should be given primarily by the ratio of single-charge-tunneling matrix elements, but apparently there are some other factors in play. This is something that we have seen consistently in our data, as well as in Ref. Ristè et al. 2013, which may be a clue toward fully understanding nonequilibrium QP dynamics in superconducting devices.

6.1.8 Summary and discussion

At the time of Ref. Serniak et al. 2018, we had performed these charge-parity correlation experiments in two nominally identical devices with the same experimental setup [Tables 6.1 and 6.2]. Aside from having $E_J/E_C \approx 20$, operating in the OCS regime, the devices were nominally identical to typical 3D transmons. It's important to note that similar charge-parity transition rates were measured in both devices with a few differences that we will

Table 6.1 | Charge-parity-correlation device parameters.

Sample	$\overline{f_{01}}$(GHz)	$2\delta f_{01}$(MHz)	$T_1(\mu s)$	$T_P(\mu s)$
A	4.400	3.18	95 ± 5	77 ± 1
B	4.255	4.96	44 ± 2	96 ± 1

Table 6.2 | Transition rates from charge-parity-correlation experiments

Sample	$1/\Gamma_{00}^{eo}(\mu s)$	$1/\Gamma_{11}^{eo}(\mu s)$	$1/\Gamma_{10}^{eo}(\mu s)$	$1/\Gamma_{01}^{eo}(\mu s)$	$1/\Gamma_{10}^{ee}(\mu s)$	$1/\Gamma_{01}^{ee}(\mu s)$
A	110 ± 1	77 ± 1	447 ± 7	400 ± 5	182 ± 1	6500 ± 900
B	135 ± 2	92 ± 2	920 ± 80	400 ± 10	61 ± 1	10000 ± 4000

now describe. Sample A is the device reported in the previous sections, and Sample B was measured in a separate cooldown under nominally identical conditions, though we did not study the temperature dependence of its conditional transition rates. The limit on T_1 of sample A (sample B) imposed by QPs is $(\Gamma_{10}^{eo} + \Gamma_{01}^{eo})^{-1} = 211 \pm 3\ \mu s\,(278 \pm 8\ \mu s)$, while all non-QP loss mechanisms limit T_1 to $(\Gamma_{10}^{ee} + \Gamma_{01}^{ee})^{-1} = 177 \pm 2\ \mu s\,(61 \pm 1\ \mu s)$. QP-induced transitions account for $\Gamma_{10}^{eo}/\Gamma_{10} = 0.29 \pm 0.01\,(0.06 \pm 0.01)$ of all relaxation events, and $\Gamma_{01}^{eo}/\Gamma_{01} = 0.94 \pm 0.02\,(0.96 \pm 0.03)$ of all excitation events. The ratio of QP-induced excitation and relaxation rates $\Gamma_{01}^{eo}/\Gamma_{10}^{eo} = 1.12 \pm 0.02\,(2.3 \pm 0.2)$, indicating that the source of charge-parity switches is "hot." Further experiments are necessary to understand this observation of sample B, as it does not agree with any current theory. Conversely, we find that other the combination of all other dissipative baths are "cold": $\Gamma_{01}^{ee}/\Gamma_{10}^{ee} = 0.03 \pm 0.01\,(0.006 \pm 0.002)$.

We thus have shown either that QPs are more energetic than a Fermi-Dirac distribution accounting for their apparent density x_{QP} would suggest, or that some other process, such as PAT, is responsible for charge-parity switches in transmon qubits. One should note that the authors of Ref. Ristè et al. 2013 reported T_P one order of magnitude greater than what we have presented in Ref. Serniak et al. 2018. We know that proper filtering of RF lines, light-tight shielding [Barends et al. 2011; Córcoles et al. 2011], and well-thermalized components are now standard ingredients for reducing the QP density which were already included in our measurement setup. Our most recent work in Ref. Serniak et al. 2019 demonstrated that *additional* high-frequency filtering is required to further reduce x_{QP}, the results of which will be presented in the next section as well as the next chapter. It's not obvious that this additional filtering

would be necessary, and our ongoing work is aimed to understand the exact mechanism by which QP-generating radiation is infiltrating our measurement apparatus such that the community can adopt effective preventative measures.

In conclusion, the correlations between charge-parity switches and qubit transitions in an offset-charge-sensitive transmon indicate that QP-induced loss can be responsible for a significant fraction of dissipation in state-of-the-art superconducting qubits. Additionally, we confirm that charge-parity switching processes are responsible for the residual excited-state population at low temperature in our samples. The techniques described above, building upon Ref. [Ristè et al. 2013], provide a tool to distinguish the influences of various experimental factors on QP generation and assess QP-reduction techniques, such as induced Abrikosov vortices [Wang et al. 2014; Nsanzineza and Plourde 2014; Vool et al. 2014; Taupin et al. 2016] or galvanically connected QP traps [Booth et al. 1993; Court et al. 2008; Peltonen et al. 2011; Rajauria et al. 2012; van Woerkom, Geresdi, and Kouwenhoven 2015; Riwar et al. 2016; Hosseinkhani et al. 2017; Patel et al. 2017]. Our efforts in this arena will be discussed in the next chapter.

6.2 Dispersive readout of the joint plasmon and charge-parity state

This section covers our recent work in Ref. Serniak et al. 2019, where we describe an efficient technique for detecting the charge-parity of an OCS transmon. Instead of relying on coherent pulses to map the charge-parity onto the transmon's plasmon state, we take advantage of charge-parity dependent hybridization of the OCS transmon and an ancillary readout mode. This produces a charge-parity-dependent dispersive shift that agrees well with the predictions of quantum circuit theory.

The basic building blocks of quantum circuits—e.g. capacitors, inductors, and nonlinear elements such as Josephson junctions [Josephson 1962] and electromechanical transducers [Teufel et al. 2011]—can be combined and arranged to realize device Hamiltonians engineered for specific tasks [Vool and Devoret 2017]. This includes a wide variety of superconducting qubits for quantum computation [Bouchiat et al. 1998; Mooij et al. 1999; Chiorescu et al. 2003; Koch et al. 2007; Manucharyan et al. 2009], quantum-limited microwave

amplifiers [Castellanos-Beltran et al. 2009; Bergeal et al. 2010; Macklin et al. 2015], and frequency converters for quantum signal routing [Andrews et al. 2014]. These circuits can be probed using standard microwave measurement techniques and understood within the theoretical framework of circuit quantum electrodynamics (cQED) [Blais et al. 2004], which has been used to accurately predict energy levels and intermode coupling strengths in novel and complex circuits [Janvier et al. 2015; Smith et al. 2016; Kou et al. 2017]. Arguably the most well-studied quantum circuit is the capacitively shunted Josephson junction [Bouchiat et al. 1998; Koch et al. 2007], which is parameterized by the ratio of the Josephson coupling energy E_J to the charging energy E_C. This circuit is typically operated in either the Cooper-pair box ($E_J/E_C \approx 1$) [Bouchiat et al. 1998] or transmon ($E_J/E_C \gtrsim 50$) [Koch et al. 2007] extremes of offset-charge sensitivity. We will focus on circuits that fall in the range between these two extremes. There, the characteristic plasmonic eigenstates (which we will refer to as plasmon states) of the circuit can be superpositions of many charge states, like a usual transmon, but with measurable offset-charge dispersion of the transition frequencies between eigenstates, like a Cooper-pair box. This defines what we refer to as the offset-charge-sensitive (OCS) transmon regime.

Devices fabricated in the OCS regime are particularly useful for investigations of interesting mesoscopic phenomena. For example, these devices can be used to probe deviations from the typical sinusoidal Josephson current-phase relation, which will change the offset-charge dependence of circuit eigenenergies and transition matrix elements [Ginossar and Grosfeld 2014; Yavilberg, Ginossar, and Grosfeld 2015]. Additionally, this offset-charge dependence in devices with standard Al/AlOx/Al junctions can facilitate sensitive measurements of environmental charge noise and quasiparticle dynamics [Schreier et al. 2008; Ristè et al. 2013; Serniak et al. 2018]. This is important because the performance of superconducting devices, especially qubits, can be limited by dissipation due to nonequilibrium quasiparticles (QPs) [Lutchyn, Glazman, and Larkin 2005; Martinis, Ansmann, and Aumentado 2009; Catelani et al. 2011]. The fact that the observed ratio of these nonequilibrium QPs to Cooper pairs ($x_{\mathrm{QP}} \approx 10^{-8}$ to 10^{-5} [Aumentado et al. 2004; Segall et al. 2004; Shaw et al. 2008; Martinis, Ansmann, and Aumentado 2009; Vool et al. 2014; Nsanzineza and Plourde 2014; Wang et al. 2014; Visser et al. 2014a; Gustavsson et al. 2016; Taupin et al. 2016; Serniak et al. 2018]) is many orders of magnitude greater

than would be expected in low-temperature experiments (~ 20 mK) remains an unsolved mystery. Nonetheless, given this observed phenomenological range of x_{QP}, the natural combination of cQED and BCS theory [Bardeen, Cooper, and Schrieffer 1957] leads to quantitative modeling of QP-induced dissipation that has shown good agreement with experiments [Lutchyn, Glazman, and Larkin 2005; Martinis, Ansmann, and Aumentado 2009; Catelani et al. 2011; Lenander et al. 2011; Wang et al. 2014]. Recent work has demonstrated that the effects of QPs can even be distinguished from other sources of dissipation in OCS transmons [Ristè et al. 2013; Serniak et al. 2018]. These experiments were able to correlate qubit transitions with changes in the charge-parity of the circuit: a signature of QPs interacting with the qubit [Catelani 2014]. This development has provided a foundation for experiments aiming to mitigate QP-induced dissipation and identify the generation mechanisms of nonequilibrium QPs [Bespalov et al. 2016; Catelani and Basko 2019; Houzet et al. 2019].

Here, we present a new, efficient method to monitor the charge parity of an OCS transmon. This method takes advantage of significant hybridization between the higher-excited plasmon states in an OCS transmon and an ancillary readout mode, resulting in a charge-parity-dependent shift of that readout-mode frequency, even when the transmon is in its ground plasmon state. We leverage this effect to perform direct, high-fidelity dispersive readout of the joint plasmon and charge-parity state of an OCS transmon over a wide range of offset-charge configurations. This is in contrast to the experiments described in the previous section that monitored the charge parity of OCS transmons by relying on state transitions induced by coherent pulses [Fig. 6.3] [Ristè et al. 2013; Serniak et al. 2018]. The measured charge-parity-dependent dispersive shifts agree with the predictions of quantum circuit theory [Manucharyan 2012; Zhu et al. 2013; Smith et al. 2016], and we show that this readout scheme provides a straightforward probe of charge-parity switching rates in OCS transmons. This idea of a parametric susceptibility can be extended to study other sources of decoherence, such as charge and flux noise, in cQED systems.

Finally, we apply this technique to quantify the effect of high-frequency filtering on quasiparticle dynamics in transmons. Measuring the exact same device as in Ref. Serniak et al. 2018 presented in the previous section, we find that improved filtering of radiation with frequency of order $2\Delta/h$ (where Δ is the superconducting energy gap) increases the timescale between QP-tunneling

events by almost two orders of magnitude to ≈ 6 ms. We observe an equilibrium excited-state population $\mathcal{P}_1^{\text{eq}} \approx 1.5\%$ and an average energy relaxation time $T_1 \approx 210\ \mu$s, which agrees with the predictions of Ref. Serniak et al. 2018 in this regime of reduced x_{QP} wherein QPs are *not* a dominant dissipation mechanism.

6.2.1 Experimental setup

Our experimental setup has already been described in Section 4.3.2, and focuses on an OCS transmon with $E_J/E_C \approx 17$. In fact, the experiments presented here were performed on the exact same device as in Ref. Serniak et al. 2018 presented in the last section. To recapitulate, an OCS transmon is coupled to a Al 3D waveguide cavity [Paik et al. 2011] and the transmon state is read out through a standard microwave input/output chain by detecting the amplitude and phase of a signal reflected from the input of the cavity. During the six months since the experiments reported in Ref. Serniak et al. 2018, the device was stored in air at room temperature. In this time, the Al-AlOx-Al Josephson junction "aged" [Pop et al. 2012], decreasing E_J such that $E_J/E_C = 23 \rightarrow 17$ and $\overline{f_{01}} = 4.4004\,\text{GHz} \rightarrow 3.7837\,\text{GHz}$. Here, $\overline{f_{01}} = |f_{01}^{ee}(n_g) + f_{01}^{oo}(n_g)|/2$ for any value of n_g, and is also the time-average of both f_{01}^{ee} and f_{01}^{oo} assuming ergodic fluctuations of n_g. This shift produced a corresponding change of the maximum charge dispersion of the 0-1 transition $\delta f_{01}(0) = 1.6\,\text{MHz} \rightarrow 6.3\,\text{MHz}$. Crucially for our experiment, the charge dispersion of higher-excited states ($i \geq 2$) is greatly increased such that there is significant variation of the OCS transmon-resonator mode dispersive shift with n_g. The microwave lines and filters [Fig. 4.8] are similar to those shown in the Supplemental Material of Ref. [Serniak et al. 2018]. There are a few differences, namely an additional Al shield surrounding the sample and improved microwave low-pass filtering on the input/output line inside of this shield. We attribute an observed reduction of x_{QP} to the latter, which will be discussed later.

6.2.2 Charge-parity dependent dispersive shifts

Our experiment utilizes a charge-parity dependent dispersive shift $\chi_{i,p}$ (also called the Lamb shift) of an ancillary readout mode due to the OCS transmon occupying state $|i,p\rangle$, where i denotes the plasmon level and p, the charge parity.

As presented in Section 4.2 and Ref. Manucharyan 2012, $\chi_{i,p}$ can be written as

$$\chi_{i,p} = g^2 \sum_{j \neq i} \frac{2\omega_{ij}^{pp} \left| \langle j, p|\hat{n}|i, p\rangle \right|^2}{(\omega_{ij}^{pp})^2 - \omega_r^2}. \tag{6.12}$$

Here $\langle j, p|\hat{n}|i, p\rangle$ are transition matrix elements of the charge operator in the energy eigenbasis, and ω_{ij}^{pp} are charge parity conserving transition frequencies. We calculate these quantities by numerical diagonalization in the charge ($\hat{n}$) basis, as shown in Fig. 6.11. It is worth noting that the dominant matrix elements are relatively insensitive to n_g. It is only necessary to consider transitions out of the two lowest-energy transmon eigenstates because the steady-state thermal population of higher levels can be neglected in the regime where $hf_{01} \gg k_B T$. For visual clarity, we plot only the transitions belonging to the "odd" charge-parity manifold; the "even" transition frequencies and matrix elements are mirror symmetric about the degeneracy point $n_g = 0.25$.

The parameters chosen for Fig. 6.11 reflect the experimental device that will be discussed in the next sections: $E_J/h = 6.14\,\text{GHz}$, $E_C/h = 356\,\text{MHz}$, and readout mode frequency $f_r = \omega_r/2\pi \approx 9.202$ GHz. Notice that, in this parameter regime, $f_{03}^{oo}(n_g)$ comes close to the bare readout frequency at $n_g = 0$, and that $f_{14}^{oo}(n_g)$ crosses the resonator mode frequency near $n_g = 0.1$. These lead to substantial changes of the dispersive shifts of the readout resonator as a function of n_g. Given a readout mode frequency f_r in the typical range of cQED systems, only modest tuning of E_J and E_C is required to observe the dispersive effects discussed above, as long as the ratio E_J/E_C is sufficiently low. Fig. 6.12 shows the magnitude of these dispersive shifts as a function of n_g calculated with the above parameters with the addition of the vacuum-Rabi splitting $g/2\pi = 40\,\text{MHz}$, which we estimate from our data.

6.2.3 Frequency-dependent phase response

We performed microwave reflectometry of the single-port readout resonator in the overcoupled regime, in which energy loss through the input/output port is stronger than loss to internal degrees of freedom. In this regime, the reflection coefficient is characterized by a full 2π phase roll as a function of frequency with

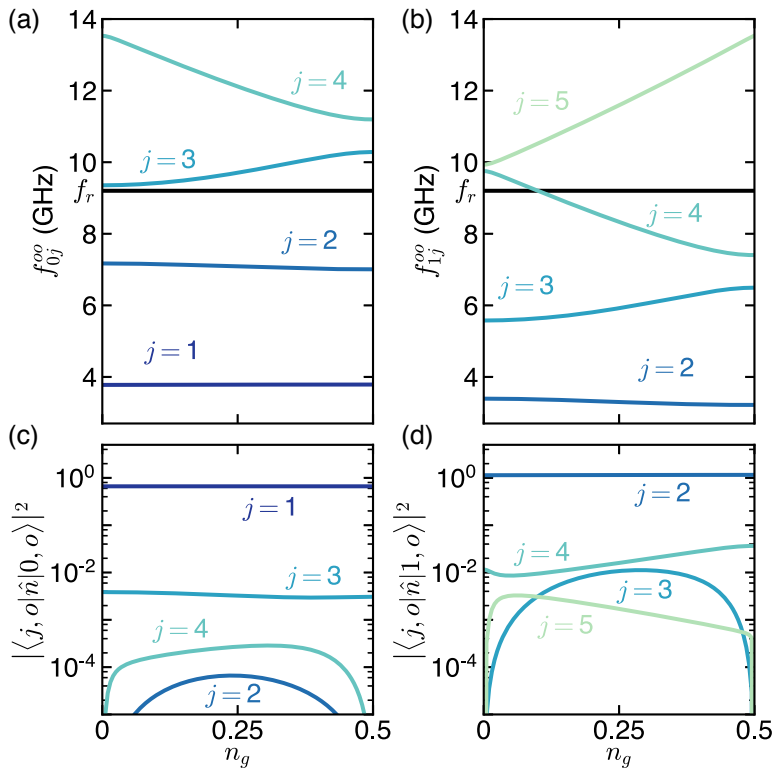

Figure 6.11 | Theoretically calculated OCS transmon-resonator spectrum as a function of n_g. Plasmon transition frequencies out of the ground state (a) and first-excited state (b) of an OCS transmon with $E_J/E_C = 17$ with odd charge parity. In this parameter regime, the detuning between f_{03}^{oo} and the resonator frequency f_r varies by a factor of ≈ 8 as a function of the parameter n_g. Additionally, f_{14}^{oo} crosses f_r near $n_g = 0.1$. Matrix elements of the transmon charge operator for transitions out of the ground (c) and first excited (d) states with "odd" charge parity. These matrix elements are finite and relevant for calculating the transmon-resonator dispersive shifts in our devices. In the transmon limit of large E_J/E_C, matrix elements between non-nearest-neighbor states will be suppressed.

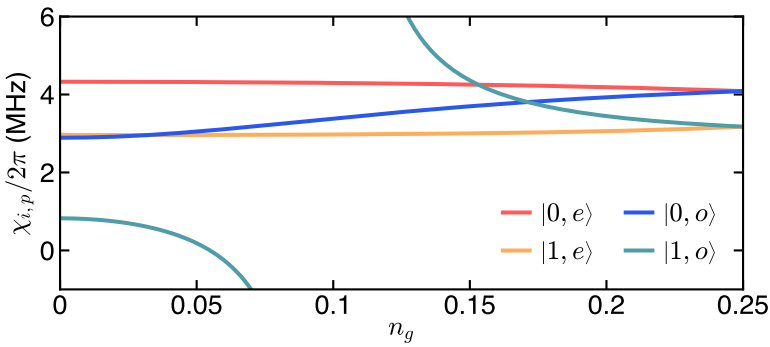

Figure 6.12 | Theoretically calculated charge-parity-dependent dispersive shifts of the readout mode frequency due to the OCS transmon occupying state $|i,p\rangle$. Parameters chosen for this simulation are those described in the text.

no amplitude response:

$$S_{11}^{i,p}(\omega) = \frac{\omega - \left[\omega_r + \chi_{i,p}(n_g)\right] + i\kappa/2}{\omega - \left[\omega_r + \chi_{i,p}(n_g)\right] - i\kappa/2}. \tag{6.13}$$

Here, $S_{11}^{i,p}(\omega)$ is the frequency-dependent reflection coefficient, and the measured phase is given by $\mathrm{Arg}[S_{11}^{i,p}(\omega_{\mathrm{ro}})]$. The bare resonator mode, without coupling to the transmon, is characterized by frequency $\omega_r/2\pi$ and linewidth κ We resolve this in Fig. 6.13, where we plot histograms of the measured reflected phase as a function of readout probe frequency, with and without a pulse preceeding each measurement to scramble the plasmon state between 0 and 1. We observe the expected 2π phase roll for each joint qubit and charge-parity state, which allows for the straightforward extraction of $\chi_{i,p}(n_g)$. The quoted values of n_g in each row are obtained by comparison to the data in Fig. 6.14(c). Though there is good agreement with the frequency dependent predictions of Eq. 6.13, impedance mismatches within our room-temperature RF-interferometry setup skew these curves. This contributes a weak background electrical delay to the measured curves. Operating with a single frequency (as we did for the measurements presented in the main text) avoids this complication. This technique is particularly convenient for directly observing the charge-parity-dependent dispersive shifts $\chi_{i,p}(n_g)/2\pi$ of the readout mode frequency due to the transmon occupying state $|i,p\rangle$ [Fig. 6.12].

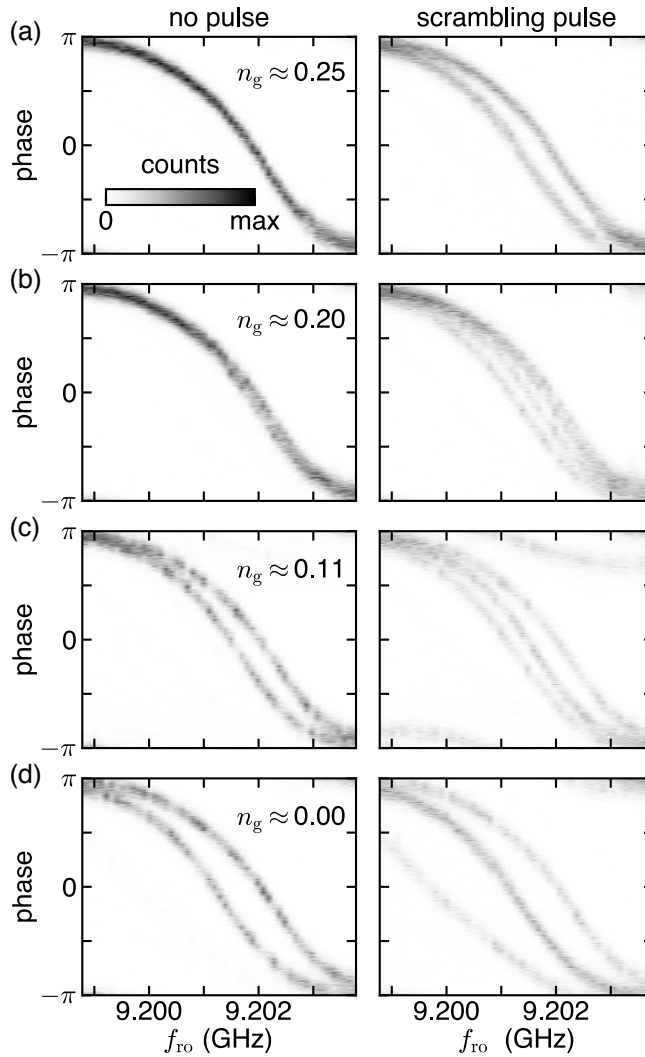

Figure 6.13 | OCS transmon plasmon- and charge-parity-state dependent readout resonator response. (a-d) Histograms of phase of the signal reflected by the readout resonator as a function of probe frequency at different instances of n_g. The right (left) column is the response with (without) a state-scrambling pulse.

6.2.4 Measurement protocol

Figs. 6.14, 6.15, and 6.16 describe the main experimental result of this section: the direct-dispersive measurement of the joint plasmon and charge-parity state

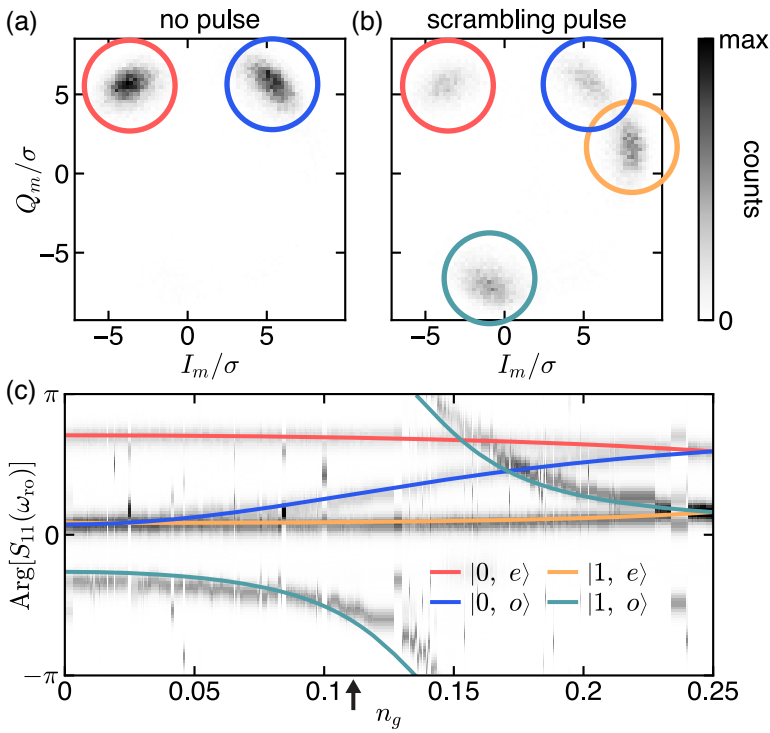

Figure 6.14 | Direct dispersive readout of the joint plasmon and charge-parity state of an OCS transmon. (a) Histogram in the complex plane of 2×10^4 sequential shots separated by 200 μs and integrated for 4.16 μs, normalized by σ, the standard deviation of the measurement distributions obtained by projecting onto the I_m axis and fitting to a sum of two Gaussian functions [Fig. 4(a)]. Measurements circled in red (blue) are assigned to denote the state $|0, e\rangle$ ($|0, o\rangle$). (b) Histogram obtained under the same conditions as in (a), but with a pulse applied before each measurement to scramble the qubit state. Measurements circled in yellow (green) are assigned to denote the state $|1, e\rangle$ ($|1, o\rangle$). (c) Histograms of the phase of the readout signal sorted by n_g. The histograms in (a) and (b) correspond to the data marked by the black arrow at $n_g = 0.11$.

of an OCS transmon. Due to the charge dispersion of the OCS transmon energy levels, the dispersive shift of the readout mode will vary in time as n_g drifts. At values of n_g away from the degeneracy point $n_g(\text{mod } 1/2) = 1/4$, the dispersive shifts corresponding to even- and odd-charge-parity will be distinguishable. With the aid of a quantum-limited Josephson parametric converter [Bergeal et al. 2010], the microwave readout signal was amplified such that the state of the OCS transmon could be detected with high fidelity in a single shot. For the measurements presented in the next few sections, we probed the readout resonator at $f_{\text{ro}} = 9.20178$ GHz with an integration time per shot of 4.16 μs. The average number of photons occupying the readout mode during measurement was ≈ 10. We characterized this readout scheme as a function of time and measured the timescales associated with n_g drifts and charge-parity fluctuations. This simple experiment was composed of three steps:

1. A Ramsey interference experiment was performed to determine the instantaneous n_g. Specifically, we measured $\delta f_{01}(n_g) = \delta f_{01}(0)\cos(2\pi n_g)$, the detuning of f_{01}^{ee} from $\overline{f_{01}}$ [Fig. 6.2].

2. We acquired 2×10^4 high-fidelity dispersive-measurement shots which determine the state of the transmon at a repetition rate of 5 kHz.

3. We repeated step 2, but with each shot preceded by a pulse with carrier frequency $\overline{f_{01}}$ to "scramble" the transmon state, transferring some population from $|0, p\rangle$ to $|1, p\rangle$.

This protocol was repeated 500 times, once every 40 s. Pulses addressing the transmon had a Gaussian envelope with a carrier frequency $\overline{f_{01}}$, which was equally detuned from f_{01}^{oo} and f_{01}^{ee} at all values of n_g so as to be charge-parity insensitive. The width of this Gaussian envelope was chosen to be 20 ns to avoid driving the 1-2 transition. We refer to these as "scrambling" pulses because they produced inefficient rotation of the qubit due to the large charge dispersion $\delta f_{01}(n_g)$. We note that due to symmetry of the transition spectrum about $n_g = 0$ and the degeneracy point $n_g = 0.25$, the Ramsey measurement maps all values of n_g into the "half-Brillouin zone" $[0, 1/4] \subset \mathbb{R}$. Thus, we will restrict our discussion of n_g to that range. Below we will describe the outcome of this three-step experiment, emphasizing separate but related results.

6.2.5 Single-shot readout of charge-parity

Fig. 6.14(a) shows an example histogram of 2×10^4 measurement shots (step 2 of the experiment), where two equally weighted distributions are visible (a histogram of the data projected onto the I_m-axis is plotted in Fig. 6.15(b)). The shots in the histogram of Fig. 6.14(b) were obtained after applying a scrambling pulse to the qubit (step 3), resulting in four visible distributions. Prior to acquiring these two histograms, a Ramsey measurement (step 1) was performed to determine that $n_g = 0.11$. Each instance of this protocol gave us the readout signal in equilibrium and with scrambled qubit population as a function of n_g as it varied in time. Fig. 6.14(c) shows histograms of the phase of the readout signal (step 3) sorted by n_g as determined from step 1. The solid lines denote the expected phase for each $\chi_{i,p}$, according to the theory presented earlier and assuming a perfectly reflected signal from an overcoupled resonator [Eq. 6.13] For our calculation, we fixed $\omega_r/2\pi = 9.1979$ GHz to match the cavity frequency measured at high probe power (≈ 1 nW at the input of the cavity), beyond the point at which the transmon and readout modes have decoupled [Reed et al. 2010; Verney et al. 2019]. In our device, the readout mode linewidth $\kappa/2\pi = 2.5$ MHz. The dispersive shifts $\chi_{i,p}(n_g)$ are computed from Eq. 3, where $g/2\pi = 40$ MHz was chosen to match the data. The charge matrix elements and transition frequencies ω_{ij}^{pp} were obtained from numerical simulation [Fig. 6.11]. This analysis allows us to confidently assign a joint plasmon and charge-parity state to each distribution in the measurement histogram when $|n_g| \lesssim 0.22$ ($\sim 90\%$ of the range). The calculated values of $\chi_{i,p}(n_g)$ are shown in in Fig. 6.12.

Our use of second-order perturbation theory [Eq. 6.12] is justified by numerical simulations, which show that the perturbation of the OCS-transmon eigenstates due to the coupling to the readout mode is small over the majority of the $\hat{n}$ range when the number of photons in the readout mode is $\lesssim 10$. The wavefunction overlap between the coupled and uncoupled transmon is $> 95\%$, except in the range $0.125 \leq n_g \leq 0.126$ for the ground state, and when $0.032 \leq n_g \leq 0.034$ or $0.091 \leq n_g \leq 0.109$ for the excited state. For example, this approximation breaks down when f_{14}^{oo} crosses the bare readout frequency and a more sophisticated theory would need to be employed [Zhu et al. 2013]. We can thus use simple dispersive readout to probe charge-parity correlations over the majority of n_g configurations, and in the next section we will consider the equilibrium case [Fig. 6.14(a)] where transitions between $|0, e\rangle$ and $|0, o\rangle$ di-

rectly measure charge-parity switches.

6.2.6 Charge-parity dynamics

In contrast to previous works studying QP dynamics that required coherent operations to map the charge parity of an OCS transmon onto its plasmon eigenstate [Ristè et al. 2013; Serniak et al. 2018], here we use our direct readout scheme to track the charge-parity as a function of time. In Step 2 of the experiment described above, we measured the OCS transmon state as a function of time with readout parameters that discriminated between the states $|0,e\rangle$ and $|0,o\rangle$ (a portion of which is shown in Fig. 4(a)) and applied a single-threshold (black dashed line) state assignment (red and blue denote $|0,e\rangle$ and $|0,o\rangle$, respectively) of the charge parity. This threshold was determined by fitting the distribution of measurement outcomes projected onto the I_m-axis to a sum of two Gaussian distributions and taking the midpoint [Fig. 3(b)]. Here we ignore the residual excited-state population $\mathcal{P}_1^{\text{eq}} = 0.014 \pm 0.002$, corresponding to an effective temperature of ~ 40 mK, which is close to the base temperature of our cryostat (≈ 20 mK).

Having measured the charge parity $P(t)$ of the transmon as a function of time and assuming stationarity and ergodicity, we can compute by a sliding average the charge-parity autocorrelation function

$$\langle P(0)P(\tau)\rangle = \mathcal{F}^2 e^{-2\tau/T_P}. \tag{6.14}$$

For consistency with previous literature, we have defined the charge-parity lifetime T_P as the characteristic time *between charge-parity switches*. This is a factor of two larger than the timescale for the decay of charge-parity correlations, which is due to equal even-odd and odd-even switching rates. In this instance where $n_g = 0.11$, the fidelity of the charge-parity measurement $\mathcal{F} \approx 0.99$, though this varies with n_g as the two measurement distributions become indistinguishable when n_g approaches the degeneracy point $n_g = 0.25$. An exponential fit of $\langle P(0)P(\tau)\rangle$ [Fig. 6.15(c)] yields $T_P \approx 6$ ms, almost an order of magnitude greater than previously reported in Ref. Ristè et al. 2013 and almost two orders of magnitude greater than in our previous report Ref. Serniak et al. 2018.

We attribute this improvement of T_P to additional high-frequency filtering on the input/output line connected to our OCS transmon-cavity system. The added filter is a 1 cm-long coaxial line filled with Eccosorb CR-110 high-frequency ab-

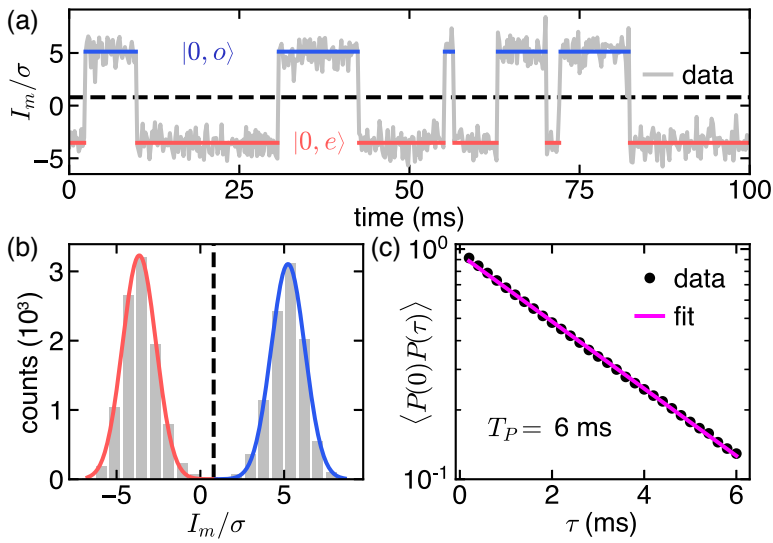

Figure 6.15 | Charge-parity jumps in an OCS transmon. (a) Snapshot of a ~ 4 s time trace from the same data as in Fig. 3(a) projected onto the I_m axis (grey). Charge-parity assignments (red and blue) within the ground-state manifold are obtained with a single threshold at the black-dashed line. (b) Histogram of all of the measurements from Fig. 6.14(a) fit to a sum of two Gaussian distributions, where the colors denote charge-parity assignment. (c) Charge-parity autocorrelation function $\langle P(0)P(\tau)\rangle$ computed from the time trace partially shown in (a) with an exponential fit.

sorber [Halpern et al. 1986], designed to present an impedance of $50\,\Omega$ in the range $2-10$ GHz [Pop et al. 2014]. Empirically, placing the filter inside of the sample shielding [Chapter 7] is crucial to reducing QP-generating radiation at energies greater than 2Δ, the pair-breaking energy. Further studies to understand this effect and the source of high-frequency, QP-generating radiation are ongoing. This observation suggests that high-frequency photons are somehow infiltrating the RF lines of our setup. The improvement of the filtering when placed within the sample shielding could imply one of two things. First: microwave connectors are leaky at > 100 GHz, and these photons are entering the lines near the sample, or second: the Eccosorb absorber performs better in smaller ambient magnetic field.

6.2.7 Time dependence of T_P

The three step experiment was repeated 500 times, the results of which are summarized in Fig. 6.16. Ramsey experiments (step 1) [Fig. 6.16(a)] determined n_g as a function of time. Fig. 6.16(b) shows histograms of the phase of the readout signal as a function of time, where the overlaid dotted state assignments come from our previous analysis of $\chi_{i,p}(n_g)$ using the measured values of n_g in Fig. 5(a). We compute $\langle P(0)P(\tau)\rangle$ at each of these times [Fig. 6.16(c)], except in the range $0.22 \lesssim n_g \leq 0.25$ where the readout distributions corresponding to states $|0,e\rangle$ and $|0,o\rangle$ are indistinguishable. We find an average $\overline{T_P} = 5.6$ ms with standard deviation 0.8 ms.

Nonequilibrium QP tunneling will result in a T_P proportional to $1/x_{\mathrm{QP}}$. Comparing to the results in Ref. [Ristè et al. 2013] and [Serniak et al. 2018] (in which both T_P and x_{QP} are reported), we estimate that the effective residual QP density $x_{\mathrm{QP}} \sim 10^{-9}$ in this device [6], which to the best of our knowledge is the lowest reported value for similar devices. We find no discernible correlation in T_P as a function of time, though in this experiment we are only sensitive on the minute timescale. This sampling rate is limited by the interleaved Ramsey experiment

[6] Although it is not critical for the analysis presented here, it is worth noting that the definition of T_P, chosen for clarity and convenience, varies slightly from that in the previous sections and references Ristè et al. 2013 and Serniak et al. 2018. This stems from the fact that the rate of charge-parity switches depends on the plasmon state of the OCS transmon. The timescale reported here is dominated by the rate of transitions between $|0,o\rangle$ and $|0,e\rangle$ (equivalent to Γ_{00}^{eo}), whereas the previously reported $1/T_P$ is effectively the average of this and the rate between $|1,o\rangle$ and $|1,e\rangle$. Conveniently, if one assumes that the branching ratio of charge-parity transitions is kept fixed, this produces only a small deviation in the assumed x_{QP}.

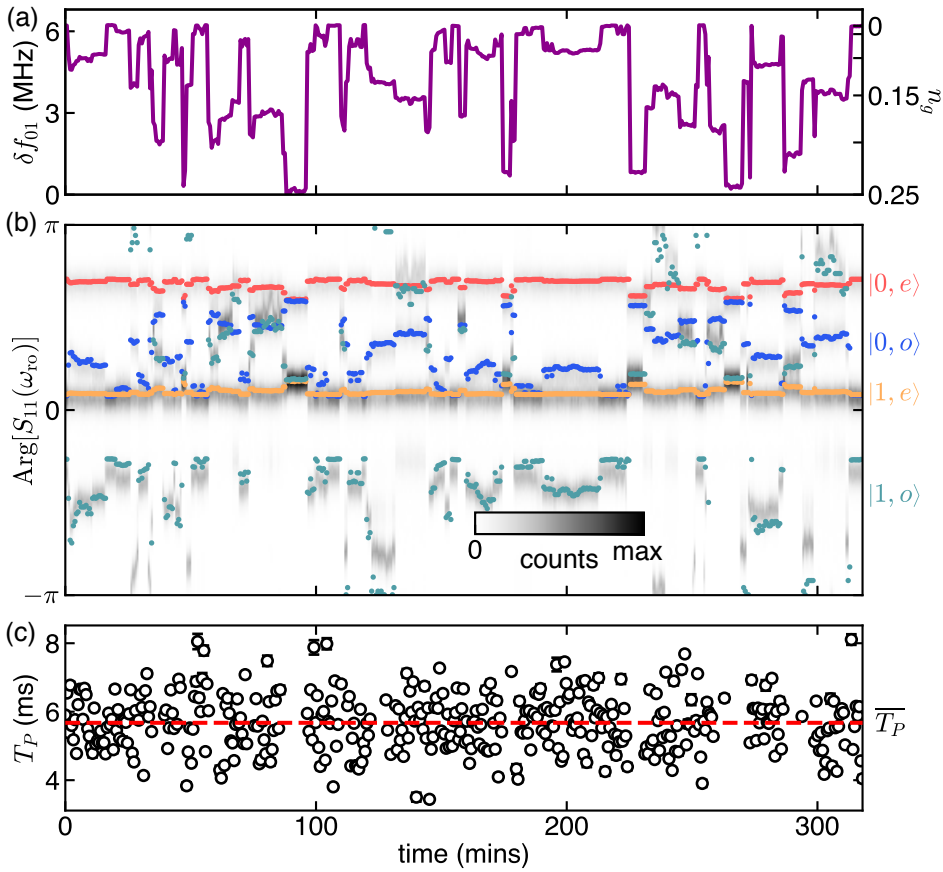

Figure 6.16 | Simultaneous detection of slow and fast charge dynamics. (a) Slow drift of n_g probed via a Ramsey experiment [Fig. 6.2]. The frequency of Ramsey oscillations δf_{01} is the shift of the qubit transition frequency from its average value $\overline{f_{01}}$. The right axis converts δf_{01} to n_g. (b) Histograms of the phase of repeated dispersive measurements after a state-scrambling pulse [Fig. 6.14(b)] as a function of time. Each instance contains 2×10^4 measurement shots acquired immediately after the Ramsey experiment described in (a). Colored dots correspond to the predicted phases of each joint plasmon and charge-parity state (labeled on the right) using the theory from the main text, assuming an overcoupled readout resonator. (c) Charge-parity lifetime T_P obtained from the decay of $\langle P(0)P(\tau)\rangle$ as a function of time.

(step 1) and could trivially be increased to ≈ 1 Hz, at which point more information could be extracted about the spectrum of QP density fluctuations [Grünhaupt et al. 2018]. There is also no dependence of T_P on n_g, which is not surprising since $\delta\epsilon_0/k_B \ll 20$ mK, the base temperature of our dilution refrigerator.

6.2.8 Qubit relaxation and excitation

As a further characterization of the sample, we performed standard T_1 measurements by applying a scrambling pulse to the qubit and measuring the time it takes for the qubit to thermalize to its equilibrium population distribution in free decay [Fig. 6.17]. We find that the average $\overline{T_1} \approx 207$ μs, but fluctuates in time with a standard deviation of 42 μs. At all times, the population decay is well described by a single exponential [Fig. 6.17(c)].

These results support those in Ref. [Serniak et al. 2018], which claim that the T_1 of this exact device was previously limited to a significant extent by QP processes

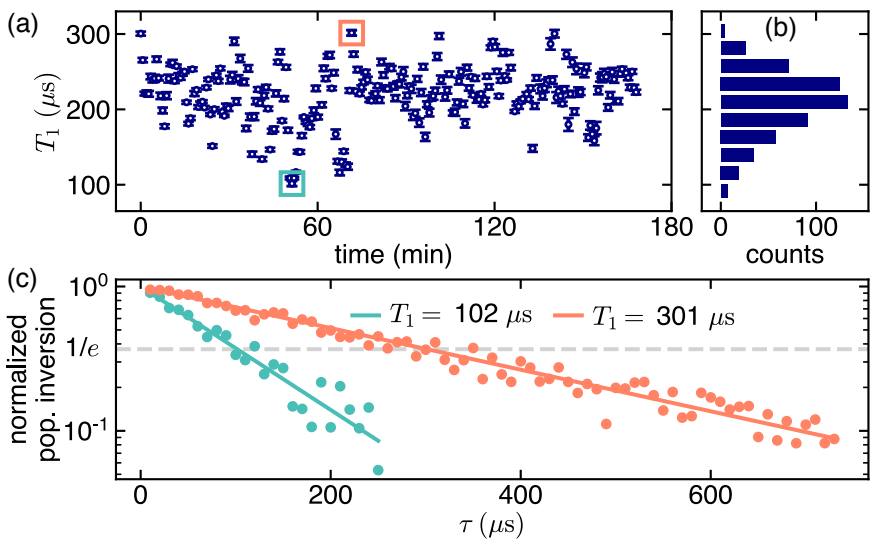

Figure 6.17 | Fluctuations of OCS transmon energy relaxation time. (a) Relaxation time T_1 of the OCS transmon device sampled every $\sim$ 40 s. (b) Histogram of all T_1 measurements (including others not shown in (a)), where the average $\overline{T_1} = 207$ μs. (c) Data and fits from the two extremal T_1 measurements in (a), marked with green and orange boxes.

that change the charge parity. In that report, we predicted that if this type of dissipation were to be reduced to a negligible level then the transmon would have a residual dielectric quality factor of $\sim 4.9 \times 10^6$ and the equilibrium thermal population of the qubit would be drastically decreased. Here, with improved RF filtering to reduce QP generation, the measured $\overline{T_1}$ and $\overline{f_{01}}$ correspond to a total qubit quality factor of 5.0×10^6, extremely close to the predicted "non-QP" limit. Suprisingly, we found in Ref. Serniak et al. 2018 that QP-induced excitation events were the dominant source of residual excited-state population of our OCS transmon. We see now that with lower QP density the qubit effective temperature is ~ 40 mK, compared to ~ 160 mK previously. These observations indicate that the device was limited in this experiment by dielectric loss.[7] The large fluctuations observed in the measured T_1 as a function of time are therefore not due to a fluctuating QP density, but instead to a time dependent coupling to lossy dielectric channels. Although the source of QP-generating radiation is still unknown, the efficacy of increased filtering at these high frequencies ($\gtrsim 100$ GHz for our Al-based devices) to reduce QP-induced dissipation is clear.

6.2.9 Discussion and conclusions

We have demonstrated a powerful application of OCS-transmon devices through dispersive monitoring of the dynamics of nonequilibrium QPs, which can impair the performance of superconducting quantum circuits. This technique can be used to extract the rates of all QP-induced qubit transitions as in Refs. Ristè et al. 2013 and Serniak et al. 2018. Additionally, by implementing hidden Markov analysis [Vool et al. 2014; Hays et al. 2018], this can be done with good precision even when the readout SNR is < 1. Again, we stress that the QP-tunneling rates observed in OCS transmons will be similar to those in traditional high E_J/E_C transmons by factors of order unity [See Chapter 5].

The observed charge-parity-dependent dispersive shifts of our readout resonator agree well with our simple application of quantum circuit theory [Vool and Devoret 2017] with the Cooper-pair-box Hamiltonian. This strong agreement further supports the idea that the Cooper-pair-box circuit can be used as a testbed for the physics of novel quantum circuit elements. Of particular in-

[7] This was later confirmed by qubit-state-conditioned charge-parity autocorrelation measurements similar in theory to those described in the previous sections, but performed with the direct dispersive technique presented here.

terest are Josephson junctions made from proximity-coupled semiconductors with large spin-orbit coupling and Landé g-factor, which may play host to Majorana fermions when tuned with applied magnetic field into the topological regime [Lutchyn, Sau, and Das Sarma 2010; Oreg, Refael, and Oppen 2010]. Proposals suggest embedding these junctions into magnetic-field compatible OCS transmon circuits to look for signatures of this phase transition in spectroscopy experiments [Ginossar and Grosfeld 2014; Yavilberg, Ginossar, and Grosfeld 2015]. These can be observed as changes in transition frequencies or the brightness of certain transitions as a function of n_g. In light of our experiments, these features can also be observed in n_g-dependent dispersive shifts which are influenced by both the transition frequencies and charge-matrix elements.

Additionally, since there is a one-to-one correspondence between the reflected phase indicating $|0, o\rangle$ and n_g, one could use an OCS transmon and the techniques described above as a fast charge sensor with the charge-parity lifetime acting as an upper bound on integration time. We find the unoptimized charge sensitivity of our OCS-transmon device near $n_g = 0.11$ to be $\approx 4.4 \times 10^{-4}$ e/$\sqrt{\text{Hz}}$, which does not change appreciably over the majority of the n_g range. While the RF-SET has better sensitivity to charge fluctuations [Aassime et al. 2001], the OCS transmon may prove useful for wireless charge sensing with minimal measurement backaction. Furthermore, our work frames the idea of the "quantum-capacitance detector" [Shaw et al. 2009; Bueno et al. 2010; Stone et al. 2012; Echternach et al. 2018] in the language of cQED and OCS transmons with symmetric superconducting islands, which may have applications for astronomical detectors.

In conclusion, we have achieved direct, dispersive readout of the joint plasmon and charge-parity states of an OCS transmon, i.e. without performing any coherent operations on the qubit. We have demonstrated that, with improved RF filtering, the charge-parity lifetime of typical 3D transmons can be extended to many milliseconds. This has also extended the T_1 of our OCS transmon to ≈ 210 μs. Having reduced the effect of nonequilibrium QPs on qubit performance to a negligible level, this provides a clear experimental foundation for further attempts to mitigate other mechanisms of dissipation in superconducting qubits, such as surface dielectric loss [Wang et al. 2015; Dunsworth et al. 2017; Calusine et al. 2018]. This will be discussed further in the next chapter.

7

Reducing QP Density

Nonequilibrium QPs [Aumentado et al. 2004] are a detriment to a variety of superconducting devices, including high-quality-factor superconducting resonators [Barends et al. 2011; Nsanzineza and Plourde 2014; Visser et al. 2014b], JJ based superconducting qubits [Lutchyn, Glazman, and Larkin 2005; Shaw et al. 2008; Martinis, Ansmann, and Aumentado 2009; Lenander et al. 2011; Catelani et al. 2011; Córcoles et al. 2011; Sun et al. 2012; Wenner et al. 2013; Ristè et al. 2013; Pop et al. 2014; Vool et al. 2014; Bal et al. 2015; Riwar et al. 2016; Grünhaupt et al. 2018; Serniak et al. 2018; Serniak et al. 2019], kinetic-inductance [Day et al. 2003; Monfardini et al. 2012; Grünhaupt et al. 2018] and quantum-capacitance [Shaw et al. 2009; Bueno et al. 2010; Stone et al. 2012; Echternach et al. 2018] detectors, devices for current metrology [Pekola et al. 2008], Andreev qubits [Olivares et al. 2014; Janvier et al. 2015; Hays et al. 2018], and proposed Majorana qubits [Higginbotham et al. 2015; Albrecht et al. 2017]. It is therefore a worthwhile endeavor to understand them, and an important technical challenge to rid our superconducting devices of them.

Though the precise source of nonequilibrium QPs in galvanically isolated superconducting devices at dilution refrigerator temperatures ($T \sim 20$mK) is not well known, it is understood that they can be generated by radiation at frequencies $> 2\Delta/h$, where Δ is the superconducting energy gap. This radiation could be from nonequilibrium photons or phonons in the environment that couple to the superconducting condensate. When this occurs, a *pair* of QPs are produced in order to preserve fermion parity. As discussed in Chapter 5, QPs couple to the dynamical phase of superconducting circuits, making them most dangerous when they reside in high-impedance regions of a device.

Various techniques have been implemented to reduce the effects of QPs on superconducting devices, and they can be sorted into two main categories: techniques that reduce the number of QPs that are generated, and techniques that make devices less sensitive to QPs that are already present. The former takes advantage of cryogenic expertise in order to properly thermalize the noise inherent to the measurement apparatus to the base experimental temperature, which should be $\ll 2\Delta/k_B$. In principle this can be done, but it is difficult, if not impossible, to completely isolate the measurement setup from the rest of the

world. For example, we do our best to protect our superconducting qubits from any and all unintended radiation, however, stray photons at the readout frequency ($\sim$ 5 GHz) are often the leading mechanism of dephasing [Sears et al. 2012; Wang et al. 2019], and high frequency radiation of some sort can leak in, generating QPs [Córcoles et al. 2011; Barends et al. 2011; Houzet et al. 2019]. Both Córcoles et al. 2011 and Barends et al. 2011 demonstrated improved performance of devices when shielded from external radiation, and instituted a standard of including light-tight[1] radiation shields and infrared absorbing coatings around our samples. Along this direction, we have demonstrated that further high-frequency filtering of our *RF lines* can greatly reduce QP-induced dissipation [Serniak et al. 2019]. In the next section, we will describe in more detail our experimental results.

There are a handful of techniques used to reduce the effects of QPs already occupying the device. Recently, an active approach was taken by Gustavsson et al. 2016, in which they were able to "pump" QPs out of the small islands of a flux qubit. This relied on preparing the qubit in its excited state, which allows the qubit to impart some energy to the QPs during QP-induced relaxation events, which speed-up QP diffusion away from the JJs.[2] This technique is useful for devices with small superconducting islands, but not particularly helpful for traditional transmon qubits that have large JJ electrodes where fast QP diffusion ensures that the QP density is relatively homogeneous. Another elegant way to reduce the effects of nonequilibrium QPs is to engineer the qubit circuit such that there is an intrinsic protection against QP-induced dissipation. The most common example of this is the fluxonium qubit [Manucharyan et al. 2009], which has intrinsic protection against QP-induced dissipation when flux-biased to $\Phi_0/2$ due to coherent destructive interference of electron-like and hole-like QP tunneling trajectories [Pop et al. 2014]. Similar suppression can occur in flux qubits [Catelani et al. 2011].

The most common approach to negating the effects of preexisting QPs is by attempting to locally suppress the QP density near the JJs of a circuit using gap-engineered QP traps. This is possible by engineering regions of lower superconducting gap in the device, such that when QPs diffuse to the trap region they may relax by phonon emission and be unable to diffuse back toward the JJs. This a

[1] or at least, *approximately* light tight at all frequencies up to some cutoff

[2] As discussed in Chapter 5, QPs are most detrimental when located near JJs in a qubit.

technique that been used extensively in superconducting photon detectors, electronic cryocoolers, and electrometers[3] to trap QPs in a particular region of the device. These traps could be Abrikosov vortices[4] induced in thin superconducting films, normal metal regions, or lower gap superconductors. Superconducting qubits and other coherent devices put limitations on these sort materials and techniques that can be used to trap QPs [Vion et al. 2002; Lang et al. 2003; Shaw et al. 2008; Sun et al. 2012; Wang et al. 2014; Nsanzineza and Plourde 2014; Vool et al. 2014; Riwar et al. 2016; Hosseinkhani et al. 2017]. For instance, *too many* vortices can lead to dissipation [Wang et al. 2014], and normal metal traps can support dissipative currents which can introduce unwanted loss if not carefully implemented [Riwar et al. 2016; Hosseinkhani et al. 2017; Riwar, Glazman, and Catelani 2018].

In an attempt to engineer QP traps compatible with high-coherence JJ-based qubits, we created regions of suppressed superconducting gap in transmon qubits via the proximity effect of a lower gap superconductor. This technique has the opportunity to achieve higher trapping efficiency by reducing the gap in the JJ electrode itself, as opposed to the trap only being accessible to QPs through a tunnel barrier. In short, we were able to proximitize our Al JJ electrodes with Ti (which has a critical temperature $T_c^{\mathrm{Ti}} \approx 400$ mK) that was selectively deposited away from the JJ using angled-evaporation technique. We saw mixed success, and our efforts will be described in Section 7.2.

7.1 Attenuating Cooper-pair-breaking radiation

Our experimental setups typically include coaxial cavity filters on RF lines leading to our qubits, which are potted with commercially available Eccosorb CR-110. This is a castable, magnetically loaded resin that acts as an absorber of high-frequency photons. At frequencies relevant for the readout and control of our qubits (lets say ≈ 8 GHz), its absorption coefficient is only about 2 dB/cm of filter

[3] of which there are many examples [Booth 1987; Kraus et al. 1989; Goldie et al. 1990; Booth et al. 1993; Mears, Labov, and Barfknecht 1993; Golubov et al. 1994; Irwin et al. 1995; Pekola et al. 2000; Segall et al. 2004; Court et al. 2008; MacLeod, Kafanov, and Pekola 2009; Peltonen et al. 2011; Rajauria et al. 2012; Saira et al. 2012; Nguyen et al. 2013; Maisi et al. 2013; van Woerkom, Geresdi, and Kouwenhoven 2015], and surely more that I've missed.

[4] Vortices support Caroli-de Gennes-Matricon states: subgap bound states [Caroli, de Gennes, and Matricon 1964] that can trap QPs [Wang et al. 2014; Taupin et al. 2016; Nsanzineza and Plourde 2014]. In high-carrier-density superconductors, these states appear as a quasi-continuum, hence why it's often said that vortices have a "normal core."

length. Conveniently, at frequencies greater than $2\Delta_{\mathrm{Al}}/h \approx 100$ GHz this increases to $\gtrsim 20$ dB/cm [Halpern et al. 1986], which should significantly attenuate Cooper-pair-breaking radiation. It's exactly for this reason that we include these filters on every RF input and output line connected to our samples.

After the experiments in Ref. Serniak et al. 2018, we were perplexed by two main observations. First, that the charge-parity lifetime T_P of our devices was measured to be an order of magnitude lower than measured in similar devices at Delft [Ristè et al. 2013], and second, that the excited state population of our OCS transmon was due to QP related events, and was very high, $> 20\%$! There had been some folklore in the lab about our Eccosorb filters, with some people claiming that putting them *near* the device was responsible for a lower excited state population (I certainly remember Zaki Leghtas and Steven Touzard reporting this around 2015). So we figured we would give this a try, to see if the reported effect had anything to do with QPs. Additionally, we mounted a new OCS transmon in a Cu 3D cavity instead of Al, to make our experiments closer in implementation to those in Delft. Over several cooldowns we studied the effect that the position of an *additional* Eccosorb filter had on T_P and $\mathcal{P}_0$, the equilibrium ground state population.

Fig. 7.1 shows the cryogenic microwave setup at the base-stage of our dilution refrigerator. Visible at the top of the figure are Eccosorb filters on each RF line, which were always present in our experiments and will remain fixed throughout the following discussion. The first cooldown was to characterize the new transmon with nearly the same experimental setup as in Ref. Serniak et al. 2018, the difference being that we replaced our Cryoperm magnetic shield with one that housed an accompanying Al shield inside. Also present was an unused input line that was 50-ohm terminated outside of this shield, and thermalized to the mixing chamber. This was here historically in case we found that we could not drive the qubit through the circulators out-of-band, but was ultimately unnecessary. For the sake of brevity in the following discussion, mostly qualitative changes in T_P will be quoted, however Fig. 7.2 displays T_P, $\mathcal{P}_0$, T_1, and $\overline{f_{01}}$ of the device on each independent cooldown. The initial cooldown was unsurprising: the addition of an Al shield within the cryoperm and the fact that we mounted our sample in a Cu cavity had no effect on T_P, and in fact it was slightly lower than previously measured.

For the second cooldown, we included additional Eccosorb filters on both

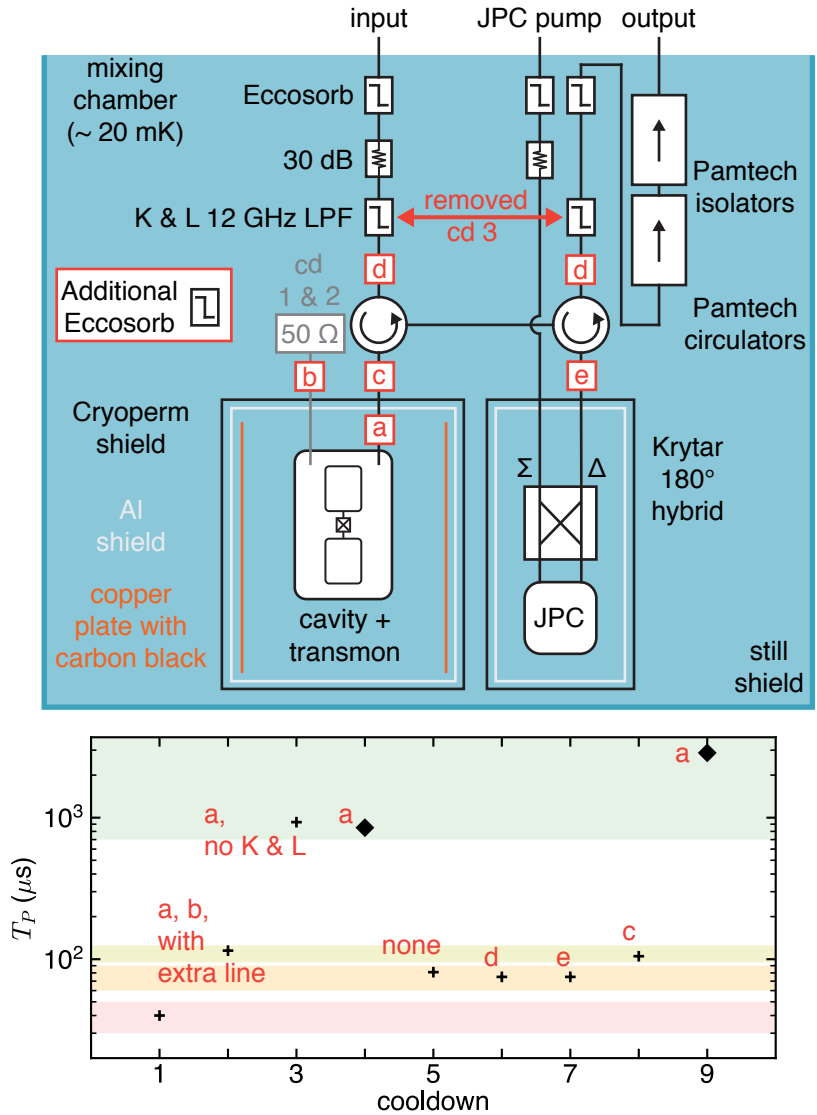

Figure 7.1 | Top: Cryogenic microwave setup used for tests of Eccosorb filter position, which are denoted with red labeled boxes. Bottom: Charge-parity lifetime T_P over many cooldowns varying the position of an additional Eccosorb filter. See text for details.

lines leading to the cavity, in positions "a" and "b" in Fig. 7.1. Note that position "a" is what we'll later call the "optimum" position of a single filter: its location being within our Cryoperm shield. On this cooldown we observed a factor of ~ 3 improvement in T_P, which was still significantly less than measured in Ref. Ristè et al. 2013. We suspected our K & L brand low pass filters may be poorly thermalized, as they are made from stainless steel and no strong precautions (such as a direct OFHC copper link) were taken to ensure they were in good thermal contact with the mixing chamber. On the next cooldown we removed them to see if maybe they were part of the issue, as well as removing the superfluous, unused input line. In doing so, we saw a significant improvement of T_P, up to the values reported at Delft. At this point we were both excited and terrified, as it suggested that either the K & L filters and/or the unnecessary extra input line were a significant contributor of QP-generating radiation. Luckily for us and for K & L, the next cooldown confirmed that their filters were not the culprit.[5] After reintroducing the K & L filters we found a similarly high T_P.

To check whether or not the superfluous input line was the source of high-frequency radiation, in cooldown 5 we chose not to put it back into our setup, but to remove the Eccosorb filter in position "a." Doing so reduced the T_P to what is, in hindsight, a very suspicious value that was approximately twice that of cooldown 1, in which both lines connected to the cavity with no additional Eccosorb filters. At this point we assumed that something in our setup wasn't thermalizing well, and so we placed an additional Eccosorb filter below the K & L filters on both the input and output lines (positions "d"). Here we saw no improvement of T_P. We then thought, well, what if it's the JPC or the microwave hybrid that accompanies it? Removing the filters from position "d" and inserting one at position "e" showed that this wasn't the issue. That left the circulators, which were firmly mounted to an OFHC Cu bracket which should be well-thermalized to the mixing chamber. To test these, the Eccosorb was moved from position "e" to position "c" in cooldown 8, which showed some modest improvement of T_P, at a value very close to that of cooldown 2. On the final cooldown we moved the filter back to the "optimum position" ("a") inside the Cryoperm shield and found a T_P of a few milliseconds, the highest we had measured up to that point in time.

That story is a lot to unpack, however it can be easily summarized by a few key observations, and assuming that T_P is proportional to the power incident on the

[5] At least not at this level of radiation.

qubit cavity system at frequencies $> 2\Delta/h$. First, it would appear that **each RF line connected to the qubit/cavity system without an additional Eccosorb filter contributed the same incident pair-breaking power**, since T_P of cooldown 5 was suspiciously about twice that of cooldown 1. Furthermore, we find that **it is crucial that we place the additional Eccosorb filter inside of our Cryoperm shield**, as evidenced by the fact that cooldowns 3, 4, and 9 produced the highest T_P, while cooldown 2 and cooldown 8 showed similarly low T_P (when the filter was *outside* the shield). Even though cooldown 2 had an Eccosorb filter placed in the optimum position "a," we believe that the incident power was dominated by the superfluous line with a filter occupying position "b."

Turning to Fig. 7.2, we see that there is clear correlation between T_P and $\mathcal{P}_0$, in support of the claims of all of the manuscripts written during this dissertation [Serniak et al. 2018; Serniak et al. 2019; Houzet et al. 2019]. In words, we showed that a QP-related process was the source of the residual excited state population in our devices, and by attenuating QP generating radiation with this filter we have improved both of these metrics. We also see that T_1 is also cor-

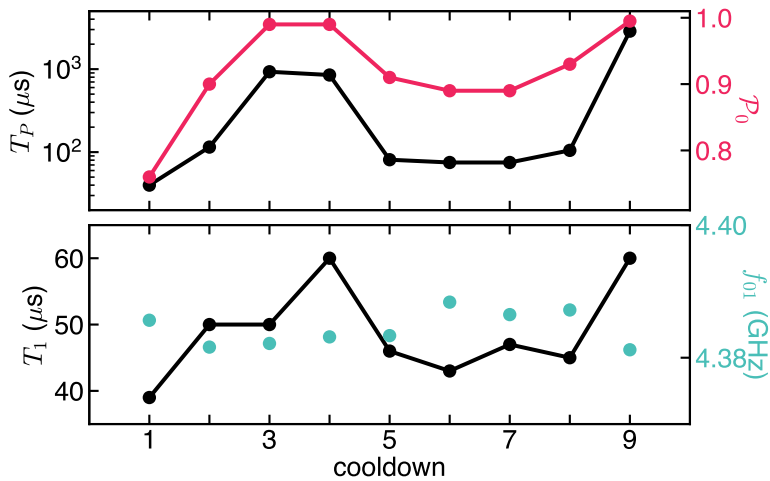

Figure 7.2 | Correlating charge-parity lifetime with other qubit metrics as a function of filter position. Data points connected as a guide for the eye to emphasize the correlation between curves. Top panel shows the charge-parity lifetime T_P and equilibrium ground state population $\mathcal{P}_0$. Lower panel shows the energy relaxation time T_1 and the offset-charge-averaged transmon transition frequency $\overline{f_{01}}$ [See Fig. 4.9].

related with T_P, indicating that our qubits are limited to a $T_1 \approx 2T_P$ [Serniak et al. 2018].[6] When T_P is long, the T_1 is limited by other mechanisms such as dielectric loss, as was shown in charge-parity correlation measurements on each of these cooldowns that are not presented here. It is also worth noting that the offset-charge-averaged transmon frequency $\overline{f_{01}} = f_{01}(n_g = 1/4)$ did not change appreciably over these cooldowns, which spanned approximately one-and-a-half months.

So what can we take away from this? At the time of this writing, more experiments are unfortunately needed to understand need for a shielded Eccosorb filter. Until we do so, however, it's not a bad idea to put an Eccosorb filter[7] within an approximately light-tight magnetic shield. Our observations could be explained by some combination of three effects:

1. Maybe, trivially, the Eccosorb filter is better thermalized to the mixing chamber when it is mounted within the Cryoperm shield. In position "a," the filter is bolted to a Cu bracket that contacts the mixing chamber plate (in actuality it is bolted to a gold-plated mezzanine that is itself bolted to the mixing chamber plate), whereas in position "c" it is thermalized to the mezzanine with an OFHC Cu braid.

2. It could be that the Eccosorb filter performs better in the lower ambient magnetic field afforded by the Cryoperm/Al shield combination. Eccosorb is a resin of suspended Fe particles, which could lead to magnetic-field-dependent absorption properties. Initial experiments suggest that this is indeed the case.

3. The pair-breaking radiation may be entering the lines somewhere between the filter in position "c," and the filter in position "a." The Cryoperm shield is approximately light-tight, as all the seams are sealed with Cu tape that has a conductive adhesive. If this is the case, it would suggest that the pair breaking radiation is infiltrating the superconducting RF line linking the filter at position "c" to the qubit/cavity. If this is the conclusion, the weakest link of this coaxial line is certainly the SMA connector attached to the sample-side of the filter.

[6] This is a scaling that we have observed in our experiments, however it depends crucially on the mechanism of charge-parity switching events, be it QP tunneling, PAT, or something else.

[7] or any filter proven to attenuate pair-breaking radiation

Experiments are currently underway the assess which, if any, of these propositions are the root cause of the observed effects.

7.2 Proximitized-superconducting QP traps

Prior to our work on OCS transmons, we began developing Ti-proximitized-Al QP traps with the goal of implementing them in the fluxonium qubit, which we suspected to be paritally limited by nonequilibrium QPs in its JJ-array superinductance [Vool et al. 2014]. Eventually, we settled on transmon qubits as the optimal testbed for these QP traps, due primarily to the simplicity of the circuit. The idea is simple, to reduce the superconducting gap *of the Al JJ electrodes*, and to do so *selectively* away from the JJ itself [Figs. 7.3 and 7.4]. We would do so using the proximity effect of a lower-gap superconductor, in our case Ti ($T_c^{\mathrm{Ti}} \approx 400$ mK). This sort of *proximitized-superconducting QP trap* would offer two advantages over tunnel-coupled normal-metal QP traps: increased trapping efficiency and less dissipation. By using the proximity effect one would create the QP traps within the JJ electrodes themselves, without relying on QP tunneling through an opaque barrier to become trapped. Importantly, the use of a lower-gap superconductor should ensure that there are no QP states below that lower gap. In the case of a normal metal, the proximity effect produces a nonzero density of states at the Fermi energy, which could result in excess *thermal* QPs in the trap, and could lead to additional dissipation.[8]

We fabricated our devices in a single step of electron-beam lithography. Selective deposition of Ti away from the JJ was achieved using simple angled-evaporation techniques, similar to those used in the "bridge-free technique" of JJ fabrication [Lecocq et al. 2011]. This relies on narrow constrictions in the electron-beam lithography pattern such that evaporations at high angle do not deposit metal on the substrate, but on the sidewalls of the resist in regions of the device where you *do not* want to deposit material. Ti was chosen as the lower-gap superconductor primarily out of convenience: we already had the crucible loaded in our evaporator, and it has a sort of Goldilocks $T_c^{\mathrm{Ti}} \approx 400$ mK that is much greater than the temperature of our experiments and significantly less than that of Al ($T_c^{\mathrm{Al}} \approx 1.3$ K).

[8] Although, this can be made very small by ensuring that the thickness of the normal metal layer is much less than the effective coherence length of the superconductor and the thickness of the superconducting layer [Gueron 1997].

Table 7.1 | Summary of Ti-proximitized-Al bilayers. Estimated imprecision on values of T_c' is ± 0.01 K for Al samples and proximitized bilayers. Estimated imprecision on values of T_c' for Ti layers is ± 0.03.

Sample	d_{Al} (nm)	d_{Ti} (nm)	T_c' (K)
I	15	-	1.44
II	20	-	1.37
III	35	-	1.32
IV	50	-	1.28
V	-	20	0.47
VI	-	40	0.58
VII	15	20	0.93
VIII	20	20	0.94
IX	35	20	1.03
X	50	20	1.03
XI	15	40	0.72
XII	20	40	0.85
XIII	35	40	0.88
XIV	50	40	0.94

The Ti-Al bilayer region can be characterized by a single proximitized superconducting gap Δ' in the limit that the interface transparency between the two films is near unity and each layer is much thinner than their effective coherence lengths. We accomplish this by depositing both layers without breaking vacuum. This can be modelled quantitatively using the Usadel theory as described in [Golubov et al. 1994; Gueron 1997; Martinis et al. 2000; Fominov and Feigel'man 2001; Brammertz et al. 2001; Brammertz et al. 2002; Zhao et al. 2018]. The proximitized gap depends on the relative carrier densities of the two films, the relative thickness compared to the effective coherence lengths in the two films, and the interface transparency. Qualitatively, the proximity effect can be thought of as arising from the Cooper-paired electrons "feeling" the superconducting pair potential of the neighboring layer. Another way of saying this is that the electronic pair correlations extend beyond the region with a given pair potential due to the delocalized nature of the electrons. We characterized the proximitized gap via the proximitized critical temperature T_c' of a variety of Al-Ti bilayers with varying thickness, as reported in Table 7.1, and plotted in Fig. 7.3(c).

These measurements were performed in a dilution refrigerator (with temperature control of the mixing-chamber stage) using standard lock-in techniques.

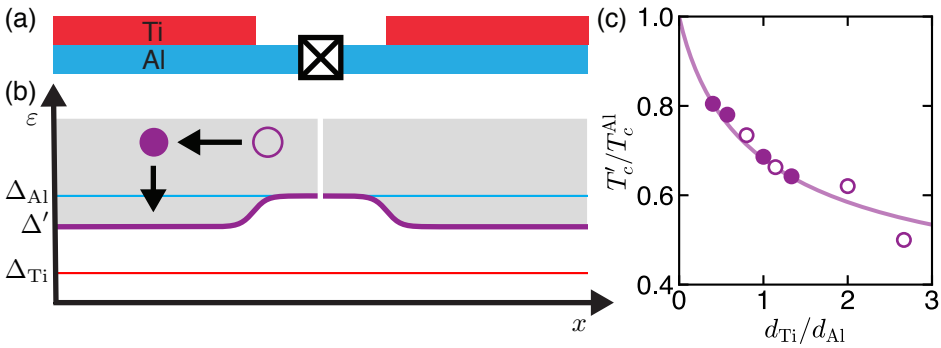

Figure 7.3 | (a) Schematic of a transmon qubit with Ti-proximitized-Al QP traps. The JJ would be formed by an Al-AlOx-Al junction like in traditional qubits, but Ti would be selectively deposited away from the JJ in nearly perfect ohmic contact with the Al. This would have the effect of reducing the superconducting gap in the Al regions below the Ti. (b) Superconducting gap and DOS in the excitation picture. The proximitized gap Δ' would fall somewhere in between the bare gaps of Al (Δ_{Al}) and Ti (Δ_{Ti}). Ideally, if QPs were generated near the JJ they would quickly diffuse to the trap region and cool to the proximitized gap edge via phonon emission. (c) Proximitized critical temperature T_c' of Al-Ti bilayers, as a function of the ratio of Ti thickness to Al thickness $d_{\mathrm{Ti}}/d_{\mathrm{Al}}$, and normalized by T_c^{Al}. Filled points represent bilayers with varied d_{Al} and fixed $d_{\mathrm{Ti}} = 20$ nm, open points have fixed $d_{\mathrm{Ti}} = 40$ nm. The solid line is derived from Usadel theory for an S-S′ bilayer assuming an interface transmission coefficient of 0.02.

Though these results have not been published, similar values were reported recently in Ref. Zhao et al. 2018. Interestingly, we found that the critical temperature of Ti is increased in thin films compared to its bulk value, and that we can achieve $T_c'/T_c^{\mathrm{Al}} \sim 0.7$. However, the ideal case for QP traps would be to have $T_c' < T_c^{\mathrm{Al}}/3$, such that phonons emitted by QP-pair recombination at the proximitized gap edge (with energy $\approx 2\Delta'$) would not be energetic enough to excite other QPs out of the trap,[9] though this is a weak effect in the limit of few QPs.

7.2.1 Wireless QP-injection

These next two sections outline experiments performed on 3D transmon qubits with Ti-proximitized-Al QP traps as depicted in Fig. 7.4. The traps in these devices were capped with a thin Al layer to prevent oxidation of the Ti. We estimate that the $\Delta' \approx 0.75\Delta_{\mathrm{Al}}$ in these layers. Following Wang et al. 2014 and Riwar et al.

[9] provided those QPs were also residing at proximitized gap edge

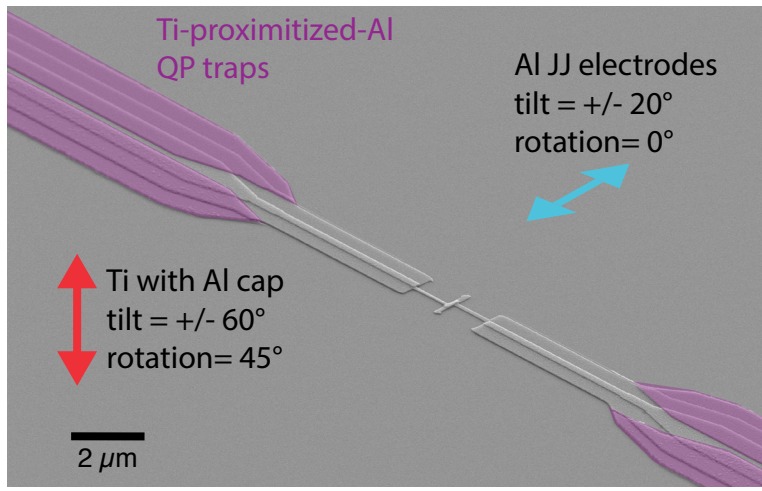

Figure 7.4 | Scanning electron micrograph of a transmon qubit with Ti-proximitized-Al quasiparticle traps false-colored in purple. Sample was coated with a thin Ir anti-charging layer for imaging. Blue arrows indicate the direction of evaporation of the Al JJ electrodes, and red arrows denote the direction of Ti deposition to form the proximitized trap. An Al capping layer is deposited to protect the Ti from oxidation.

2016, we set out to characterize the performance of the QP traps by the recovery time of the transmon T_1 after a QP injection pulse. We will not go into all of the details of this measurement here [see Wang et al. 2014], but we will offer an intuitive picture to understand the data. The brevity is partially due to the fact that not all of our data fit the models proposed in the above references, which led us to pursue the charge-parity correlation experiments.

The experiment is performed by first applying a high-power microwave pulse at the bare readout-mode frequency [Fig. 7.5(a, inset)]. This power produces an oscillating voltage across the JJ that instantaneously biases the junction at a voltage $> 2\Delta/e$, allowing for single-charge transport across the JJ, producing many QPs. This we call a wireless QP injection pulse.[10] This produces an elevated QP density x_{QP} immediately after the pulse, which proportionally decreases T_1. We then measure T_1 as a function of time after the injection, and characterize the recovery by a timescale τ_{ss}. The functional form of τ_{ss} in various regimes is described in Refs. Wang et al. 2014 and Riwar et al. 2016. We will not go into detail

[10] "Wireless" in contrast to experiments that apply a DC voltage bias across the JJ with a galvanically connected lead [Lenander et al. 2011; Wenner et al. 2013; Patel et al. 2017].

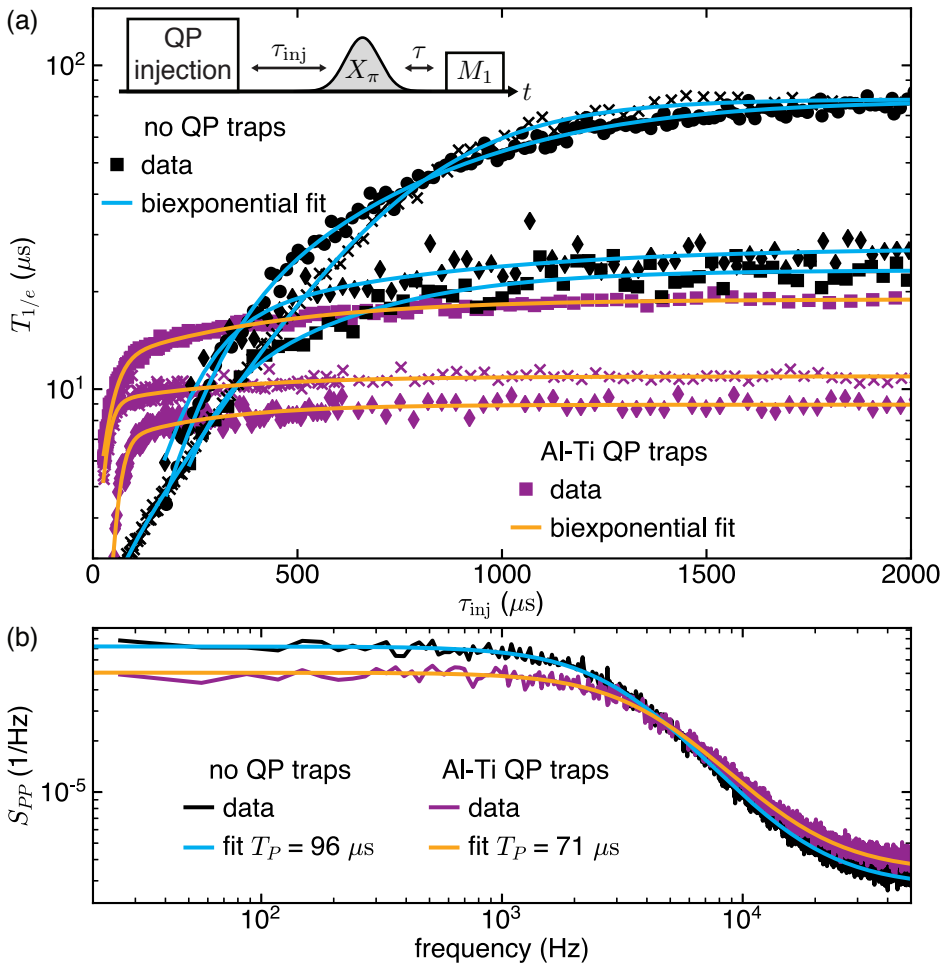

Figure 7.5 | (a) Wireless QP injection experiment. Inset: Experimental pulse sequence, in which a QP generating injection pulse is applied, followed by a delay $\tau_{\rm inj}$, after which a T_1 measurement is performed. Main: $1/e$ decay time of the T_1 measurement as a function of $\tau_{\rm inj}$. Purple data is from devices with Al-Ti proximitized QP traps, and black data is from standard transmon devices. Different markers denote different devices. Qualitatively, the recovery of T_1 is faster in devices with QP traps. (b) Power spectral density of charge-parity fluctuations S_{PP} in a device with and without QP traps [See Fig. 6.4 and associated discussion]. Here, QP traps seem to have little to no effect on the equilibrium charge-parity dynamics.

here because the devices with QP traps did not fit well to the theory. Instead, fits shown in Fig. 7.5 are to biexponential functions. Here we only make the qualitative argument that the recovery of T_1 after the QP injection is significantly faster in devices with QP traps than without, indicating that the x_{QP} local to the JJ decreases faster in these devices, which one would interpret as effective trapping of the generated QPs.

7.2.2 Charge-parity correlation experiments

While QP-injection experiments are a nice probe of QP dynamics *out of equilibrium*[11], the most important behavior is that of the steady-state nonequilibrium QPs present in our quantum-information-processing experiments. As a more direct study of this phenomena, we chose to characterize our proximitized-superconducting QP traps using the charge-parity correlation measurements developed at Delft [Ristè et al. 2013], described extensively in Chapter 6 and in Ref. Serniak et al. 2018. If the QP traps were working effectively, there would be an improvement in the charge-parity lifetime. Some of our results are shown in Fig. 7.5(b), in which we found no improvement of the charge-parity lifetime, indicating that the traps were *not effective* at reducing QP tunneling events.

7.2.3 Summary of Ti-proximitized-Al QP traps

Our experiments on Ti-proximitized-Al QP traps were performed prior to our implementation of additional Eccosorb filtering [Serniak et al. 2019], and prior to our understanding of QP-related qubit heating [Serniak et al. 2018] and possible PAT processes [Houzet et al. 2019]. In light of this, one would *not expect* the QP traps to result in any significant reduction of QP-induced dissipation if this dissipation is arising from PAT processes at the JJ. In this case, QPs would be generated at the junction and cause qubit transitions before ever diffusing to the trap region of the device. Even if PAT processes are not the dominant charge-parity switching mechanism, if QPs are unable to cool to the gap edge[12] the trapping effect would be at least suppressed, if not improbable. If PAT processes were indeed responsible for our observed charge-parity switches at the ~ 10 kHz level, it may be worth measuring these devices again now that the parity lifetime has

[11] or really, *further out of nonequilibrium*

[12] as would be evidenced by the fact that they are just as likely to excite or relax our transmons

been improved. If QP-tunneling processes dominate the charge-parity dynamics after implementing improved high-frequency filtering, it could be that these QP traps would extend the charge-parity lifetime even further. One technical challenge that needs to be overcome is that the introduction of Ti into our fabrication processes consistently produced lower T_1 in devices with Al-Ti QP traps. While the exact mechanism is unknown, one possibility is that the electron-beam resist was degraded under the high temperature required for Ti deposition,[13] which could have contaminated the deposited superconductors. Fabricating these devices using inorganic stencil masks could be a way to reduce this effect and improve device performance. [14]

[13] Ti is a refractory metal.

[14] These types of masks are currently being developed for qubit fabrication in our group by Ioannis Tsioutsios.

8

Conclusions and future directions

This dissertation has focused on our recent work probing nonequilibrium QP excitations in superconducting qubits. We found that QP-related processes can be responsible for the vast majority of excitation events in our transmon qubits, and can be a non-negligible contributor to T_1 in these devices [Serniak et al. 2018]. Furthermore, we found that charge-parity switching events were just as likely to excite as to relax our transmons, indicating that either the energy distribution of nonequilibrium QPs is far from the assumed quasithermal distribution or there is another charge-parity switching mechanism in play. Our recent theoretical work identified a potential culprit, in the form of photon-assisted QP generation and tunneling processes [Houzet et al. 2019]. In light of this work, one important question remains: are PAT processes or "hot" nonequilibium QPs the cause of our charge-parity dynamics and QP induced dissipation?

8.1 Future experiments

The following two experiments build from the work presented in this thesis. They are both currently in progress, and serve as tests of whether the detected charge-parity switches are due to nonequilibrium QP-tunneling processes or PAT processes in 3D transmons.

8.1.1 Probing PATs in an OCS SQUID

As shown in Fig. 5.5, QP-tunneling- and PAT- induced charge-parity transition rates depend on the transmon frequency f_{01} (or E_J/E_C, if you prefer). One way to tune this in situ is with with by replacing the JJ of the OCS transmon with a superconducting quantum interference device (SQUID). A SQUID is two JJs in parallel connected by superconducting wires. By threading an externally applied magnetic flux Φ_{ext}, the supercurrent through this element can be tuned, and even destructively interfere. The JJs may have different Josephson energies E_{J1} and

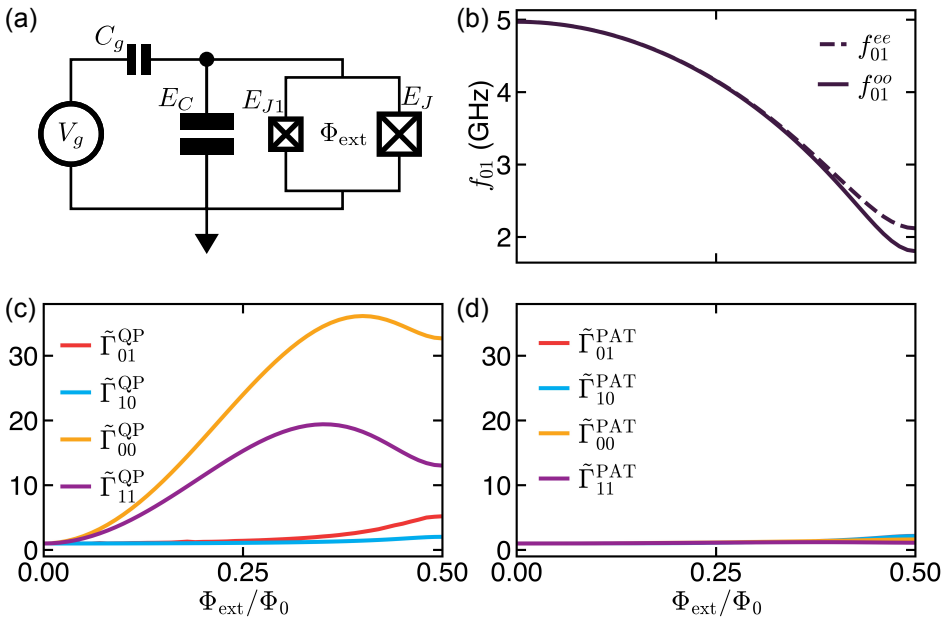

Figure 8.1 | (a) Circuit diagram of an OCS SQUID device. Compared to the OCS transmon [Fig. 4.1] the only difference is that the single JJ is replaced by a SQUID. In principle, the SQUID can be asymmetric, with $E_{J1} \neq E_{J2}$. (b) Ground to first excited state transition frequency for even (f_{01}^{ee}) and odd (f_{01}^{oo}) charge-parity states at $n_g = 0$, with $E_{J1}/h = 4.03$ GHz, $E_{J2}/h = 6.05$ GHz, and $E_C/h = 356$ MHz. This transition frequency is finite at $\Phi_{\rm ext}/\Phi_0 = 0.5$ due to the junction asymmetry. (c) QP-tunneling induced charge-parity transition rates $\tilde{\Gamma}_{ij}^{\rm QP}$, relative to their value at $\Phi_{\rm ext} = 0$, as a function of the externally applied flux through the SQUID loop $\Phi_{\rm ext}$ normalized by the flux quantum Φ_0. Simulation assumes a thermally generated $x_{\rm QP} = 10^{-7}$ (d) Relative rates plotted in (b) but for PAT induced charge-parity transitions $\tilde{\Gamma}_{ij}^{\rm PAT}$, assuming monochromatic pair-breaking radiation with frequency $\omega_\nu = 3.4\,\Delta/\hbar$.

E_{J2}, in which case the critical current is never fully suppressed, producing the dependence of f_{01} on Φ_{ext} depicted in Fig. 8.1(b).

Using the numerical techniques discussed in Section 5.4.1, we simulate the eigenspectrum and charge-parity transition rates for an OCS SQUID device. It is particularly interesting how these rates change as a function of the flux through the SQUID loop, so we plot these rates *relative* to their $\Phi_{\text{ext}} = 0$ values for QP tunneling [Fig. 8.1(c)] and for PAT processes [Fig. 8.1(d)]. OCS SQUID parameters chosen for this simulation are $n_g = 0$, $E_{J1}/h = 4.03$ GHz, $E_{J2}/h = 6.05$ GHz, and $E_C/h = 356$ MHz. For the QP-tunneling-induced transition rates $\tilde{\Gamma}_{ij}^{\text{QP}}$, we choose a thermally generated $x_{\text{QP}} = 10^{-7}$, though this does not strongly effect the simulation. For PAT-induced transition rates $\tilde{\Gamma}_{ij}^{\text{PAT}}$, we assume a monochromatic high-frequency photon source with frequency $\omega_\nu = 3.4\Delta/\hbar$ and a *frequency dependent* coupling rate g [Houzet et al. 2019].

Clearly the expected transition rates for the two types of processes have very different functional dependence on Φ_{ext}, which could be used to distinguish PAT-induced transitions from QP-tunneling induced transitions. For example, at $\Phi_{\text{ext}}/\Phi_0 = 0.25$, $\tilde{\Gamma}_{00}^{\text{QP}} \approx 24$ whereas $\tilde{\Gamma}_{00}^{\text{PAT}} \approx 1$. By measuring these rates as a function of flux, one would almost certainly be able to distinguish between PAT and QP-tunneling processes, or expose a gap in our understanding.

8.1.2 Probing PATs with a Nb-blocked OCS transmon

Another way to distinguish between QP-induced charge-parity switches and those induced by PAT processes relies on monitoring the branching ratio between charge-parity-transition rates Γ_{ij}^{eo} [see Fig. 5.6]. Again, the branching ratio just a name for the relation between those rates (various ratios, such as $\Gamma_{11}^{eo}/\Gamma_{10}^{eo}$, $\Gamma_{01}^{eo}/\Gamma_{10}^{eo}$, etc.). In particular, we discussed that the branching ratios should be different between QP-tunneling processes and PAT processes. To distinguish these effects, this proposed experiment relies on various experimental parameters and timescales to be aligned in a convenient way.

The rate of QP tunneling through a JJ is approximately proportional to x_{QP} [Fig. 5.6]. In our typical transmon devices, this corresponds to tens, hundreds, or thousands of QPs occupying each JJ electrode, which tunnel back and forth symmetrically such that there is no preferred charge-parity of the JJ.[1] How-

[1] As a reminder, we define the charge parity as the parity of the total number of single QPs that have tunneled through the JJ.

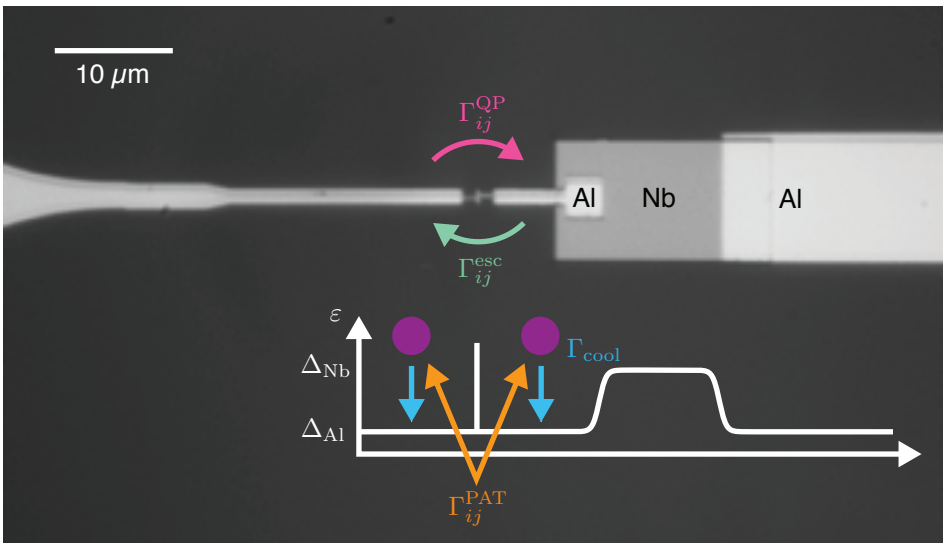

Figure 8.2 | Optical micrograph of an OCS transmon fabricated with a single Nb QP blocker in close proximity to the JJ. Inset: energy band diagram in the excitation picture showing the superconducting gap as a function of position along the device. See text for more details.

ever, if *one* of the JJ electrodes is made to be very small, such that the total number of QPs on that island $N_{\mathrm{QP}}^{i} < 1$ on average, there will indeed be a preferred charge parity of the JJ. A CPB or OCS transmon device fabricated with this asymmetry would show a preferred charge parity, but what does this mean for the statistics of charge-parity transitions? A preferred charge-parity would break the degeneracy between even and odd transition rates such that $\Gamma_{ij}^{eo} \neq \Gamma_{ij}^{oe}$, even if $\delta\epsilon_i, \delta\epsilon_j \ll k_B T$. The signature of this effect in an OCS transmon device would be charge-parity switches that are *pair-correlated in time*. This can be understood simply as an effect of the instantaneous x_{QP}^{i} on the small island: as soon as one QP tunnels onto the island x_{QP}^{i} will be greater than the x_{QP} on the large island, causing it to quickly escape the small island back through the JJ. This may be visible provided that the volume of the small island $v < 1/x_{\mathrm{QP}} n_{\mathrm{QP}}$, where $n_{\mathrm{QP}} = 4 \times 10^6\ \mu\mathrm{m}^{-3}$ is the Cooper-pair density in Al. This constrains $v \lesssim 1\ \mu\mathrm{m}^3$ for Al-based JJ electrodes for $x_{\mathrm{QP}} = 10^{-7}$, and $v \lesssim 100\ \mu\mathrm{m}^3$ for $x_{\mathrm{QP}} = 10^{-9}$.

An optical micrograph of a proposed device is shown in Fig. 8.2, overlaid with arrows representing relevant processes, along with the superconducting gap spectrum that is crucial for the experiment. Here, both device electrodes are large,

like those in Fig. 4.7, but the right electrode is interrupted by a patch of superconducting Nb, which has a much larger superconducting gap $\Delta_{\mathrm{Nb}}/h \approx 330$ GHz compared to that of Al $\Delta_{\mathrm{Al}}/h \approx 50$ GHz. This has the effect of blocking the diffusion of QPs near the gap of Al into the larger pad on the right,[2] effectively confining the QPs in the volume v of the small Al island. This effect could also be achieved just with a small island without a Nb blocker or additional Al electrode, however this would constrain the minimum E_C attainable in a coplanar device geometry.

With this picture in mind, how can we distinguish between nonequilibrium QP tunneling and PAT processes? There are many rates that matter in this scenario: the measurement rate at which we can determine the charge-parity and plasmon state of the OCS transmon Γ_m, the rates of PAT-induced transitions $\Gamma_{ij}^{\mathrm{PAT}}$, the rate at which QPs generated by PAT processes cool to the gap edge by phonon emission Γ_{cool}, the rate of transitions due to nonequilibrium QPs tunneling *onto* the small island $\Gamma_{ij}^{\mathrm{QP}}$, and the rates of single QP escape from the small island back through the JJ onto the large island, $\Gamma_{ij}^{\mathrm{esc}}$. The goal is to engineer a situation where $\Gamma_{ij}^{\mathrm{QP}}, \Gamma_{ij}^{\mathrm{PAT}} < \Gamma_{ij}^{\mathrm{esc}} < \Gamma_{\mathrm{cool}} < \Gamma_m$, which is realistic given recent experimental results [Ristè et al. 2013; Serniak et al. 2018; Serniak et al. 2019].[3]

In this regime, one just needs to compare the branching ratio of the first and second charge-parity transitions in pair-correlated events. In a situation where $\Gamma_{ij}^{\mathrm{QP}} \ll \Gamma_{ij}^{\mathrm{PAT}}$, the branching ratios will be different: the first of the pair correlated events will have a branching ratio corresponding to that of PAT events, and the second will have that corresponding to QP-tunneling. This would be confirmation that PAT events, which generate QPs at the JJ, are responsible for the majority of the observed charge-parity switches, and put to rest the notion of "hot" nonequilibrium QPs with a highly athermal energy distribution. Of course, this experiment relies on proper understanding of QP scattering and careful device design, making it more challenging than the aforementioned experiment with OCS SQUIDs.

[2] A sort of QP trap, but not in the way one would typically want for a superconducting qubit. This is, however, very similar to the QP traps implemented for STJ detectors [Segall et al. 2004]

[3] Assuming, of course, that the charge-parity dynamics arise from some combination of the mechanisms we've discussed.

8.2 Perspectives

Nonequilibrium QPs are a bit unique in the forest of loss mechanisms that can limit superconducting qubits. By coupling the BCS theory of superconductivity with the theory of quantum circuits, one can not only write a Hamiltonian that includes both qubit and QP degrees of freedom, but also calculate, based on microscopic details of the circuit, the expected QP-induced relaxation and dephasing rates of the qubit. For this reason, some may say that studying QP-induced loss is a bit like "searching for your lost keys under a streetlamp," in the sense that we have a relatively complete set of tools with which to begin tackling the problem. Viewed from the opposite angle, however, this affords us the opportunity to leverage the technological developments within the field of superconducting qubits for the purpose of studying mesoscopic superconductivity. For instance, this is partly why it is important that we determine the mechanism for QP-induced excitation of our transmons, be it PAT processes or something else that will expand our understanding. Another prime example of this notion is recent work utilizing circuit QED techniques to study Andreev bound states in various types of Josephson junctions [Janvier et al. 2015; Hays et al. 2018; Tosi et al. 2019]. Similar studies could be performed with OCS transmons to probe the current phase relation of these junctions [Ginossar and Grosfeld 2014; Yavilberg, Ginossar, and Grosfeld 2015; Li et al. 2018; Keselman et al. 2019], using the techniques outlined in this dissertation.

From a technological standpoint, if QP-generating radiation is reduced universally to the the level we reported in Ref. Serniak et al. 2019, QP induced dissipation would not be a concern for the T_1 of transmon qubits until significant improvements are made toward the mitigation of dielectric loss (when we reach T_1 of several milliseconds). This is an extreme challenge in and of itself that fortunately can be aided by the work presented here. I would argue that it is absolutely crucial for any experiment seeking to probe or improve dielectric quality factors to first perform these sort of charge-parity autocorrelation measurements to confirm that they are indeed limited by dielectric loss, especially because of the apparent dependence on specific details of the measurement setup, such as high-frequency filtering. This is a check that one might think isn't necessary: just like we thought before performing the experiments in Ref. Serniak et al. 2018, which were quite illuminating for this exact reason.

A

Qubit Fabrication

The devices presented in this thesis were fabricated with the same procedure as most devices in our group, which starts out with a c-plane sapphire wafer acquired from a company called CrysTec. The dielectric constant in sapphire is anisotropic, and "c-plane" means that the crystalline axis with lower permittivity is normal to the surface of the wafer. The wafer is initially cleaned by sequential sonication in 1-methyl-2-pyrrolidone (NMP), acetone, and then methanol, for three minutes each. This sequence is chosen to minimize residue and is ordered by decreasing solvent "strength." NMP is a strong organic resist stripper that will also remove some oils, acetone is a weaker resist stripper that is also very polar, and methanol is a less polar solvent that reacts less with things in the air so as to leave minimal residue. Quickly after the last step, the wafer is blown dry with dry nitrogen or argon, also to avoid residue.

Once the wafer is clean, we spin coat a bilayer of electron-beam-sensitive resists. First, we spin Microchem MMA[1] (8.5) MAA[2] EL13 for 100 s at 2000 RPM, which is then baked at ~ 180 °C for five minutes. The top layer is 950 PMMA[3] A4, also spun for 100 s at 2000 RPM and baked at ~ 180 °C for five minutes. These are spun at relatively low speed to achieve thicker resist layers (about 800 nm and 250 nm, respectively). This was originally chosen for convenience when tuning doses for bridge-free junction fabrication [Lecocq et al. 2011], however this is not strictly necessary, and it would be wiser to use a less dilute resist to get the similar thickness at higher spin speeds.

One slight difficulty that one has to deal with when doing electron-beam lithography on sapphire substrates is charge buildup. Because sapphire (crystalline Al_2O_3) is a good insulator, a focused electron beam can produce a trail of trapped charges that can *deflect* the beam, leading to poor resolution and inconsistent dosing. To avoid this, an "anticharging layer" of conducting material (such as a metal or conductive polymer) can be deposited on top of the e-beam resist to help disperse the charge. For this, we typically use a thin layer of Au, deposited in a Cressington 108 sputter coater. Au is convenient as it is a good metal,

[1] methyl methacrylate
[2] methacrylic acid
[3] polymethyl methacrylate

it doesn't oxidize, and is pretty ductile. The electron beam tends to heat the resist locally while writing, and the anticharging layer needs to be able to stretch and deform to accommodate thermal expansion of the resist. We've also tried Al and Ag for the anticharging layer, however they often bubble and crack, potentially leading to defects in the pattern. Anecdotally, this rarely (if ever) causes issues near small features like Josephson junctions, but can be a problem on large features that see a stronger integrated dose. In the Cressington 108, Au (99.99% purity) is sputtered by an Ar plasma with 30 mA emission current for 45 s, which results in a layer ∼10-15nm thick. Other targets can be installed in this machine, such as Ag, however it requires a different e-beam dose because it emits fewer secondary electrons.

We write the patterns using a 100-kV Raith-Vistec EBPG-5000, with beam currents as high as 100 nA for large features, and typically 10 to 50 nA for small features such as JJs[4]. The particular bilayer described above requires a dose of $\sim$ 600 μC/cm^2 for large features and $\sim$ 1100 μC/cm^2 to properly expose a long, 1 μm wide line. One thing to look out for:

- It is crucial to check the ability of the EBPG to autofocus on colloidal Au nanoparticles supplied by YINQE. The machine does this procedure by measuring the height of the wafer with a laser, and sets the focus based on a value from a look-up table, assuming that there is no beam deflection from charging effects. IF THERE IS AN ISSUE WITH THE ANTICHARGING LAYER, IT WILL BE VISIBLE ON THE SEM. Sometimes you will find that the autofocus procedure actually *defocuses* the image of the Au particles, which can be indicative that the beam is being deflected by charge buildup.

After the write, one needs to remove the anticharging layer. One can wet-etch the Au (or Ag, or Al) with an aqueous KI/I solution, which can be bought from Transene and is called Au etchant[5]. The Au etch rate for undiluted etchant is approximately 10 nm/s. The etchant does not attack the resist stack[6], therefore it's safe to leave the wafer submerged for many seconds.

- The etchant will stain both skin and clothing, so try not to spill (also, use it in a hood with proper protective equipment).

[4] EBPG stands for electron-beam pattern generator
[5] This etchant is slightly basic
[6] At least not very quickly

- After etching, quickly rinse the wafer with deionized water, and immediately blow-dry with dry nitrogen or argon.
- Before continuing, inspect the wafer for any leftover Au, especially near the edges, as we don't want to contaminate our evaporation tools with Au. Any oils transferred from the EBPG wafer holder or from handing with gloves can act as an etch stop and protect the Au. Au and Al don't mix well, sometimes creating an intermetallic layer referred to as the Purple Plague.

After etching away the Au, the pattern is developed with a mixture of 3:1 isopropanol to deionized water at 6 °C [Rooks et al. 2002]. For the lithographic process described above, the development consists of submerging the wafer and agitating lightly for two minutes, then quickly blow-dry with dry nitrogen or argon. If you inspect the wafer after development with an optical microscope you can see if the lithography turned out properly. The edges of features should be relatively smooth, not jagged (which would indicate underdosing). One can also get a sense for the health of the JJs (for bridge-free, Dolan, or any other process that utilizes controlled undercuts). It takes some experience, but the relative brightness of the undercut region is a solid indicator of proper junction dosing.

Most of our devices rely on a Plassys UMS-300 electron-beam-evaporation system for Al deposition. Prior to deposition of Al, an *in situ* Ar/O_2 (30 sccm and 10 sccm flow rates, respectively) ion-beam cleaning is performed in the loadlock of the Plassys. This step conveniently limits the amount of aging (decrease of critical current) that the JJ experiences [Pop et al. 2012]. After a 4 min Ti evaporation (without deposition) to improve the vacuum to $\lesssim 5 \times 10^{-9}$ Torr, Al junction electrodes (in our case, these layers were 20 and 30 nm thick[7]) were deposited at angles of $\pm 20^\circ$ in a dedicated evaporation chamber. Between the Al evaporations, the sample was transferred to a third chamber for thermal oxidation of the first electrode to form the junction barrier. This was performed at ambient temperature in a 17:3 $Ar:O_2$ mixture at a pressure of 30 Torr for 10 min. These oxidation parameters yield a junction critical-current density of ~ 50 A/cm^2, though this can be varied to taste[8]. To passivate the surface before exposure to air, another thermal oxidation step is performed following the second Al evaporation

[7] The important thing is to make the counterelectrode thicker than the first electrode to ensure that it climbs the sidewall

[8] Reasonable oxidation parameters typically put the critical-current density somewhere in a range of 10-100 A/cm^2.

at 50 Torr for 5 min. Now that the JJs are formed, be careful to avoid electrostatic discharge around the wafer. Oftentimes people will fabricate a "shorting strap" that can be scratched away before sample mounting for a low-impedance path around the JJ. Typically this is not necessary unless working with extremely large JJ electrodes as long as you take precautions such as avoiding static-building foot covers and using a wrist-grounding strap.

Following the deposition process, the remaining resist and extra Al can be removed by a hot NMP (~ 75 °C) liftoff process for one hour with a 30 s sonication step at the end. This could also be done with acetone. While there are many variations on this technique that can be used, we found the following to consistently result in clean liftoff (when the doses were correct).

- Submerge the wafer face-up in hot NMP (75° C for $\sim$1 hour). This will remove any remaining resist and the superfluous Al that is coating it.
- Sonicate the entire beaker for $\sim$30 seconds.
- Quickly rinse the wafer with acetone and then methanol upon removal from the NMP bath, taking care that the wafer does not dry with any Al flakes on the surface, otherwise Van der Waals forces will stick them to the wafer.

Now one can check the resistance of the JJs. One can be safe and use a dedicated source-meter or lock-in amplifier for this purpose, but a digital multimeter can also be used as long as you limit the current output (set it to the highest tolerable resistance range, don't let it "auto-range").

To protect the devices during dicing we typically spin a thick layer of photoresist S1827 at 1500 RPM (~ 5 μm) for 2 minutes, then bake at 90° C for 9 minutes. After dicing, rinse each chip individually in NMP, then acetone, then methanol, and blow-dry. Before mounting a sample, sonicate in each for a few seconds and blow-dry.

References

Aassime, A., G. Johansson, G. Wendin, R. J. Schoelkopf, and P. Delsing, "Radio-Frequency Single-Electron Transistor as Readout Device for Qubits: Charge Sensitivity and Backaction", Physical Review Letters **86**, 3376–3379 (2001).

Albrecht, S. M., E. B. Hansen, A. P. Higginbotham, F. Kuemmeth, T. S. Jespersen, J. Nygård, P. Krogstrup, J. Danon, K. Flensberg, and C. M. Marcus, "Transport Signatures of Quasiparticle Poisoning in a Majorana Island", Physical Review Letters **118**, 137701 (2017).

Andrews, R. W., R. W. Peterson, T. P. Purdy, K. Cicak, R. W. Simmonds, C. A. Regal, and K. W. Lehnert, "Bidirectional and efficient conversion between microwave and optical light", Nature Physics **10**, 321–326 (2014).

Aumentado, J., M. W. Keller, J. M. Martinis, and M. H. Devoret, "Nonequilibrium Quasiparticles and 2 e Periodicity in Single-Cooper-Pair Transistors", Physical Review Letters **92**, 066802 (2004).

Bal, M., M. H. Ansari, J.-L. Orgiazzi, R. M. Lutchyn, and A. Lupascu, "Dynamics of parametric fluctuations induced by quasiparticle tunneling in superconducting flux qubits", Physical Review B **91**, 195434 (2015).

Bardeen, J., L. N. Cooper, and J. R. Schrieffer, "Theory of Superconductivity", Physical Review **108**, 1175–1204 (1957).

Barends, R., J. Wenner, M. Lenander, Y. Chen, R. C. Bialczak, J. Kelly, E. Lucero, P. O'Malley, M. Mariantoni, D. Sank, H. Wang, T. C. White, Y. Yin, J. Zhao, A. N. Cleland, J. M. Martinis, and J. J. A. Baselmans, "Minimizing quasiparticle generation from stray infrared light in superconducting quantum circuits", Applied Physics Letters **99**, 113507 (2011).

Bergeal, N., R. Vijay, V. E. Manucharyan, I. Siddiqi, R. J. Schoelkopf, S. M. Girvin, and M. H. Devoret, "Analog information processing at the quantum limit with a Josephson ring modulator", Nature Physics **6**, 296–302 (2010).

Bespalov, A., M. Houzet, J. S. Meyer, and Y. V. Nazarov, "Theoretical Model to Explain Excess of Quasiparticles in Superconductors", Physical Review Letters **117**, 117002 (2016).

Blais, A., R. S. Huang, A. Wallraff, S. M. Girvin, and R. J. Schoelkopf, "Cavity quantum electrodynamics for superconducting electrical circuits: An architecture for quantum computation", Physical Review A **69**, 062320 (2004).

Booth, N. E., "Quasiparticle trapping and the quasiparticle multiplier", Applied Physics Letters **50**, 293–295 (1987).

Booth, N. E., P. L. Brink, R. J. Gaitskell, D. J. Goldie, A. D. Hahn, G. L. Salmon, and A. M. Swift, "Superconducting tunnel junctions and quasiparticle trapping", Journal of Low Temperature Physics **93**, 521–532 (1993).

Bouchiat, V., D. Vion, P. Joyez, D. Esteve, and M. H. Devoret, "Quantum Coherence with a Single Cooper Pair", Physica Scripta **T76**, 165 (1998).

Brammertz, G., A. A. Golubov, P. Verhoeve, R. den Hartog, A. Peacock, and H. Rogalla, "Critical temperature of superconducting bilayers: Theory and experiment", Applied Physics Letters **80**, 2955–2957 (2002).

Brammertz, G., A. Poelaert, A. A. Golubov, P. Verhoeve, A. Peacock, and H. Rogalla, "Generalized proximity effect model in superconducting bi- and trilayer films", Journal of Applied Physics **90**, 355–364 (2001).

Bretheau, L., Ç. Ö. Girit, H. Pothier, D. Esteve, and C. Urbina, "Exciting Andreev pairs in a superconducting atomic contact.", Nature **499**, 312–5 (2013).

Bretheau, L., "Localized Excitations in Superconducting Atomic Contacts: PROBING THE ANDREEV DOUBLET", PhD thesis (Ecole Polytechnique X, Feb. 2013).

Bueno, J., M. D. Shaw, P. K. Day, and P. M. Echternach, "Proof of concept of the quantum capacitance detector", Applied Physics Letters **96**, 103503 (2010).

Bylander, J., S. Gustavsson, F. Yan, F. Yoshihara, K. Harrabi, G. Fitch, D. G. Cory, Y. Nakamura, J.-S. Tsai, and W. D. Oliver, "Noise spectroscopy through dynamical decoupling with a superconducting flux qubit", Nature Physics **7**, 565–570 (2011).

Calusine, G., A. Melville, W. Woods, R. Das, C. Stull, V. Bolkhovsky, D. Braje, D. Hover, D. K. Kim, X. Miloshi, D. Rosenberg, A. Sevi, J. L. Yoder, E. Dauler, and W. D. Oliver, "Analysis and mitigation of interface losses in trenched superconducting coplanar waveguide resonators", Applied Physics Letters **112**, 062601 (2018).

Caroli, C., P. de Gennes, and J. Matricon, "Bound Fermion states on a vortex line in a type II superconductor", Physics Letters **9**, 307–309 (1964).

Castellanos-Beltran, M., K. Irwin, L. Vale, G. Hilton, and K. Lehnert, "Bandwidth and Dynamic Range of a Widely Tunable Josephson Parametric Amplifier", IEEE Transactions on Applied Superconductivity **19**, 944–947 (2009).

Catelani, G., "Parity switching and decoherence by quasiparticles in single-junction transmons", Physical Review B **89**, 094522 (2014).

Catelani, G., L. I. Glazman, and K. E. Nagaev, "Effect of quasiparticles injection on the ac response of a superconductor", Physical Review B **82**, 134502 (2010).

Catelani, G., R. J. Schoelkopf, M. H. Devoret, and L. I. Glazman, "Relaxation and frequency shifts induced by quasiparticles in superconducting qubits", Physical Review B **84**, 064517 (2011).

Catelani, G. and D. Basko, "Non-equilibrium quasiparticles in superconducting circuits: photons vs. phonons", SciPost Physics **6**, 013 (2019).

Chang, J.-J. and D. J. Scalapino, "Kinetic-equation approach to nonequilibrium superconductivity", Physical Review B **15**, 2651–2670 (1977).

Chiorescu, I., Y. Nakamura, C. J. P. M. Harmans, and J. E. Mooij, "Coherent quantum dynamics of a superconducting flux qubit.", Science **299**, 1869–71 (2003).

Chow, J. M., L. DiCarlo, J. M. Gambetta, F. Motzoi, L. Frunzio, S. M. Girvin, and R. J. Schoelkopf, "Optimized driving of superconducting artificial atoms for improved single-qubit gates", Physical Review A **82**, 040305 (2010).

Chubov, P. N., V. V. Eremenko, and Y. A. Pilipenko, "Dependence of the Critical Temperature and Energy Gap on the Thickness of Superconducting Aluminum Films", Soviet Physics JETP **28** (1969).

Clerk, A. A., M. H. Devoret, S. M. Girvin, F. Marquardt, and R. J. Schoelkopf, "Introduction to quantum noise, measurement, and amplification", Reviews of Modern Physics **82**, 1155–1208 (2010).

Córcoles, A. D., J. M. Chow, J. M. Gambetta, C. Rigetti, J. R. Rozen, G. A. Keefe, M. Beth Rothwell, M. B. Ketchen, and M. Steffen, "Protecting superconducting qubits from radiation", Applied Physics Letters **99**, 181906 (2011).

Court, N. A., A. J. Ferguson, R. Lutchyn, and R. G. Clark, "Quantitative study of quasiparticle traps using the single-Cooper-pair transistor", Physical Review B **77**, 100501 (2008).

Day, P. K., H. G. LeDuc, B. A. Mazin, A. Vayonakis, and J. Zmuidzinas, "A broadband superconducting detector suitable for use in large arrays", Nature **425**, 817–821 (2003).

de Gennes, P.-G., *Superconductivity of Metals and Alloys* (Advanced Book Program, Perseus Books, 1999).

Devoret, M. H. and R. J. Schoelkopf, "Superconducting circuits for quantum information: an outlook.", Science **339**, 1169–74 (2013).

DiCarlo, L., J. M. Chow, J. M. Gambetta, L. S. Bishop, B. R. Johnson, D. I. Schuster, J. Majer, A. Blais, L. Frunzio, S. M. Girvin, and R. J. Schoelkopf, "Demonstration of two-qubit algorithms with a superconducting quantum processor", Nature **460**, 240–244 (2009).

Dunsworth, A., A. Megrant, C. Quintana, Z. Chen, R. Barends, B. Burkett, B. Foxen, Y. Chen, B. Chiaro, A. Fowler, R. Graff, E. Jeffrey, J. Kelly, E. Lucero, J. Y. Mutus, M. Neeley, C. Neill, P. Roushan, D. Sank, A. Vainsencher, J. Wenner, T. C. White, and J. M. Martinis, "Characterization and reduction of capacitive loss induced by sub-micron Josephson junction fabrication in superconducting qubits", Applied Physics Letters **111**, 022601 (2017).

Echternach, P. M., B. J. Pepper, T. Reck, and C. M. Bradford, "Single photon detection of 1.5 THz radiation with the quantum capacitance detector", Nature Astronomy **2**, 90–97 (2018).

Feynman, R. P., "Simulating physics with computers", International Journal of Theoretical Physics **21**, 467–488 (1982).

Fominov, Y. V. and M. V. Feigel'man, "Superconductive properties of thin dirty superconductor–normal-metal bilayers", Physical Review B **63**, 094518 (2001).

Fowler, A. G., M. Mariantoni, J. M. Martinis, and A. N. Cleland, "Surface codes: Towards practical large-scale quantum computation", Physical Review A **86**, 032324 (2012).

Gambetta, J., A. Blais, D. I. Schuster, A. Wallraff, L. Frunzio, J. Majer, M. H. Devoret, S. M. Girvin, and R. J. Schoelkopf, "Qubit-photon interactions in a cavity: Measurement-induced dephasing and number splitting", Physical Review A **74**, 042318 (2006).

Ginossar, E. and E. Grosfeld, "Microwave transitions as a signature of coherent parity mixing effects in the Majorana-transmon qubit", Nature Communications **5**, 4772 (2014).

Girvin, S. M., "Circuit QED: superconducting qubits coupled to microwave photons", in *Quantum machines: measurement and control of engineered quantum systems* (Oxford University Press, June 2014), pp. 113–256.

Goldie, D. J. and S. Withington, "Non-equilibrium superconductivity in quantum-sensing superconducting resonators", Superconductor Science and Technology **26**, 015004 (2013).

Goldie, D., N. Booth, C. Patel, and G. Salmon, "Quasiparticle trapping from a single-crystal superconductor into a normal-metal film via the proximity effect", Physical Review Letters **64**, 954–957 (1990).

Golubov, A. A., E. P. Houwman, J. G. Gijsbertsen, J. Flokstra, H. Rogalla, J. B. le Grand, and P. A. J. de Korte, "Quasiparticle lifetimes and tunneling times in a superconductor-insulator-superconductor tunnel junction with spatially inhomogeneous electrodes", Physical Review B **49**, 12953–12968 (1994).

Gottesman, D., A. Kitaev, and J. Preskill, "Encoding a qubit in an oscillator", Physical Review A **64**, 012310 (2001).

Grünhaupt, L., N. Maleeva, S. T. Skacel, M. Calvo, F. Levy-Bertrand, A. V. Ustinov, H. Rotzinger, A. Monfardini, G. Catelani, and I. M. Pop, "Loss Mechanisms and Quasiparticle Dynamics in Superconducting Microwave Resonators Made of Thin-Film Granular Aluminum", Physical Review Letters **121**, 117001 (2018).

Gueron, S., "Quasiparticles in a diffusive conductor: Interaction and pairing", PhD thesis (CEA Saclay, 1997).

Gustavsson, S., F. Yan, G. Catelani, J. Bylander, A. Kamal, J. Birenbaum, D. Hover, D. Rosenberg, G. Samach, A. P. Sears, S. J. Weber, J. L. Yoder, J. Clarke, A. J. Kerman, F. Yoshihara, Y. Nakamura, T. P. Orlando, and W. D. Oliver, "Suppressing relaxation in superconducting qubits by quasiparticle pumping.", Science **354**, 1573–1577 (2016).

Halpern, M., H. P. Gush, E. Wishnow, and V. De Cosmo, "Far infrared transmission of dielectrics at cryogenic and room temperatures: glass, Fluorogold, Eccosorb, Stycast, and various plastics", Applied Optics **25**, 565 (1986).

Hays, M., G. de Lange, K. Serniak, D. J. van Woerkom, D. Bouman, P. Krogstrup, J. Nygård, A. Geresdi, and M. H. Devoret, "Direct Microwave Measurement of Andreev-Bound-State Dynamics in a Semiconductor-Nanowire Josephson Junction", Physical Review Letters **121**, 047001 (2018).

Hazard, T. M., A. Gyenis, A. Di Paolo, A. T. Asfaw, S. A. Lyon, A. Blais, and A. A. Houck, "Nanowire Superinductance Fluxonium Qubit", Physical Review Letters **122**, 010504 (2019).

Higginbotham, A. P., S. M. Albrecht, G. Kiršanskas, W. Chang, F. Kuemmeth, P. Krogstrup, T. S. Jespersen, J. Nygård, K. Flensberg, and C. M. Marcus, "Parity lifetime of bound states in a proximitized semiconductor nanowire", Nature Physics **11**, 1017–1021 (2015).

Hosseinkhani, A., R.-P. Riwar, R. J. Schoelkopf, L. I. Glazman, and G. Catelani, "Optimal Configurations for Normal-Metal Traps in Transmon Qubits", Physical Review Applied **8**, 064028 (2017).

Houck, A. A., J. A. Schreier, B. R. Johnson, J. M. Chow, J. Koch, J. M. Gambetta, D. I. Schuster, L. Frunzio, M. H. Devoret, S. M. Girvin, and R. J. Schoelkopf, "Controlling the Spontaneous Emission of a Superconducting Transmon Qubit", Physical Review Letters **101**, 080502 (2008).

Houzet, M., K. Serniak, G. Catelani, M. H. Devoret, and L. I. Glazman, "Photon-assisted charge-parity jumps in a superconducting qubit", Physical Review Letters **123**, 107704 (2019).

Irwin, K. D., S. W. Nam, B. Cabrera, B. Chugg, and B. A. Young, "A quasiparticle-trap-assisted transition-edge sensor for phonon-mediated particle detection", Review of Scientific Instruments **66**, 5322–5326 (1995).

Ithier, G., E. Collin, P. Joyez, P. J. Meeson, D. Vion, D. Esteve, F. Chiarello, A. Shnirman, Y. Makhlin, J. Schriefl, and G. Schön, "Decoherence in a superconducting quantum bit circuit", Physical Review B **72**, 134519 (2005).

Janvier, C., L. Tosi, L. Bretheau, Ç. Ö. Girit, M. Stern, P. Bertet, P. Joyez, D. Vion, D. Esteve, M. F. Goffman, H. Pothier, and C. Urbina, "Coherent manipulation of Andreev states in superconducting atomic contacts.", Science **349**, 1199–202 (2015).

Jin, X. Y., A. Kamal, A. P. Sears, T. Gudmundsen, D. Hover, J. Miloshi, R. Slattery, F. Yan, J. Yoder, T. P. Orlando, S. Gustavsson, and W. D. Oliver, "Thermal and Residual Excited-State Population in a 3D Transmon Qubit", Physical Review Letters **114**, 240501 (2015).

Josephson, B., "Possible new effects in superconductive tunnelling", Physics Letters **1**, 251–253 (1962).

Kaplan, S. B., C. C. Chi, D. N. Langenberg, J. J. Chang, S. Jafarey, and D. J. Scalapino, "Quasiparticle and phonon lifetimes in superconductors", Physical Review B **14**, 4854–4873 (1976).

Keselman, A., C. Murthy, B. van Heck, and B. Bauer, "Spectral response of Josephson junctions with low-energy quasiparticles", ArXiv:1905.03275 (2019).

Koch, J., T. M. Yu, J. Gambetta, A. A. Houck, D. I. Schuster, J. Majer, A. Blais, M. H. Devoret, S. M. Girvin, and R. J. Schoelkopf, "Charge-insensitive qubit design derived from the Cooper pair box", Physical Review A **76**, 042319 (2007).

Kou, A., W. C. Smith, U. Vool, R. T. Brierley, H. Meier, L. Frunzio, S. M. Girvin, L. I. Glazman, and M. H. Devoret, "Fluxonium-Based Artificial Molecule with a Tunable Magnetic Moment", Physical Review X **7**, 031037 (2017).

Krantz, P., M. Kjaergaard, F. Yan, T. P. Orlando, S. Gustavsson, and W. D. Oliver, "A Quantum Engineer's Guide to Superconducting Qubits", ArXiv:1904.06560 (2019).

Kraus, H., F. von Feilitzsch, J. Jochum, R. Mössbauer, T. Peterreins, and F. Pröbst, "Quasiparticle trapping in a superconductive detector system exhibiting high energy and position resolution", Physics Letters B **231**, 195–202 (1989).

Kubo, R., "The fluctuation-dissipation theorem", Reports on Progress in Physics **29**, 306 (1966).

Lang, K., S. Nam, J. Aumentado, C. Urbina, and J. Martinis, "Banishing quasiparticles from Josephson-junction qubits: Why and how to do it", IEEE Transactions on Appiled Superconductivity **13**, 989–993 (2003).

Lecocq, F., I. M. Pop, Z. Peng, I. Matei, T. Crozes, T. Fournier, C. Naud, W. Guichard, and O. Buisson, "Junction fabrication by shadow evaporation without a suspended bridge.", Nanotechnology **22**, 315302 (2011).

Lenander, M., H. Wang, R. C. Bialczak, E. Lucero, M. Mariantoni, M. Neeley, A. D. O'Connell, D. Sank, M. Weides, J. Wenner, T. Yamamoto, Y. Yin, J. Zhao, A. N. Cleland, and J. M. Martinis, "Measurement of energy decay in superconducting qubits from nonequilibrium quasiparticles", Physical Review B **84**, 024501 (2011).

Li, T., W. A. Coish, M. Hell, K. Flensberg, and M. Leijnse, "Four-Majorana qubit with charge readout: Dynamics and decoherence", Physical Review B **98**, 205403 (2018).

Lutchyn, R. M., J. D. Sau, and S. Das Sarma, "Majorana fermions and a topological phase transition in semiconductor-superconductor heterostructures", Physical Review Letters **105**, 077001 (2010).

Lutchyn, R., L. Glazman, and A. Larkin, "Quasiparticle decay rate of Josephson charge qubit oscillations", Physical Review B **72**, 014517 (2005).

Machlup, S., "Noise in Semiconductors: Spectrum of a Two-Parameter Random Signal", Journal of Applied Physics **25**, 341–343 (1954).

Macklin, C., K. O'Brien, D. Hover, M. E. Schwartz, V. Bolkhovsky, X. Zhang, W. D. Oliver, and I. Siddiqi, "A near-quantum-limited Josephson traveling-wave parametric amplifier.", Science **350**, 307–10 (2015).

MacLeod, S. J., S. Kafanov, and J. P. Pekola, "Periodicity in Al/Ti superconducting single electron transistors", Applied Physics Letters **95**, 052503 (2009).

Maisi, V. F., S. V. Lotkhov, A. Kemppinen, A. Heimes, J. T. Muhonen, and J. P. Pekola, "Excitation of Single Quasiparticles in a Small Superconducting Al Island Connected to Normal-Metal Leads by Tunnel Junctions", Physical Review Letters **111**, 147001 (2013).

Manucharyan, V. E., "Superinductance", PhD thesis (Yale University, 2012).

Manucharyan, V. E., J. Koch, L. I. Glazman, and M. H. Devoret, "Fluxonium: single cooper-pair circuit free of charge offsets.", Science **326**, 113–6 (2009).

Martinis, J. M., M. Ansmann, and J. Aumentado, "Energy Decay in Superconducting Josephson-Junction Qubits from Nonequilibrium Quasiparticle Excitations", Physical Review Letters **103**, 097002 (2009).

Martinis, J. M., G. Hilton, K. Irwin, and D. Wollman, "Calculation of TC in a normal-superconductor bilayer using the microscopic-based Usadel theory", Nuclear Instruments and Methods in Physics Research Section A: Accelerators, Spectrometers, Detectors and Associated Equipment **444**, 23–27 (2000).

Masluk, N. A., I. M. Pop, A. Kamal, Z. K. Minev, and M. H. Devoret, "Microwave characterization of josephson junction arrays: Implementing a low loss superinductance", Physical Review Letters **109**, 137002 (2012).

Mears, C. A., S. E. Labov, and A. T. Barfknecht, "High-resolution superconducting x-ray detectors with two aluminum trapping layers", Journal of Low Temperature Physics **93**, 561–566 (1993).

Minev, Z. K., I. M. Pop, and M. H. Devoret, "Planar superconducting whispering gallery mode resonators", Applied Physics Letters **103**, 142604 (2013).

Mirrahimi, M., Z. Leghtas, V. V. Albert, S. Touzard, R. J. Schoelkopf, L. Jiang, and M. H. Devoret, "Dynamically protected cat-qubits: a new paradigm for universal quantum computation", New Journal of Physics **16**, 045014 (2014).

Monfardini, A., A. Benoit, A. Bideaud, N. Boudou, M. Calvo, P. Camus, C. Hoffmann, F.-X. Désert, S. Leclercq, M. Roesch, K. Schuster, P. Ade, S. Doyle, P. Mauskopf, E. Pascale, C. Tucker, A. Bourrion, J. Macias-Perez, C. Vescovi, A. Barishev, J. Baselmans, L. Ferrari, S. J. C. Yates, A. Cruciani, P. De Bernardis, S. Masi, C. Giordano, B. Marghesin, H. G. Leduc, and L. Swenson, "The Néel IRAM KID Arrays (NIKA)", Journal of Low Temperature Physics **167**, 834–839 (2012).

Mooij, J. E., T. P. Orlando, L. Levitov, L. Tian, C. H. van der Wal, and S. Lloyd, "Josephson persistent-current qubit", Science **285**, 1036–9 (1999).

Naaman, O. and J. Aumentado, "Time-domain measurements of quasiparticle tunneling rates in a single-Cooper-pair transistor", Physical Review B **73**, 172504 (2006).

Nguyen, H. Q., T. Aref, V. J. Kauppila, M. Meschke, C. B. Winkelmann, H. Courtois, and J. P. Pekola, "Trapping hot quasi-particles in a high-power superconducting electronic cooler", New Journal of Physics **15**, 085013 (2013).

Nsanzineza, I. and B. L. T. Plourde, "Trapping a Single Vortex and Reducing Quasiparticles in a Superconducting Resonator", Physical Review Letters **113**, 117002 (2014).

Nyquist, H., "Thermal Agitation of Electric Charge in Conductors", Physical Review **32**, 110–113 (1928).

Olivares, D. G., A. L. Yeyati, L. Bretheau, Ç. Ö. Girit, H. Pothier, and C. Urbina, "Dynamics of quasiparticle trapping in Andreev levels", Physical Review B **89**, 104504 (2014).

Oreg, Y., G. Refael, and F. von Oppen, "Helical Liquids and Majorana Bound States in Quantum Wires", Physical Review Letters **105**, 177002 (2010).

Paik, H., D. I. Schuster, L. S. Bishop, G. Kirchmair, G. Catelani, A. P. Sears, B. R. Johnson, M. J. Reagor, L. Frunzio, L. I. Glazman, S. M. Girvin, M. H. Devoret, and R. J. Schoelkopf, "Observation of high coherence in Josephson junction qubits measured in a three-dimensional circuit QED architecture.", Physical Review Letters **107**, 240501 (2011).

Patel, U., I. V. Pechenezhskiy, B. L. T. Plourde, M. G. Vavilov, and R. McDermott, "Phonon-mediated quasiparticle poisoning of superconducting microwave resonators", Physical Review B **96**, 220501 (2017).

Pekola, J. P., D. V. Anghel, T. I. Suppula, J. K. Suoknuuti, A. J. Manninen, and M. Manninen, "Trapping of quasiparticles of a nonequilibrium superconductor", Applied Physics Letters **76**, 2782–2784 (2000).

Pekola, J. P., J. J. Vartiainen, M. Möttönen, O.-P. Saira, M. Meschke, and D. V. Averin, "Hybrid single-electron transistor as a source of quantized electric current", Nature Physics **4**, 120–124 (2008).

Peltonen, J. T., J. T. Muhonen, M. Meschke, N. B. Kopnin, and J. P. Pekola, "Magnetic-field-induced stabilization of nonequilibrium superconductivity in a normal-metal/insulator/superconductor junction", Physical Review B **84**, 220502 (2011).

Pop, I. M., T. Fournier, T. Crozes, F. Lecocq, I. Matei, B. Pannetier, O. Buisson, and W. Guichard, "Fabrication of stable and reproducible submicron tunnel junctions", Journal of Vacuum Science & Technology B **30**, 010607 (2012).

Pop, I. M., K. Geerlings, G. Catelani, R. J. Schoelkopf, L. I. Glazman, and M. H. Devoret, "Coherent suppression of electromagnetic dissipation due to superconducting quasiparticles.", Nature **508**, 369–72 (2014).

Preskill, J., *Lecture notes for physics 229: Quantum information and computation* (California Institute of Technology, 1998).

Rajauria, S., L. M. A. Pascal, P. Gandit, F. W. J. Hekking, B. Pannetier, and H. Courtois, "Efficiency of quasiparticle evacuation in superconducting devices", Physical Review B **85**, 020505 (2012).

Redfield, A. G., "On the Theory of Relaxation Processes", IBM Journal of Research and Development **1**, 19–31 (1957).

Reed, M. D., L. DiCarlo, B. R. Johnson, L. Sun, D. I. Schuster, L. Frunzio, and R. J. Schoelkopf, "High-Fidelity Readout in Circuit Quantum Electrodynamics Using the Jaynes-Cummings Nonlinearity", Physical Review Letters **105**, 173601 (2010).

Ristè, D., C. C. Bultink, M. J. Tiggelman, R. N. Schouten, K. W. Lehnert, and L. DiCarlo, "Millisecond charge-parity fluctuations and induced decoherence in a superconducting transmon qubit.", Nature Communications **4**, 1913 (2013).

Riwar, R.-P., L. I. Glazman, and G. Catelani, "Dissipation by normal-metal traps in transmon qubits", Physical Review B **98**, 024502 (2018).

Riwar, R.-P., A. Hosseinkhani, L. D. Burkhart, Y. Y. Gao, R. J. Schoelkopf, L. I. Glazman, and G. Catelani, "Normal-metal quasiparticle traps for superconducting qubits", Physical Review B **94**, 104516 (2016).

Rooks, M. J., E. Kratschmer, R. Viswanathan, J. Katine, R. E. Fontana, and S. A. MacDonald, "Low stress development of poly(methylmethacrylate) for high aspect ratio structures", Journal of Vacuum Science & Technology B: Microelectronics and Nanometer Structures **20**, 2937 (2002).

Saira, O.-P., A. Kemppinen, V. F. Maisi, and J. P. Pekola, "Vanishing quasiparticle density in a hybrid Al/Cu/Al single-electron transistor", Physical Review B **85**, 012504 (2012).

Sank, D., Z. Chen, M. Khezri, J. Kelly, R. Barends, B. Campbell, Y. Chen, B. Chiaro, A. Dunsworth, A. Fowler, E. Jeffrey, E. Lucero, A. Megrant, J. Mutus, M. Neeley, C. Neill, P. J. J. O'Malley, C. Quintana, P. Roushan, A. Vainsencher, T. White, J. Wenner, A. N. Korotkov, and J. M. Martinis, "Measurement-Induced State Transitions in a Superconducting Qubit: Beyond the Rotating Wave Approximation", Physical Review Letters **117**, 190503 (2016).

Schoelkopf, R. J., A. A. Clerk, S. M. Girvin, K. W. Lehnert, and M. H. Devoret, "Qubits as Spectrometers of Quantum Noise", in *Quantum noise in mesoscopic physics* (Springer Netherlands, Dordrecht, 2003), pp. 175–203.

Schreier, J. A., A. A. Houck, J. Koch, D. I. Schuster, B. R. Johnson, J. M. Chow, J. M. Gambetta, J. Majer, L. Frunzio, M. H. Devoret, S. M. Girvin, and R. J. Schoelkopf, "Suppressing charge noise decoherence in superconducting charge qubits", Physical Review B **77**, 180502 (2008).

Sears, A. P., A. Petrenko, G. Catelani, L. Sun, H. Paik, G. Kirchmair, L. Frunzio, L. I. Glazman, S. M. Girvin, and R. J. Schoelkopf, "Photon shot noise dephasing in the strong-dispersive limit of circuit QED", Physical Review B **86**, 180504 (2012).

Segall, K., C. Wilson, L. Li, L. Frunzio, S. Friedrich, M. C. Gaidis, and D. E. Prober, "Dynamics and energy distribution of nonequilibrium quasiparticles in superconducting tunnel junctions", Physical Review B **70**, 214520 (2004).

Serniak, K., S. Diamond, M. Hays, V. Fatemi, S. Shankar, L. Frunzio, R. J. Schoelkopf, and M. H. Devoret, "Direct Dispersive Monitoring of Charge Parity in Offset-Charge-Sensitive Transmons", Physical Review Applied **12**, 014052 (2019).

Serniak, K., M. Hays, G. de Lange, S. Diamond, S. Shankar, L. D. Burkhart, L. Frunzio, M. Houzet, and M. H. Devoret, "Hot Nonequilibrium Quasiparticles in Transmon Qubits", Physical Review Letters **121**, 157701 (2018).

Shaw, M. D., J. Bueno, P. Day, C. M. Bradford, and P. M. Echternach, "Quantum capacitance detector: A pair-breaking radiation detector based on the single Cooper-pair box", Physical Review B **79**, 144511 (2009).

Shaw, M. D., R. M. Lutchyn, P. Delsing, and P. M. Echternach, "Kinetics of nonequilibrium quasiparticle tunneling in superconducting charge qubits", Physical Review B **78**, 024503 (2008).

Slichter, D. H., R. Vijay, S. J. Weber, S. Boutin, M. Boissonneault, J. M. Gambetta, A. Blais, and I. Siddiqi, "Measurement-Induced Qubit State Mixing in Circuit QED from Up-Converted Dephasing Noise", Physical Review Letters **109**, 153601 (2012).

Smith, W. C., A. Kou, U. Vool, I. M. Pop, L. Frunzio, R. J. Schoelkopf, and M. H. Devoret, "Quantization of inductively shunted superconducting circuits", Physical Review B **94**, 144507 (2016).

Stone, K. J., K. G. Megerian, P. K. Day, P. M. Echternach, J. Bueno, and N. Llombart, "Real time quasiparticle tunneling measurements on an illuminated quantum capacitance detector", Applied Physics Letters **100**, 263509 (2012).

Sun, L., L. DiCarlo, M. D. Reed, G. Catelani, L. S. Bishop, D. I. Schuster, B. R. Johnson, G. A. Yang, L. Frunzio, L. Glazman, M. H. Devoret, and R. J. Schoelkopf, "Measurements of Quasiparticle Tunneling Dynamics in a Band-Gap-Engineered Transmon Qubit", Physical Review Letters **108**, 230509 (2012).

Taupin, M., I. M. Khaymovich, M. Meschke, A. S. Mel'nikov, and J. P. Pekola, "Tunable quasiparticle trapping in Meissner and vortex states of mesoscopic superconductors", Nature Communications **7**, 10977 (2016).

Teufel, J. D., T. Donner, D. Li, J. W. Harlow, M. S. Allman, K. Cicak, A. J. Sirois, J. D. Whittaker, K. W. Lehnert, and R. W. Simmonds, "Sideband cooling of micromechanical motion to the quantum ground state", Nature **475**, 359–363 (2011).

Tinkham, M., *Introduction to Superconductivity* (Dover Publications, 2004).

Tosi, L., C. Metzger, M. F. Goffman, C. Urbina, H. Pothier, S. Park, A. L. Yeyati, J. Nygård, and P. Krogstrup, "Spin-Orbit Splitting of Andreev States Revealed by Microwave Spectroscopy", Physical Review X **9**, 011010 (2019).

van Woerkom, D. J., A. Geresdi, and L. P. Kouwenhoven, "One minute parity lifetime of a NbTiN Cooper-pair transistor", Nature Physics **11**, 547–550 (2015).

Verney, L., R. Lescanne, M. H. Devoret, Z. Leghtas, and M. Mirrahimi, "Structural Instability of Driven Josephson Circuits Prevented by an Inductive Shunt", Physical Review Applied **11**, 024003 (2019).

Vion, D., A. Aassime, A. Cottet, P. Joyez, H. Pothier, C. Urbina, D. Esteve, and M. H. Devoret, "Manipulating the quantum state of an electrical circuit", Science **296**, 886–9 (2002).

Visser, P. J. de, J. J. A. Baselmans, J. Bueno, N. Llombart, and T. M. Klapwijk, "Fluctuations in the electron system of a superconductor exposed to a photon flux.", en, Nature Communications **5**, 3130 (2014).

Visser, P. J. de, D. J. Goldie, P. Diener, S. Withington, J. J. A. Baselmans, and T. M. Klapwijk, "Evidence of a Nonequilibrium Distribution of Quasiparticles in the Microwave Response of a Superconducting Aluminum Resonator", Physical Review Letters **112**, 047004 (2014).

Vool, U., I. M. Pop, K. Sliwa, B. Abdo, C. Wang, T. Brecht, Y. Y. Gao, S. Shankar, M. Hatridge, G. Catelani, M. Mirrahimi, L. Frunzio, R. J. Schoelkopf, L. I. Glazman, and M. H. Devoret, "Non-Poissonian Quantum Jumps of a Fluxonium Qubit due to Quasiparticle Excitations", Physical Review Letters **113**, 247001 (2014).

Vool, U. and M. Devoret, "Introduction to quantum electromagnetic circuits", International Journal of Circuit Theory and Applications **45**, 897–934 (2017).

Wang, C., C. Axline, Y. Y. Gao, T. Brecht, Y. Chu, L. Frunzio, M. H. Devoret, and R. J. Schoelkopf, "Surface participation and dielectric loss in superconducting qubits", Applied Physics Letters **107**, 162601 (2015).

Wang, C., Y. Y. Gao, I. M. Pop, U. Vool, C. Axline, T. Brecht, R. W. Heeres, L. Frunzio, M. H. Devoret, G. Catelani, L. I. Glazman, and R. J. Schoelkopf, "Measurement and control of quasiparticle dynamics in a superconducting qubit.", en, Nature Communications **5**, 5836 (2014).

Wang, Z., S. Shankar, Z. Minev, P. Campagne-Ibarcq, A. Narla, and M. Devoret, "Cavity Attenuators for Superconducting Qubits", Physical Review Applied **11**, 014031 (2019).

Wangsness, R. K. and F. Bloch, "The Dynamical Theory of Nuclear Induction", Physical Review **89**, 728–739 (1953).

Wenner, J., Y. Yin, E. Lucero, R. Barends, Y. Chen, B. Chiaro, J. Kelly, M. Lenander, M. Mariantoni, A. Megrant, C. Neill, P. J. J. O'Malley, D. Sank, A. Vainsencher, H. Wang, T. C. White, A. N. Cleland, and J. M. Martinis, "Excitation of Superconducting Qubits from Hot Nonequilibrium Quasiparticles", Physical Review Letters **110**, 150502 (2013).

Woods, W., G. Calusine, A. Melville, A. Sevi, E. Golden, D. K. Kim, D. Rosenberg, J. L. Yoder, and W. D. Oliver, "Determining Interface Dielectric Losses in Superconducting Coplanar-Waveguide Resonators", Physical Review Applied **12**, 014012 (2019).

Yamamoto, T., Y. A. Pashkin, O. Astafiev, Y. Nakamura, and J. S. Tsai, "Demonstration of conditional gate operation using superconducting charge qubits", Nature **425**, 941–944 (2003).

Yan, F., S. Gustavsson, A. Kamal, J. Birenbaum, A. P. Sears, D. Hover, T. J. Gudmundsen, D. Rosenberg, G. Samach, S. Weber, J. L. Yoder, T. P. Orlando, J. Clarke, A. J. Kerman, and W. D. Oliver, "The flux qubit revisited to enhance coherence and reproducibility", Nature Communications **7**, 12964 (2016).

Yavilberg, K., E. Ginossar, and E. Grosfeld, "Fermion parity measurement and control in Majorana circuit quantum electrodynamics", Physical Review B **92**, 075143 (2015).

You, J. Q., X. Hu, S. Ashhab, and F. Nori, "Low-decoherence flux qubit", Physical Review B **75**, 140515 (2007).

Yu, T. and J. H. Eberly, "Qubit disentanglement and decoherence via dephasing", Physical Review B **68**, 165322 (2003).

Zhao, S., D. J. Goldie, C. N. Thomas, and S. Withington, "Calculation and measurement of critical temperature in thin superconducting multilayers", Superconductor Science and Technology **31**, 105004 (2018).

Zhu, G., D. G. Ferguson, V. E. Manucharyan, and J. Koch, "Circuit QED with fluxonium qubits: Theory of the dispersive regime", Physical Review B **87**, 024510 (2013).